The detection of defects in tubes and plates using guided waves

Bradley Oaker

For completion of a

Masters in Science in Mechanical Engineering

August 2011

For completion of a

Masters in Science in Mechanical Engineering

Declaration

I declare that:

- I know that plagiarism is wrong. Plagiarism is to use another's work and to pretend that it is one's own.
- All sources of information in this report have been clearly referenced according to IEEE convention.
- This report is my own work. I have and will not allow any other person to use this report, or parts of it and pass it off as their own work.

Bradley Oaker (Student No.: OKRBRA001)

August 2011

Acknowledgement

The author would like to express his thanks to the following people:

- To my wife, Bertha for her unwavering support and inspiration throughout this project and my children, Bronte and Brinlee for their understanding.
- To my supervisor, Prof. Bob Tait, for his guidance and assistance on a continuous basis, throughout the project.
- To Dr Philip Loveday and the team at CSIR for their insights into guided waves and assistance in making their facilities available for testing.
- To Graham Wilson for his assistance and insights in ultrasonic NDE in general.
- To Professor Peter Cawley and Andrea Galvagni for their assistance with modelling of ultrasonic guided waves and hosting me at Imperial College, London.

I was most grateful for their help and would not have been able to complete this Thesis without their help and support.

Thank you

Bradley Oaker

Abstract

Eddy current testing is the non-destructive test method of choice for the inspection of condenser tubes. However, unplanned shutdowns of power stations, due to unexpected condenser tube failures, still occur despite rigorous eddy current inspection programs. In addition to the improvement required in the reliability of inspections, there is also a need to shorten the duration of inspections. Ultrasonic guided waves have the ability to inspect the full volume of the tube from a single location and although guided wave techniques cannot determine the remaining wall thickness, it is a potential candidate to supplement eddy current inspection methods, and bring about an improvement in inspection reliability and inspection rate.

Inspection methods that use guided waves are complex and require expensive equipment that is not readily available. The first part of this thesis concerns the use of basic, conventional (bulk wave) ultrasonic equipment to generate guided waves in plates and tubes. It serves to reinforce the theoretical concepts of guided waves but also provides an opportunity to perform preliminary tests prior to more advance testing of condenser tubes. A novel method that exploits the successive group velocity minima of the S_m and A_m modes (m = 1, 2, 3…) is applied to mild steel plates of varying thickness to explore guided wave concepts. It was found that a 4MHz shear wave transducer, excited by a spike generator, produces good directionality, coherence and sensitivity over a distance of approximately 300mm in plates. A 1MHz longitudinal wave transducer produced equally good results over a distance of 800mm in copper tubes. Defects with a cross sectional area of the order of 0.4mm^2 were detected using this system. These group velocity minima also exist for tubes and it is recommended that further research be conducted to exploit this novel idea both to develop the understanding and for potential industrial applications.

Limited research has been conducted that investigates the capability of guided wave inspection methods to detect defects that represent a wall loss of less than 1% of the tube's cross sectional area. Isolated pitting in condenser tubes can achieve through wall depth while still having a wall loss of less than 1% of the tube cross sectional area. A laser vibrometer outputs a toneburst signal which excites a transducer to generate the L(0,2) mode at frequencies of 120kHz, 135kHz and 150kHz in 1.8m length copper tubes. The reflected signals' axial displacement is measured at 48 nodes around the circumference of the tube. This aspect of the thesis investigates the interaction of the L(0,2) ultrasonic guided wave mode with isolated pitting and ammonia grooving defects, simulated by machined holes and grooves. In particular, the capability of the method to detect pits with a cross sectional area ranging from 0.2mm^2 (0.3% of the tube cross sectional area) to 1mm^2 (1.5%) is investigated in 22mm OD condenser tubes. The ability to distinguish between pitting and grooving is also explored.

It was found that a 0.2mm^2 pit could be detected experimentally and that a pit could be distinguished from a groove using guided waves. The experimental results were supported by the results obtained from modelling.

Contents

List of Figures

List of Tables

Chapter 1

Introduction

1.1 Background and motivation

In the electric power generation industry, exhaust steam from the turbines is condensed inside a condenser. The condenser is a heat exchanger that cools the steam and it also serves the purpose of a large reservoir from where the condensed steam is extracted and returned to a boiler. The transfer of heat takes place across the surface of thousands of tubes in the condenser. These tubes are subjected to a harsh environment and require periodic testing to confirm their structural integrity. Eddy current testing is the non-destructive test method of choice for the inspection of condenser tubes. There is an abundance of highly skilled eddy current operators that apply robust, tried and tested procedures. However, unplanned power station shutdowns in Eskom[1] due to unexpected condenser tube failures have occurred despite a rigorous eddy current inspection program. At one power station in South Africa, over a period of 4 months and involving 6 units, 17 individual tube leak events occurred resulting in a loss of more than 68000MWh over that period. A bar chart of the number of tube leaks at each major power station over the years 2009 and 2010 is shown in Figure 1.1 [1]. The tube leaks are widespread and lead to deterioration in secondary system chemistry, which has a negative impact on the long term reliability of the feed water systems and boiler tubes. The latter aspect

[1] Eskom is the South African electric power utility with an installed generating capacity of over 40 000MW.

often leads to far more significant production loss and costly repairs. Furthermore, in periodic inspections, only a small percentage of the total number of tubes in the condenser is inspected, due to the limited time available. This further increases the probability of unexpected tube failure because tubes with defects may not all be inspected. These shortcomings have highlighted the need for an alternative or supplementary non-destructive test method that would be fast and enable more tubes to be inspected in a shorter period of time. The alternative method would still need to have a high degree of defect detection capability. Appropriate action can then be taken timeously to prevent unexpected condenser tube failures.

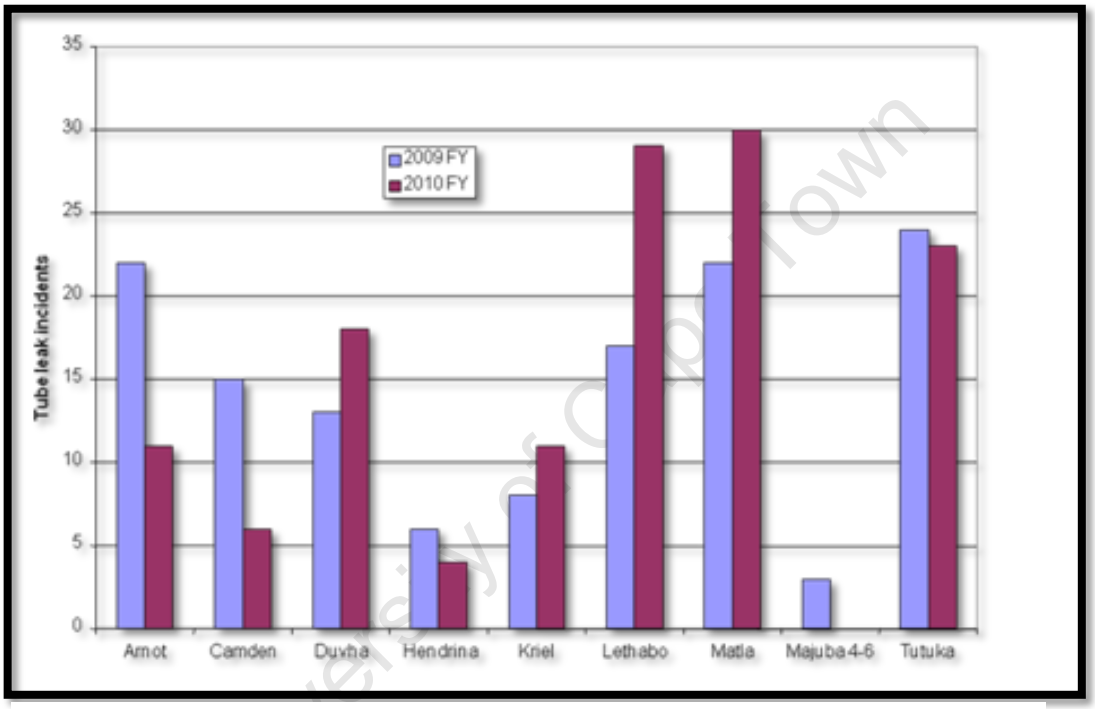

Figure 1.1: The number of condenser tube leaks at various power stations in 2009 and 2010. The 2010 Figures are cumulative to August 2010.

Ultrasonic guided waves have been investigated and may provide the answer as an alternative or supplementary method of inspecting condenser tubes as noted by several authors [2], [3], [4]. Their findings, whilst promising, have not lead to widespread implementation of ultrasonic guided waves as a suitable supplementary method of condenser tube testing. Its main drawback is its inability to determine remaining wall thickness. However, its inherent advantages are that it can inspect the full volume of the tube from a single location resulting in a high inspection rate when compared to eddy current testing [5]. The ability to detect defects that represent a wall loss of less than 1% (in the order of 0.3%) as well as the ability to characterise defects present in condenser tubes (for example, distinguish between a pit and a groove) will enhance its usefulness as a screening tool to determine the health of condenser tubes.

In addition, several other applications for ultrasonic guided waves have also been proposed [6], [7], [8]. The long range inspection of piping has been shown to be commercially successful [9] however the application of guided waves for defect detection remains largely in the research and development stage. The equipment is expensive and generally there are limited numbers of skilled personnel to facilitate the study and application of guided waves. Benefit can perhaps be gained from the use of readily available, conventional (bulk wave) ultrasonic equipment to generate guided waves for research purposes and to facilitate the study of this complex technique that has thus far only had limited successful industrial application.

1.2 Ultrasonic guided waves

Ultrasonic guided waves may be regarded as elastic waves that propagate in a guide. They are different from the typical ultrasonic bulk waves in that an infinite number of modes exist and their velocity is dependent on frequency and the geometry of the waveguide which, in the context of this thesis, is either a tube or a plate. The velocity of guided waves as a function of frequency-thickness for a tube is displayed on a dispersion curve shown in Figure 1.2 (phase velocity) and Figure 1.3 (group velocity). The dispersion curve is an important concept in the study of guided waves. It provides valuable insights with regards to the guided wave modes present at various frequencies, the degree of dispersion of the modes, phase and group velocities and the effect of plate or tube thickness on velocity. The naming convention applicable for tubes is [10]:

Longitudinal modes: L(0, m),

Torsional modes: T(0, m),

Flexural modes: F(n, m).

Where n = 1, 2, 3... is the mode of flexing in the cylinder and m = 1, 2, 3... is the mode of vibration. 0 indicates the axisymmetric mode. The longitudinal modes and torsional modes are axisymmetric meaning that the wave shape is symmetric around the circumference as it propagates along the z-axis. The flexural modes on the other hand are non-axisymmetric. A detailed discussion on dispersion curves is provided in Chapter 2.

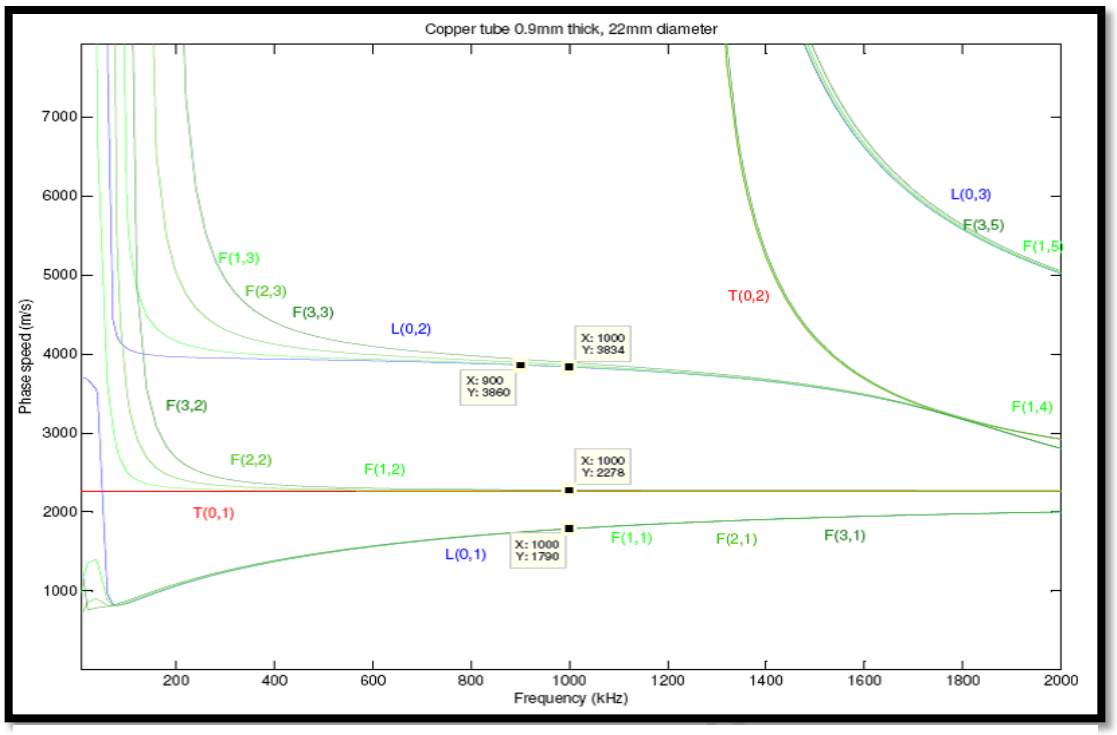

Figure 1.2: Phase velocity dispersion curves for 0.9mm thick, 22mm diameter copper tube.

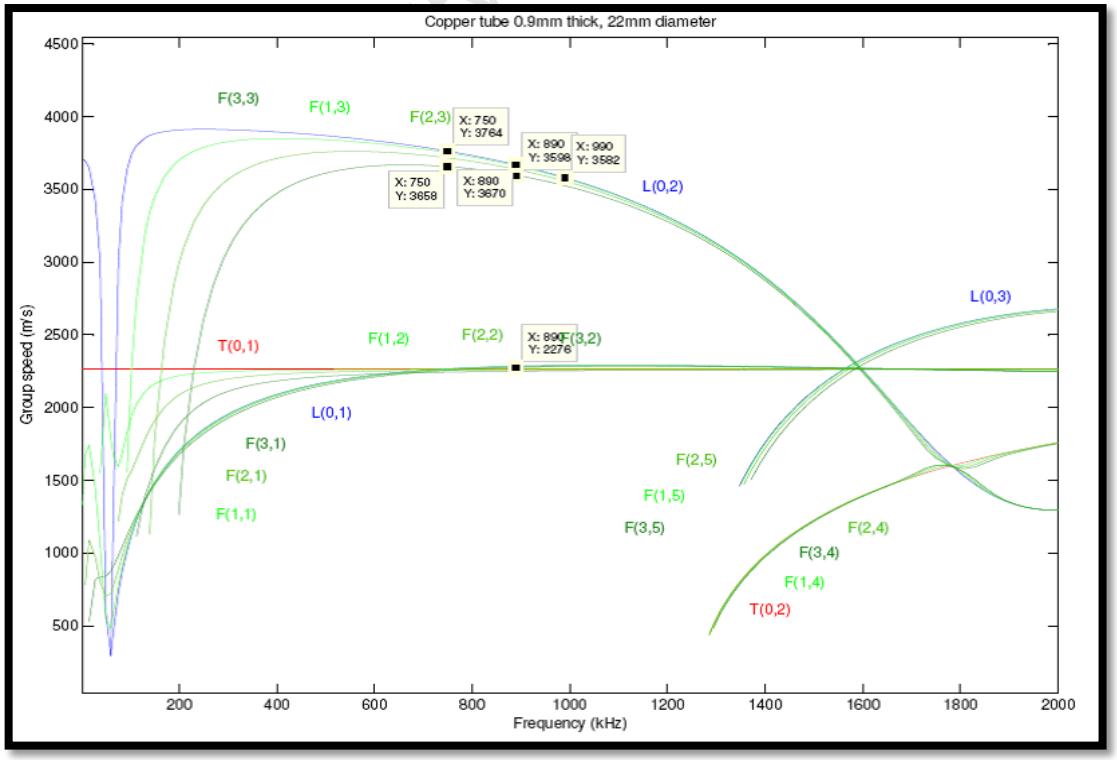

Figure 1.3: Group velocity dispersion curves for 0.9mm thick, 22mm diameter copper tube.

1.3 Thesis objectives

The objectives of this thesis are as follows:

First, a novel method of generating guided waves using standard, bulk wave equipment is investigated. Concepts of back wall reflection coefficient and mode conversion, synonymous with guided waves, are studied by inspecting various thickness mild steel plates, as well as copper tubes with drilled holes and machined slots, to simulate pits and grooves respectively.

Second, the objective is to assess the capability of the L(0,2) mode to detect isolated pitting along the length of copper condenser tubes. The pits have a cross sectional area of 0.2mm^2 (0.3% of the tube cross sectional area) to 1mm^2 (1.5%) which is amongst the smallest defects that have been investigated by researchers in this field [4]. The actual pit dimensions in this investigation are based on an experimental study of actual pit defects that have occurred in condenser tubes. The extent to which signal processing and mode separation can improve defect detection and recognition is also explored.

Finally, the capability of ultrasonic guided waves to go beyond just detection of defects in condenser tubes has been investigated. In particular, aspects such as the circumferential location of the defect and the ability to distinguish between an isolated pit and an ammonia groove are investigated. Here, reflection coefficients of the zero order and first order modes are studied based both on experimental results and on finite element modelling.

1.4 An overview of the thesis

This chapter provides the motivation for this thesis. It highlights the fact that an unacceptable failure rate of condenser tubes currently exist and that guided waves may be a potential candidate to improve both the rate and reliability of inspection. It also provides a basic understanding of one of the most important concepts in guided waves, namely the dispersion curve (dispersion curves are discussed in more detail in Chapter 2). The objectives of the thesis are then listed before providing an overview of the remaining contents of the thesis.

Chapter 2 provides the background relevant to the study. There are two main aspects discussed here, namely condenser tube defect characteristics and the fundamentals (theory) of guided waves. The section on condenser tube defect characteristics includes photographs of actual pitting, ammonia grooving and erosion defects. The failure mechanisms and defect geometry is described, as well as the challenges that the condenser design poses for a guided wave inspection system. This section provides the basis for the dimensions of the defects used in the

experimental study and the finite element model. It also provides typical tube plugging criteria. The section on the fundamentals of guided waves provides the background theory of guided waves in plates and tubes. The study includes both high frequency (1MHz to 4MHz) guided waves as well as lower frequency (120kHz to 150kHz) guided waves. It begins with Navier's wave equation and goes on to describe various types of guided waves. Dispersion curves for plates and tubes are then discussed in detail before describing the method for generating guided waves using Snell's law.

The literature review is provided in Chapter 3. The review covers research in the field of defect detection in plates, pipes and tubes using a range of guided wave modes and frequencies. It first discusses the history of guided waves including the work of pioneers in the field. The principles of guided wave mode selection, frequency variation and signal analyses are discussed next. The application of guided waves in industry is then provided which includes a review of the commercial systems available and some of their important performance characteristics. Relevant aspects of conventional bulk wave equipment are then described along with the advantages and disadvantages of guided wave and eddy current testing specifically relating to the inspection of condenser tubes. Finally, a summary of relevant work pertaining to defect detection and sizing in plates and tubes is provided.

Chapter 4 presents the experimental work conducted using basic, conventional (bulk wave) equipment to detect pits and grooves in steel plates and copper tubes. The experimental program which consists of three studies is provided first. A novel method of generating guided waves in steel plates using a 4MHz shear wave transducers is described next. This is followed by a description of the techniques applied to inspect 800mm length copper tubes using a 1MHz longitudinal wave transducer. The results of the three studies are then presented and discussed. A summary is provided at the end of the chapter.

Chapter 5 presents the experimental work conducted using a laser vibrometer at the CSIR[2] facilities in Tshwane, South Africa. The experimental details are provided first and include a description of the equipment layout and defect specifications. The methodology used to inspect copper tubes, 1.8m long containing pits and grooves is described next. The results of the experimental work is then presented and discussed before the chapter is summarised.

The procedures, results and discussion of the Finite Element modelling of the interaction of the L(0, 2) mode with pits and grooves in 200mm copper tube is provided in Chapter 6. The modelling is done using ***ABAQUS*** at the mechanical engineering facilities at Imperial College in London. A summary of the work is provided at the end of the chapter.

Chapter 7 provides a discussion on the important findings from the research conducted in Chapter 4 (conventional bulk wave equipment) and Chapter 5 (Laser vibrometer). Where relevant, reference is also made to the findings from the modelling.

Finally, Chapter 8 provides the conclusions and recommendations for future work.

[2] The Council for Scientific and Industrial Research (CSIR) is a South African governmental organisation tasked with research and development to improve the country's competitiveness and the quality of life of its people.

Chapter 2

Background to condenser tube defects and guided waves

2.1 Introduction

When developing an inspection method, it is important that the type of defect and the potential challenges to the inspection method are understood. The ultrasonic guided wave inspection method has many variables which can be changed to suit the application and ensure optimum detectability of the defect. The first part of this chapter describes the defect geometry that can be encountered in a condenser tube. The important design features of the condenser and condenser tubes as well as the tube plugging criteria are also discussed. In the second part of this chapter, the fundamentals (theory) of guided waves are discussed. It provides a theoretical understanding of the various guided wave concepts and serves as the foundation for the literature review provided in Chapter 3. The defect geometry used in the experimental work, discussed in Chapter 4 and Chapter 5, is based on the findings pertaining to the defect geometry in this chapter.

2.2 Condenser design and condenser tube failures

In order to determine the types of failures that occur in condenser tubes, a comprehensive review of failure investigations conducted over the last 15 years at various power stations in Eskom was undertaken. In addition, a detailed inspection of the condenser at one of the power stations was conducted and 10 full length tubes were extracted and both visually inspected and inspected using eddy current testing. Finally, personnel at the corrosion department in Eskom as well as the condenser asset management engineers were interviewed.

Several damage mechanisms that lead to condenser tube defects and condenser tube failures were identified. The most notable of these damage mechanisms are listed below, along with their primary defect type listed in brackets [11]:

- Dezincification (pitting and wall thinning)
- Microbiologically induced corrosion (MIC) (pitting)
- Condensate corrosion (grooving)
- Erosion-corrosion (wall thinning)
- Stress corrosion cracking (cracks)
- Under deposit corrosion (pitting)
- Vibration damage (fretting, cracking)

The above list is not exhaustive. A comprehensive account of condenser tube degradation methods can be found elsewhere [12], [13]. Three of the most common damage mechanisms affecting the Eskom condenser tubes, and resulting in unexpected failure, are identified and discussed in this section. These are:

- Wall thinning due to erosion.
- Ammonia grooving
- Pitting due to dezincification and MIC.

Wall thinning (erosion), generally occurs more gradually. Pitting and grooving defect profiles are investigated to determine their interaction with ultrasonic guided waves. These two defect profiles are considered an appropriate sample for the initial assessment of the effectiveness of guided waves as a suitable inspection method for condenser tubes for the following reasons:

- Pitting and grooving are amongst the most common defects experienced in condenser tubes and are a major cause of tube failures.
- Pitting has a very small cross-sectional area, even once it has reached through wall proportion. It therefore presents a significant challenge for NDT methods, particularly for thin wall tubing.
- Grooving has a significantly different profile to pitting. Grooves have shallow depth and a relatively long circumferential length while pits have negligible circumferential length but significant depth in relation to through wall thickness.

These two defect profiles potentially provide bounding cases for condenser tube defects that are predominantly circumferentially oriented (as opposed to axially oriented). In the next section, condenser design and tube specifications are discussed.

2.2.1 Condenser design and tube specifications

A large majority of the Eskom fleet use admiralty brass tubes in their condensers with titanium or stainless steel tubes in the air extraction zone. Copper tubes instead of admiralty brass tubes are used in some cases.

Typical condenser tube dimensions are as follows:

Dimension	Size range
Tube length	6.5m to 12m
Tube outside diameter	19mm to 25.4mm
Wall thickness	1mm to 1.5mm
Tube inside diameter	Approx. 17.5mm to 23.9mm

Table 2.1: The range of tube sizes used in the condensers.

Eskom operates typical steam surface condensers. A typical steam surface condenser is shown in Figure 2.1.

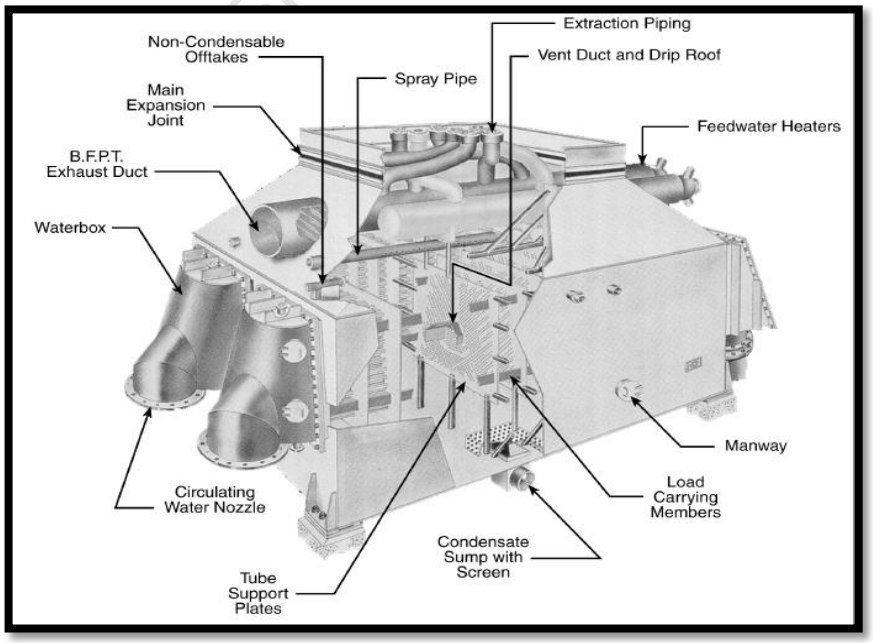

Figure 2.1: Typical steam surface condenser design [11].

An inspection of the condenser at a power station was undertaken in May 2010. Figure 2.2 and Figure 2.3 are pictures of the water box and steam space respectively of the condenser at the power station.

Figure 2.2: The inside of a water box at a power station. The condenser was in the process of being re-tubed.

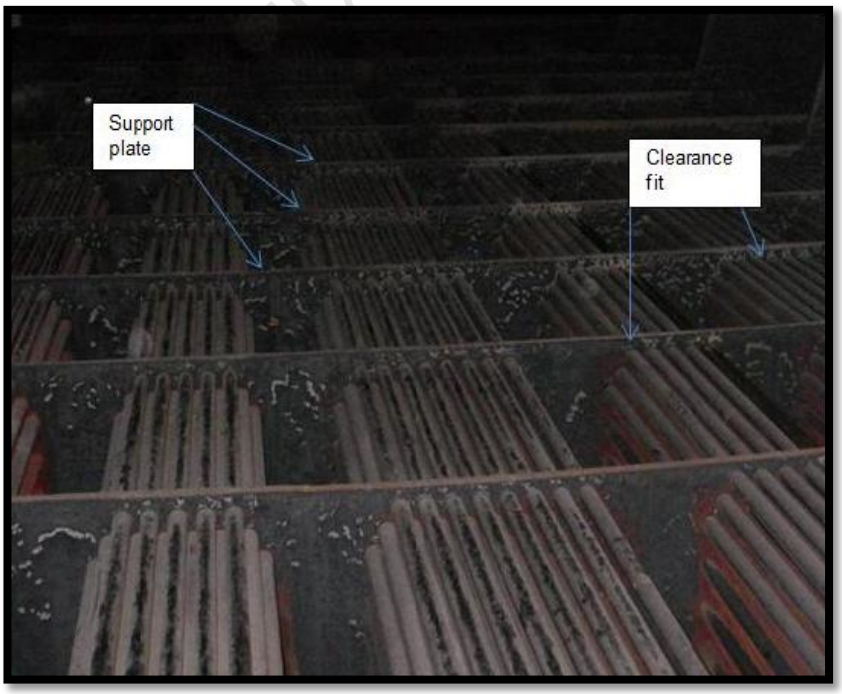

Figure 2.3: Condenser steam space showing the tube bundles and tube support plates.

The following design characteristics are considered relevant when applying guided waves as a defect detection method in condenser tubes:

- Tube lengths – high frequency has higher defect detection capability but higher attenuation [14].
- Accessibility – Access to the tube is through the water box and therefore the internal diameter of the tube at the tube sheet. The tube end can only be accessed with some difficulty.
- Tube sheet – the tube sheet provides interference at both ends of the tube. Typically, the tube is expanded into the tube sheet and leads to ultrasonic coupling between the tube and tube sheet as well as a change in the tube wall thickness and diameter. Reflection of the guided waves occur at the tube sheet with some energy loss into the tube sheet as a result of leakage [15].
- The tube support plates – the tubes rest onto the tube support plates which results in interference at the support. Reflection of the guided wave occurs at the location of the tube support plate [2]. The tube support plates present a significant challenge as interference may not be symmetric leading to non-axisymmetric reflection [16]. Furthermore, a significant percentage of energy may be reflected if the interference between the support plates and tube is significant.
- Seamless tubes – the tubes do not have bends (except for minimal sagging) and do not have a welded seam or any other welds.

Other design parameters noted and considered typical of several of the power station designs that are relevant for the inspection system are given in Table 2.2.

Parameter	Measure
Clearance of tube support plate and tube	0.4mm
Tube sheet material	Bronze
Tube sheet thickness	32mm – tube expanded
Tube support plate material	Mild steel
Support plate thickness	16mm
Distance between support plates	0.8m

Table 2.2: Relevant condenser dimensions and material properties.

The minimum available space perpendicular to the tube sheet in the water box is 0.8m. The tube bundle support plates (sag plates) provide a clearance fit for individual tubes. All tubes are

straight lengths (no bends).

2.2.2 Condenser tube damage mechanisms

As discussed in Section 1.2, from the review conducted of the failure investigation data, interviews with relevant staff and a comprehensive literature review, it was determined that there are three specific defect types that dominate. These are:

- Pitting due to dezincification and MIC.
- Wall thinning due to erosion.
- Ammonia grooving

Each of these is discussed below:

2.2.2.1 Pitting

Pitting is the most common defect type experienced in admiralty brass tubes. It can occur on both the inside and outside of the tube. Pitting is due to a variety of reasons; the most common are listed below [11]:

- Organic debris which decompose to form corrosive concentration of organic compounds (sulfides).
- Manganese precipitation leading to pitting corrosion.
- Microbiologically influenced corrosion.
- Plug type dezincification which is localised de-alloying of the material by an electrochemical process.
- Under deposit corrosion due to precipitation, particulate or biological fouling.
- Cavitation and erosion due to high velocity, turbulent flow and entrained bubbles.

The pit morphology and growth rates will vary depending on the underlying cause. Typical examples of pitting in condenser tubes are given in Figures 2.4 to 2.9 [17], [18], [19].

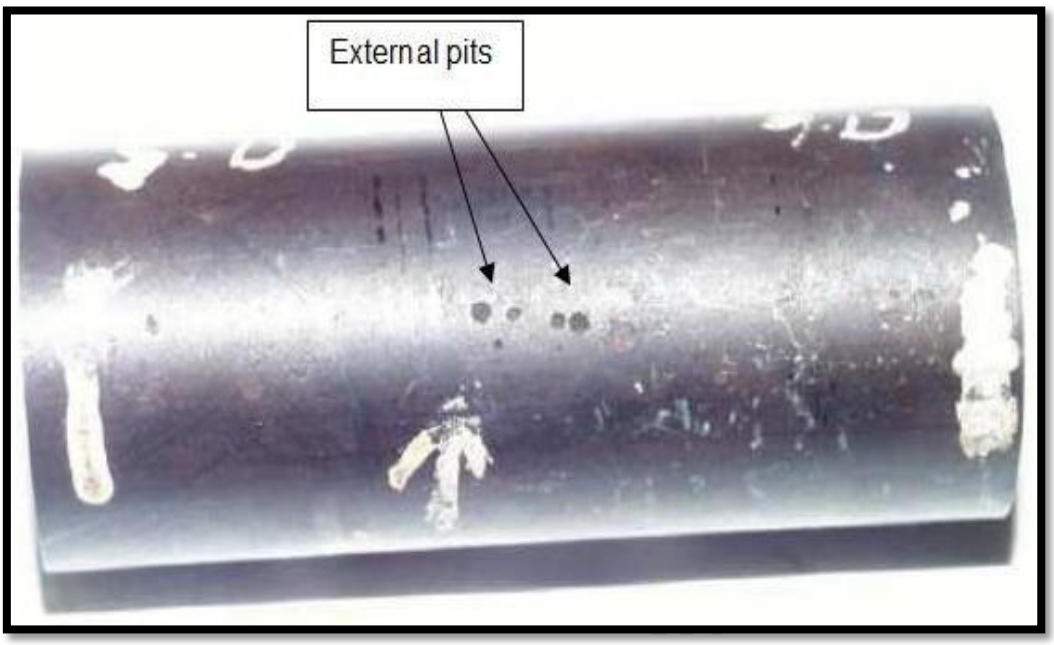

Figure 2.4: External pitting cluster in stainless steel tube [17].

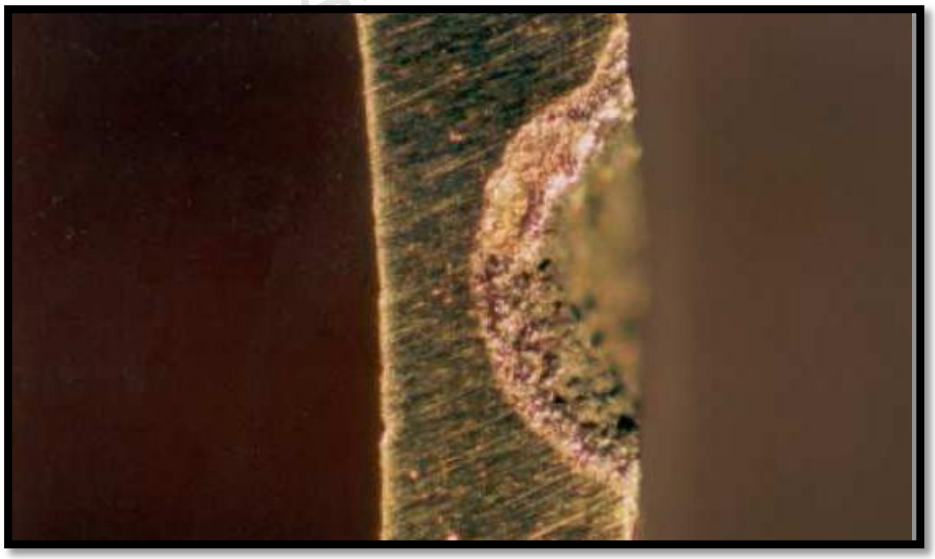

Figure 2.5: Profile of an external pit [17].

Figure 2.6: Internal pits filled with corrosive product [18].

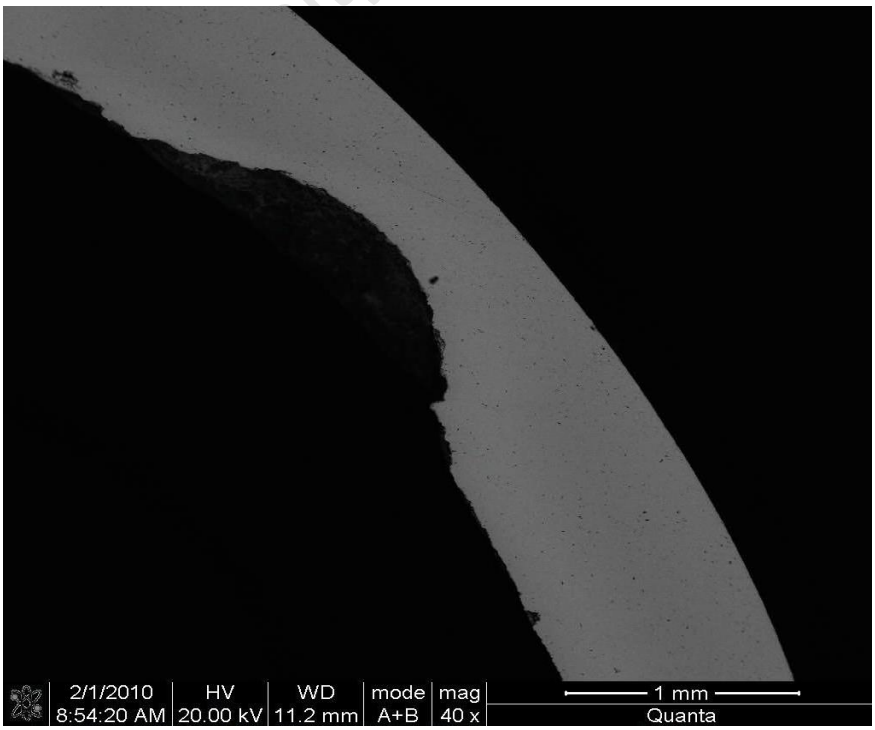

Figure 2.7: Scanning electron microscope (SEM) image of internal pit [19].

Figure 2.8: Isolated pit with asymmetrical shape [18].

Figure 2.9: Isolated, symmetrical pit [17].

Pitting was observed at any location along the length of the tube but was more common on the inside of the tube. When pitting occurred on the inside of the tube, it was more common on the bottom of the tube while the external pitting occurred more commonly at the top of the tube [11]. Diameter to depth ratio of the pit of 2.5 to 1 was typically observed however, given the broad range of underlying mechanisms, this could vary. Through thickness depth could be achieved while the defect cross sectional area remained below 1% of the tube cross sectional area [13]. Pitting occurred in clusters and as isolated cases.

2.2.2.2 Internal Erosion-Corrosion

Erosion-corrosion results in loss in wall thickness that is characterised by the direction of flow. The causes of erosion-corrosion are as follows:

- Turbulent, high velocity flow usually at the inlet to the tube.
- Excessive cleaning (mechanical or chemical) that results in the removal of the protective oxide layer.
- Obstruction of the tube or tube profile changes such as sleeves or dents that leads to turbulent flow at that location.
- Presence of silt, debris or other pollutants in the cooling water that causes abrasion and accelerated wear.

Depending on the above, wear rates could vary considerably. Examples of internal erosion-corrosion are illustrated in Figures 2.10 to 2.13 [17].

Figure 2.10: Internal erosion over long length [17].

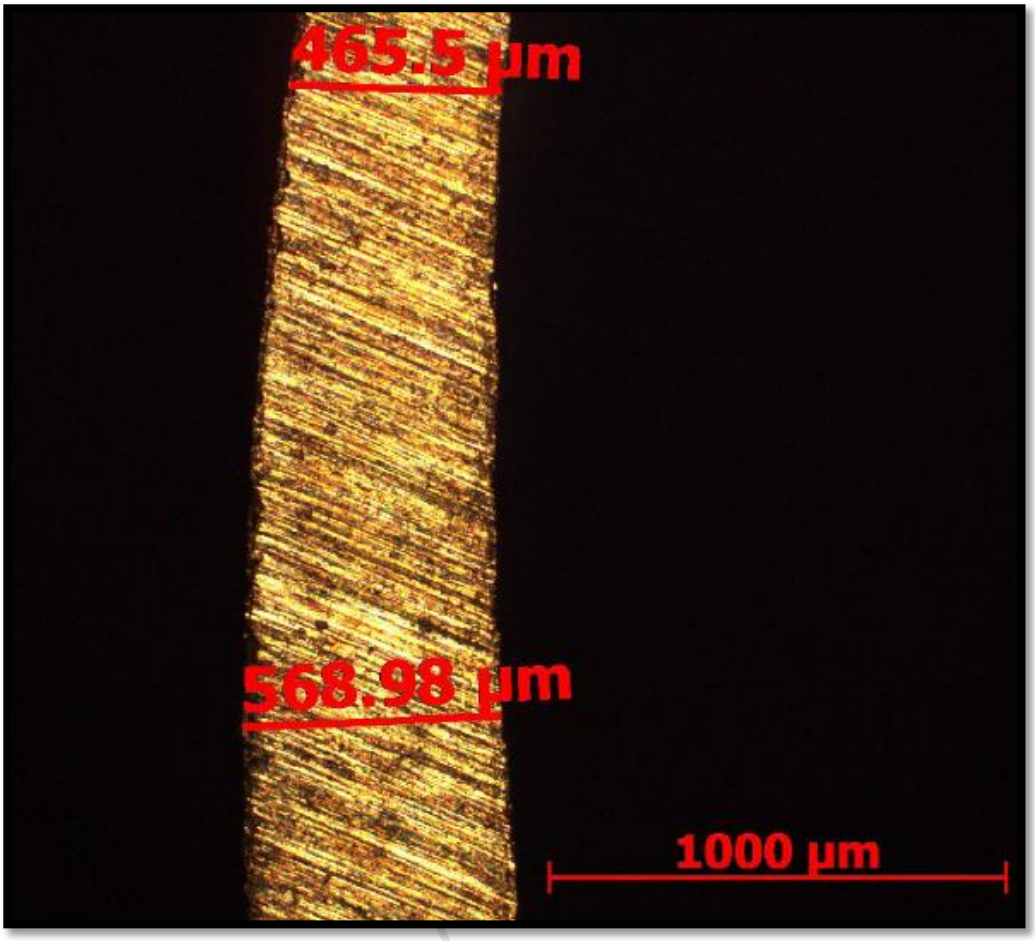

Figure 2.11: Internal erosion at different locations along the circumference.

Figure 2.12: Internal erosion at the end of sleeve [17].

Figure 2.13: Non-axisymmetric erosion over an extended length [17].

The wall loss experienced due to erosion-corrosion can vary in geometry depending on the underlying cause. Affected areas typically have a longitudinal length (along the tube axis) that is several times longer than the circumferential length. It can occur at any location along the tube but is more prevalent at the inlet to the tubes and do not extend around the full circumference. Erosion can present a complex profile that may present a significant challenge to simulate. An example of such an erosion defect is shown in Figure 2.14.

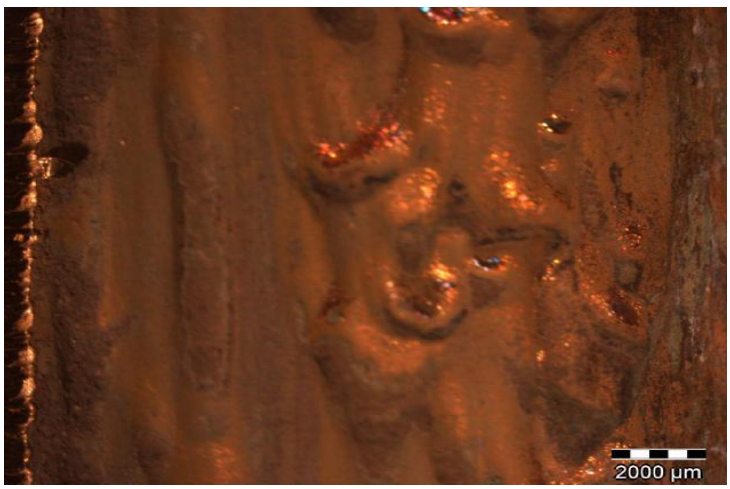

Figure 2.14: Erosion - complex profile of cavities.

2.2.2.3 Ammonia grooving

Ammonia grooving occurs when ammonia condensates collect on the outside of the tubes in the oxygen rich air extraction zone of the tube bundle. To mitigate this risk, most of the stations have titanium or stainless steel 316 tubes in their air extraction zone. Typical examples of ammonia grooving [17], [18], [20] are shown in Figures 2.15 to 2.17.

Figure 2.15: Ammonia grooving at an advanced stage [17].

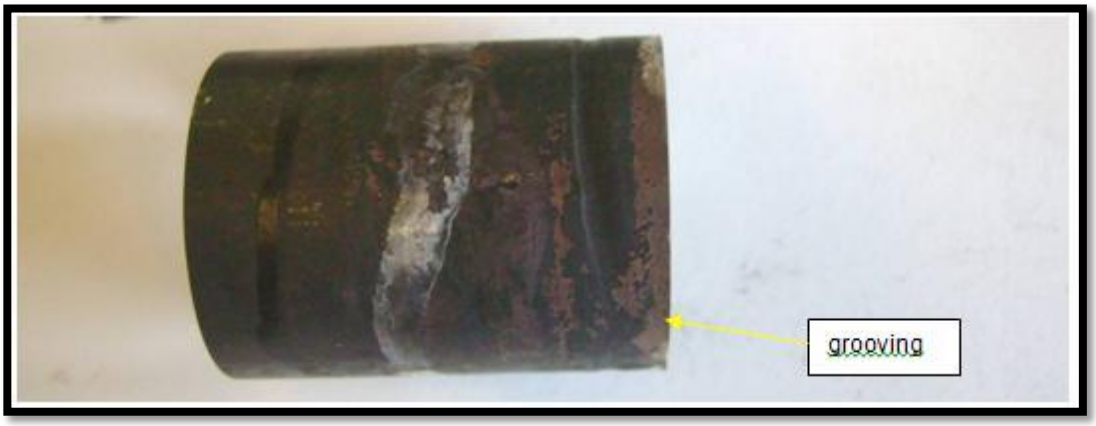

Figure 2.16: Ammonia grooving at a slight angle to the tube axis [18].

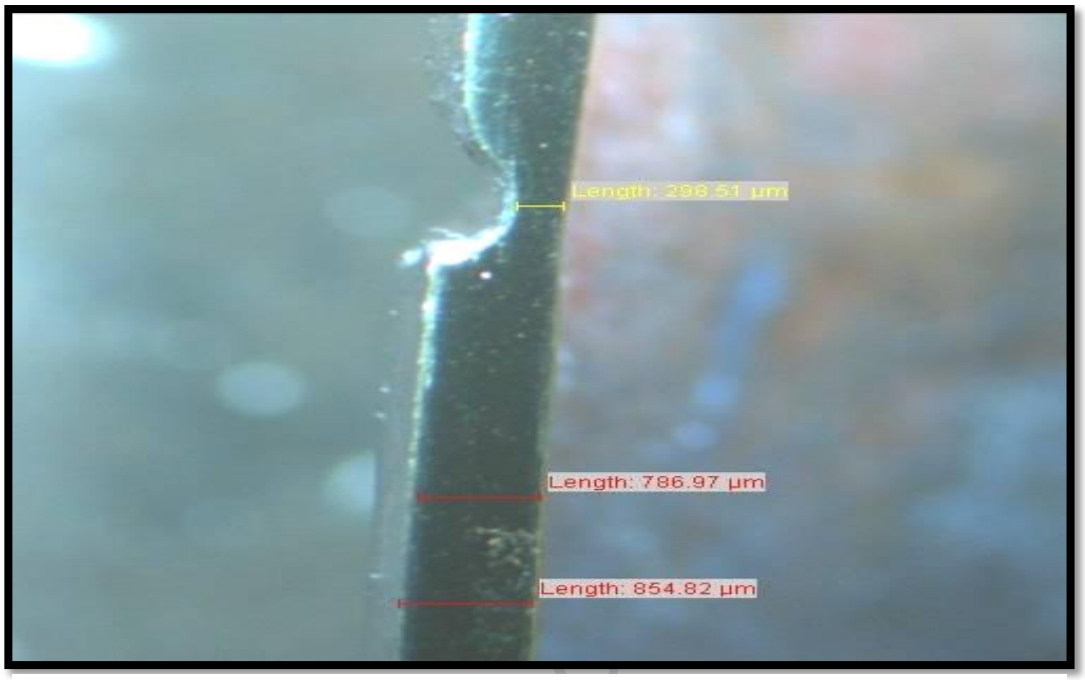

Figure 2.17 : Ammonia groove depth 0.7mm [20].

Ammonia grooving typically occurs close to support plates in the air extraction zone and typically do not extend beyond 50% of the circumference. The axial extent (width of groove) is usually consistent but may not be perpendicular to the axis of the tube and may instead have a slight angle (<10 degrees). The axial extent of grooves is typically between 1mm and 2mm.

2.2.3 Tube plugging criteria

An eddy current testing defect classification system applied in Eskom is shown below:

- Class A 0 to 20% wall loss
- Class B >20% to 40%wall loss
- Class C >40% to 60% wall loss
- Class D >60% to 80% wall loss
- Class E >80% to 100% wall loss

Common practice in Eskom is to plug tubes that have class D and E defects based on eddy current test results.

2.2.4 Eddy current test methods

Eddy current testing is the preferred non-destructive test method for inspecting condenser tubes and heat exchanger tubes in Eskom. It has however not always been effective in identifying defects timeously and as a result, has led to unplanned plant shutdowns as discussed earlier. The theory of eddy current testing is outside the scope of this thesis. However, for a review of the advantages and disadvantages of eddy current testing versus guided wave testing, see Chapter 3.

2.3 Fundamental theory of guided waves

Non-destructive testing (NDT) using guided waves is significantly more complex than classical ultrasonic techniques. This is largely as a result of the dispersive nature of the waves but also due to the influence that the structure's geometry has on the behaviour of the guided wave and the fact that multiple modes exist simultaneously [21].

The fundamentals of guided waves in plates, tubes and pipes are discussed in this section. It outlines the mathematical basis and behaviour of the various types of guided waves starting with Navier's wave equation. A thorough review of the mathematical relationships is important for the understanding of the dispersion curves and the particle motion of the various guided wave types. Dispersion curves and particle motion is discussed in detail and provides the basis for selecting the most appropriate modes in defect detection. Finally, methods of generating guided waves are discussed before conclusions are drawn.

Throughout the text, guided waves in plates are discussed first and the theory extended to guided waves in hollow cylinders (pipes and tubes).

2.3.1 The wave equation – bulk waves in plates

Navier's wave equation is given by:

$$\rho \frac{\partial^2 u}{\partial t^2} = (\chi + \mu)\nabla(\nabla \bullet u) + \mu \nabla^2 u \qquad (2.1)$$

Where u and ∇ are vectors in three dimensions that represent the particle displacement and the Laplacian respectively. The density, ρ, and Lame's constants, χ and μ, are the remaining variables. Equation 2.1 is the basis for the behaviour of all ultrasonic waves. The difference in

behaviour between the different types of ultrasonic waves depends on the boundary conditions of the medium or media in which the ultrasonic wave is propagating [22]. What follows is an abridged derivation of the mathematical equations that describe various types of ultrasonic guided waves in Cartesian (plates) and cylindrical (tubes and pipes) form. These mathematical equations are derived with varying degrees of detail by Rose [22], Cheeke and David [23], Viktorov [24], Achenbach [25], Auld [26] and Gazis [27].

The displacement can be rewritten [24] in the form of potentials ϕ (scalar) and ψ (vector) as:

$$\vec{u} = \overrightarrow{\nabla\phi} + \vec{\nabla} \times \overrightarrow{\psi} \qquad \text{or} \qquad \vec{u} = grad\phi + rot\,\psi \tag{2.2}$$

Substituting Equation 2.2 back into Equation 2.1 and applying the [3]Helmholtz identity in vector analysis we get (∇ and ψ are vectors in three dimensions):

$$\nabla\left(\rho\frac{\partial^2\phi}{\partial t^2} - (\chi + 2\mu)\nabla^2\phi\right) + \nabla\times\left(\rho\frac{\partial^2\psi}{\partial t^2} - \mu\nabla^2\psi\right) = 0 \tag{2.3}$$

The laplacian, ∇ is given by:

$$\nabla^2 = \frac{\partial^2}{\partial x^2} + \frac{\partial^2}{\partial y^2} + \frac{\partial^2}{\partial z^2}$$

The first term consisting of the scalar potential, ϕ is associated with longitudinal waves and the second term consisting of the vector potential, ψ is associated with transverse (shear) waves. The two terms can be separated as two independent equations which also mean that the transverse and the longitudinal waves are independent of each other in unbounded media and can be written as [22]:

[3] The Helmholtz identity states that a vector field can be resolved into a curl free component and a divergence free component as given in Equation 2.2.

$$\rho \frac{\partial^2 \phi}{\partial t^2} = (\chi + 2\mu)\nabla^2 \phi \quad (2.4)$$

$$\rho \frac{\partial^2 \psi}{\partial t^2} = \mu \nabla^2 \psi \quad (2.5)$$

In Cartesian form, with co-ordinates shown in Figure 2.18, the particle displacement equations are [25]:

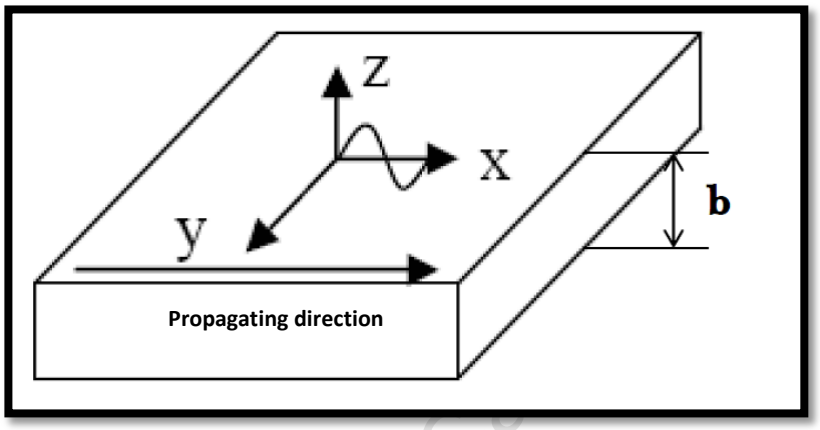

Figure 2.18: Cartesian co-ordinate system showing the wave propagation direction and corresponding particle motion planes.

$$u_x = \frac{\partial \phi}{\partial x} + \frac{\partial \psi_z}{\partial y} - \frac{\partial \psi_y}{\partial z} \quad (2.6)$$

$$u_y = \frac{\partial \phi}{\partial y} - \frac{\partial \psi_z}{\partial x} + \frac{\partial \psi_x}{\partial z} \quad (2.7)$$

$$u_z = \frac{\partial \phi}{\partial z} + \frac{\partial \psi_y}{\partial x} - \frac{\partial \psi_x}{\partial y} \quad (2.8)$$

Equation 2.4 and Equation 2.5 defines the bulk wave equations (travelling in the bulk of the material as opposed to the boundaries or interfaces where the wave is subjected to reflection and transmission and possible mode conversion) with longitudinal velocity, C_L and transverse velocity, C_T respectively.

With reference to Figure 2.18, propagation of the longitudinal (compression) and transverse (shear) waves occur in the x-direction. There are two shear modes, a shear vertical and a shear

horizontal mode. The shear horizontal mode has particle displacement in the y direction only while the shear vertical and the longitudinal waves have particle displacement in the z direction only. The wave motion is depicted in Figure 2.19 and Figure 2.20 [23].

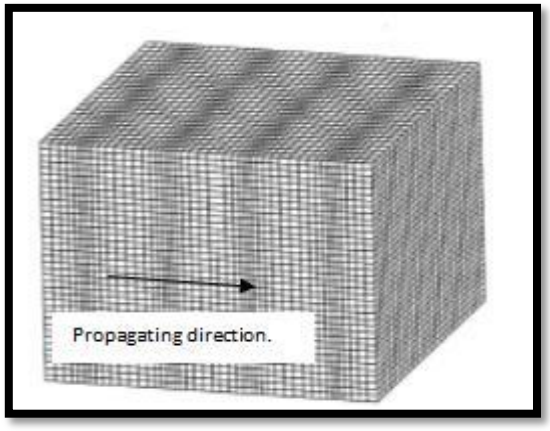

Figure 2.19: Shear vertical wave motion [23].

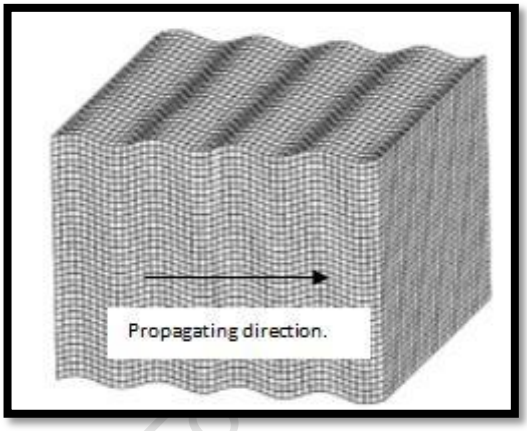

Figure 2.20: Longitudinal wave motion [23].

The velocity of both the longitudinal and shear vertical waves is constant and is given by Equation 2.9 and Equation 2.10.

$$c_T = \sqrt{\frac{E}{\rho}\frac{1}{2(1+\upsilon)}} = \sqrt{\frac{G}{\rho}} \tag{2.9}$$

$$c_L = \sqrt{\frac{E}{\rho}\frac{1-\upsilon}{(1+\upsilon)(1-2\upsilon)}} \tag{2.10}$$

E is Young's modulus, ν is Poisson's ratio and G is the modulus of rigidity. The shear horizontal wave is a guided wave having infinite number of modes with only the fundamental mode, SH_0 having a constant velocity. SH_0 is discussed in the next section.

2.3.2 Shear Horizontal modes

Shear horizontal waves is the simplest form of guided waves. The shear horizontal dispersion equation is given by Equation 2.11 [22].

$$\frac{\omega^2}{c_T^2} - \frac{\omega^2}{c_p^2} = \left(\frac{m\pi}{2b}\right)^2 \tag{2.11}$$

Where c_p is the phase velocity and ω is the angular frequency. The phase and group velocity for the shear horizontal wave is given by Equation 2.12 and 2.13 respectively [22]:

$$c_p(SH) = 2c_T\left[\frac{fb}{\sqrt{4(fb)^2 - m^2c_T^2}}\right] \tag{2.12}$$

$$c_g(SH) = c_T\left[\sqrt{1 - \frac{\left(\frac{m}{2}\right)^2}{\left(\frac{fb}{c_T}\right)^2}}\right] \tag{2.13}$$

The notation applied is SH_m where m = 0, 1, 2... , is the mode number. SH_0 is the fundamental mode and has a constant velocity, i.e. no dispersion such that:

$$c_g = c_p = c_T$$

The wave motion for shear horizontal waves is depicted in Figure 2.21 [14] and the phase velocity dispersion curve is given in Figure 2.22 [28]. Particle motion occurs in the y-direction only and wave propagation is in the x direction:

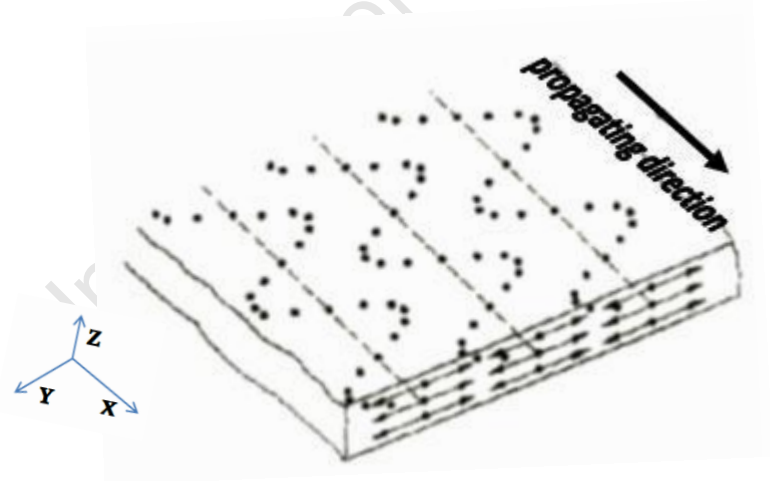

Figure 2.21: Wave propagation motion of SH modes. Particle motion is restricted to the y-direction only. Wave propagation is the x direction as shown [14].

The SH_0 mode is the subject of great interest and has been studied extensively for the following reasons (see for example Ratassepp et al [29], Kwun and Kim [30] and Rajagopal and Lowe [31]):

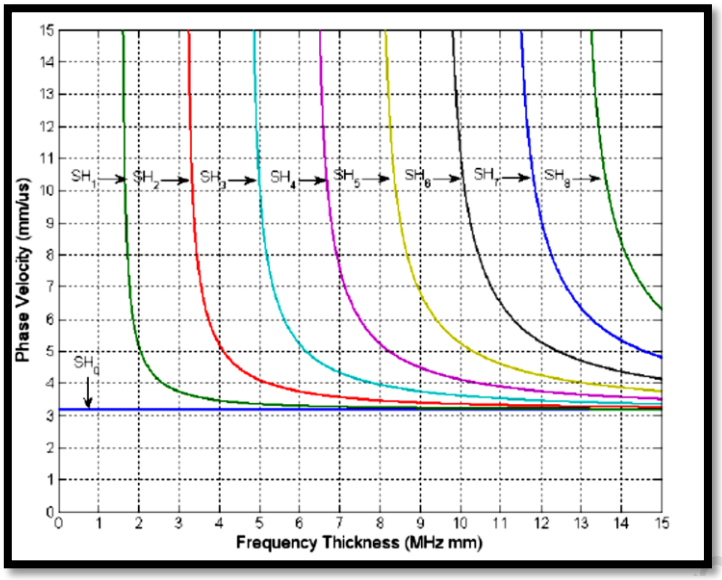

Figure 2.22: Dispersion curve for shear horizontal waves in steel plate [28].

- It has a constant velocity throughout the frequency thickness range.
- The in-plane particle motion makes it less susceptible to attenuation particularly when the test material is submerged in fluid or in physical contact with an external object.
- It is easily generated using magnetostriction and then less susceptible to generating unwanted modes.

An equivalent mode to SH modes that propagate in hollow cylinders is the torsional mode discussed later.

2.3.3 Rayleigh waves

Rayleigh waves are surface waves discovered by Lord Rayleigh [32]. They have strong similarities to the fundamental Lamb wave modes which are discussed in the next section. Rayleigh waves propagate at a constant velocity, C_R. From Equation (2.2):

$$\vec{u} = \overrightarrow{\nabla\phi} + \vec{\nabla} \times \overrightarrow{\psi}$$

It can be shown that the Rayleigh equation is given by [24]:

$$\eta^6 - 8\eta^4 + 8\left(3 - 2\xi^2\right)\eta^2 - 16\left(1 - \xi^2\right) = 0 \qquad (2.14)$$

Where

$$\eta = \frac{c_R}{c_T} \qquad \xi = \frac{c_T}{c_L}$$

C_L and C_T are the bulk wave velocities given by Equations 2.9 and 2.10 respectively. Equation 2.14 has one real root, η_R. An approximate solution to the Rayleigh equation is given by [24]:

$$\eta_R = \frac{0.87 + 1.12\upsilon}{1+\upsilon}$$

and

$$C_R = \frac{0.87 + 1.12\nu}{1+\nu} C_T \qquad (2.15)$$

The Rayleigh wave decays rapidly (but not to zero) along the z axis from the surface such that particle displacement is minimal beyond a depth of one wavelength, λ_R. Wave motion for a Rayleigh wave is depicted in Figure 2.23 [23].

The cylindrical Rayleigh waves that propagate in the θ direction (see Figure 2.25), travels at a slightly higher velocity [26]. The mathematical derivation is given by Auld [26] and is not repeated here.

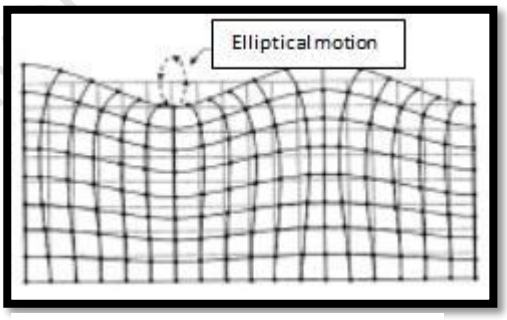

Figure 2.23: Rayleigh wave particle motion [23].

2.3.4 Lamb Waves in traction free plates

Lamb waves were discovered by Horace Lamb and published in his work, "On waves in an elastic plate" in 1917. It is often referred to as plate waves or Rayleigh-Lamb waves due to the

similarities in behaviour between the Rayleigh wave and particularly the fundamental Lamb wave modes, A_0 and S_0.

Once again, working from Equation 2.2,

$$\vec{u} = \overrightarrow{\nabla\phi} + \vec{\nabla} \times \overrightarrow{\psi}$$

The x and z components of particle displacement are given by Equations 2.6 and 2.8:

$$u_x = \frac{\partial \phi}{\partial x} + \frac{\partial \psi_z}{\partial z}$$

$$u_z = \frac{\partial \phi}{\partial z} - \frac{\partial \psi_x}{\partial x}$$

There is no y component of displacement. The particle displacement is shown in Figure 2.24. The possible solutions to the partial differential equations are obtained by applying the transverse resonance principle [26].

$$\phi(z) = A_1 \sin(k_L z) + A_2 \cos(k_L z) \tag{2.16}$$

$$\psi(z) = B_1 \sin(k_T z) + B_2 \cos(k_T z) \tag{2.17}$$

Where k_L and k_T are the Lamb wave numbers given by:

$$k_L^2 = \frac{\omega^2}{c_L^2} - \beta^2 \tag{2.18}$$

$$k_T^2 = \frac{\omega^2}{c_T^2} - \beta^2 \tag{2.19}$$

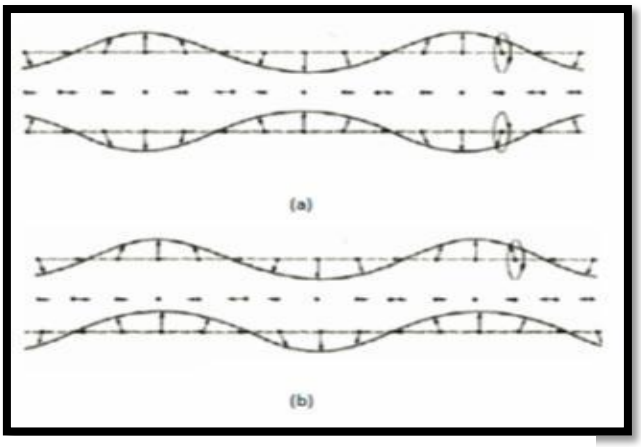

Figure 2.24: Symmetrical, (a), and asymmetrical, (b), Lamb waves in plates indicating the particle motion [23].

Applying stress free boundary conditions at the free surface where $z = \pm b/2$ we derive the Rayleigh-Lamb frequency equation [26]:

$$\frac{\tan\left(k_L \, b/2\right)}{\tan\left(k_T \, b/2\right)} = \frac{-\left(k_T^2 - \beta^2\right)^2}{4\beta^2 k_T k_L} \qquad \text{For symmetric modes} \qquad (2.20)$$

$$\frac{\tan\left(k_L \, b/2\right)}{\tan\left(k_T \, b/2\right)} = \frac{-4\beta^2 k_T k_L}{\left(k_T^2 - \beta^2\right)^2} \qquad \text{For anti-symmetric modes} \qquad (2.21)$$

The dispersion curves are obtained from Equation 2.20 and 2.21. The dispersion curves are discussed in Section 2.3.6. The naming convention for Lamb waves in plates is as follows:

- Symmetrical waves, S_m.
- Asymmetrical waves, A_m.

Where m = 0, 1, 2...

The mathematical relationship for guided waves in hollow cylinders is more complicated and is discussed in the next section.

2.3.5 Guided waves in traction free hollow cylinders

The mathematical relationship for guided waves in hollow cylinders is best described by Gazis [27] but a good account is also provided by Rose [22]. The corresponding analysis for a solid cylinder (rod) was derived by Meeker and Meitzler [33] but is not the subject of interest in this thesis. The cylindrical co-ordinate system applied is shown in Figure 2.25.

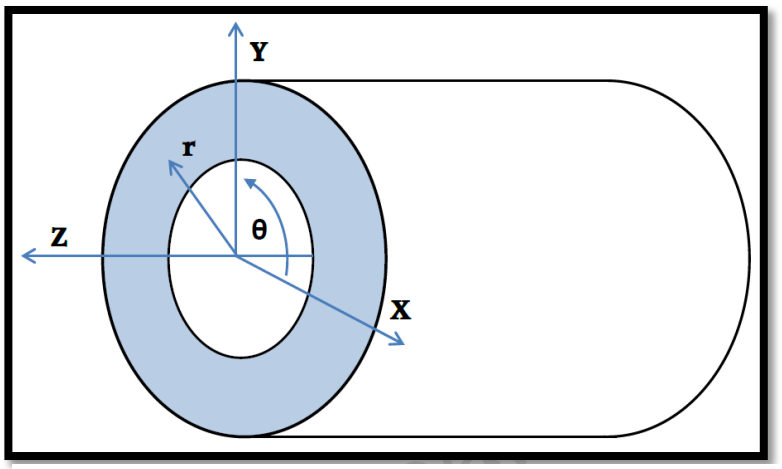

Figure 2.25: Cylindrical co-ordinate system applied.

Once again, Equation 2.1 provides the basis for the three modes of guided waves in hollow cylinders discussed here. The longitudinal modes and torsional modes are axisymmetric meaning that the wave shape is symmetric around the circumference as it propagates along the z-axis. The flexural modes on the other hand are non-axisymmetric. The assumed particle displacement components in the radial (r), circumferential (θ) and axial (z) directions are given by [27];

$$u_r = U_r \cos(n\theta)\cos(\omega t + kz)$$

$$u_\theta = U_\theta \sin(n\theta)\cos(\omega t + kz)$$

$$u_z = U_z \cos(n\theta)\sin(\omega t + kz)$$

Where U_r, U_θ and U_z represent functions composed of Bessel functions [34] and functions of r and n. The wave propagation motion is shown in Figures 2.26 to 2.28 [35]:

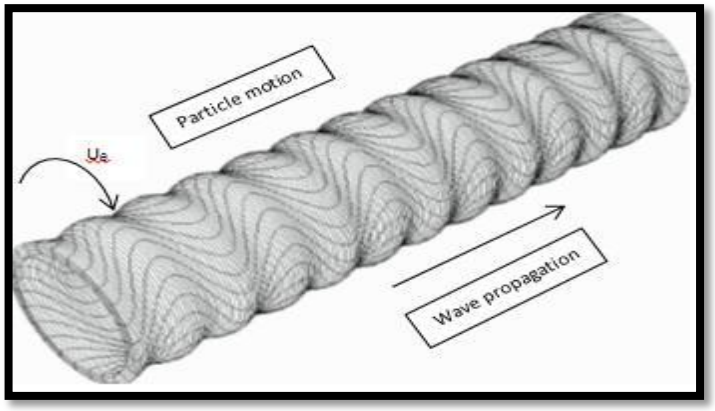

Figure 2.26: Torsional mode, T(0,1), showing particle motion (Uθ only) and wave propagation direction [35].

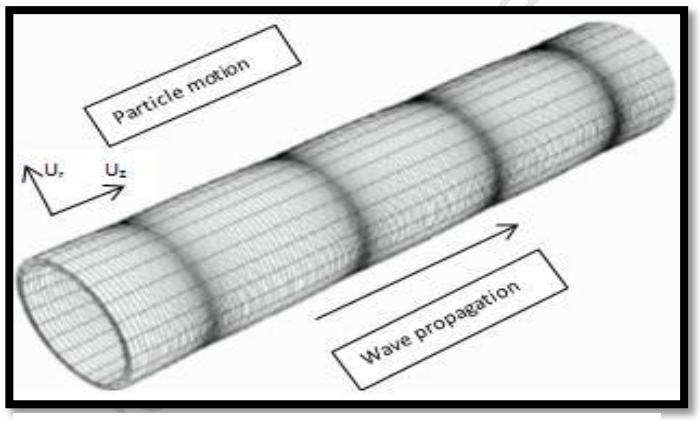

Figure 2.27: Longitudinal mode, L(0,m), showing particle motion (Ur and Uz) and wave propagation direction [35].

The particle motion for the longitudinal mode is restricted to the radial and axial direction. The particle motion for the torsional motion is in the circumferential direction only and the flexural mode particle motion is in the radial, circumferential and axial direction. The longitudinal, torsional and flexural modes are relevant to the inspection of condenser tubes using guided waves and are discussed further here and in later sections.

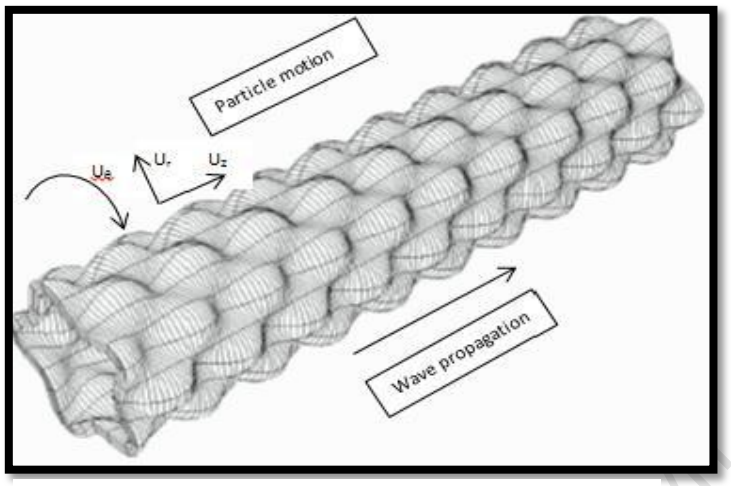

Figure 2.28: Flexural mode, F(n,m) showing particle motion (Ur, Uz and Uθ) and wave propagation direction [35].

The frequency equation for longitudinal modes up to the 6th order is given by Gazis [27]:

$$\begin{vmatrix} c_{11} & c_{12} & c_{14} & c_{15} \\ c_{31} & c_{32} & c_{34} & c_{35} \\ c_{41} & c_{42} & c_{44} & c_{45} \\ c_{61} & c_{62} & c_{64} & c_{65} \end{vmatrix} = 0 \qquad (2.22)$$

And the frequency equation for torsional modes up to the 6th order:

$$\begin{vmatrix} c_{23} & c_{26} \\ c_{53} & c_{56} \end{vmatrix} = 0 \qquad (2.23)$$

C_{ij} , i, j = 1 to 6, is composed of Bessel functions and functions of angular wave number, angular frequency, longitudinal velocities, transverse velocities and the radial dimensions. These frequency equations are solved using numerical methods to generate dispersion curves for guided waves in hollow cylinders, discussed in Section 2.3.6.

2.3.6 Dispersion Curves for plates and hollow cylinders

Dispersion curves are an essential element in the study of guided waves and provide many insights into the behaviour of guided waves. In order to plot the dispersion curve, the frequency equations, namely Equations 2.20 and 2.21 for plates and Equations 2.22 and 2.23 for cylinders, must be solved. As mentioned previously, the frequency equations cannot be solved by inspection and is solved using numerical methods. A detailed procedure for solving the frequency equations is provided by Rose [22]. Various methods and techniques have been applied to plot dispersion curves in plates and cylinders, see for example Honarvar et al [36], Kim et al [37] and Hayashi and Rose [38].

Software packages are available to plot dispersion curves for various materials and geometries. ***Disperse*** [39], ***PACshare*** (supplied by Physical Acoustics Corporation as shareware) and ***PCDISP*** [40] are three software tools that can plot dispersion curves. The latter two are available for download from http://www.pacndt.com and http://www.iai.csic.es respectively and have been used extensively for the plotting of the dispersion curves in the experimental and development work for this thesis. ***PACshare*** can plot dispersion curves in plates for a range of material types. It has useful zoom functions to obtain accurate data points. It does not provide plots for stress, displacement or energy distribution. Figure 2.29 and Figure 2.30 are plots of group velocity and phase velocity respectively for mild steel plate and a frequency-thickness product of 12MHz-mm. The plots are made using ***PACshare***. Figure 2.31 is a plot of a dispersion curve of group velocity for copper tubes with an outside diameter of 22mm and a wall thickness of 1mm using ***PCDISP***.

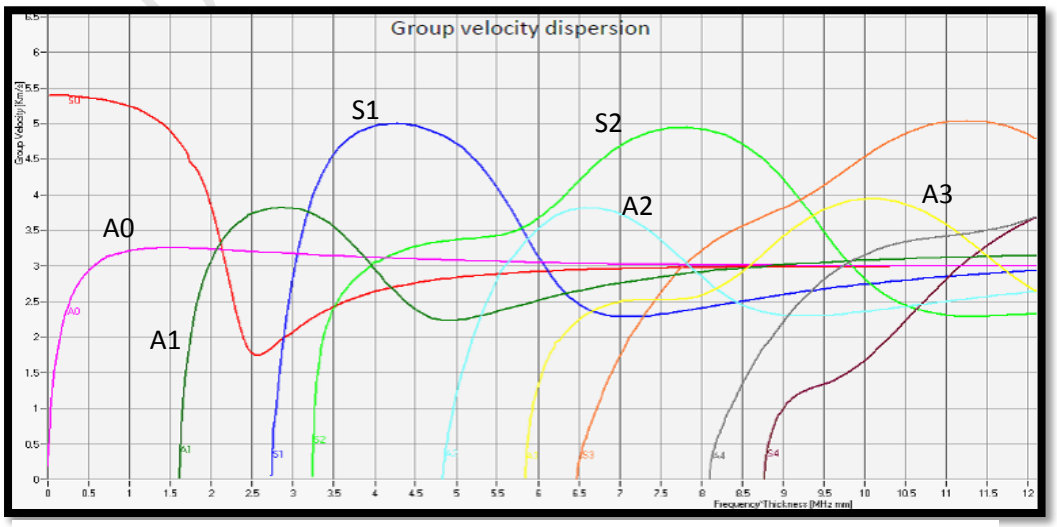

Figure 2.29: Group velocity dispersion curve for 3mm thick steel plate and a frequency of 4MHz using the *PACshare* software tool.

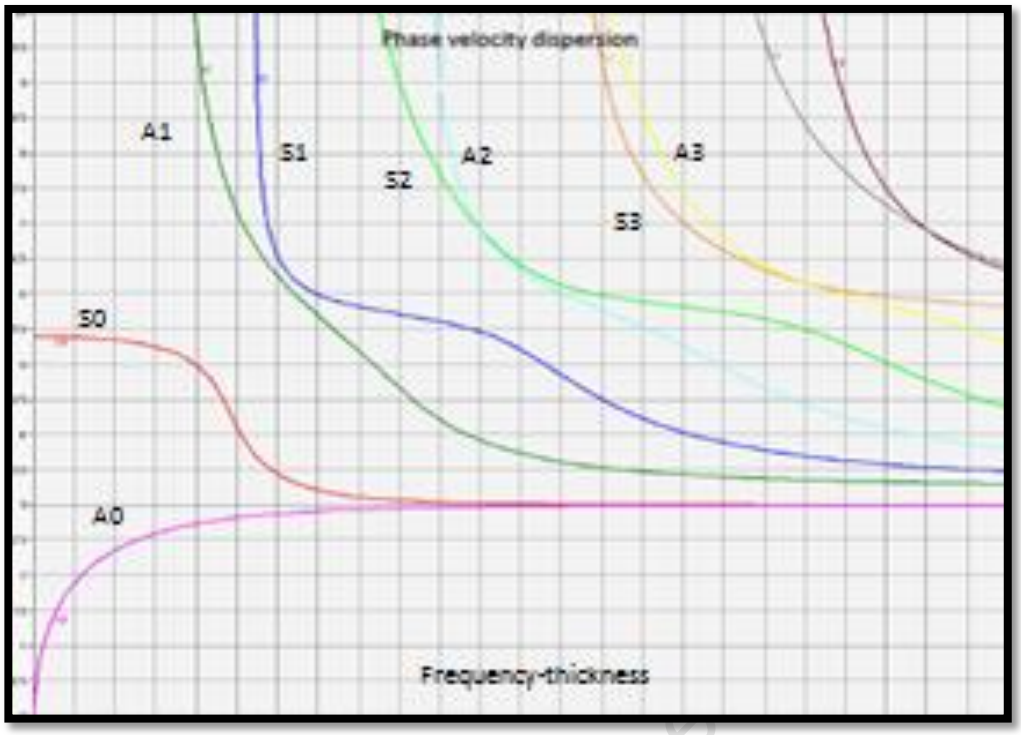

Figure 2.30: Phase velocity dispersion curve for steel plate. Curves plotted using the *PACshare* software tool.

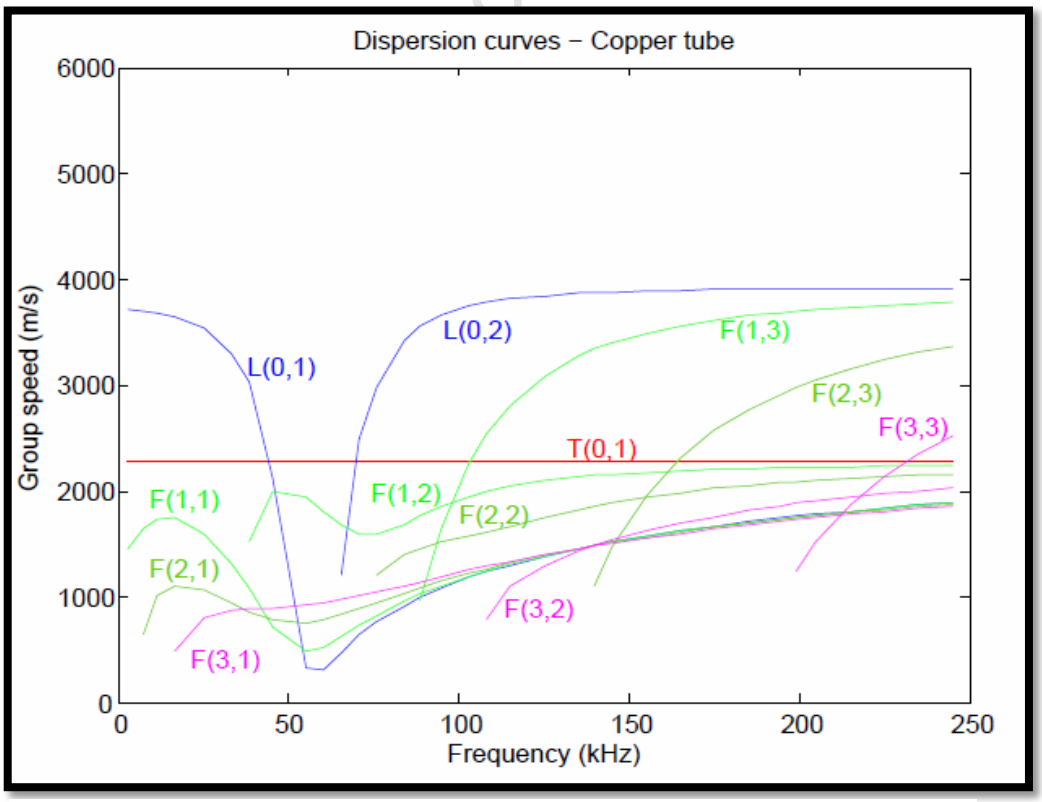

Figure 2.31: Group velocity dispersion curve for 22mm diameter, 1mm wall thickness copper tube and a frequency of 250kHz.

The dispersion curve has phase velocity, c_p or group velocity, c_g as its vertical axis and the frequency, f or frequency-thickness, f X b as the horizontal axis. ***PCDISP*** can also provide graphics of the wave form similar to those given in Figures 2.26 to 2.28 and more importantly, it can provide the particle displacement of the guided wave modes at given frequencies. At frequencies above 2MHz, curve generation is slow and the L(0,2) and L(0,3) modes 'cross over' due to an error in the code. The difference between the group velocity and the phase velocity gives an indication of the degree of dispersion. When no dispersion is evident then

$$c_g = c_p$$

The relationship between c_g and c_p according to Rose [22] is

$$c_g = c_p^2\left[c_p - (fb)\frac{dc_p}{d(fb)}\right]^{-1} \qquad (2.24)$$

Several observations can be made with regard to guided wave behaviour from analysing the dispersion curves given in Figures 2.29, 2.30 and 2.31. Important observations to note from Figures 2.29 and 2.30 (guided waves in plates) are:

- There are regions where certain modes have constant group and/or phase velocity, for example A_0 has a group velocity of 3100m/s above a freq.-thickness of 4MHz-mm. Its phase velocity, at 3000m/s, is nearly equal to its group velocity indicating negligible dispersion. From Equation 2.24, $\frac{dC_p}{d(fb)} = 0$ giving C_g=C_p.
- Below approximately 1.5MHz-mm, only two modes exist namely A_0 and S_0. They are easily distinguishable from each other due to the large difference in group velocity between them. Furthermore, S_0 has negligible dispersion in the range 0 to 1MHz-mm while A_0 has negligible dispersion in the range beyond 3MHz-mm.
- A_0 and S_0 converge as freq.-thickness increases and tend towards c_R. In fact, the motion of A_0 and S_0 combine to form a Rayleigh wave on either the upper or lower surface of the plate [24]. This re-inforces the description given "Rayleigh-Lamb" waves.
- The symmetrical peak velocities are higher than the asymmetrical peak velocities. The particle motion at low frequencies being predominantly in the x-direction for symmetrical modes and in the z-direction for asymmetrical modes.

- Both the symmetrical and asymmetrical modes (excluding the fundamental modes) have repeated minima at the same group velocity of approximately 2300m/s. This is an interesting observation and is explored further in Chapter 4.

Important observations to note from Figure 2.31 (guided waves in hollow cylinders) are:

- There is virtually zero dispersion of the L(0,2) mode beyond 120kHz. The torsional mode, T(0,1) is not dispersive at all over the full frequency range.
- Below approximately 60kHz, the L(0,2) mode does not exist and the only axisymmetric modes are the T(0,1) and L(0,1). There is therefore no need to suppress the generation of L(0,2) mode when generating the L(0,1) or T(0,1) mode at this frequency.
- There are several flexural modes that exist in the 0 to 250kHz range however only one has a velocity similar to the L(0,2) mode namely the F(1,3) mode.
- At frequencies above 200kHz, several flexural modes show reduced levels of dispersion.

The selection of guided wave or Lamb wave mode is an important factor when designing an inspection method. Not only must the selected mode be able to detect the flaw, but it must also be possible to analyse the reflected signal and not get lost in the noise of unwanted modes either generated unintentionally or occurring as a result of mode conversion. The generation of guided waves is discussed in the next section.

2.3.7 Generating and receiving guided waves

There are various transducers used to generate guided waves. Electromagnetic transducers and piezoelectric (PZT) transducers are the most popular. Several authors have also published works on the use of lasers for the generation and analysis of Lamb waves [41], [42] are two examples of such publications. The advantages and disadvantages of electromagnetic and piezoelectric transducers are discussed next.

2.3.7.1 The advantages and disadvantages of electromagnetic and piezoelectric transducers

The physical phenomena of magnetostrictive and piezoelectricity are very similar and can be described by similar mathematical equations. There are however differences both in the construction and application of the two types of transducers. An important difference is the fact that in electromagnetic transducers, magnetostriction is applied via an air gap between the

transducer and the test sample (ferromagnetic material such as steel). The induced magnetic field results in an ultrasonic wave in the test sample. The piezoelectric effect on the other hand is applied to crystalline material (such as quartz and some ceramics) which is incorporated into the transducer. The resultant wave is then transmitted into the test piece via a couplant or displacement (stress and strain) in the case of direct (bonded or dry coupled) coupling. A piezoelectric transducer requires contact with the test sample whereas electromagnetic transducers do not require contact.

There are also inherent differences between the relevant ferromagnetic material properties and the corresponding crystalline material properties. The piezomagnetic and piezoelectric coefficients for ferromagnetic material and crystalline material respectively result in strains of the order of magnitude of 10^{-5} for magnetostrictive effect and 10^{-9} for piezoelectric effect in ultrasonic wave generation [43]. To generate the magnetic field (magnetostrictive) requires higher currents than the electric field (PZT).

Electromagnetic transducer main advantages are:

- No physical contact between the test sample and the transducer is required. This brings with it several advantages such as the ability to automate inspections, no damage to test sample surface, less requirements for surface cleanliness.
- Different modes of Lamb waves can easily be generated. Electromagnetic transducers are more suitable particularly for Shear Horizontal (SH) mode ultrasonic wave generation.

The Piezoelectric transducer main advantages are:

- It is equally suitable for ferrous and nonferrous material.
- It utilises less energy and is more compact.

The advantages and disadvantages are tabulated in Table 2.3.

	Advantages	Disadvantages
Electromagnetic	• No contact between test sample and transducer. • More suited for some guided wave modes such as shear horizontal mode.	• Higher power requirements, less compact. • Less suitable for non-ferrous materials.
Piezoelectric	• More energy efficient and compact. • Equally suitable for ferrous and non ferrous materials.	• Requires contact to transmit ultrasonic wave. • Generation of certain guided wave modes is difficult to achieve.

Table 2.3: The advantages and disadvantages of electromagnetic and piezoelectric transducers.

Commercial equipment has been designed and developed more recently that makes reception and analysing Lamb waves much less complex. The available commercial equipment will be discussed in Chapter 3. The generation and reception of ultrasonic Lamb waves using PZT transducers and Snell's law is discussed in the next section.

2.3.7.2 Generating guided waves in plates using Snell's law

Ultrasonic Lamb waves can be generated by using either longitudinal or shear wave transducers. Both Krautkrämer [14] and Viktorov [24] provide guidance on how to generate Lamb waves.

Viktorov published the "wedge method" depicted in Figure 2.32:

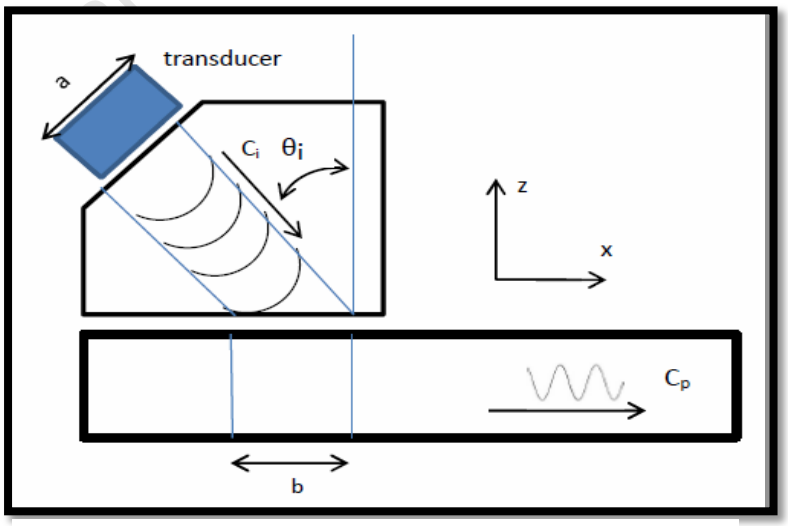

Figure 2.32: The wedge method [24] of generating Lamb waves in a plate. The mode generated in the test specimen, Cp, is determined by the phase velocity of the incident wave, Ci.

The stresses in the test specimen vary as θ varies from 0^0 to 90^0 [24]. The maximum stress is proportional to b up to a maximum value. Furthermore, as the test specimen thickness increases, the amplitude of the excited wave decreases.

The modes generated in the test specimen are determined by Equation 2.25, Snell's law:

$$\frac{C_i}{sin\ \theta_i} = \frac{C_p}{\sin 90} \qquad (2.25)$$

With the wedge method, Viktorov was able to selectively generate different Lamb wave modes by varying the angle of incidence, θ_i. The number of modes generated is dependent on the size of the transducer (a and b) and its frequency spectrum [44]. The ability to selectively generate specific modes is a prime consideration in the design of transducers for guided wave applications.

Worlton published a method in 1965 using an immersed plate and PZT transducer as shown in Figure 2.33 [45]:

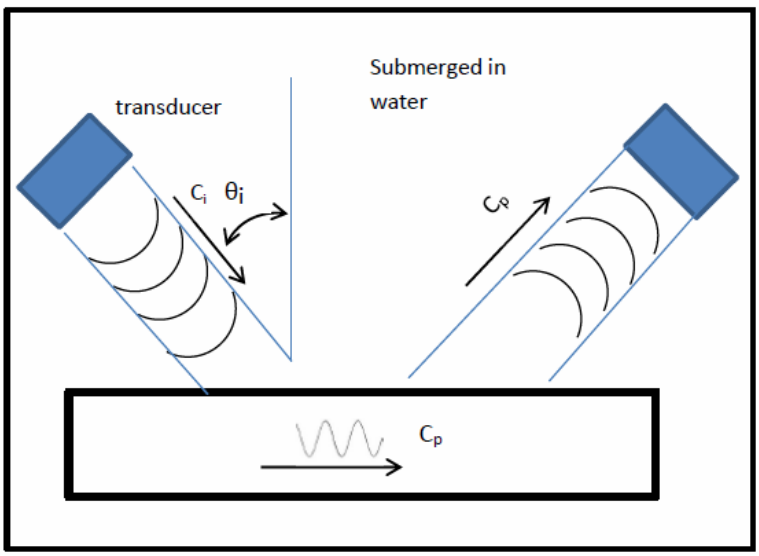

Figure 2.33: Worlton's patent to generate Lamb waves. The test specimen and transducers were submerged in water to implement Snell's law [45].

The same equation, Equation 2.25 is applied. In this method, only longitudinal modes can be generated as shear waves cannot be sustained in water. The longitudinal velocity in water, C_i = 1430m/s [14]. Worlton's publication followed on from Firestone [46] who published a similar method.

In general, Lamb waves can be generated using a standard longitudinal wave or transverse wave transducer at an oblique angle. The incident wave undergoes mode conversion and reflection at the interface resulting in guided waves in the plate. Figure 2.34 provides the angle of incidence required to generate that particular Lamb wave mode using a transverse wave transducer [14]. For example, a 45 degree incident shear wave transducer will generate an A1 Lamb wave mode at frequency-thickness of approximately 5MHz-mm as indicated on the dispersion curve in Figure 2.34 [14].

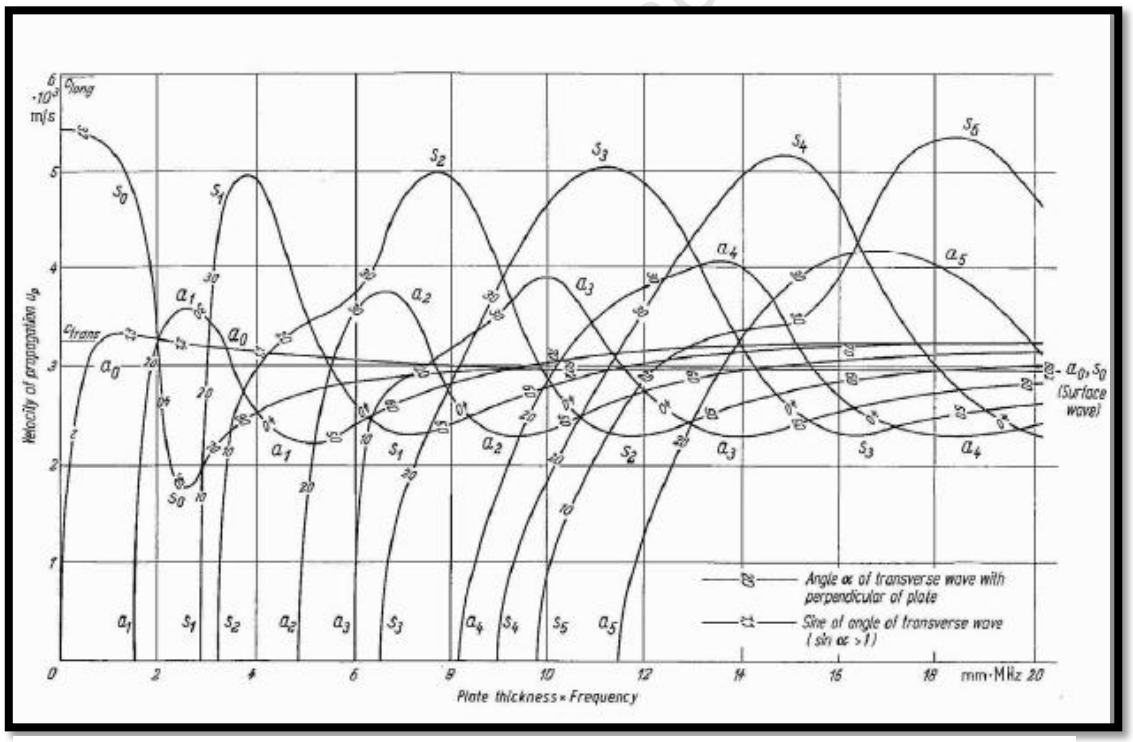

Figure 2.34: Dispersion curve for steel plate showing the angle of incidence required to generate specific modes using a transverse wave transducer [14]. At approximately 5MHz-mm, a 45 degree shear wave transducer will generate A1 at 2300m/s

2.3.7.3 Generating guided waves in tubes using Snell's law

The wedge in Figure 2.35 can be suitably adapted to generate guided waves in tubes using Snell's law. This is a non-axisymmetric method to generate both longitudinal and flexural modes [47]. The wedge angle is varied in order to vary the frequency and the modes that are generated. It was found that the full volume of the pipe is not exposed to the propagating waves however frequency tuning can be used to obtain complete tube coverage [48]. Also the wedge can be rotated around the tube if accessibility permits this. The procedure is applied in Chapter 4.

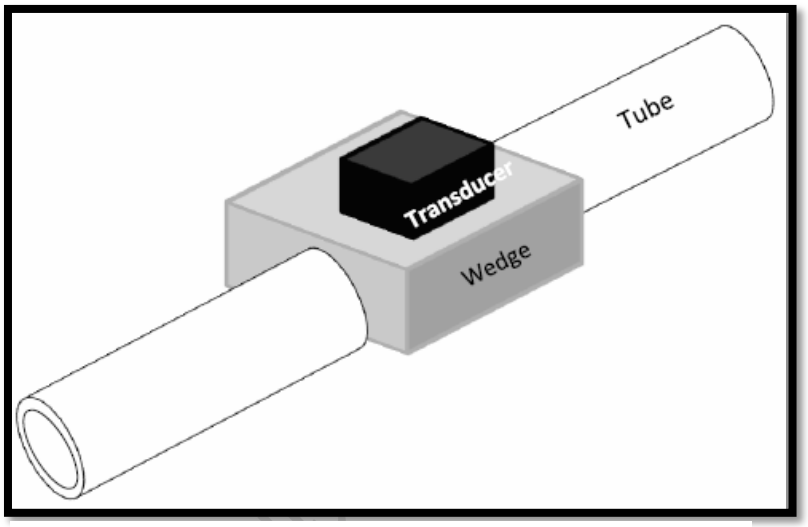

Figure 2.35: A wedge fitted onto a tube to generate axisymmetric and non-axisymmetric guided waves. The wedge angle can be changed to alter the phase velocity introduced into the tube and hence change the frequency and the modes that are generated.

2.3.8 Other guided waves

There are several other ultrasonic guided waves that are not discussed in this thesis. Love waves, Stonely waves and circumferential guided waves are examples of guided waves that do not specifically fall into the scope of this thesis and are described by Rose [22]. These waves have been the subject of research in NDT and circumferential guided waves may have some relevance in future work on defect detection and sizing in thin walled tubing. Research into circumferentially oriented guided waves has been undertaken by Zhao and Rose [49], Jezzine and Lhemery [50] and Van Velsor et al [51].

2.4 Summary

Condenser tube failures can lead to production loss and can cause long term negative effects on the feed water systems including the boiler tubes. Pitting, grooving and wall thinning are amongst the most common defect types experienced. Pitting defects typically have an aspect ratio of 2.5:1 and can reach through wall dimension while still having a wall loss of less than 1%. Grooves have an axial extent of between 1 and 2mm and usually do not extend beyond 50% of the circumference. The tube sheet and tube support plates present a challenge to effective inspection using guided waves. Tubes with localised wall loss greater than 60% are plugged. Eddy current testing has been found to be in-effective in some instances to identify condenser tube defects timeously to prevent plant shutdown.

Navier's wave equation governs the behaviour of all ultrasonic waves. Guided waves are complex in nature due to their dispersive properties and dependence on the shape of the medium in which they propagate. Strong similarities exist between the Rayleigh wave and the fundamental Lamb wave modes, A0 and S0. Dispersion curves are essential in understanding guided wave behaviour. It is also an essential tool for developing an inspection method utilising guided waves. In particular, the dispersion curve provides the region (frequency and velocity) and applicable modes that would be most suited to a specific application. Repeated minima on the group velocity dispersion curve occur at the same velocity for S_m, A_m (m = 1, 2, 3…) and L(0,m) (m = 3, 4, 5…) in plates and tubes respectively. Finally, Guided waves can be generated using Snell's Law in plates and tubes.

Chapter 3

Literature review: Ultrasonic guided waves for defect detection and sizing

3.1 Introduction

Significant progress has been made in the understanding and application of guided waves and a wide variety of research has been published that documents the rich potential of guided waves as an NDT technique, see for example [6], [7], [52], [53]. This chapter provides a review of the research published in the field of guided waves. It begins with the history of guided waves and discusses the contributions made by pioneers in the field. The principles employed by various defect detection and sizing methodologies are discussed next with commentary on the theoretical basis of these principles. Mode selection, frequency tuning and mode conversion are amongst those principles discussed. Applications of guided waves in industry remains limited and the possible reasons for this can be found in the advantages and disadvantages of guided waves, also documented in this chapter. It then goes on to report on modern day guided wave inspection systems available commercially.

Important research published in the field of defect detection using guided waves in plates, tubes and pipes is reported next. In particular, a detailed review of work done by Edalati et al [54] (plates), Demma et al [55] (pipes) and Vinogradov et al [5] (tubes) is provided. Relevant work on defect detection in tubes by Vogt et al [2], EPRI [4], Rose et al [15] and Mohr and Höller [56] is also reviewed.

Finally, a summary is provided at the end of this chapter which includes the contribution made by this thesis, to the field of guided waves.

3.2 The history of guided waves

In 1917, Horace Lamb [57] published his work on what was to become known as Lamb waves. It followed on from the work done by Pochhammer [58] and Lord Rayleigh [59] (Figure 3.1) in 1876 and 1885 respectively. Horace Lamb (Figure 3.2) provided a mathematical description of Lamb waves. The mathematical link between Lamb and Rayleigh waves was also made. Practical applications of Lamb waves did not occur until the 1940's when Firestone patented a method to generate surface waves [60] and then more specifically patented a method to generate Lamb waves [46]. These methods were very simple in nature and did not directly result in practical industry applications.

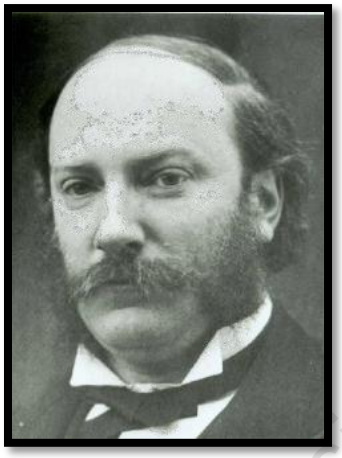

Figure 3.1: Lord Rayleigh, born 12 November 1842, discovered the Rayleigh wave [61].

Figure 3.2: Horace Lamb, born 29 November 1849, discovered Lamb waves [62].

DC Worlton continued the work of Firestone and published several patents in the late 1950's and early 1960's including a method for measuring wall thickness using Lamb waves [63]. The method, while potentially very accurate, was not robust as it relied on the ability to generate and measure only specific modes at very high centre frequencies such as 10MHz. The method used to generate Lamb waves was based on Equation 2.25, as was so often the case back then. From 1960 to late 1980s very little progress was made in the application of Lamb waves to NDT. This was largely due to the complexity of Lamb waves and the need for sophisticated equipment and powerful computers. During this period however, Viktorov [24], Achenbach [25], Auld [26], Graff [64] and Krautkramer [14] published books that advanced the theory and understanding

of Lamb waves. In contrast, during this same period, NDT based on bulk waves advanced due to its simplicity.

Figure 3.3: Prof Joseph Rose published the well-known text, Ultrasonic Waves in Solid Media [66].

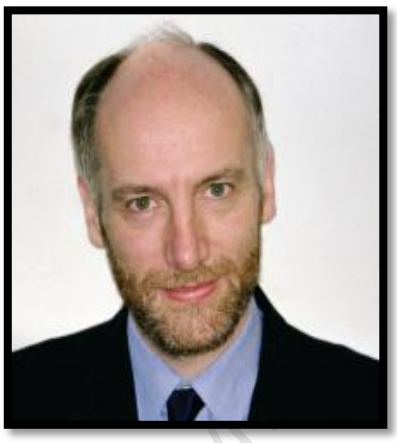

Figure 3.4: Prof Peter Cawley, a pioneer in commercialising guided wave technology, holds several patents [65].

In the late 1980's, there was renewed interest in Lamb waves spurred on by the development of computers and electronics but also the demand for more advanced NDT methods. In the oil and gas industry, vast amounts of buried pipe required inspection and existing methods were expensive and time consuming [53]. In the power generation industry, aging plant required more sophisticated inspection methods to ensure continued safe, reliable operation [52]. In the 1990's computer modelling of Lamb waves [39], [68], amongst others, was being done at the major research institutions. These methods continue to improve and extensive modelling capability currently exist which is applied in a wide variety of guided wave research applications.

In the last 10 to 15 years, commercial equipment has become available that is quite sophisticated but expensive. These guided wave inspection systems have been developed by a limited number of academic and research institutions that are recognised as centres of excellence in the field of guided waves. Pennsylvania State University, Imperial College of London and Southwest Research Institute are three such centres of excellence. Two modern day researchers that have made significant advances in the study of guided waves in defect detection and sizing are Prof. Joseph Rose (Pennsylvania State University) and Prof. Peter Cawley (Imperial College, London) pictured in Figures 3.3 and 3.4 respectively. Thus far, limited real world industrial applications exist that utilise guided wave inspection techniques. Long range pipe inspections [8], [69], [70] stand out as the most advanced applications of guided waves and is used routinely. Applications to rail [71], [72] and the inspection of sheet metal

during manufacturing [14] are other examples of successful commercial NDT applications of guided waves. Guided wave inspection systems and applications are discussed in Section 3.5.

Most recently, research into structural health monitoring and permanently installed monitoring devices using guided waves is being conducted [73], [74]. The ability to separate modes [75], and clever imaging techniques [9], [76], are also current research focus areas. Work also continues on finding an accurate or universal method of determining defect depth using guided waves, if this method indeed exists.

3.3 Defect detection and sizing principles using guided waves

The detection and sizing of defects have been researched extensively by several authors; Alleyne [77], Mohr and Höller [56] and Demma et al [55] are some good examples of this in plates, tubes and pipes respectively. Several key principles are commonly applied when implementing guided waves for defect detection and sizing. Some of these principles are discussed below.

3.3.1 Guided wave mode selection

Certain modes are more effective than others in detecting and sizing specific types of defects [15]. When selecting a mode the following aspects need to be taken into account:

- The sensitivity of the mode to the defect of interest. This is dependent on the extent (amplitude) of the particle motion as a result of the guided wave and hence stresses in the region of the defect [78]. The higher the stresses produced by the Lamb wave in the region of the defect, the greater the change in reflected signal. For example, the fundamental modes, A_0 and S_0, are more sensitive to surface defects than defects at the centre of the material cross section. A1 and S2 are affected differently compared to the fundamental modes when interacting with defects [78].
- The dispersive nature of the mode over the frequency of interest. As discussed in Section 2.3.6, certain modes have zero (or low) dispersion over a limited frequency range. L(0,2) for example has a region of low dispersion above approximately 120kHz in a 23mm outside diameter brass tube. T(0,1) is non dispersive over the full frequency range. The T(0,1) mode was initially used exclusively by electromagnetic transducer systems such as the ***MSsR3030R*** system (see Section 3.5) due to the ease

with which these systems could generate this mode. However, PZT systems are now also generating this mode and it is gaining in popularity. Both the L(0,2) and T(0,1) modes are studied extensively by researchers. Kwun et al [3], EPRI [4] and Demma et al [55] are a few examples.

- The ease with which the mode can be generated and received. Unwanted signals as a result of the unintended generation of other wave modes decreases the signal to noise ratio and makes analysis of the signals more complex. At low frequencies, it is easier to generate the fundamental modes only, making analysis simple. The use of fundamental modes is therefore very popular and has been studied extensively in plates [77], [79].
- The leakage losses experienced over the length of transmission. Modes that have a particle displacement with a high radial component of displacement in tubes or high z component in plates are more susceptible to high leakage loss. SH_0 and T(0,1) have no z-component or radial component of displacement respectively and therefore have no leakage through the transducer contact surface. Attenuation dispersion curves are provided by Rose [22] for water loaded steel tube. L(0,1) does not propagate well in water loaded tubes (see Section 3.3.2).

In general, limited use is made of higher order guided waves largely due to the difficulty in generating single modes in a non-dispersive region and the higher attenuation experienced. Several unwanted modes may be generated unintentionally leading to a complex reflected signal.

Flexural (non-axisymmetric) modes, F(n, m) are also not popular due to the difficulty in generating a unique flexural mode. For example, in order to generate the F(1,3) mode in a 23mm outside diameter brass tube, at approximately 250kHz, where F(1,3) is reasonably non-dispersive, at least 9 other flexural modes also exist. However, flexural modes are important when analysing mode converted signals as it not only provides insight into the possible presence of a defect, but also provides insight into the defect geometry [55]. A comparison of the characteristics of the L(0,1), L(0,2) and T(0,1) modes is tabulated in Table 3.1. The characteristics are based on 23mm outside diameter admiralty brass tubes and refer to the dispersion curves given in Figures 3.5 (phase velocity) and 3.6 (group velocity).

Parameter	L(0,1)	L(0,2)	T(0,1)
Non-dispersive range	Below 25kHz	Above 125kHz	The full range but preferred between F(2,2) and F(3,2) cut-off frequency (65-90kHz).
Attenuation	Excellent	Reasonably low.	Good. Also Immunity to 'leakage'.
Sensitivity	Very low. Wavelengths >100mm, limited sensitivity	Approximately 5 times shorter wavelengths with improved sensitivity.	Similar to L(0,2)
Ability to generate the mode on its own	Easy. Below L(0,2) cut-off frequency.	Difficult. L(0,1) mode is also generated.	Simple.
flexural modes that can be mode converted	Flexural modes not monotonic in this range.	Easily mode converts to F(n,3)	Easily mode converts to F(n, 2).
Energy	High group velocity indicating high energy	High group velocity indicating high energy	Lower velocity, less energy

Table 3.1: Comparison of the L(0,1), L(0,2) and T(0,1) mode in 23mm diameter, 1mm thick brass tube.

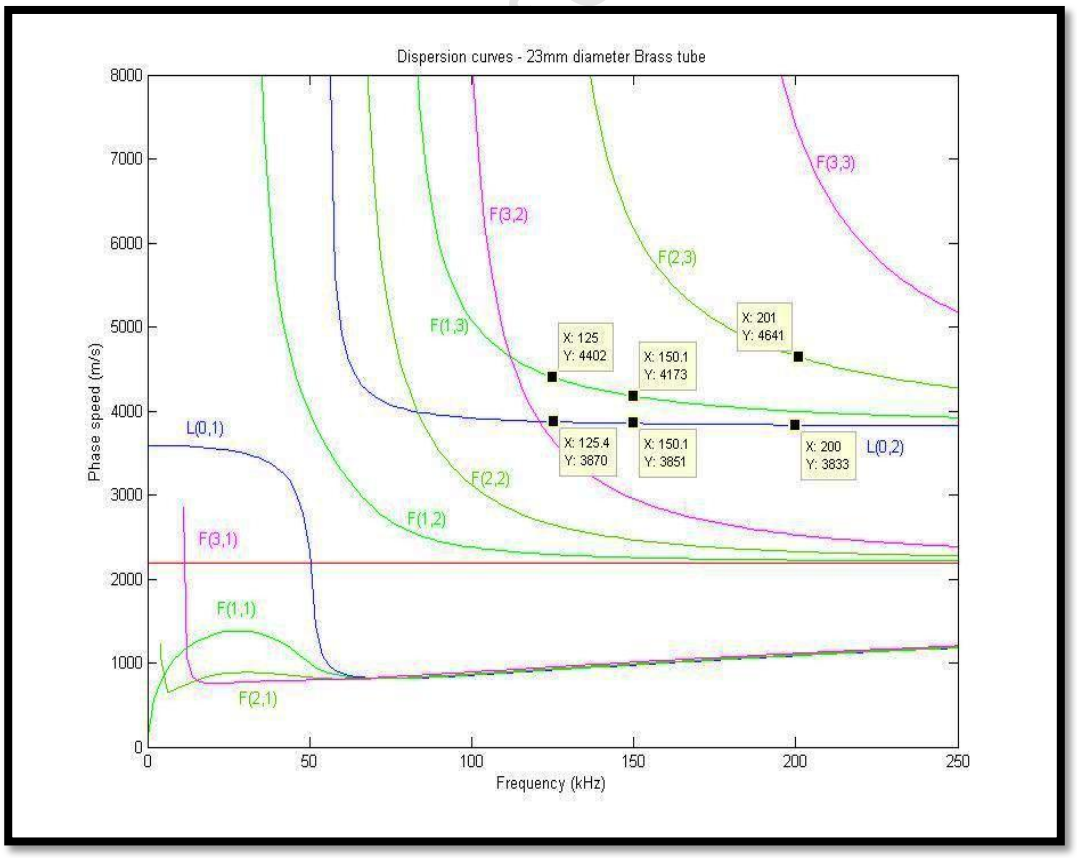

Figure 3.5: Phase velocity dispersion curve for 23mm diameter admiralty brass tube over a frequency range of 250kHz.

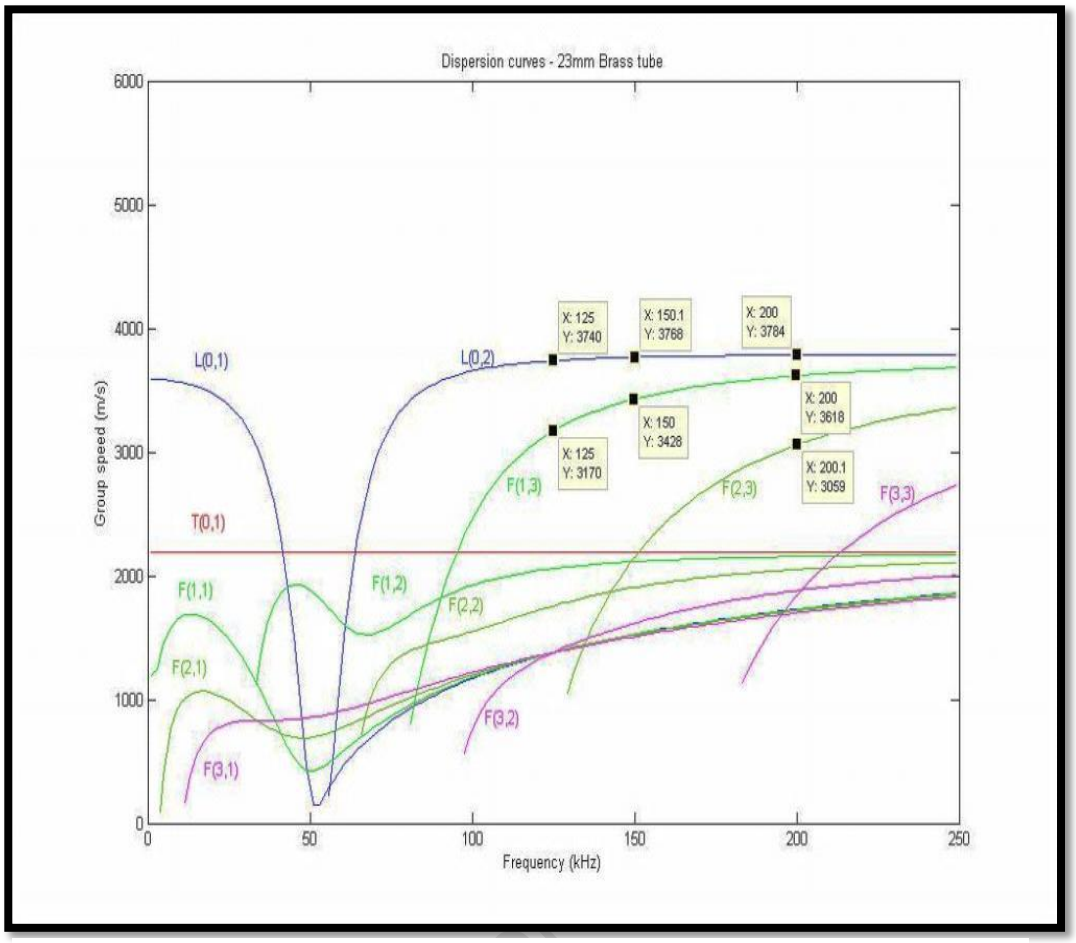

Figure 3.6: Group velocity dispersion curve for 23mm diameter admiralty brass tubes over a frequency range of 250kHz.

3.3.2 The effects of frequency variation

The effect of frequency variation on the ability to detect and size defects is best seen from the analysis of the dispersion curve for the material. The sensitivity of guided waves to a particular defect is dependent on (amongst others) the frequency-thickness product [77]. Varying the frequency for a given material thickness can enhance the reflected signal significantly [15]. As the frequency is varied, the following occurs:

- The number of modes vary. There are fewer modes at lower frequencies. At 1 MHz-mm in steel plate, only A0 and S0 modes exist. At 4MHz-mm, there are four modes that exist namely A0, S0, A1 and S1 and S2.
- The velocity of the various modes changes. There is a large variation between the velocity of the modes that exist at certain freq-thickness products which makes it easy to distinguish between modes. At other frequencies, the velocities may be very

similar. For example, at 1 MHz-mm, the group velocity in steel for A0 and S0 is 3200 m/s and 5300m/s respectively while at 2 MHz-mm they are both 3200m/s.

- Higher attenuation occurs at higher frequencies but generally better sensitivities are also achieved with higher frequencies [80]. There is therefore a trade-off between higher sensitivities and attenuation (ability of the sound wave to propagate over long distances).
- The amplitude of the particle displacement in the r, θ and z (or x, y and z) directions across the thickness of the material varies. For example, at frequencies below 50kHz in brass, the L(0,1) mode's particle displacement in the radial direction dominates however, above 50kHz, the radial displacement dominates. High radial displacement at the surface leads to 'leakage' and greater attenuation. The graph of the particle displacement when a L(0,1) mode propagates at 20kHz and 80kHz in brass tube is given in Figures 3.7 and 3.8 respectively.
- The wavelength changes. The amplitude of the reflected signal from a defect is dependent on the axial extent of the defect [55].

The location of the defect can be determined by utilising the time of flight of the reflected signal if the mode and its respective velocity is known. Furthermore, in pipes, the reflection coefficient over a non-dispersive region of certain modes interacting with through wall defects is found to be independent of frequency [55].

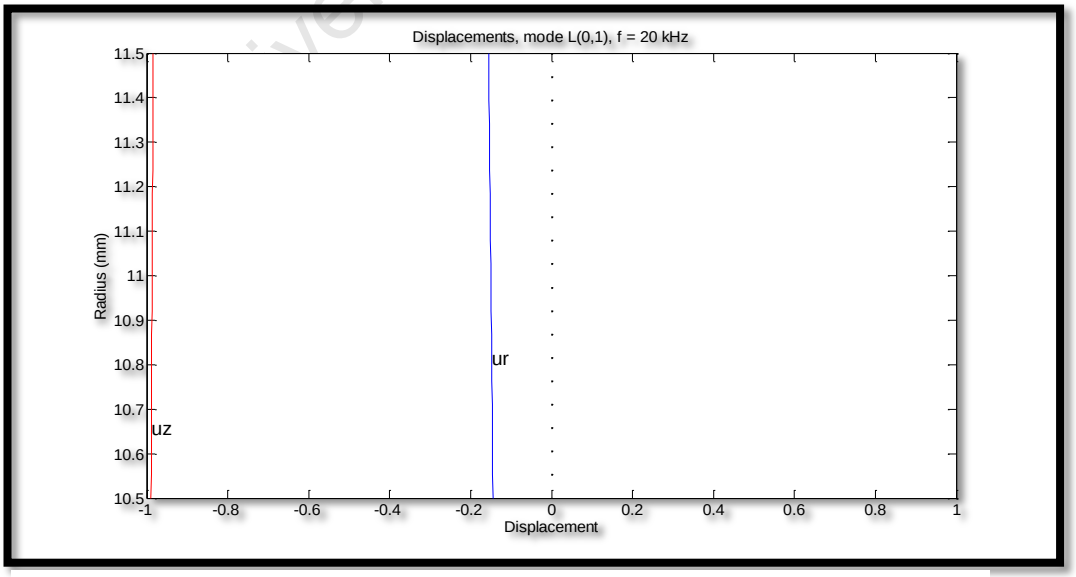

Figure 3.7: Particle displacement of the L(0,1) mode in 23mm diameter brass tube at 20kHz. The displacement in the z-direction dominates and is nearly constant over the thickness.

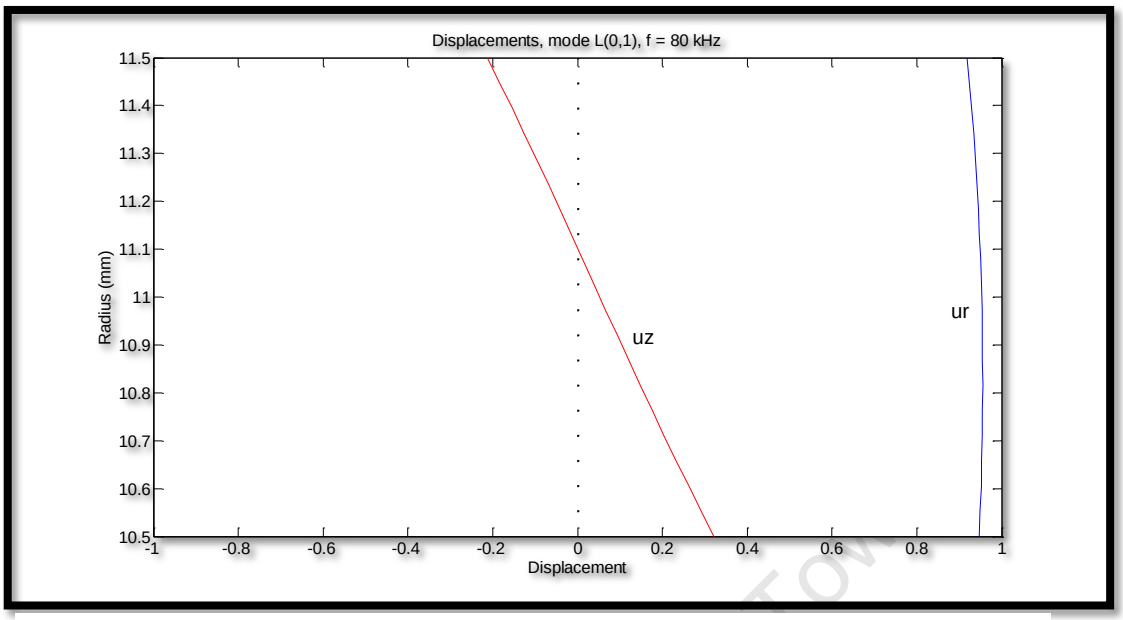

Figure 3.8: Particle displacement of the L(0,1) mode in 23mm diameter brass tube at 80kHz. The displacement in the radial direction dominates and is nearly constant over the thickness.

3.3.3 The analysis of guided wave signals

The interaction of guided waves with defects, discontinuities or notches is studied extensively by several authors. Of particular interest to defect detection and sizing is the behaviour and characteristics of the reflected signal, transmitted signal and mode converted signal. Often these are reported in terms of a reflection coefficient. The reflection coefficient is the ratio of the amplitude of the incident signal to the reflected signal (or transmitted signal) and is given by:

$$RC = \frac{R}{I} \times 100\%$$

Where:

R - The amplitude of the signal reflected (or transmitted) from the defect. This could be either the incident mode, mode converted mode or the transmitted mode.

I - The amplitude of the incident (input) signal. In some cases, the back wall amplitude obtained in the absence of a defect is used as a substitute for the input signal.

The reflection coefficient is studied extensively and is a prime parameter used for characterising defects using guided waves. The significance of the reflection coefficient is discussed below.

3.3.3.1 The reflection coefficient of the incident mode

It is found that the change in the reflected signal amplitude is proportional to the change in strain energy caused by the defect [78]. The reflection coefficient of the incident mode can be affected by the following:

- Changes in frequency (as discussed in Section 3.3.2).
- The axial extent of the defect can result in constructive or destructive interference.
- The circumferential extent of the defect.
- Different incident modes will have different reflection amplitudes.

The reflection coefficient on its own therefore does not provide sufficient information on the geometry of the defect. A graph of reflection coefficient of the incident mode (L(0,2) in this case) as a function of defect depth in pipes at various frequencies is shown in Figure 3.9 [81].

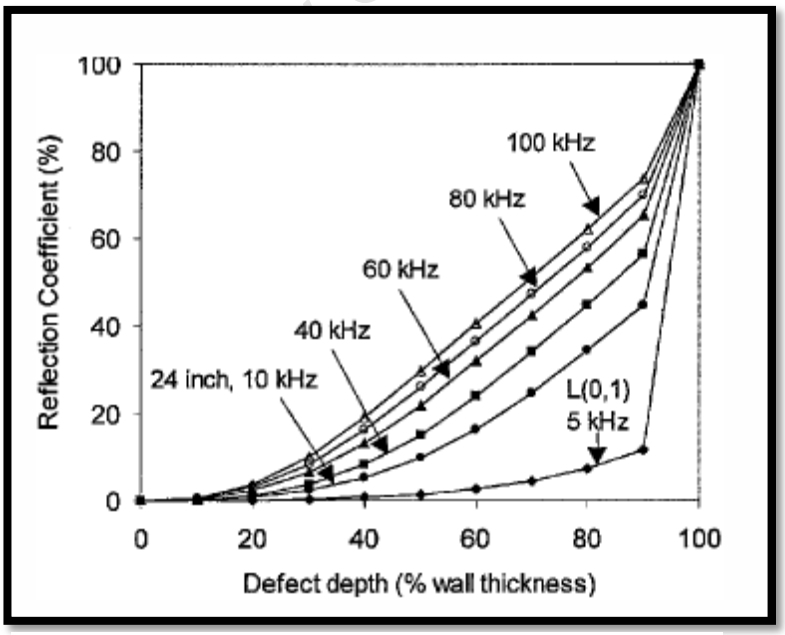

Figure 3.9: Graph showing the relationship between reflection coefficient and defect depth for axially symmetric notches [81].

3.3.3.2 The reflection coefficient of the mode converted signal

The mode converted signal represents the signal from the mode that comes into existence following the initial incident mode interacting with the defect. Mode conversion is an important aspect of defect detection and sizing in pipes and plates. An axisymmetric mode, will mode convert to a non-axisymmetric mode when interacting with a non-axisymmetric defect [82]. The reflection coefficient of the mode converted signal is affected by the amplitude of the incident mode and as such is affected in the same way as the reflection coefficient of the incident mode. Demma et al [55] used the ratio of the reflection coefficient of the mode converted signal to that of the incident mode to estimate the circumferential extent of defects in pipes. Figure 3.10 is a graph of the reflection coefficient of the F(1,3) mode (mode converted from the L(0,2) incident mode) as a function of defect depth in tubes.

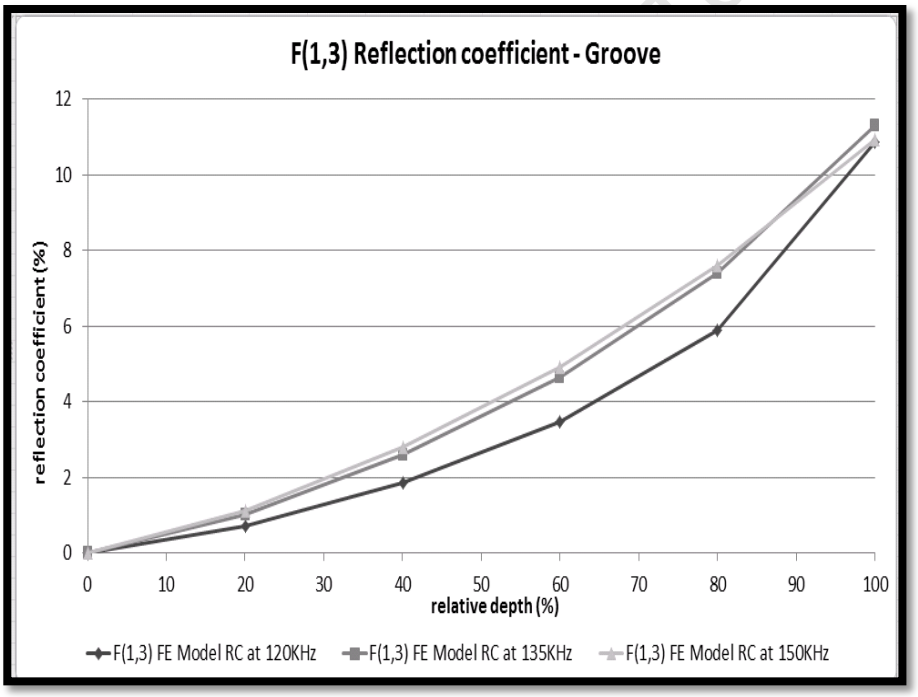

Figure 3.10: reflection coefficient of the F(1,3) mode (mode converted from the L(0,2) incident mode) as a function of defect depth in tubes.

3.4 The application of guided waves in industry

Despite the potential benefits that guided waves have to offer, there are limited practical applications of guided waves, particularly in the power generation industry in South Africa. EPRI [6] have investigated the use of guided waves for the detection of defects in reactor containment liner plates, buried (underground or lagged) pipes and heat exchanger tubes. Although promising results have been obtained with clear benefits, still more work is required before these applications will become standard applications in the power generation industry. On the other hand, the use of guided waves in the oil and gas industry for the inspection of underground and undersea piping is well established as mentioned earlier.

A paper published in 2002 by Rose [7], highlights applications based on guided waves in the aircraft, oil and gas and power generation industries. A more detailed review of the advantages and disadvantages of guided waves in inspection systems are provided in Sections 3.4.1 and 3.4.2.

3.4.1 Advantages of guided waves compared to conventional NDT methods

The advantages of guided waves compared to conventional NDT methods are as follows:

- Guided waves can propagate along the length of the material being inspected rather than through the thickness of the material. This phenomena yields many spin-offs as inspection can be done remotely from a single location. In the nuclear industry, this means inspections can be done from low radiation dose areas or in less harsh (temperature and gaseous) environments in other industries. Physical obstacles such as pipe supports, penetrations, lagging and underground or undersea conditions can be overcome by performing the inspections in an area that is easily accessible.
- Guided waves can propagate at very low frequencies, have lower attenuation and therefore can propagate over long distances. In ideal conditions, travel distances of 200m is reported with 10m of propagation in buried pipe conditions [83].
- The full volume of the specimen can be inspected from a single location. The entire cross section and in the case of cylinders, the entire circumference experiences particle displacement and therefore the potential to detect a defect exists. A significant benefit of this is the ability to perform on-line structural health monitoring.

Given that guided waves have the ability to inspect the full volume from a single location, high frequency guided waves (4 to 6 MHz range) over a short distance (200 to 300mm) may have higher probability of detection than conventional ultrasonic pulse-echo techniques in certain applications. High frequency guided waves are discussed in Chapter 4.

Collectively, advantages mentioned above provide the ability to perform inspections more quickly and therefore usually less cost.

3.4.2 Disadvantages of guided waves compared to conventional NDT methods

The disadvantages of guided waves compared to conventional NDT methods are as follows:

- The dispersive nature of the guided waves makes analysis complex. The signals' coherence, velocity changes and the amplitude changes due to dispersion are illustrated in Figure 3.11. Even though the L(0,2) mode has limited dispersion at 120kHz, significant reduction in coherence and delayed timing between the defect reflection and backwall on the second instance can be seen. Significant reduction in amplitude is also noted however this is due more to attenuation than dispersion.

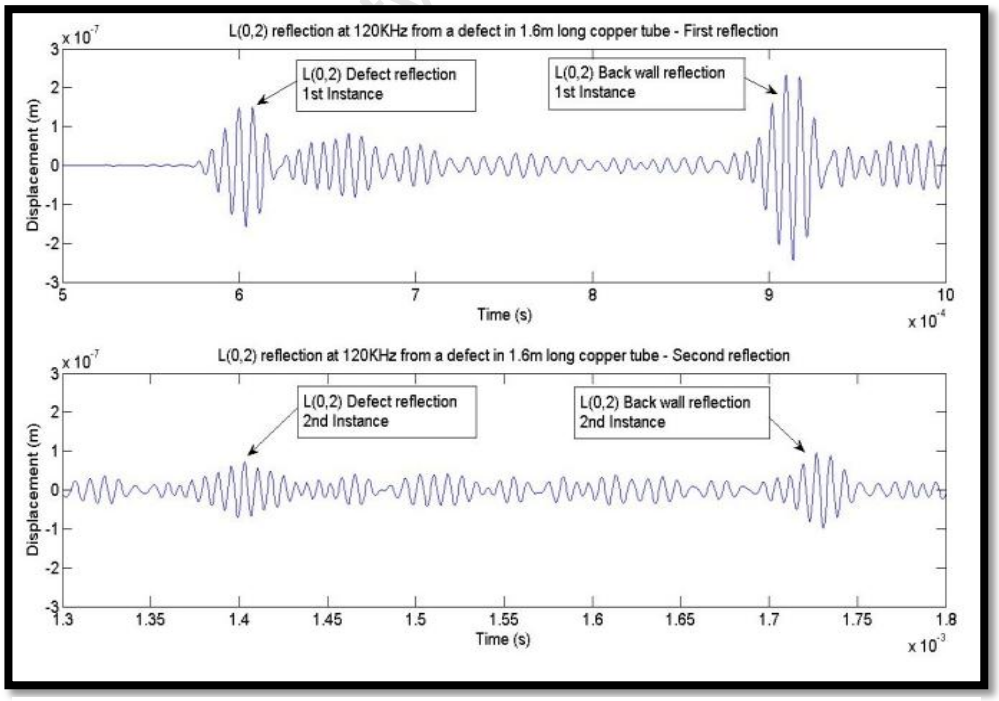

Figure 3.11: An illustration of the dispersive nature of the L(0,2) mode propagating in copper tube at 120kHz.

- The difficulty in generating selected modes at specific frequencies while preventing the generation of unwanted modes results in the need for expensive guided wave generators and receivers including transducers.
- Guided wave interaction with defects results in scattering and mode conversion to a larger extent than bulk wave ultrasonic waves. The resultant signals are complex and requires careful analysis.

The most significant drawback is that a method to determine defect depth (or remaining wall thickness) using guided waves has not been developed and proven. In particular, no research could be identified where the guided wave testing method (even for detection only) has undergone a performance demonstration type of assessment. Small volume defects such as pitting are particularly difficult to detect before it has achieved through wall dimensions in tubes [84]. Furthermore, the overwhelming majority of the research conducted to investigate guided wave inspection methods were performed in the laboratory using machined notches or modelling as opposed to real defects which suggest that the technique has not yet progressed into the field where more complex defects and external interferences will be encountered. These disadvantages, while quite significant should not detract from developing new inspection methods. The power generation industry in particular can benefit from several potential guided wave applications that can improve plant reliability.

3.4.3 Comparison between eddy current testing and guided wave testing of condenser tubes

Eddy current testing of condenser tubes and heat exchanger tubes in general is very popular and has improved significantly over the years [85]. The use of different eddy current coil types in combination provides very reliable defect detection and sizing [86]. It has been reported that the inspection rate of condenser tubes using guided waves is up to 8 times faster than eddy current testing [87]. Table 3.2 and Table 3.3 highlights the advantages and disadvantages of guided waves and eddy current testing respectively.

Guided wave inspection	
Primary advantage	Implication for condenser tube inspection
• Inspection is conducted from a single location.	• Less suceptible to the condition of the tube such as scaling and dents which cause physical obstruction. • Less time consuming since the time for the transducer to travel the length of the tube is not required. • There is less variation in the setup (e.g changes in fill factor, travel speed or magnetic field) and therefore more consistent and repeatable results can be achieved.
• The full volume of the tube is inspected.	• Several modes can be generated along the full volume of the tube which heightens defect detection capability. • Mode control can be accomplished with a single transducer – there is no need to change transducers.
• Primary disadvantage	• Implication for condenser tube inspection
• Remaining wall thickness cannot be determined.	• Additional inspection is required following initial screening.
• New technique in its development stage.	• Very few experienced operators. • High cost of capital investment required. • Off the shelf solutions are not available and would need to be developed.
• Guided waves are complex in nature.	• The presence of tube sheets and tube support plates can increase the complexity of the reflected signals making analysis difficult.

Table 3.2: The advantages and disadvantages of using guided waves for defect detection in condenser tubes.

Eddy current testing	
Primary advantage	Implication for condenser tube inspection
• It can determine remaining wall thickness directly.	• Tube plugging criteria can be applied based on inspection results.
• The technique is well developed.	• Highly trained personnel are readily available. • Equipment and procedures are available and robust.
• Primary disadvantage	• Implication for condenser tube inspection
• The probe must travel the distance of the tube.	• The tube must be cleaned which is time consuming. • Minor obstruction such as dents prevent inspection and can cause eddy current equipment damage. • The inspection itself is time consuming.

• Manual eddy current inspection is prone to operator errors and inappropriate practices.	• Poor fill factors and incorrect probe speeds can result in defects not being detected. • Interference from electromagnetic sources reduces defect detection capability.
• Multiple probes must be applied to enhance the reliability of defect detection and sizing.	• This increases the duration of testing

Table 3.3: The advantages and disadvantages of using eddy current for defect detection in condenser tubes.

3.5 Guided wave inspection systems

Commercial equipment available for generating guided waves for industrial applications is available from several suppliers. It is sophisticated and robust but prohibitively expensive. Costs range from approximately R5000 to rent a basic system for 1 day to R800 000 to purchase the basic system. Furthermore, many guided wave applications are still in their development phase and further research is required for specific applications such as condenser tubes. Given that guided wave inspection systems have only recently been developed, strong ties with their development sources and/or academic institutions still exist. Research by these institutions is often strongly biased towards the guided wave testing systems of which they have a commercial interest. A market survey was conducted to assess the available guided wave inspection systems available. Five commercial products were identified. These are (in no particular order):

- The ***MsSR3030R*** system is based on magnetostriction transducers and was developed and manufactured by *South West Research Institute (SWRI)* in San Antonio, Texas, USA. It is supplied by *Guided Wave Analysis LLC*. It is also used extensively by EPRI in its research.
- The ***Wavemaker G3*** system is based on PZT transducers and is developed and supplied by *Guided Ultrasonics Ltd* in Nottingham, UK. It builds on the development made by *Imperial college, London* and maintains close ties with that institution.
- The ***Teletest Focus Flaw detector*** is based on PZT transducers and is developed by *The Welding Institute (TWI)* and supplied by *Plant Integrity Ltd* in Cambridge, United Kingdom.

- The ***Ritec RPR4000*** system is developed by *Ritec Inc* and supplied by Ritec Inc in Warwick, USA. It can be used with electromagnetic or PZT transducers. It is used broadly for research purposes and is suitable for laboratory use only.
- The ***Temate*** system is developed and supplied by *Innerspec Technologies*. It is developed for use with EMAT transducers. Innerspec technologies is situated in Virginia, USA.

Photographs of some of the products available from the vendor websites and product manuals are provided in Figures 3.12 to 3.15 for illustration:

Figure 3.12: The *MSsR3030R* along with the in-bore transducer is developed by SwRI. It generates the T(0,1) mode and has a 250kHz bandwidth and 2 channels [88].

Figure 3.13: The *Teletest* test set supplied by Teletest and supported by TWI. It is based on PZT transducers and is designed to generate the L(0,2) and L(0,1) modes [89].

Figure 3.14: Guided Ultrasonics Limited *Wavemaker G3* with in-bore transducer. It utilises PZT transducers and has 32 channels [90].

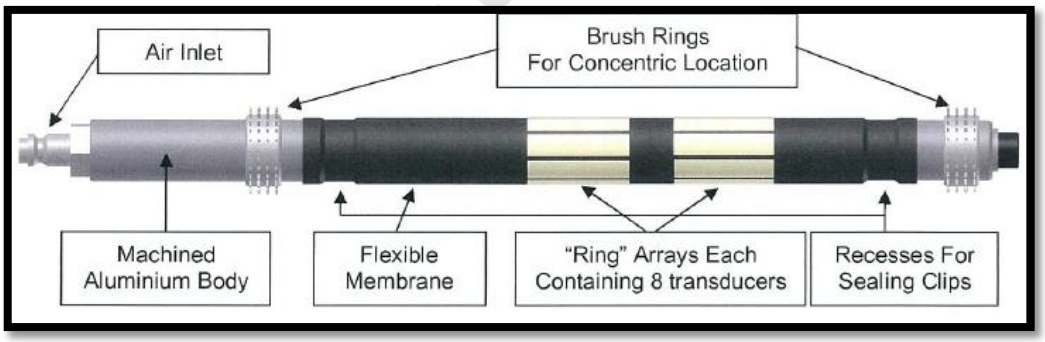

Figure 3.15: Typical in-bore transducer used for tube inspections. Two rings of transducers are used to manipulate the modes generated as well as eliminate the backward generated signal. The transducer is dry-coupled to the inside of the tube.

In South Africa, a limited number of contractors have purchased guided wave equipment and are providing pipe inspection services. *De-tect* and *Steeltest* are amongst those providing a guided wave inspection service for pipes using guided waves while the CSIR conducts research on guided waves in rails [91].

There are several important considerations when selecting an ultrasonic guided wave inspection method/system that is suitable for the detection of defects in condenser tubes. Some of the characteristics of such a system are discussed in Sections 3.5.1 to 3.5.4.

3.5.1 Transducer specifications for guided wave applications in tubes

There are several aspects of the transducer that require careful consideration. These are listed below:

- The transducer type. Piezoelectric is preferred over magnetostrictive and EMAT due to the benefits listed in Section 2.3.7.1.
- The physical dimensions of the transducer. The smallest internal diameter of the condenser tube is 17mm. The ability to fit two rings each of 8 or more transducers on the inside of the tube is a significant challenge. Such a transducer is not available commercially as a standard, off the shelf product.
- The ability of the transducer to generate the modes of interest, particularly L(0,1), L(0,2) and T(0,1) modes. The advantages and disadvantages of each of these modes are discussed in Section 3.3.1. While the transducer is designed to generate these modes, its ability to sense the flexural modes, F(n,m) is essential for defect detection and sizing. The number of transducer elements in the transducer ring should be greater than n where F(n,m) is the highest order flexural mode within the frequency range of interest [21].
- The transducer bandwidth and centre frequency. The transducer frequency must be matched to the intended input frequencies to prevent the generation of unwanted modes and noise. Typically, the number of cycles of the input tone burst signal can be increased to improve the frequency response of the transducer to match that of the input signal. This however will increase the dead zone [2].
- The footprint (area that the transducer is in contact with the test specimen). A larger footprint enables more energy to be absorped or released [24]. There are physical constraints to the number of discrete transducers that can be fitted in the inside of the tube as mentioned earlier in this section.

3.5.2 The signal-to-noise ratio of the guided wave inspection system

The signal-to-noise ratio (SNR) is a measure of the amplitude of the signal from the defect in relation to that of the background (unwanted) reflections classified as noise. The achieved signal to noise ratio is dependent on several factors both dependent and those that are independent of the guided wave system itself. SNR is more suited to describe the degree of electrical/instrument noise however it is a useful concept for determining the degree to which the defect can be recognised. SNR, in the context of signal recognition is explored in Chapter 5. In guided wave applications, the SNR is often lower than the expected norm of 3 to 1 [92] due to the number of guided wave modes that may be generated unintentionally particularly at higher frequencies. The SNR is calculated using Equation 3.1 [14].

$$SNR_{dB} = 20log_{10}\left(\frac{A_{signal}}{A_{noise}}\right) \quad (3.1)$$

An example of a guided wave application using high frequency shear wave transducers on 3mm steel plate is shown in Figure 3.16 along with the calculation of SNR_{dB}. Applying Equation 3.1,

$$SNR_{dB} = 20log_{10}\left(\frac{8}{4}\right)$$

$$SNR_{dB} = 6\text{dB}$$

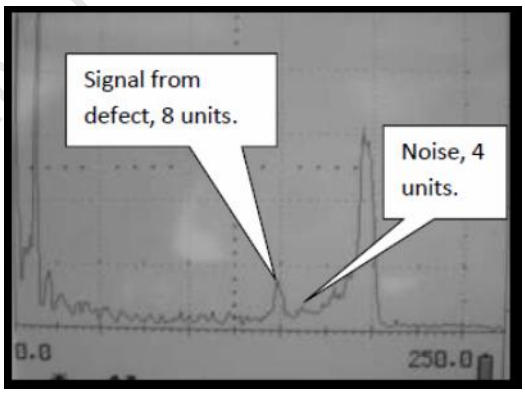

Figure 3.16: The reflection obtained from a defect in a 3mm steel plate. The guided wave was generated using a 4MHz, 45^0 shear wave transducer.

3.5.3 The frequency range of the generator and transducer

Higher frequencies have higher sensitivity to defect detection (smaller defects can be detected) however the drawback is higher attenuation. Condenser tubes in the power generation industry are typically greater than 6m long while through wall pitting can have a cross-sectional area of approximately 1% of the tube cross-sectional area. This represents a 1mm diameter pit in a 1mm wall thickness tube with an outside diameter of 25.4mm (1 inch). Attenuation and sensitivity must be carefully balanced when selecting an ultrasonic inspection frequency.

Lower frequencies also tend to increase the deadband. For the same number of cycles in a toneburst, a lower centre frequency will take longer to discharge during which time the transducer is unable to measure the received signals that may exist due to defects in the dead zone.

3.5.4 The flexibility of the analysis and control software

The extent to which the output of the generator to the transducer can be controlled, and the extent to which the input signals received by the transducer can be captured, are important considerations. The control software must have the ability to vary the input signal frequency and duration as a minimum while the analysis software must enable analysis of the received signal in the time domain and frequency domain. The ability to transfer captured data to other software packages (such as ***MATLAB***) for further analysis is an added advantage.

Other aspects that require consideration when selecting a commercial guided wave system include cost, quality and capability to deliver the product within the timeframes required.

3.6 Conventional bulkwave ultrasonic inspection systems

Conventional, commercially available ultrasonic equipment is fundamentally different from the modern guided wave equipment due to the following key aspects:

- Bulkwaves consist of primarily two wave types, transverse and longitudinal, both of which has a constant velocity and no dispersion. There is therefore no need for the wave generator to have frequency variation capability.
- Conventional systems typically generate a voltage spike containing a broad range of frequencies which excite transducers of known centre frequencies.

- The through thickness volume is inspected as opposed to the length of the specimen. Propagation distance is therefore much shorter making attenuation much less of a concern. Frequencies in the MHz range can therefore be applied to improve sensitivity.

Conventional systems are therefore typically unsuitable for guided wave applications due to the short range and the high frequencies generated as well as the inability to vary frequency. However, without the ability to limit the number of wave modes and with frequencies in the MHz range, the generation and analyses of guided wave signals using conventional bulk wave ultrasonic test equipment and transducers is a complex but an instructive exercise. Research utilising conventional equipment is not reported on, for reasons as explained above. A novel approach to the inspection of thin walled plates using high frequency guided waves is presented in Chapter 4. High frequency guided waves generated using readily available bulk wave test equipment may provide an alternative to classical pulse echo bulk wave testing where there is a need to improve the probability of detection while reducing the inspection duration.

3.7 Defect detection and sizing using guided waves in plates

Guided waves and their interaction with defects in steel plates have been studied in detail by Alleyne [77]. He found that the sensitivity of specific wave modes to particular notches was dependent on mode order, frequency-thickness product, mode type and notch geometry. His study was based on A_0, S_0 and A_1 modes interaction with machined notches in steel plates. He also found that detection was possible when $\frac{\lambda_L}{d} \approx 40$. This means that defect depths (d) of less than 0.1mm could be detected in plates below the A1 cut-off frequency of 1.6MHz in steel plates. The calculation is as follows:

$$d \approx \frac{\lambda_L}{40} \; and \; \therefore d \approx \frac{c_L}{f \times 40} \approx \frac{5850}{1.6E6 \times 40} \approx 0.09mm$$

He also suggested that monitoring the amplitude of transmission beyond the defect could provide a method of defect sizing.

Edalati et al [54] studied the interaction of the A1 and S1 modes with notches of 0.2 to 1.2mm depth in 2mm thick aluminium plate. They exploited Snell's law relation proposed by Worlton [45] and given by Equation 2.25 to generate the graph of incident angle (θ_p, the wave angle in

the Perspex) versus frequency-thickness product. The angle at which the A1 mode can be generated can be calculated as follows:

Frequency-thickness product: 2MHz X 2mm = 4MHzmm.

Phase velocity at 4MHzmm of A1 in Aluminium, C_p = 6100m/s.

Longitudinal velocity in Perspex, C_m = 2730m/s.

$$c_p = \frac{c_m}{\sin\theta_p} \;\therefore\; \theta_p = sin^{-1}\left(\frac{c_m}{c_p}\right) = sin^{-1}\left(\frac{2730}{6100}\right) = 26.6^0$$

This agrees with the graph produced by Edalati shown in Figure 3.17. They used the relation given in Equation 3.2 to locate the defect.

$$L_d = V_G \times t_{of} \qquad (3.2)$$

Where:

V_G = group velocity

T_{of} = time of flight of the Lamb wave.

L_d, L_b = location of defect and the back wall.

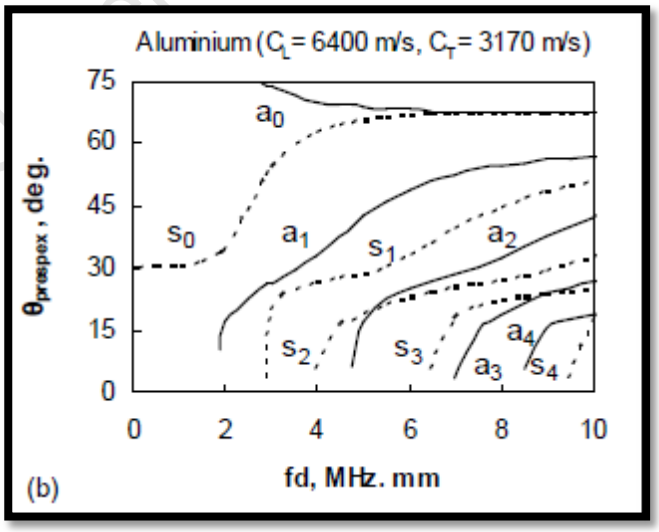

Figure 3.17: Graph of incident angle of longitudinal wave and frequency-thickness product [54].

Finally they proposed the 6dB drop method for determining the defect surface length similar to that used for conventional pulse-echo techniques.

Hee Don Jeong et al [79] investigated the optimum frequency and incident angle to generate A_0 and S_0 Lamb waves with which to detect machined defects of various diameters in 2.4mm thick steel plate. It was found that 840kHz was the optimum frequency at an incident angle of 30^0 (S_0) or 85^0 (A_0). This serves to confirm the effect of frequency on detection capability. A large variation (17%) was obtained between the expected group velocity and the experimental group velocity for S_0 which was not explained by the author.

3.8 Defect detection and sizing using guided waves in pipes and tubes

Guided waves in cylindrical structures are much more complicated than guided waves in plates [22]. The fundamentals of guided waves in cylindrical structures were formulated by Gazis [27]. In his work, he describes the behaviour of longitudinal, torsional and flexural waves from a mathematical perspective.

Guided waves for pipes and tubes are grouped because the physical/mathematical behaviour is the same (both cylindrical objects). There is however significant practical considerations that may necessitate a different approach to the inspection of thin walled (less than 2mm) surface condenser tubes compared to long length schedule 40 pipes. These practical considerations are listed below:

- Wall thickness – Condenser tubes are typically less than 2mm thick. Pipes on the other hand are usually > 5mm thick. Much higher sensitivities are therefore required for condenser tubes.
- Flange connections – There are no flanged connections on tubes which hinder transmission.
- Welded connections – There are no welded connections or seams on tubes however tube to tube sheet welds are used in some cases.
- Accessibility – The condenser tube is accessible from the inside (in-bore transducer), whereas pipes are typically accessible from the outside.

- Leakage – Condenser tubes may be submerged in water/fluid and therefore have ultrasonic energy 'leakage' on the external surface of the tube. Pipes on the other hand may be filled with liquid and/or be submerged in fluid or lagged/buried. Pipes can therefore be subjected to 'leakage' on neither, one or both surfaces.
- Supports – sag plates (tube support plates), baffle plates and tube support sheets provide interference due to the stresses on the external surfaces. These are similar to supports provided for pipes however, in the case of tubes, sag plates often have a clearance fit and therefore immune to interference.

Demma et al [55] provide a guide for interpreting corrosion measurements using guided waves in steel pipes 2" to 24". They analysed pipe size, defect size, guided wave mode and frequency on the reflection of guided waves from notches and present a map of the reflection coefficient as a function of the circumferential extent and defect depth. Their work is based on the use of L(0,2) and T(0,1) mode and is limited to frequencies for which the modes are non-dispersive.

The study was based on finite element predictions only though and like so many of the research papers, only theoretical defects are studied. Several findings of note are made namely:

- The zero order reflection coefficient between 30kHz and 65kHz is essentially constant for through thickness depth circumferential cracks and is in fact proportional to the circumferential extent.
- The axisymmetric mode incident on an axisymmetric feature (circumferential notch) results in axisymmetric reflection while an axisymmetric mode incident on a non-axisymmetric feature (part circumferential notch) results in non-axisymmetric reflection.
- The circumferential extent of a defect can be estimated by evaluating the ratio between the first order (mode converted signal) and the zero order signals. The ratio was found to be insensitive to defects with circumferential extents less than 15%.
- The axial extent of the defects has a significant effect on the reflection coefficient for part depth defects. The reflection coefficient increases monotonically from 0% to approximately 25% axial extent and then reduces again to a minimum at a relative extent of around 45%.
- The reflection coefficient increases with pipe thickness while defects on the outer wall of the pipe produce a bigger reflection than defects on the inner wall [93]. The implications for condenser tubes are that, at 1mm wall thickness, they can have significantly lower reflection coefficient than the reflection coefficients reported in this study. Also, external pitting, if

detected, can have a higher reflection coefficient than an internal pit of the same cross sectional area.

- A map, as shown in Figure 3.18 is provided to determine defect size.

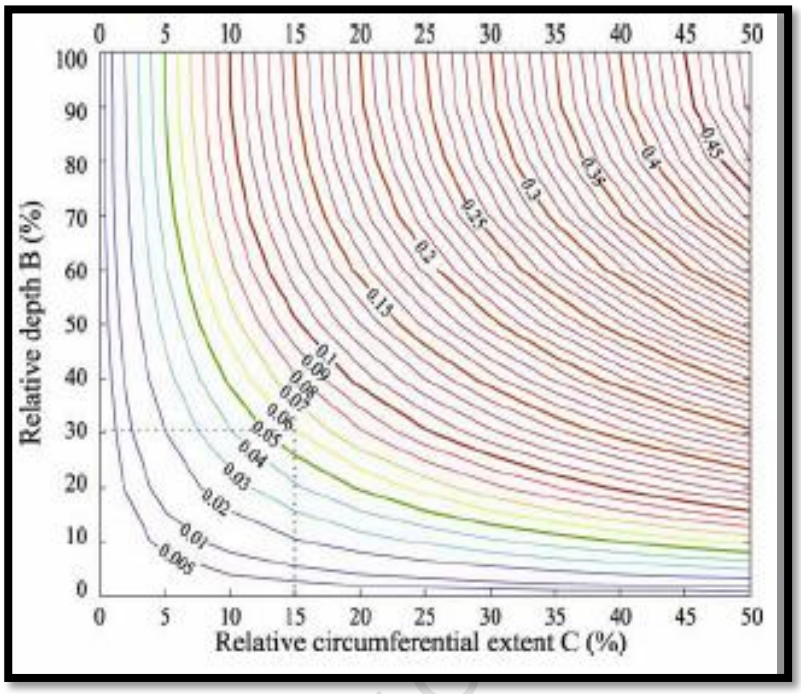

Figure 3.18: Map to determine defect size once the zero order reflection coefficient and the ratio of first order to zero order is calculated. The circumferential extent is obtained from this ratio [55].

Applying these principles to admiralty brass condenser tube with OD 23mm, a frequency higher than 75kHz (1.7MHz-mm) and 125kHz (2.8MHz-mm) would be suitable for T(0,1) and L(0,2) modes respectively. The effect on axial extent will be negligible based on the following:

$\lambda = C/f = 3650/150\,000 = 24.3$mm.

The reflection coefficient will be a minimum when:

$a_{min} = 0.45 \times 24.3 \approx 11$mm

$a_{max} = 0.25 \times 24.3 \approx 6$mm

Ammonia grooving defects are characterised by axial extents between 0.5mm and 2mm which represent a relative extent between 2% and 8% (0.5/24.3 X 100% and 2/24.3 X 100%).

Vinogradov et al [5] studied guided waves in 0.75" carbon steel heat exchanger tubes with artificial flaws to simulate erosion. Magnetostrictive sensors were used with a frequency ranging from 18 to 48kHz. The cross-sectional area of the defects studied were all greater than 1% of tube cross-sectional area. This was one of a series of papers involving the use of guided wave inspection of heat exchanger tubes from 2002 to 2009. The work was done in conjunction with EPRI and IHI Southwest Technologies. The main findings were as follows:

- Amplitude response increased dramatically for constant depth and increasing axial extent. The L(0,1) mode was used at a frequency of 32kHz. These findings are found to be in line with that of Demma et al.
- Vinogradov goes on to propose a formula for cross sectional area, D as follows:

$$D = \frac{A_{flaw}}{A_{end}} \times K_{ax} \times 100\%$$

Where:

A_{flaw} = response amplitude

A_{end} = backwall echo

K_{ax} = correction factor

The relationship provides the size of the defect cross sectional area. It does not provide the remaining wall thickness, the basis upon which tube plugging is made. It is reported that an effective size greater than 1.5% can be detected using 250kHz L(0,2) mode guided wave. The effective size, ES is defined as:

$$ES = \frac{cross - sectional\ area\ of\ defect}{cross - sectional\ area\ of\ tube} \times 100\%$$

Mohr and Holler [56] studied the L(0,2) and T(0,1) modes (they referred to T(0,1) as T(0,0)) at frequencies up to 1325kHz in austenitic tube. Defects with a depth 0f 0.05mm (5% of depth) were detected. Minimum SNR_{dB} of 6 was achieved at 1325kHz and an attenuation of 1.1dB/m. They also found that the T(0,1) mode was more sensitive than L(0,2) mode to longitudinal (axially oriented) defects .

3.9 Summary and contribution to the field of guided waves

Guided waves are inherently complex and classic ultrasonic NDT based on bulk waves have dominated the industry due to their relative simplicity. The guided wave modes, A0, S0 and SH0 (plates) and L(0,1), L(0,2) and T(0,1) (pipes and tubes) have been extensively researched. There is limited application of guided wave testing in industry beyond the current area of long range inspections of pipes. In particular, the application of guided waves for the inspection of heat exchanger tubes, remain in the developmental stage. A method to determine defect depth (remaining wall thickness) in plates or condenser tubes does not exist. Research is being conducted for applications in the power generation and oil and gas industries amongst others. Very limited research has been conducted on the interaction of guided waves with defects having a cross sectional area less than $1mm^2$. In particular, no such research could be identified where *copper* tubes were used which is highly attenuative. Furthermore, no research could be identified that involved the experimental measurement of multiple nodes on small bore tubing containing such small defects. The number of suppliers of guided wave equipment is limited and the equipment still remains in a development stage for many applications. No research could be identified that exploit the repeated minima at constant group velocity of S_m, A_m (m = 1, 2, 3…) and L(0,m) where m = 3, 4, 5….

Given the findings of the literature review, this thesis has contributed to the field of guided waves in the following way:

- A method using basic ultrasonic equipment was developed which exploits the group velocity minima at 2300m/s in steel plate.
- Copper condenser tubes containing pit defects with a cross sectional area as small as $0.2mm^2$ were inspected using guided waves.
- Elements of the work undertaken by Alleyne [21] and Demma et al [55] were extended to tubes containing defects with a circumferential extent less than 10%.
- Experimental measurements of the *axial displacement* of the L(0,2) mode were taken at 48 nodes which enabled the zero order and first order modes to be separated for analysis.

Chapter 4

Conventional equipment experimental details and results

4.1 Introduction

This chapter investigates the use of conventional ultrasonic NDT equipment to generate guided waves for research purposes. The use of equipment that is readily available to generate guided waves can be of great benefit, as commercial equipment is expensive and still in its development phase for many guided wave applications. It may also stimulate interest and accelerate development of industrial applications more quickly than has been the case thus far. However, the presence of multiple modes due to the high, broadband frequencies synonymous with this type of equipment necessitates careful analysis of received signals. This makes the use of such equipment more complicated but also very instructive.

The chapter begins by describing the equipment setup and calibration. The material and test sample specifications are then provided. Both steel plates and copper tubes, each with pits (drilled holes) and grooves (machined slots) were inspected, so their specific dispersion curves are also provided for ease of reference. The experimental program and methodology is described next and consists of a three step approach, identified as study 1, 2 and 3. Finally the results are provided for each of the studies and then discussed before the chapter is summarised.

4.2 Equipment setup and calibration

This section describes the ultrasonic flaw detector, transducers, material specification, test samples and calibration setup.

4.2.1 Conventional Ultrasonic flaw detector

A ***Krautkramer USN52L*** ultrasonic test (UT) set is used to excite the transducers in all the experiments conducted in this chapter. The UT set is pictured in Figure 4.1.

Figure 4.1: Conventional ultrasonic test set, USN52L.

The important parameters relevant to the experiments are given below [94]:

- Frequency range: 1 of 4 filters can be selected. 0.4 MHz to 10 MHz (broadband), 2 MHz to 8 MHz (midrange, centre at 4 MHz), 0.3 MHz to 4 MHz (low range), 3 MHz to 10 MHz (high range).
- Pulse type: 600V spike
- Repetition rate: low (1 pulse every 1.1ms) or high (1 pulse every 2.2ms) option.
- The ultrasonic velocity can be varied depending on material, from 0 to 9999m/s.
- The range is adjustable from 5mm to 5000mm.
- It has 4 damping resistor options, 50Ω, 75Ω, 150Ω and 1000Ω.

The frequency bandwidth generated by the UT set is shown in Figure 4.2.

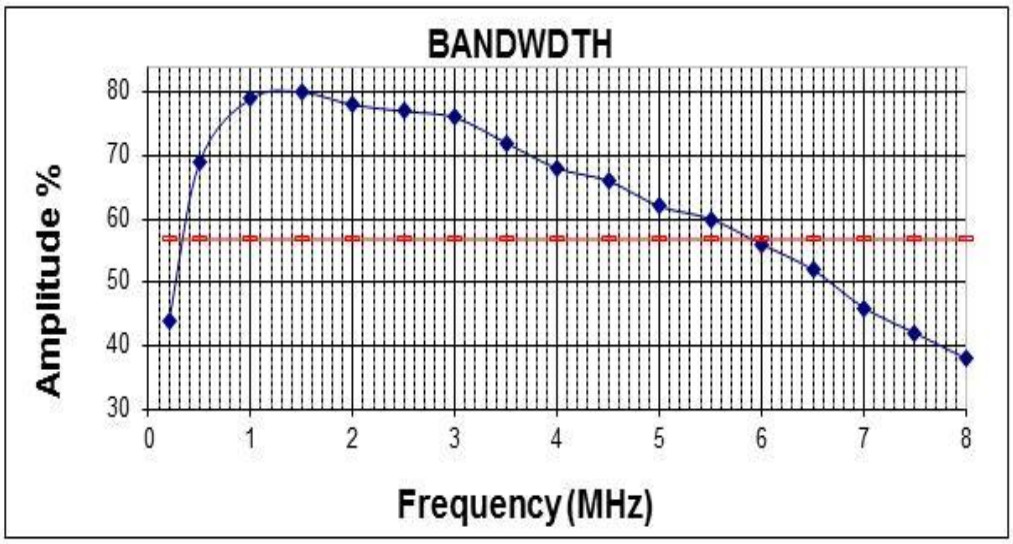

Figure 4.2: *USN52L* frequency bandwidth output measured using a spectrum analyser.

4.2.2 Transducers

Standard, bulk wave ultrasonic transducers that were used in the experiments are listed in Table 4.1 along with their calibration data.

Transducer Freq. (MHz)/ angle in steel)	Damping (Ω)	Delay (µs)	Zero (µs)	Filter (MHz)	Velocity In steel.	Index (mm)
$1/45^0$	150	0	14.2	0.3-4	5850	20
$1/0^0$	150	0	2.3	0.3-4	5850	n/a
$1.8/70^0$	1000	0	11.0	0.3-4	5850	28
$1.8/60^0$	1000	0	11.0	0.3-4	5850	30
$2/45^0$	1000	0	4.76	0.3-4	3240	11.5
$2/60^0$	1000	0	4.76	0.3-4	3240	13
$4/45^0$	1000	0	7.60	0.4-10	3240	4
$4/70^0$	1000	0	7.60	0.4-10	3240	4

Table 4.1 : Conventional ultrasonic transducers and their settings applied in the experiments.

The transducers and UT set were calibrated using the IIW-2 calibration block pictured in Figure 4.3. The transducers are reasonably broadband. The 1.8MHz, 70 degree and 60 degree longitudinal wave transducer specifications are given in Figure 4.4 and Figure 4.5 [95].

Figure 4.3: Calibration block, IIW-2, used for the calibration of the transducers.

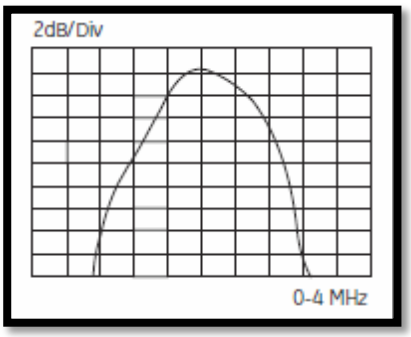

Figure 4.4: Bandwidth of the VRY60 and 70 degree transducers [95].

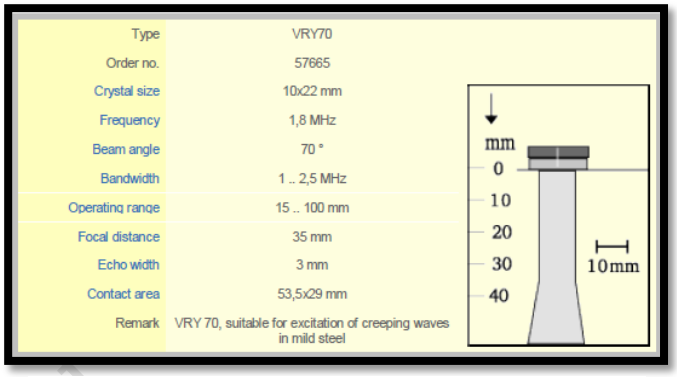

Figure 4.5: VRY60 and 70 degree transducer specifications [95].

The 4MHz, 45^0, 60^0 and 70^0 transducers are manufactured by ***Vincotte (AIB)***. Their specifications are given in Figure 4.6 and Figure 4.7. Their crystal sizes are 8X9mm. Unfortunately, not all the transducer specifications were available.

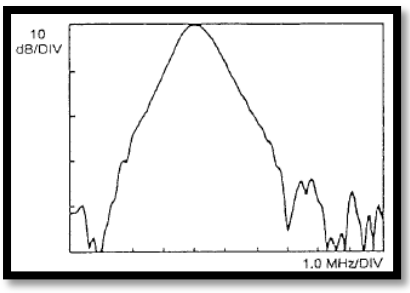

Figure 4.6: Bandwidth of the *AIB Vincotte* transducers (45^0, 60^0 and 70^0) used in the experiments.

F_{-6}	= 4.0 ± 0.3	MHz	Element size	= 8x9 ± 0.1	mm
BW_{-6}	= 35 ± 5	%	WH	= 3 ± 0.1	mm
$S/R_{(20)}$	= 55 ± 6	dB	Ns	= 17 ± 3	mm
Z_{el}	= 98 ± 25	Ω	EP	= 14 ± 1	mm
	Inductive		PD	= 7.7 ± 0.25	µs
α	= 45 ± 3	°	$IR_{(dB)}$	= -45 ± 10	dB
γ	= 0 ± 1	°	$IR_{(mm)}$	= 15 ± 5	mm
φi_{-6dB}	= 3.3 ± 0.4	°	T	= -20→+60	°C

Figure 4.7: Specifications of the *AIB Vincotte* transducer range (45^0, 60^0 and 70^0) used in the experiments.

4.3 Material and test sample specifications

The material properties of the materials used are tabulated in Table 4.2. The equations [96] to calculate the parameters in Table 4.2 are provided in Appendix A.1.

Material Type	Poisson's ratio	Velocity (Shear) (m/s)	Velocity (long) (m/s)	Density (kg/m3)	Young's modulus (GPa)	Modulus of rigidity (GPa)
Mild steel plate (various thickness)	0.3	3230	5850	7800	210	80
Copper tube (0.9 and 1mm thick)	0.34	2260	4660	8900	110	45
Admiralty Brass tube	0.34	2120	4430	8530	110	41
Perspex	N/A	1430	2730	N/A	N/A	N/A
Oil (couplant)	N/A	N/A	1740	N/A	N/A	N/A

Table 4.2: The specifications of the materials that were used in the calculations [96], [14].

Mild steel plate test samples and copper tube test samples were used for the experiments in this chapter. Detailed drawing of the mild steel test samples are contained in Appendices A.2 (grooves) and A.3 (pits). Similarly detailed drawings of the copper tube test samples are contained in Appendices A.4 (grooves) and A.5 (pits).

4.4 Dispersion curves for mild steel plate and copper tubes

The phase velocity and group velocity dispersion curves for the mild steel plate are given in Figure 4.8 and Figure 4.9 respectively. The curves were generated utilising ***PACshare©*** dispersion curve software version 1.00. The wave mode of interest is calculated using Equation 2.25. Figure 4.10 and Figure 4.11 are the phase and group velocity curves respectively for 0.9mm thick, 22mm diameter copper tubes. The curves were generated using ***PCDisp***.

Figure 4.8: Phase velocity curves for mild steel plate.

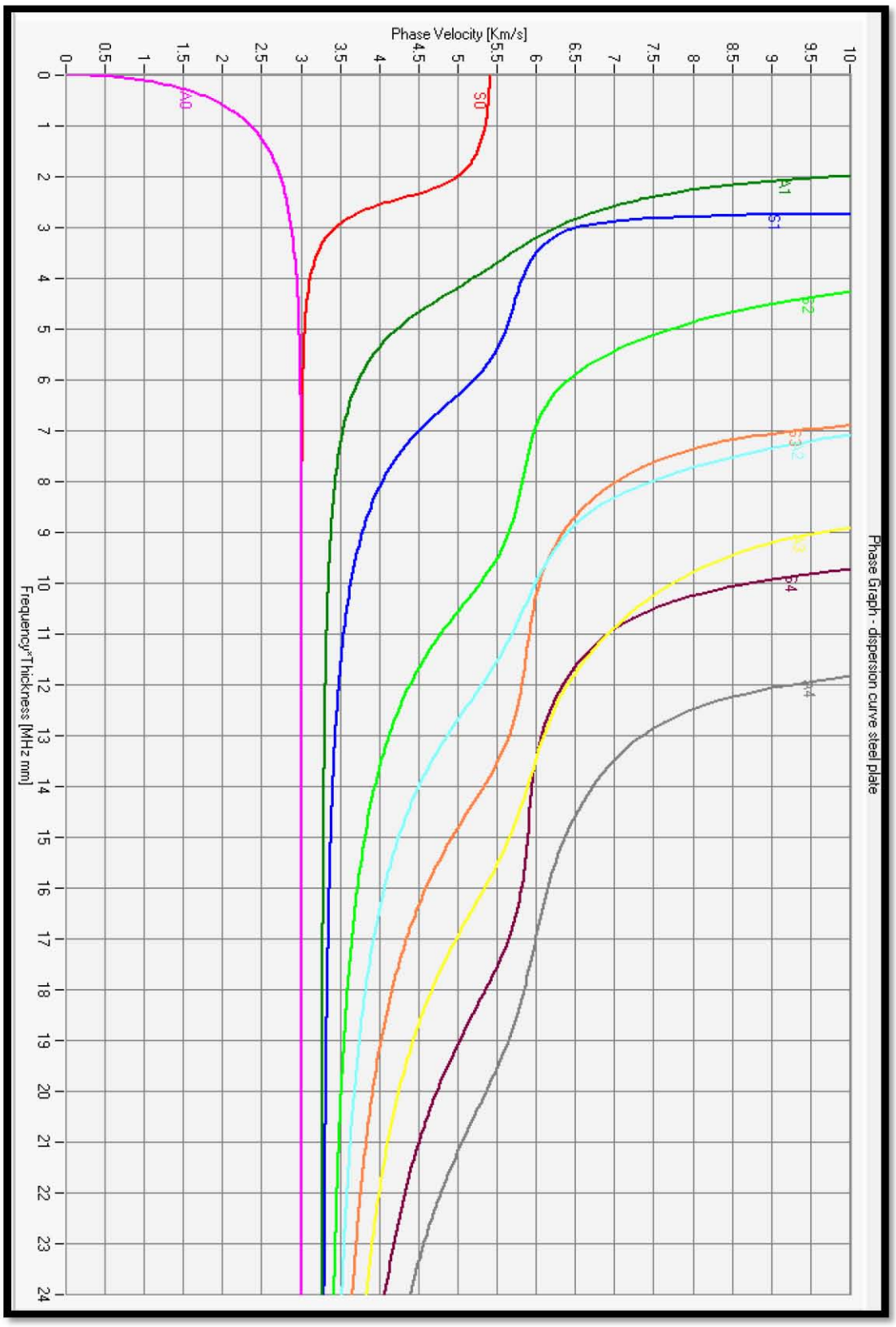

Figure 4.9: Group velocity curve for mild steel plate.

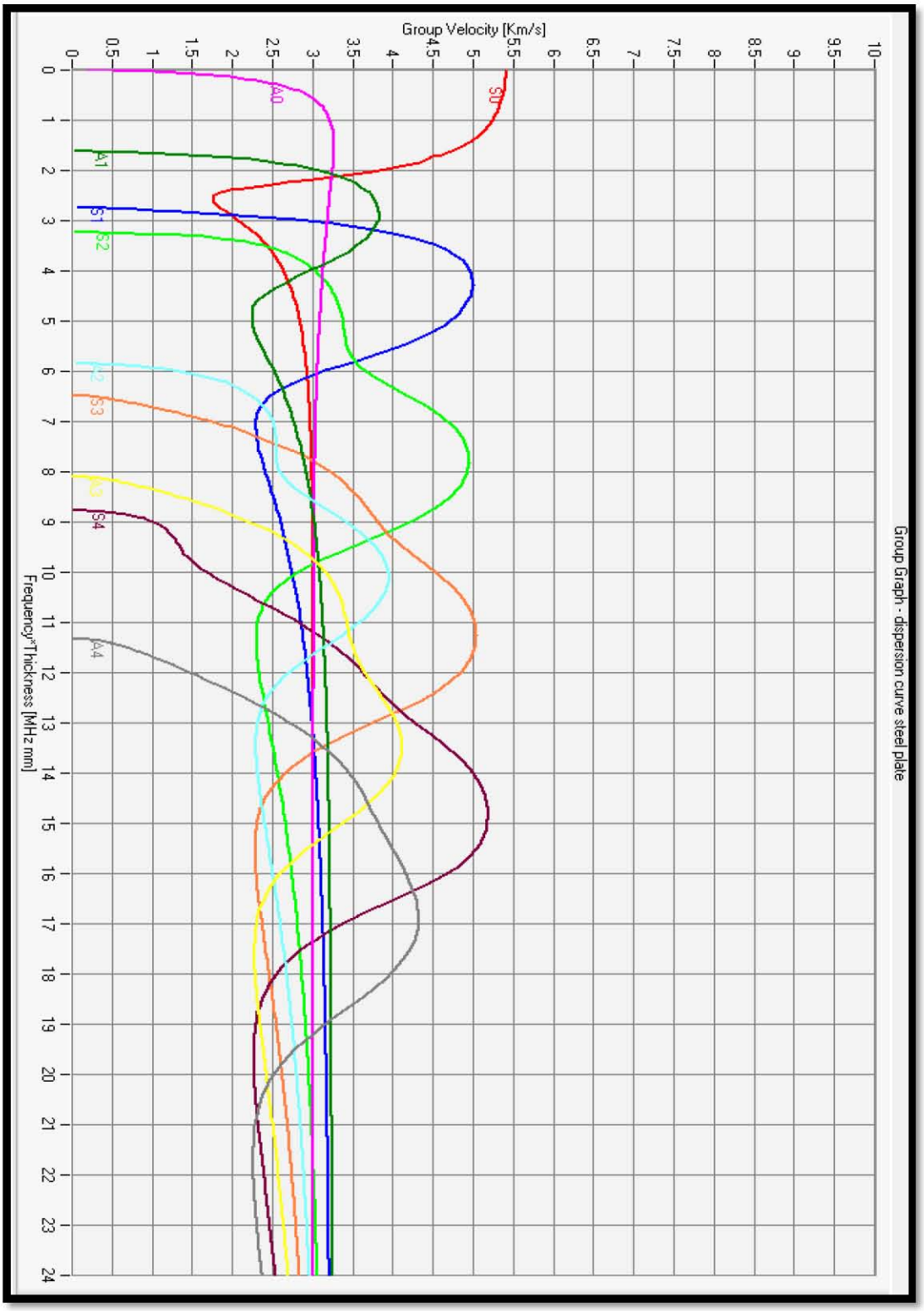

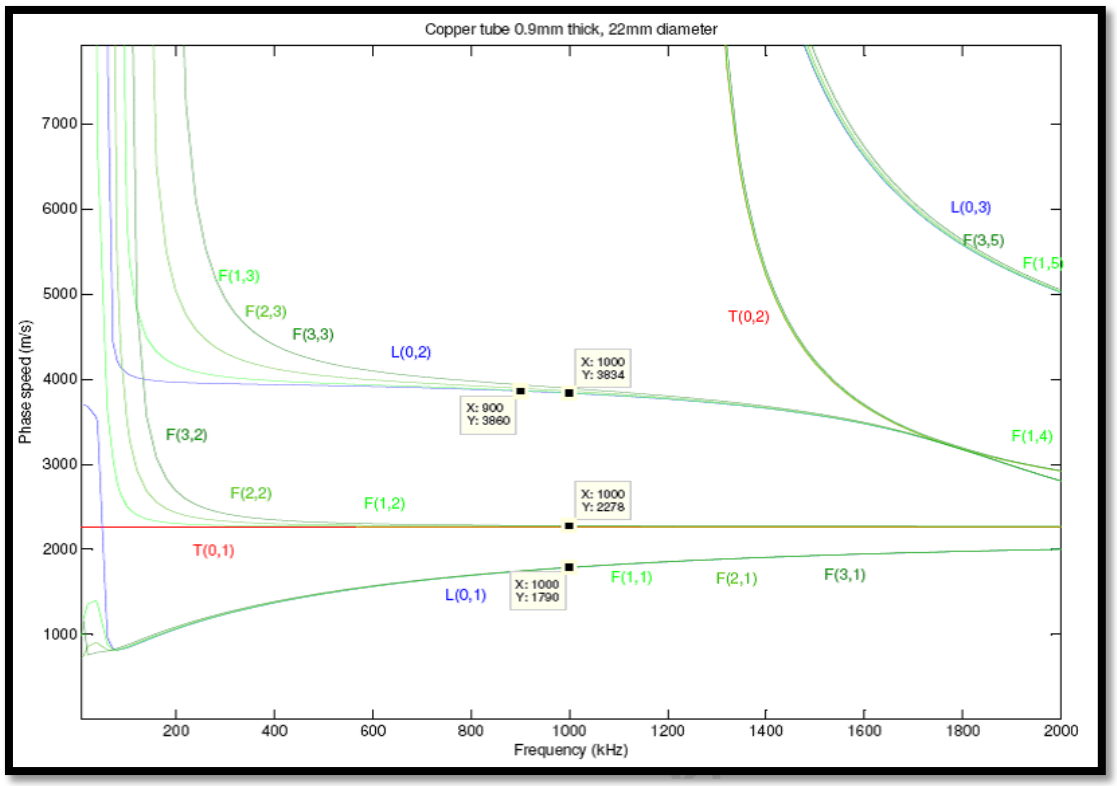

Figure 4.10: Phase velocity dispersion curves for 0.9mm thick, 22mm diameter copper tube.

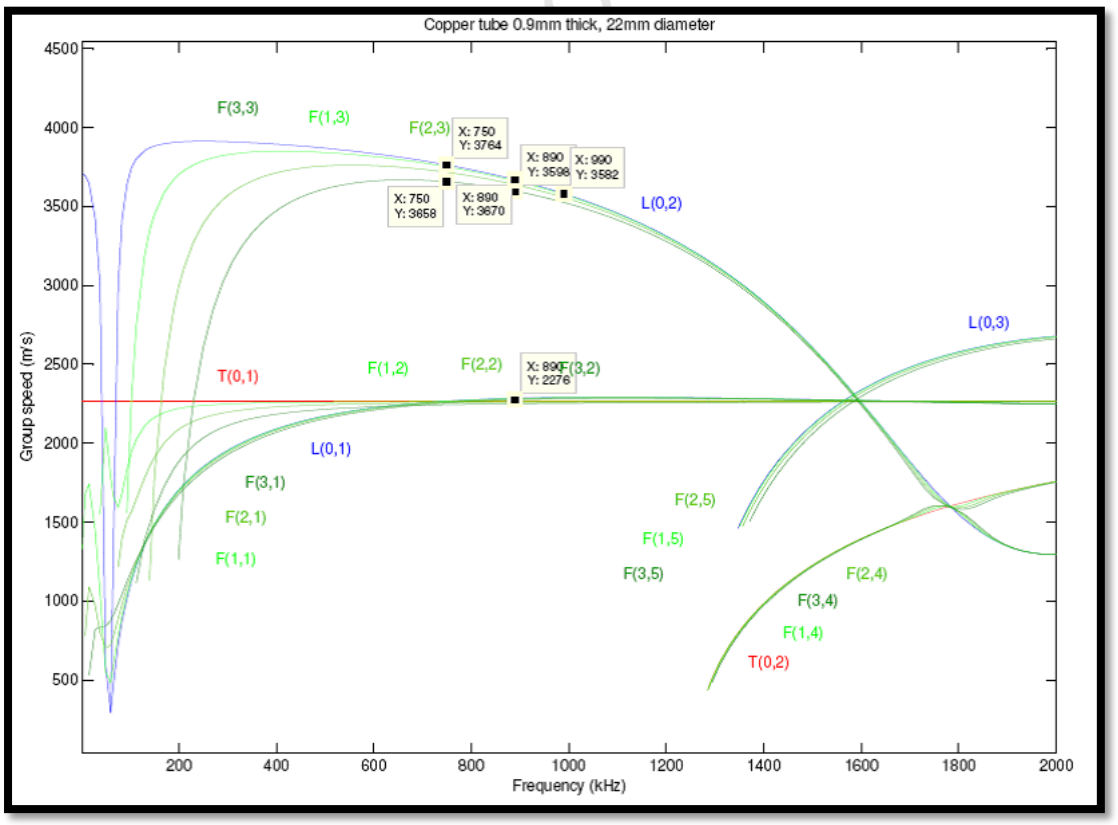

Figure 4.11: Group velocity dispersion curves for 0.9mm thick, 22mm diameter copper tube.

4.4.1 Experimental program and methodology

Three studies were conducted to determine the viability of using the basic bulk wave ultrasonic equipment to generate guided waves in pipes and tubes. The test program objectives are as follows:

First, a range of standard bulk wave transducers were excited using the USN52L to identify a transducer that could generate a particular mode or modes of guided waves in various thickness plates. Special attention was given to the group velocity minima at 2300m/s.

Second, the most suitable combination of transducer and wave modes identified in the first step, was evaluated by determining its detection capability. Steel plates of various thickness, containing pits and grooves, were inspected.

Third, the wedge method [47] shown in Figure 4.16 was applied to copper tubes containing pits and grooves. Again its detection capability was assessed as a means of evaluating its viability.

The above approach exploited the use of Snell's law, Equation 2.25 to generate guided waves in both plates and tubes. The three steps and their methodology are described in more detail in Sections 4.4.2, 4.4.3 and 4.4.4.

4.4.2 Generating guided waves in plates – study 1

Here, two methods were applied, both of which were essentially the same but differing in their intention/approach. In the first method, an attempt was made to generate specific modes although additional modes would be unintentionally generated. In the second method, the intention was to generate multiple modes which have the same group velocity. This was done by exploiting special regions, the group velocity minima, on the group velocity dispersion curve. The first method is outlined below (see Figure 4.12):

- The phase velocity for each of the transducers was determined using Equation 2.25.
- The frequency-thickness region based on the transducer bandwidth was then determined.
- The applicable mode and its group velocity could then be obtained from the dispersion curve.

Table 4.3 lists the transducers that were used to generate the selected modes of interest, the plate thickness, their phase velocity (calculated) and the expected group velocity (from dispersion the curve) in metres per second.

Transducer	Angle in perspex	Angle in steel	Calc. phase velocity	Possible Modes	Plate thickness	Group velocity (m/s)
VRY70, 1.8MHz long	26^0	70^0	6227	A2	6	3680
				A1	1.3	3800
2MHz, 45 shear	18.2^0	45^0	4578	S2	6	2290
2Mhz, 60 shear	22.5^0	60^0	3741	S0	1.3	1810
				A1	3	2510
4MHz, 45 shear	18.20	45^0	4578	S2	3	2290
4MHz, 70 shear	24.5^0	70^0	3448	A1	2	2880
				S1	3	2960
				A2	6	2985

Table 4.3: Calculated phase velocities and expected modes generated for each transducer.

An example is illustrated, in Figure 4.12 for the VRY70 transducer, which generates the A1 and S1 modes at a phase velocity of 6227m/s. Its bandwidth is 1MHz to 2.5MHz which translates to a frequency thickness region from 1.3MHz-mm to 3.25MHz-mm for the 1.3mm thick plate.

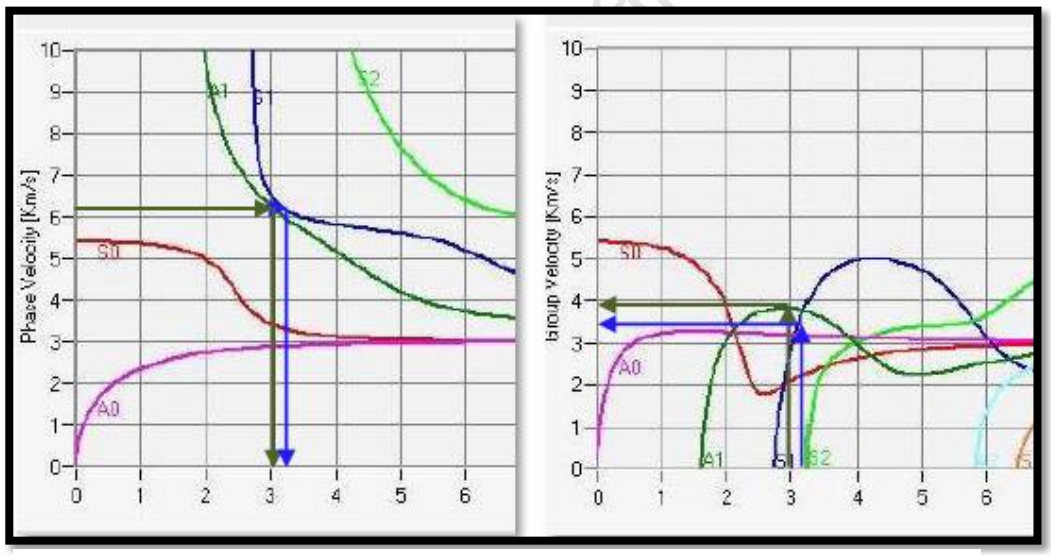

Figure 4.12: An illustration of the expected modes and group velocities obtained from the dispersion curves. The VRY70 generates the A1 and S1 modes.

For method 2:

- Three phase velocities were generated in 2mm plate using three different, standard transducers (Figure 4.13).
- The modes generated in each case were then identified based on their group velocity obtained from the UT set.

The expected modes generated are listed in Table 4.4 along with the calculated phase velocity, frequency thickness (frequency thickness region) and group velocity. The measurements were

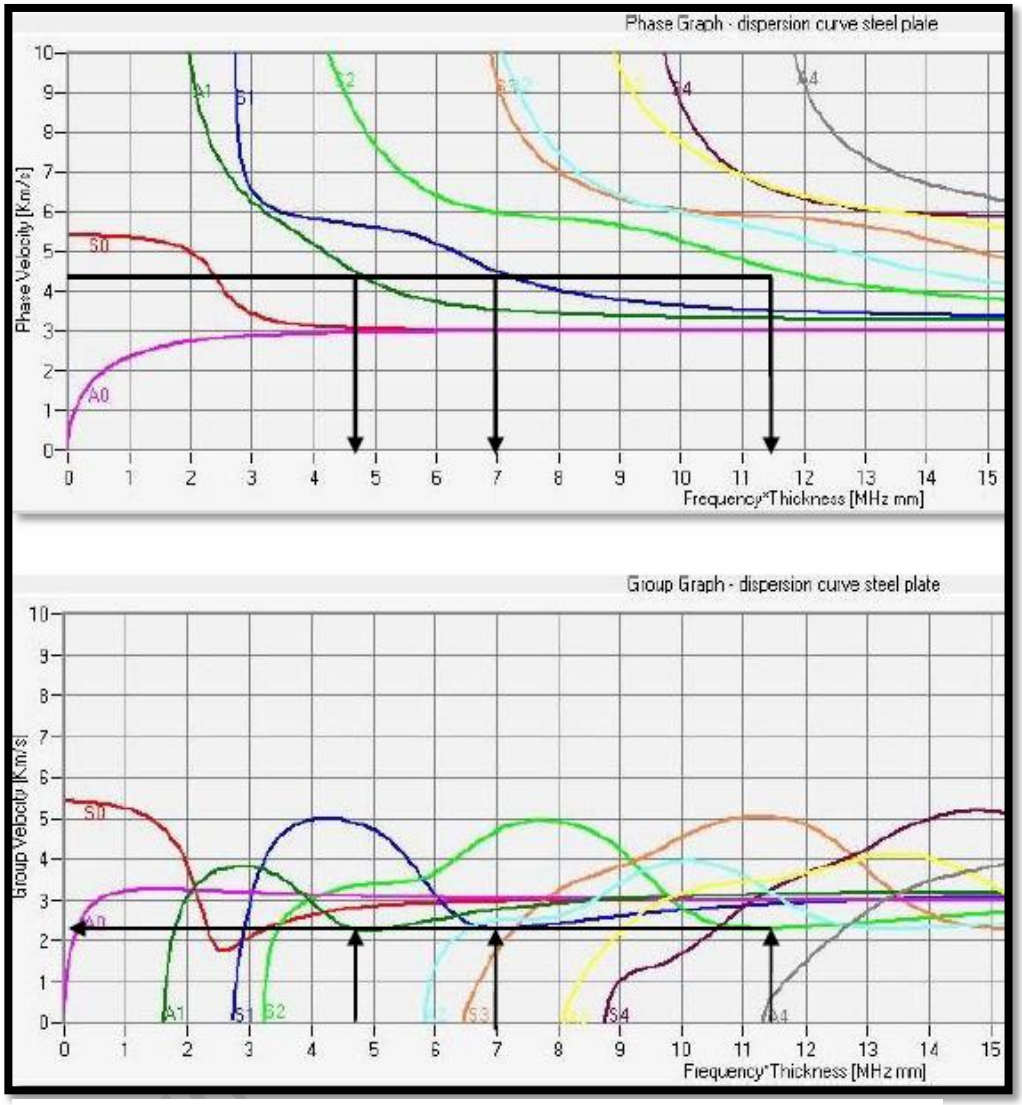

Figure 4.13: Multiple modes generated in 2mm plate using 4MHz, 45 degree transducer. Interestingly, all modes have a group velocity at a minima of approximately 2300m/s..

taken as shown in Figure 4.14. The transducer was positioned at a known distance from the edge of the plate and the UT set velocity adjusted until the back wall (BW) echo reflected the correct, known distance. The group velocity was then recorded and compared to the expected group velocity.

Transducer	Calculated phase velocity (m/s)	Frequency thickness (MHz-mm)	Possible Modes	Group velocity at phase velocity frequency (m/s)
VRY70, 1.8MHz long	6227	3.6 (2 to 5)	A1	3802
			S1	3783
2Mhz, 60 shear	3741	4 (3 to 5)	S0	1816
			A1	2500
4MHz, 45 shear	4578	8 (7.4 to 8.6)	S1	2300

Table 4.4: The expected modes generated in 2mm steel plate using standard transducers.

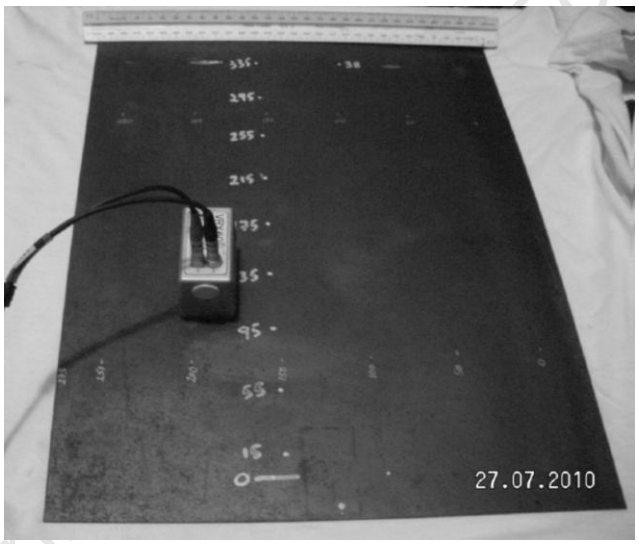

Figure 4.14: Setup of study 1. The generation of various modes using standard ultrasonic test equipment and transducers.

A photograph of the signal obtained was taken for illustration purposes and to compare the quality of the signal responses.

4.4.3 The interaction of the selected guided wave modes with defects in plates – study 2

Three sets of tests were conducted as follows:

- 1.6mm thick steel plate with 1.5mm diameter holes and varying depth.
- 3mm thick steel plate with 5mm and 15mm grooves, each of varying depth.
- 3mm thick steel plate with 1.5 and 2.5mm holes, each of varying depth.

The procedure applied is listed below:

- The transducer was positioned 200mm from the plate edge with no defect in its path and the velocity set at 2300m/s.
- The backwall was maximised to 100% full screen height by adjusting the gain on the USN52L.
- This backwall amplitude, in the absence of any defects, was taken as the incident signal.
- Each defect was then inspected in turn and the reflected signal from the defect, R_d, the reflected signal from the backwall, R_{BW} and any mode converted signal, R_m was recorded.
- No changes were made on the gain.

The setup is illustrated in Figure 4.15. The frequency thickness region of interest was 5.9MHz-mm to 6.9MHz-mm which included the S1 mode at a group velocity of 2300m/s.

Figure 4.15: Typical setup of USN52L, steel plate and 45 degree shear wave transducer for study 2.

4.4.4 The interaction of guided waves modes with defects in tubes – study 3

The wedge method, illustrated in Figure 4.16 was applied as follows (T1 to T17 are indicated on drawings in A.4 and A.5):

- The T1 defect (0.25mm depth, 1.5mm diameter drilled hole) was detected with the wedge positioned 250mm away from the defect, using the 1MHz longitudinal wave transducer.
- With the defect at the top, the L(0,2) reflection coefficient was measured for T5, T6, T7 and T8, each 3mm diameter drilled holes increasing in depth from 0.25 mm (T5) to through wall depth (T8).
- The reflection coefficient of a 360^0 groove (axially symmetric defect, T17), 0.5mm depth and 1.5mm axial extent was measured.
- Again with the defect at the top, the L(0,2) reflection coefficient was measured for T13, T14, T15 and T16, each being 20mm long grooves, increasing in depth from 0.25mm (T13) to through wall depth (T16).
- The phase velocity of L(0,2) mode in 0.9mm copper tube at 1MHz is between 3800m/s and 3900m/s (from Figure 4.10). The wedge angle, θ, is given by Equation 2.25 and the expected group velocity is between 3800 and 3500m/s, given the transducer bandwidth:

$$\Theta = \sin^{-1}(2730/3860) = 45^0$$

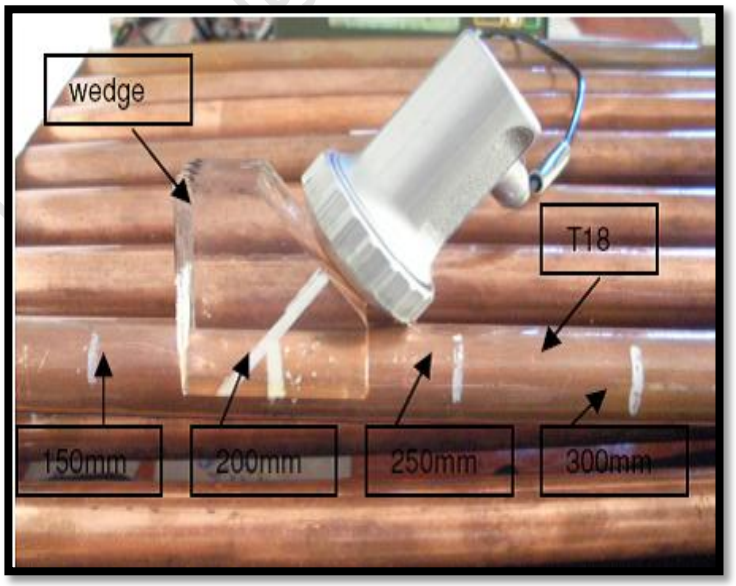

Figure 4.16: The wedge method used to generate the L(0,2) mode in study 3.

4.5 Results and discussion

The results and discussion for studies 1 to 3 are presented in Sections 4.5.1 to 4.5.3:

4.5.1 Results and discussion for study 1

The results obtained for the first method are listed in Table 4.5.

Transducer	calc phase velocity (m/s)	Identified Modes	group velocity at phase velocity freq (A) (m/s)	Actual group velocity (C) (m/s)	error between (C) and (A)	comment on signal (good/OK/bad)
VRY70, 1.8MHz long	6227	A2	3680	unclear	n/a	bad
		A1	3800	3660	-140	OK
2MHz, 45 shear	4578	S2	2290	2293	3	OK
2Mhz, 60 shear	3741	S0	1810	1780	-30	bad
		A1	2510	2480	-30	OK
4MHz, 45 shear	4578	S2	2290	2314	24	good
4MHz, 70 shear	3448	A1	2880	2953	73	OK
		S1	2960	3015	55	good

Table 4.5: The actual group velocity of guided wave modes generated using the first method. The difference between the expected and actual group velocity as well as the quality of their signals is shown.

Table 4.5 provides the identified modes for each transducer along with the calculated phase velocity. The actual group velocity is compared to the expected group velocity and the error is included in the table. A comment on the quality of the signal which is based on the ability to recognise the intended mode is also given. Sample signals obtained are listed in Figures 4.17 to Figure 4.21.

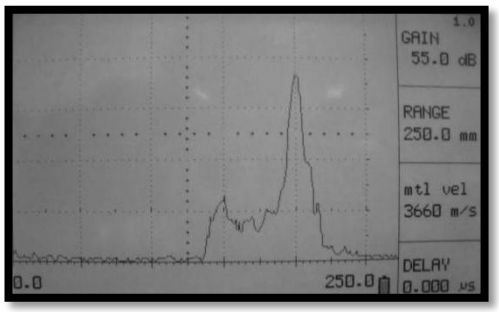

Figure 4.17: A1 mode generated using the VRY70 transducer on 1.3mm plate at a phase velocity of 6227m/s. The peak at the expected distance of 200mm is well defined but a leading peak is also present.

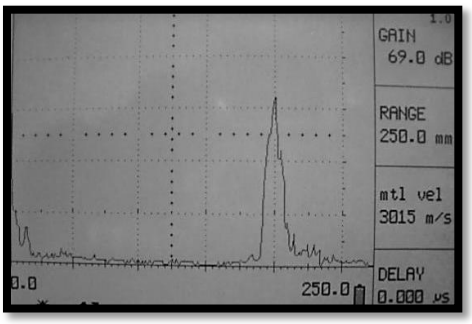

Figure 4.18: S1 generated using 70 degree, 4 MHz shear wave transducer on 3mm plate. A well-defined signal is obtained corresponding to a peak at 200mm and a velocity of 3015m/s. This compares well with the expected velocity of 2960m/s.

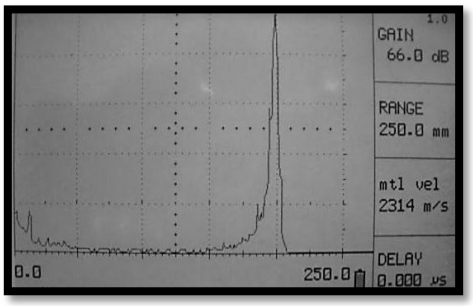

Figure 4.19: S2 and possibly A2 modes generated at 2314m/s using 4MHz, 45 degree shear wave transducer on 3mm plate. The well-defined signal corresponds well with the expected velocity of 2290m/s.

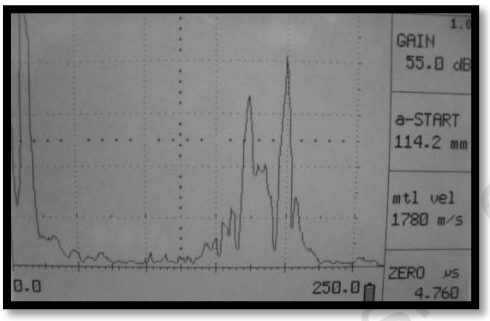

Figure 4.20: S0 mode generated using 60 degree, 2MHz shear wave transducer on 1.3mm plate. Two well defined peaks exist, one of which correspond to 1780m/s that co-insides with the expected distance of 200mm and 1810m/s.

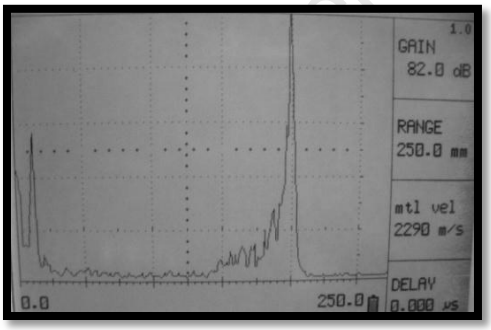

Figure 4.21: S1 generated using 4MHz, 45 degree shear wave transducer on 2mm plate. The actual group velocity of 2290m/s compares well with the expected group velocity of 2300m/s. It is possible that both S1 and A1 are generated provided the bandwidth is sufficient.

The results for the second method are tabulated in Table 4.6. The signal obtained from the 4MHz, 45^0 transducer is shown in Figure 4.19. A well-defined signal is obtained which represent the S1 mode given a frequency thickness region of 7.4MHz-mm to 8.6MHz-mm.

Transducer	calc phase velocity (m/s)	Freq-thick (MHz-mm)	Modes	group velocity at phase velocity freq (A) (m/s)	Actual group velocity (C) (m/s)	error between (C) and (A)	comment on signal (good/OK/ bad)
VRY70, 1.8MHz long	6227	3.6	A1	3802	3620	-182	bad
			S1	3783	4690	907	OK
2Mhz, 60 shear	3741	4	S0	1816	1820	4	bad
			A1	2500	2965	465	bad
4MHz, 45 shear	4578	8	S1	2300	2290	-10	good

Table 4.6: The actual group velocity of guided wave modes generated using the second method. The difference between the expected and actual group velocity as well as the quality of their signals is shown.

Several of the transducers produced well defined signals at group velocities that corresponded well with the expected group velocities. Figures 4.18, Figure 4.19 and Figure 4.21 illustrate such examples. However, in most cases, unexplained signals were also present making the use of these transducers unsuitable in these specific applications. Figure 4.17 and Figure 4.20 illustrate such examples.

Of particular significance was the ability of the 45 degree, 4MHz, shear wave transducer to generate well defined signals of the A1, A2, S1 and S2 signals in the plates ranging from 1.3mm to 6mm thick. The repeated group velocity minima of approximately 2300m/s which co-insides with a phase velocity of 4578m/s, as generated by this transducer, is the basis for these well-defined signals.

The 45^0, 4MHz shear wave transducer provided excellent agreement with the expected mode velocities. This transducer generates several modes depending on the plate thickness (frequency thickness region) that co-inside with a group velocity minimum of approximately 2300m/s. This makes it a unique angle and phase velocity at which to generate more than one mode at the same group velocity provided that the transducer is sufficiently broadband.

Several other modes could be identified with accuracy of less than 5% from the expected velocity. However, the coherence of their signals and the presence of unidentified signals make the use of these unacceptable.

4.5.2 Results and discussion for study 2

4.5.2.1 Holes of 1.5mm diameter and varying depth in 1.6mm plate

The S1 mode was generated in 1.6mm steel plate, containing partial through wall drilled holes, at a group velocity of 2300m/s using the 45 degree shear wave, 4MHz transducer. The results for these inspections are best reviewed by analysing the signals obtained. These are given in Figures 4.22 to 4.25.

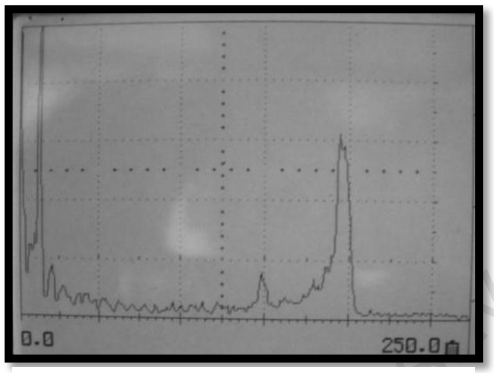

Figure 4.22: Signal response obtained from 1.2mm depth hole in 1.6mm plate. Well defined Rd was obtained but barely any mode converted signal.

Diameter: 1.5mm

Depth: 1.2mm

Mode conversion: Poorly defined mode converted signal.

R_{BW}: Approximately 60%.

R_d: 8 divisions.

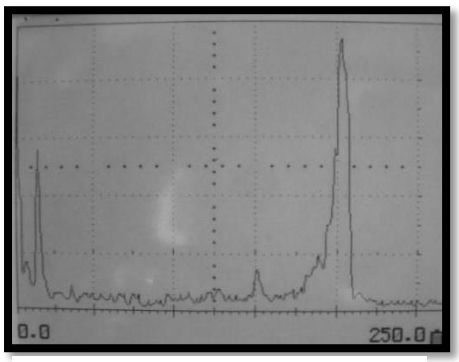

Figure 4.23: Signal response obtained from 0.8mm depth hole in 1.6mm plate. Well defined Rd was obtained but barely no mode converted signal.

Diameter: 1.5mm

Depth: 0.8mm

Mode conversion: Poorly defined mode converted signal.

R_{BW}: approximately 96%.

R_d: 7 divisions.

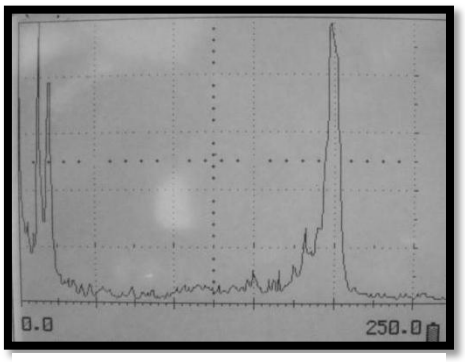

Figure 4.24: Signal response obtained from 0.5mm depth hole in 1.6mm plate. Reduced Rd but still visible and clearly defined mode converted signal.

Diameter: 1.5mm

Depth: 0.5mm

Mode conversion: clearly visible.

R_{BW}: approximately 98%.

R_d: 5.5 divisions.

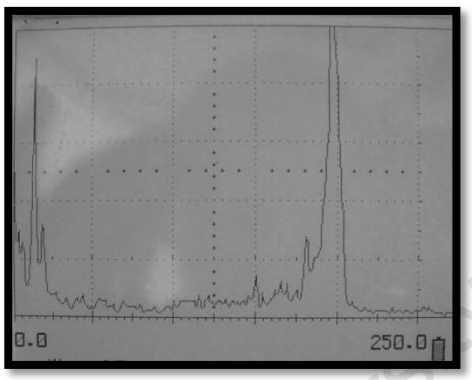

Figure 4.25: Signal response obtained from 0.2mm depth hole in 1.6mm plate. Rd approx. 7.5 divisions. A clearly defined mode converted signal was present.

Diameter: 1.5mm

Depth: 0.2mm

Mode conversion: clearly visible.

R_{BW}: approximately 100%.

R_d: 7.5 divisions.

The reflection of S1 from the defect initially decreased from 7.5 divisions at 0.2mm depth to 5.5 divisions at 0.5mm depth but then increased to 7 and then 8 divisions for 0.8mm and 1.2mm depths respectively. At 0.8mm (50% depth), the S1 reflection was clearly visible and well defined. The mode converted signal diminished as the defect depth increased. The back wall amplitude decreased with each increase in depth but decreased significantly after 50% through wall depth.

4.5.2.2 Slots of 5mm and 15mm length and varying depth in 3mm plate

The next set of results was obtained from the inspection of grooves in 3mm steel plate. The axial lengths of all grooves were constant at 1.5mm. The S2 and A2 modes were generated at a group velocity of 2300m/s. The results are tabulated in Table 4.7.

slot depth (mm)	slot width (mm)	dB of reflected signal from defect	BW echo (% FSH R_{BW})	Reflection coefficient (% R_d)	Mode conv. signal present	cross-sectional area (mm2)	slot depth (% thick)	Mode conv. RC (% R_m)
0.25	5	8.5	69	17	14.5	1.25	8.3	29%
1.5	5	45	69	90	9	2.5	50.0	18%
2.75	5	52	90	104	0	3.75	91.7	0%
3	5	60	100	120	0	15	100.0	0%
0.25	15	29.5	80	59	25	3.75	8.3	50%
1.5	15	52	17	104	10	7.5	50.0	20%
2.75	15	57	27	114	12	11.25	91.7	24%
3	15	60	26	120	0	45	100.0	0%

Table 4.7: Inspection results for grooves of varying depth and length in 3mm plate with S2 and A2 modes.

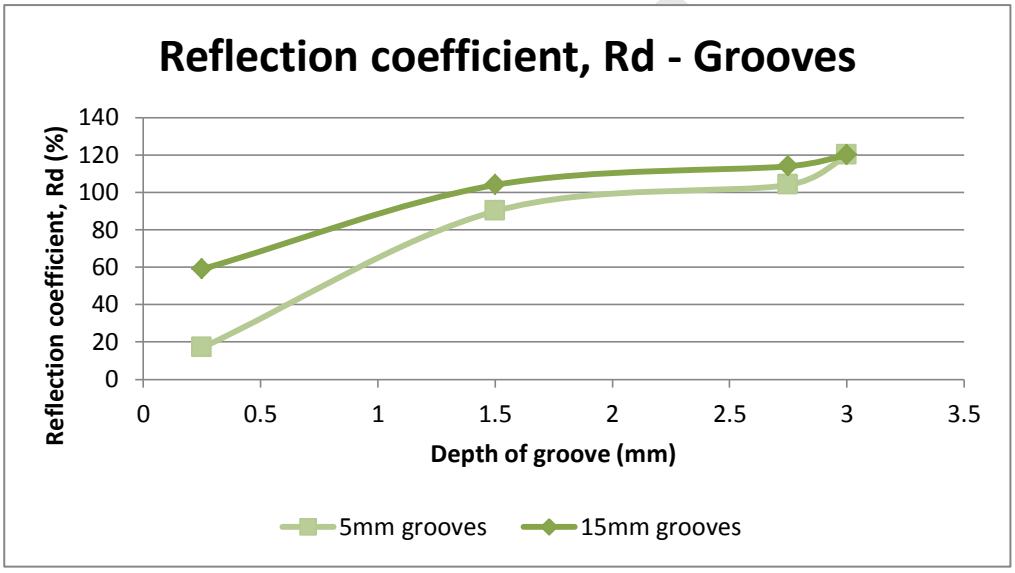

Figure 4.26: Reflection coefficient obtained from grooves in 3mm steel plate subjected to S2 and A2 modes. The reflection coefficient increases monotonically for both groove lengths as the depth increases

The reflection coefficient, Rd obtained from 5mm and 15mm long grooves in 3mm steel plate is shown in Figure 4.26. The reflection coefficient should be less than 100% by definition however, due to factors such as variations in coupling efficiency and variations in the direction of the transducer (i.e. scatter which occurs when the transducer is not perpendicular to the defect), the reflection coefficient exceeded 100%. Nevertheless, the reflection coefficient increased monotonically with depth for both the 5mm and 15mm grooves. The reflection coefficient for the 15mm groove was higher than that for the 5mm groove. This was expected as the cross

sectional area was larger for the 15mm groove. Their reflection coefficients converged as the depth increased.

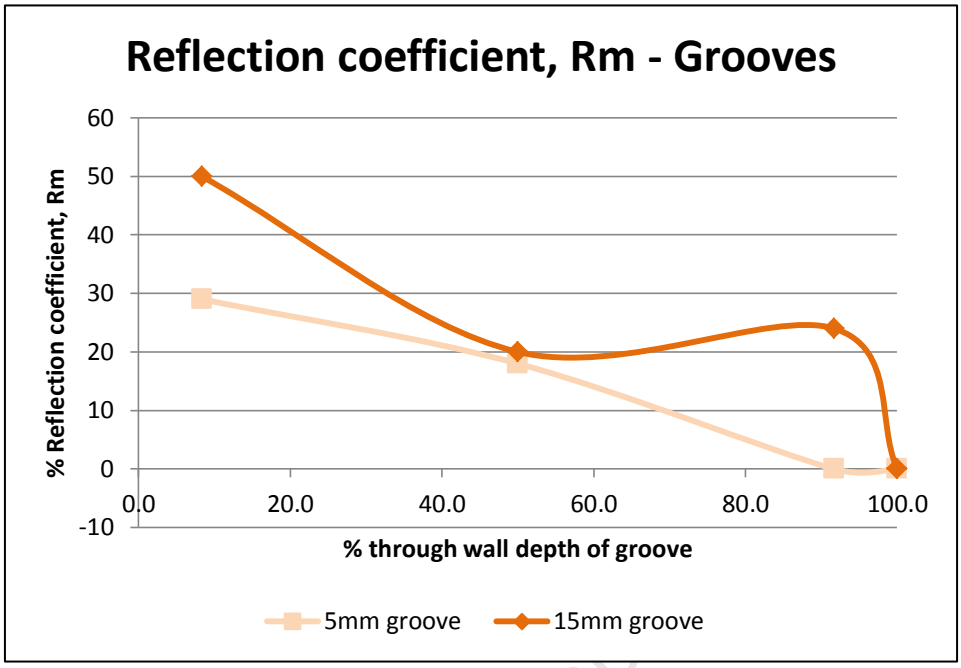

Figure 4.27: Reflection coefficient for mode converted signal, Rm obtained from grooves in 3mm steel plate subjected to S2 and A2 modes. The reflection coefficient decreases to zero when the groove is through wall

The mode converted reflection coefficient decreased from 50% to 0% and 30% to 0% for the 15mm and 5mm grooves respectively. Again, this was an expected result as the through thickness asymmetry decreased to zero once the groove reached through wall depth. The reflection coefficient, Rm is shown in Figure 4.27.

4.5.2.3 Holes of 1.5mm and 2.5mm diameter and varying depth in 3mm plate

The next set of results was obtained from the inspection of drilled holes (pits) in 3mm steel plate. There were two different diameter holes, 1.5 and 2.5mm. Again, S2 and A2 modes were generated at a group velocity of 2300m/s. The results are tabulated in Table 4.8.

Hole diameter (mm)	Hole depth (mm)	dB of refl. signal from defect	BW echo (% FSH)	% RC, Rd	cross-sectional area (mm2)	hole depth (% thick)	Mode conv. RC Rm
1.5	0.25	2	94	4	0.375	8.3	30
2.5	0.25	0	85	0	0.625	8.3	29
1.5	1.5	5.5	90	11	2.25	50.0	18
2.5	1.5	6	96	12	3.75	50.0	16
1.5	2.75	7.5	66	15	4.125	91.7	14
2.5	2.75	8.5	64	17	6.875	91.7	14
1.5	3	7.5	63	15	4.5	100.0	0
2.5	3	10.5	40	21	7.5	100.0	0

Table 4.8: Inspection results for pits of varying diameter and depth in 3mm plate with S2 and A2 modes.

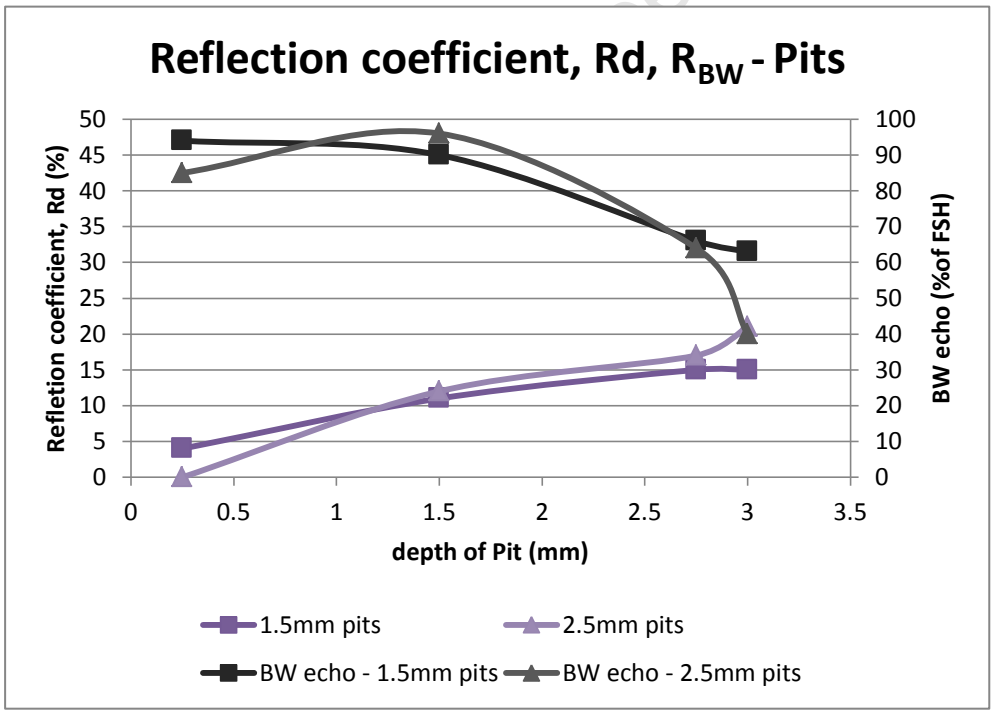

Figure 4.28: Comparison of the reflection coefficient, Rd and RBW for pits. Rd increases consistently while R_{BW} decreases significantly after 50% depth.

The reflection coefficient for the 1.5mm pits increased from 4% to 15% while that for the 2.5mm pits increased from 0 to 21% (see Figure 4.28). A value of zero for the reflection coefficient (undetectable) for 2.5mm pits at 0.25mm depth was recorded. A reduction in the back wall reflection and a mode converted signal was clearly present. The back wall reduced significantly

after 50% through wall depth had been reached. For a frequency of 4MHz, the wavelength based on the group velocity of 2300m/s was 0.575mm. This is short enough to be affected by the changes in pit diameter and can be a contributing factor to recording a lower reflection coefficient than the 1.5mm diameter pit at 0.25mm depth.

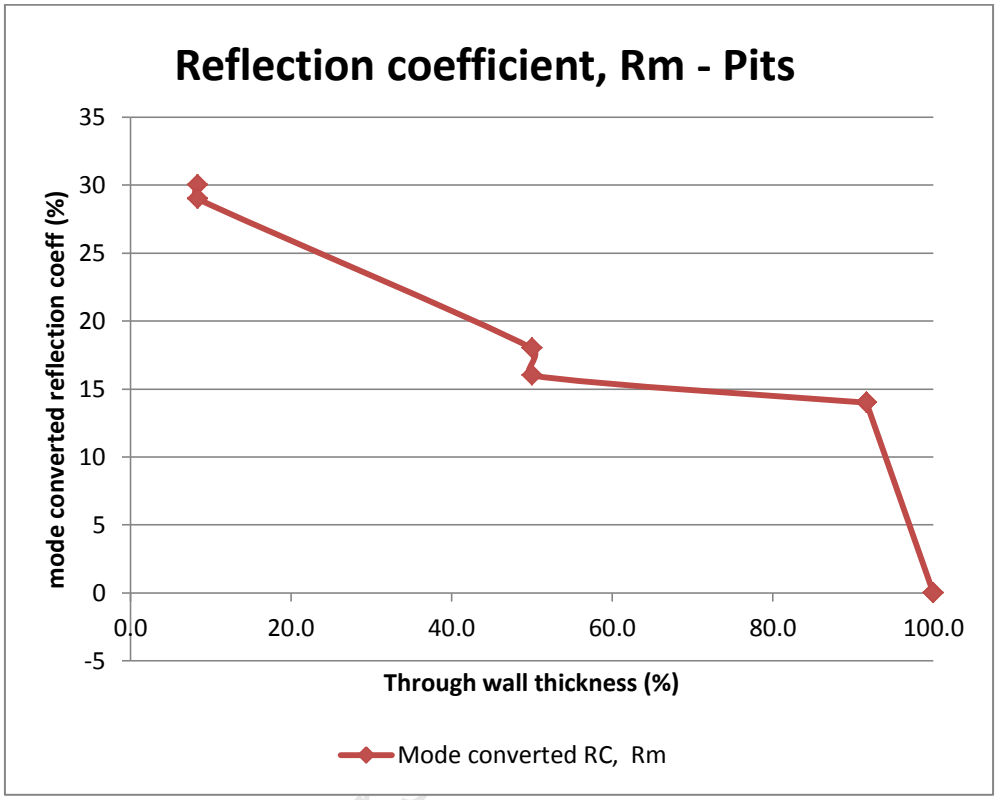

Figure 4.29: The reflection coefficient of the mode converted signal, Rm for pits. The reflection coefficient reduces to zero for both the 1.5mm and 2.5mm pits.

Pits of 1.5mm diameter and varying depth were detected consistently using a 45 degree, 4MHz shear wave transducer and a spike generator. The defect was detected (recognised) by reduction in back wall echo, the presence of mode conversion and the S1 reflection from the defect. The reflection coefficient for grooves was significantly higher than that for pits given the larger cross-sectional area. The mode converted signal amplitude decreased as the through wall depth increased (i.e. as the asymmetry decreased) for both the grooves (Figure 4.27) and the pits (Figure 4.29).

4.5.3 Results and discussion for study 3

The L(0,2) velocity obtained was approximately 3575m/s, well within the expected range. The T1 defect was clearly visible at location 200mm as shown in Figure 4.30 with the L(0,2) mode generated using the wedge method. The back wall was accurately located at 250mm. The detection limit for the wedge method applied in this experiment was better than 250um or approximately 25% of wall thickness. Significant noise however existed in the 0 to 100mm range due to the reflections from the wedge itself. This can be reduced through improved wedge design.

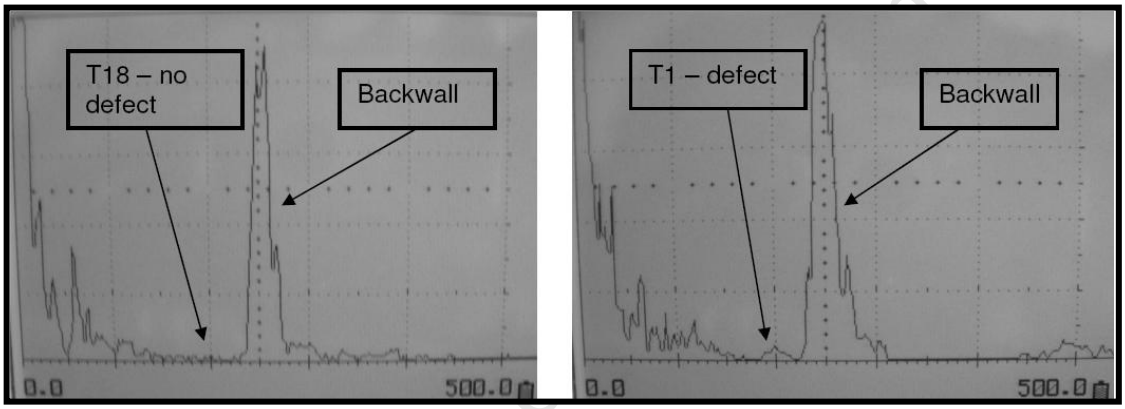

Figure 4.30: The wedge method limit of detection. 1.5mm diameter, 0.25mm depth hole detected at 200mm using the L(0,2) mode.

The signals obtained from a symmetric defect (T17), 360^0 circumferential length, 0.5mm depth and 1.5mm axial width is shown in Figure 4.31. The reflection coefficient for the L(0,2) mode is 34/48 = 71%. The reflection coefficient was large as expected with significant back wall reflection amplitude reduction.

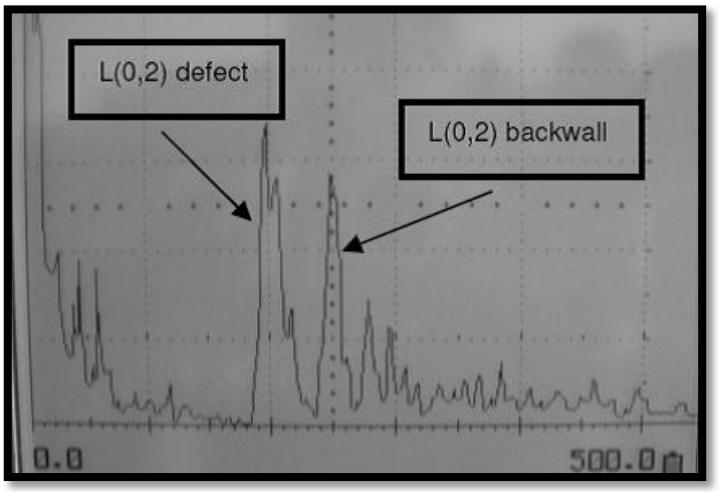

Figure 4.31: Signal obtained from a symmetric defect (T17) subjected to L(0,2) mode at 3575m/s, 250mm from the edge of the tube. The L(0,2) mode is generated using the wedge method.

The reflection coefficient of an axisymmetric defect (T17) was high at 71%. Mode converted flexural modes are not expected for axisymmetric defects [82] however several indications of flexural modes were identified. These were as a result of the wedge method of generation. The wedge generation method itself is non-axisymmetric and generates flexural modes [47].

The measured reflection coefficient for the drilled holes and the grooves are given in Table 4.9 and Table 4.10 respectively.

Tube	depth (mm)	diameter (mm)	L(0,2) reflection	Input	Reflection coefficient
5	0.25	3	5	48	10%
6	0.50	3	5.5	48	11%
7	0.75	3	13	48	27%
8	through	3	14.5	48	30%

Table 4.9: Reflection coefficient for drilled holes of T5, T6, T7 and T8 obtained using the wedge method.

Tube	depth (mm)	Circumf. length	L(0,2) reflection	Input	Reflection coefficient
13	0.25	20	22	48	46%
14	0.50	20	10.5	48	22%
15	0.75	20	43	48	90%
16	through	20	42	48	88%

Table 4.10: Reflection coefficient for grooves in T13, T14, T15 and T16 obtained using the wedge method.

The reflection coefficient for the drilled holes was less than that obtained for grooves. This was expected as the cross sectional area of the grooves were larger than that for holes for the same depth and axial extent. This is illustrated in Figure 4.32. Furthermore, the reflection coefficient increased significantly beyond 50% of defect depth in both cases (grooves and pits).

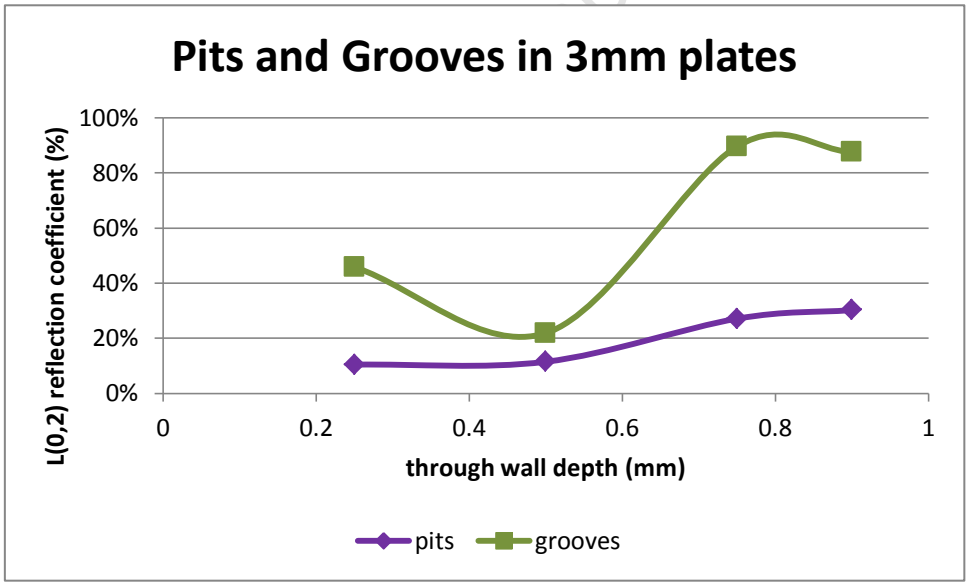

Figure 4.32: Reflection coefficient for drilled holes (pits) is less than that for grooves due to the increased cross sectional area for grooves for the same through thickness depth.

4.6 Summary

It is reported that, if $\frac{\lambda_L}{d} \approx 40$, where λ_L is the Lamb wave length and d is the defect depth, then detection of the defect is possible in plates [77]. At 4MHz, this translates to defect depths of around 15µm. In this study, it was demonstrated that defect depths of less than 200µm (1.5mm diameter) could be detected using standard bulk wave equipment to generate the S2 and A2

modes. Furthermore, the defect cross sectional area is less than 0.4mm^2. The drawback is the high attenuation that is experienced at such high frequencies. However, several NDT applications do not require long range propagation. Long range propagation is one of guided waves advantages that have been explored successfully as discussed in the literature review. Another advantage is its ability to inspect a large volume from a single location. This coupled with excellent sensitivity can significantly improve the probability of detection over distances of approximately 300mm. Further research into industrial applications for this method is warranted.

The directionality, coherence and sensitivity obtained using standard bulk wave equipment makes it suitable for research purposes in certain applications. Some of the theoretical concepts pertaining to the behaviour of guided waves could be demonstrated using this method. These are:

- There is a reduction in back wall reflection as the reflection from a defect increases.
- A mode converted signal is present when an asymmetrical defect is encountered.
- The reflection coefficient, Rd is sensitive to cross sectional area and not defect depth.

The bulk wave equipment was also applied to tubes where a modified , wedge method, was used similar to that employed by Rose et al [47] but here, a standard bulk wave generator and transducer was used. Again, theoretical concepts could be explored and confirmed such as those listed above.

Chapter 5

Laser vibrometer experimental details and results

5.1 Introduction

Access to the condenser tubes for inspection is only via the condenser water box (see Figure 2.2). The steam space (Figure 2.3), whilst accessible, only provides access to the tubes on the outside of the tube bundle. Inspections therefore need to be performed from the inside of the tube or the tube edge. The tube end is expanded into the tube sheet so access to the tube edge is challenging but not impossible. A transducer ring can be fitted to the inside of the tube (see Figure 3.15) but physical constraints limit the number of individual transducers (nodes) that can be fitted. These are some of the practical challenges that would need to be resolved in developing a guided wave inspection technique for condenser tubes. In this study, PZT transducers were fitted to the end of the condenser tubes to generate the L(0,2) mode. A Laser vibrometer was used to measure the displacement at 48 nodes on the transducer. The capability of the L(0,2) mode to detect pitting and grooving over a range of depths, including defects that represent a cross sectional area as small as 0.2mm^2 was investigated. Guided waves have already been proposed as a screening tool for heat exchanger tubes [2], [5]. However, guided wave technology is not routinely used in industry to inspect condenser or heat exchanger tubes, partly due to the challenges discussed earlier. Eddy current testing (ECT) is the preferred method of non-destructive testing of condenser tubes and heat exchanger tubes in general. The method is routinely applied in the power generation industry as discussed in Chapter 2. However, benefits can be derived from a guided wave inspection technique that is potentially faster and more reliable. Even marginal improvements in the time taken to inspect each tube

can lead to significant improvement in inspection duration due to the volume of tubes in condensers. The need to clean the condenser tubes prior to ECT further enhances the need for an alternative that could inspect the full volume of the tube from a single position. The benefits and limitations of ECT are discussed in more detail in Section 3.4.3.

The chapter begins with a description of the experimental details. The main objectives, equipment setup and a description of the defect geometry are then provided. The relevant group velocity dispersion curve is also given which is followed by the experimental methodology used in the tests. Selected results are presented and discussed before a summary is provided at the end of the chapter. The test facilities were provided by the South African Council for Scientific and Industrial Research (CSIR).

5.2 Experimental details

In this section, the setup of the equipment is described as well as the geometry of the defects. The methodology applied is also provided.

5.2.1 Equipment setup

The setup of the equipment is shown in Figure 5.1. The laser vibrometer produces the toneburst output to the power amplifier which was used to excite the transducer. Damping was applied to the transducer to improve its performance at the centre frequencies of interest. Damping was also applied between the tube and the surrounding environment to prevent unwanted vibration. Each tube had its own transducer fitted to the end of the tube as shown in Figure 5.1. The transducer remained bonded to the tube throughout the experiment, from initial (no defect) until through wall defect depth had been achieved. Instead of multiple, separate transducers that were excited using multiple channels, in this setup, a single transducer was used and the displacement at 48 positions on the transducer was measured using the laser vibrometer. The input to the transducer was kept constant, however minor variations in the input signal between measurements were noted (see Appendix A.8).

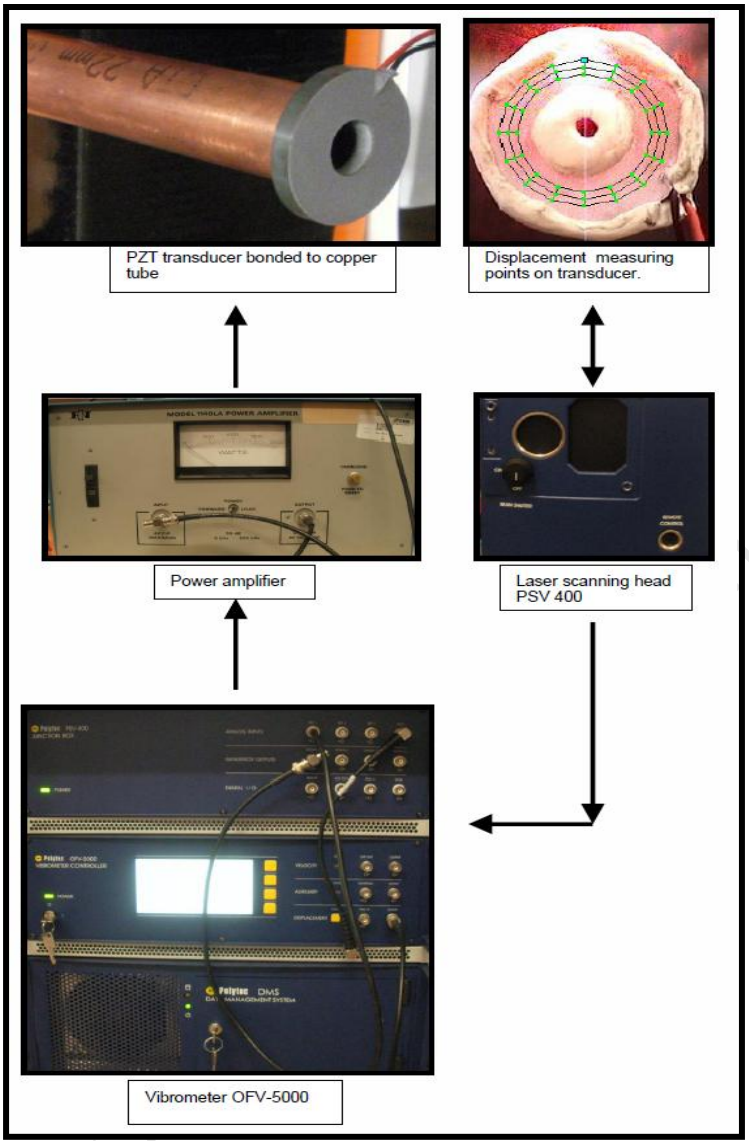

Figure 5.1: The laser vibrometer outputs a toneburst signal which excites a transducer. The displacement at 48 points on the transducer is measured using a laser.

5.2.2 Defect description and dispersion curves

Two defect types were investigated, namely, ammonia grooves and isolated pitting. In each case, the defect was located at 1.1m along the tube length, away from the transducer. Drawings of the condenser tube test samples are given in Appendix A.6 (grooves) and A.7 (pits). The material specifications are listed in Chapter 4, Table 4.2. The defect geometry for the groove and pit defects is shown in Figure 5.2 and Figure 5.3 respectively and is summarised in Table 5.1 and Table 5.2 respectively.

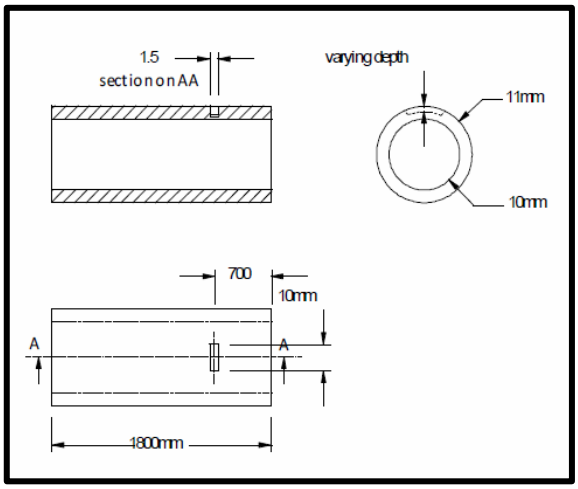

Figure 5.2: The groove defect has a circumferential extent of 10mm and the axial extent is 1.5mm. The depth varies from 0mm to 1mm (through wall) depth.

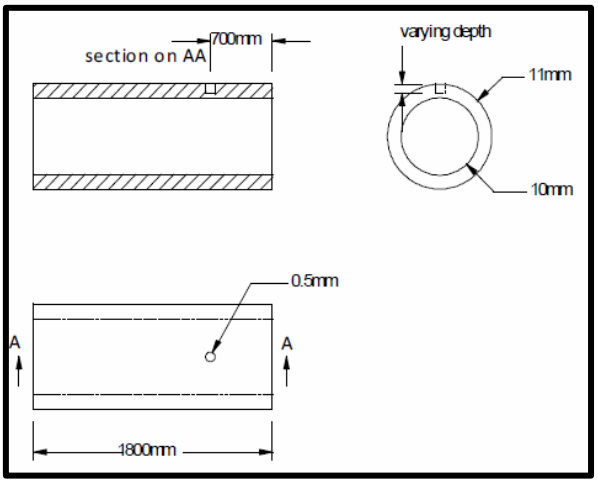

Figure 5.3: The pit defect has a diameter of 1mm. The depth varies from 0mm to 1mm (through wall) depth.

Pit defect dimensions (Tube 22)						
depth (mm)	0.2	0.4	0.5	0.6	0.8	1
diameter (mm)	1	1	1	1	1	1
x-section area (mm^2)	0.2	0.4	0.5	0.6	0.8	1
Wall loss (%)	0.3	0.6	0.8	0.9	1.2	1.5

Table 5.1: The dimensions of the pit defect.

Groove defect dimensions (Tube 23)				
depth (mm)	0.3	0.5	0.8	1
Circumferential length (mm)	10	10	10	10
Axial width (mm)	1.5	1.5	1.5	1.5
x-section area (mm^2)	3	4.9	7.7	9.5
Wall loss (%)	4.5	6	11.7	14.5

Table 5.2: The dimensions of the groove defect.

The group velocity dispersion curve for 22mm outside diameter, 1mm thick copper tube is shown in Figure 5.4. The dispersion curve is based on a density of 8900kg/m^3 and a Young's modulus of 110GPa. As can be seen from the slope of the curve (see Equation 2.24), the dispersion of the L(0,2) is negligible (not zero) over the range from 120kHz to 150kHz. The F(1,3) mode however is highly dispersive in this region while the F(2,3) only occurs beyond approximately 135KHz.

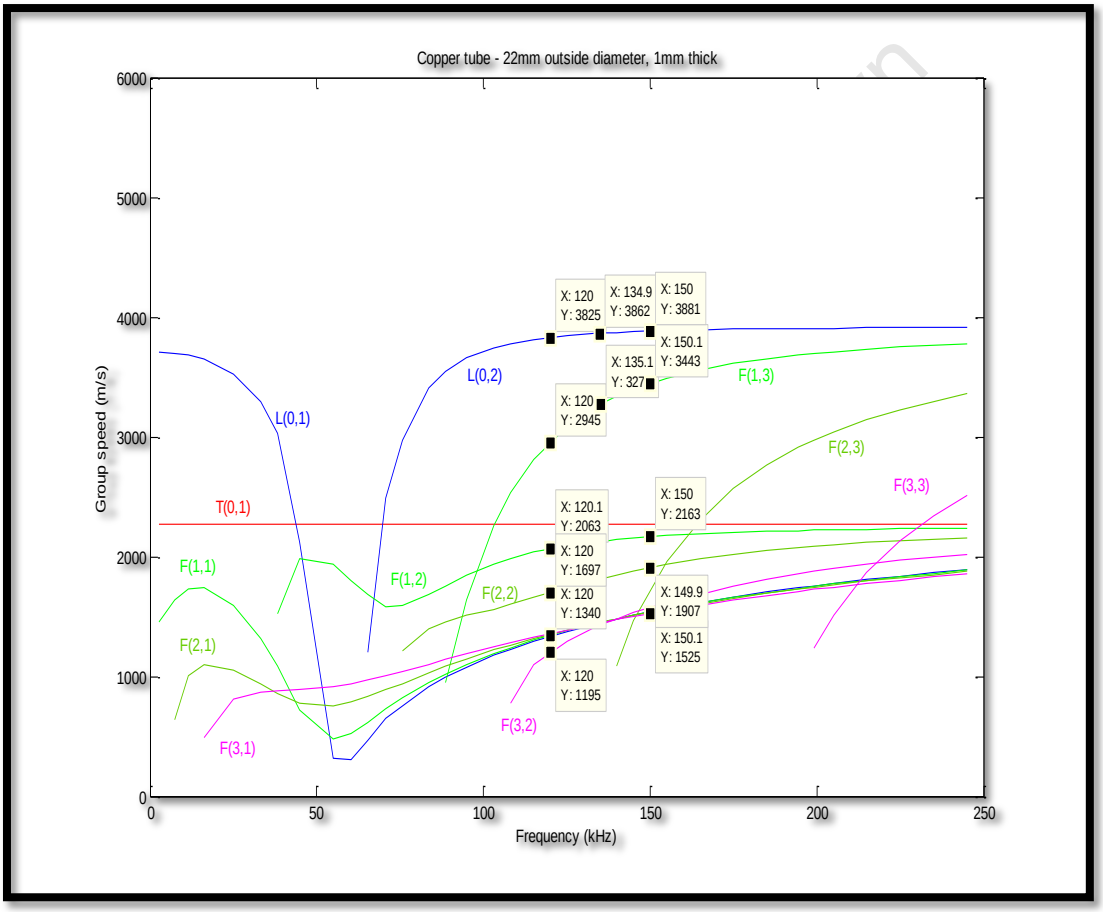

Figure 5.4: Group velocity dispersion curve for copper tube, 1mm thick and 22mm outside diameter.

5.2.3 Methodology

The transducer input signal was generated by the laser vibrometer and is shown in Figure 5.5. It consisted of a 5.5 cycle tone burst enclosed by a Hanning window. The defect was always located on the axis of nodes 5, 21 and 37 for both the groove and the pit. The node locations

and numbering is illustrated here in Figure 5.6. At each node, the time varying displacement was captured after 20 measurements and averaged.

Data was obtained for three centre frequencies namely 120kHz, 135kHz and 150kHz. The displacement of the transducer was measured using the laser vibrometer at 48 locations (nodes) on the transducer face (axial, z-axis displacement) as pictured in Figure 5.1. Particles excited by the L(0,2) mode and its family of flexurals, F(n, 3) modes have a dominantly axial displacement compared to the L(0,1) mode which is dominantly radial. This setup is therefore suitable, if not ideal, for studying the L(0,2) mode's interaction with the defects. The data was captured, manipulated and analysed in ***MATLAB***, as discussed in Section 5.3.

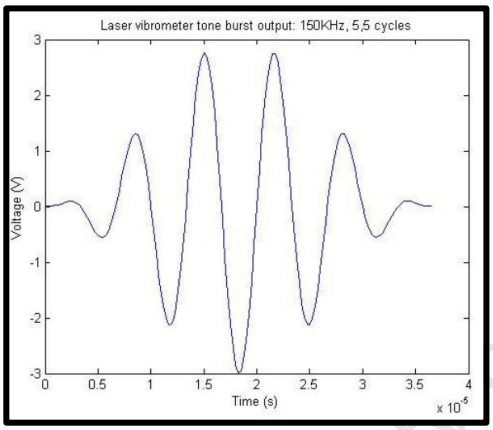

Figure 5.5: An example of the 150kHz, 5,5 cycle tone burst output from the laser vibrometer.

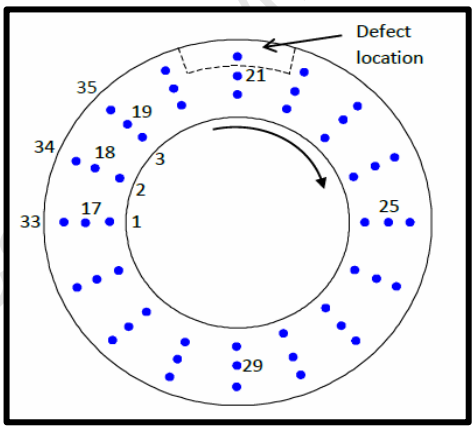

Figure 5.6: Measurement node locations on the transducer face. 48 nodes arranged in 3 circles with the defect located at nodes 5, 21 and 37.

Although measurements were taken at 16 equally spaced locations around the 3 circles, only one set of 16 measurements is needed for the purpose of this study. The outer nodes (nodes 33 to 48) were used in this study unless otherwise stated. The variation in displacement between the three circles, each with 16 nodes is not explored in this thesis.

5.3 The results and discussion

Figure 5.7 is a graphical illustration of a typical set of data obtained for each defect depth. The graph represents the reflected signals obtained for the 120kHz input signal in tube 23 (groove defect) at 50% through wall depth. It consists of a plot for each of the 48 nodes and extends over 3.2ms, sufficient to include three back wall reflections.

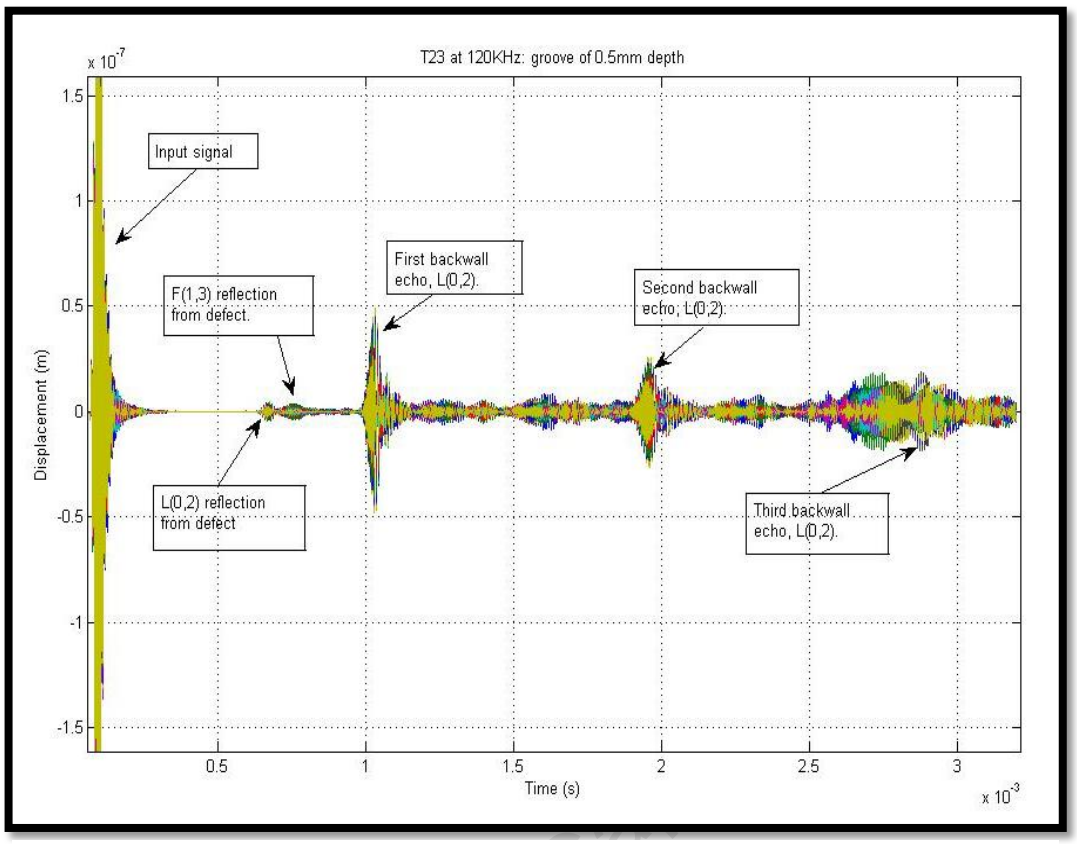

Figure 5.7: Graph illustrating the typical data obtained from all 48 nodes for each defect depth. This graph represents the displacement as a function of time for the groove defect (T23) at a defect depth of 0.5mm.

Significant dispersion is experienced beyond the first back wall reflection and is more severe at 120kHz. The F(1,3) mode is more dispersive at 120kHz where the ratio of group velocity to phase velocity is 61% (2945/4824) compared to that at 150kHz where the ratio is 78% (3442/4396).

The L(0,2) reflection from the defect and the mode converted reflected signal, F(1,3) is illustrated in Figure 5.8 for the same defect depth. The time period of most interest is from 0.6ms to 0.8ms and most of the graphs will zoom in on this time period which contains the L(0,2) and F(1,3) reflections from the defect.

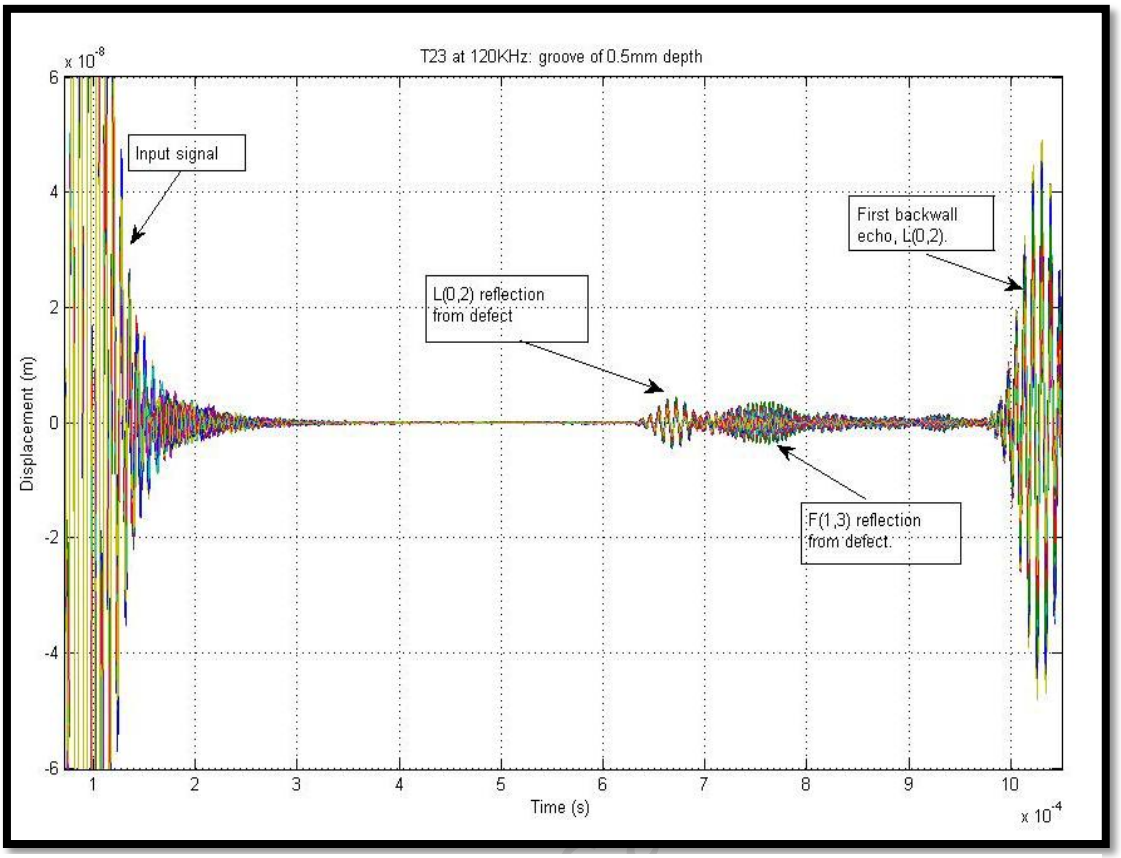

Figure 5.8: Graph illustrating the typical data obtained from all 48 nodes for each defect depth. This graph represents the displacement as a function of time for T23 at a defect depth of 0.5mm for the period up to the first backwall reflection only.

A data set as illustrated graphically in Figure 5.8 was obtained for each defect (data point) listed in Table 5.1 (pitting – tube 22) and Table 5.2 (grooving – tube 23). In addition, two copper tubes, T20 (pit – 2mm, 100% depth) and T21 (groove – 10mm circumferential length, 100% depth) were also tested at 120kHz, 135kHz and 150kHz. These tubes were 1.6m long, 22mm outside diameter and 1mm thick. A complete set of graphs for T22 and T23 is contained in Appendix A.10. It includes plots of all 16 nodes as well as a plot of the first order and zero order for each defect depth. An animation of the reflected signal is provided by the laser vibrometer and the author of this thesis has also compiled a ***MATLAB*** routine to animate the experimental data. The ***MATLAB*** code is included in Appendix A.11.

5.3.1 Incident mode and defect location

The incident mode could be confirmed as the L(0,2) mode by comparing its group velocity obtained from the dispersion curve (Figure 5.4) to the velocity, C_{mode} calculated as follows:

$$C_{mode} = \frac{2 \times L}{(T_{BW} - T_i)} \quad (5.1)$$

Where:

C_{mode} is the velocity of the mode generated .

T_{BW} is the time at which the C_{mode} reflected signal from the backwall occurs on the graph.

T_i is the time at which the input signal is generated.

The defect could be located as follows:

$$D_p = \frac{1}{2}\left(T_{dL(0,2)} - T_i\right) C_{L(0,2)} \quad (5.2)$$

Where:

D_p is the distance of the defect from the transducer (meters) .

$T_{dL(0,2)}$ is the time at which the L(0,2) reflection from the defect occurs on the graph.

T_i is the time at which the input signal is generated.

$C_{L(0,2)}$ is the velocity of the L(0,2) mode at the relevant frequency taken from the dispersion curve, Figure 5.4.

The F(1,3) mode converted signal from the defect could then be expected at the following time:

$$T_{F(1,3)} = T_i + \frac{D_p}{C_{L(0,2)}} + \frac{D_p}{C_{F(1,3)}} \quad (5.3)$$

Where:

$T_{F(1,3)}$ is the time on the graph at which the F(1,3) mode converted signal from the defect occurs.

$C_{F(1,3)}$ is the velocity of F(1,3) and is obtained from the dispersion curve (Figure 5.4) at the relevant frequency.

T_i , T_{BW} and the calculated velocity, C_{mode} is listed in Table 5.3 for each defect depth, and at each frequency, for T22 and T23. C_{mode} was calculated for each of the frequencies and

compared to the L(0,2) velocity, $C_{L(0,2)}$ taken from the group velocity dispersion curve. At each frequency, the difference between C_{mode} and $C_{L(0,2)}$ was less than 1.5% which confirmed that the L(0,2) mode was indeed the incident mode. The difference between C_{mode} and $C_{L(0,2)}$ is mainly due to the difference in the material properties and particularly Young's modulus used in the calculation of the dispersion curves. The difference between C_{mode} and $C_{L(0,2)}$ was well within 1% for T23. A complete table of results for T22 and T23 is provided in Appendix A.8 and A.9 respectively.

T22			
Frequency (kHz)	**Ave. velocity, C_{mode} (m/s)**	**$C_{L(0,2)}$ (m/s)**	**Difference (%)**
120	3875	3825	1.3
135	3917	3862	1.4
150	3924	3881	1.1
T23			
Frequency (kHz)	**Ave. velocity, C_{mode} (m/s)**	**$C_{L(0,2)}$ (m/s)**	**Difference (%)**
120	3850	3825	0.7
135	3868	3862	0.2
150	3885	3881	0.1

Table 5.3: Comparison of the calculated and expected L(0,2) mode velocity at 120kHz, 135kHz and 150kHz.

Frequency	$C_{L(0,2)}$ (m/s)	$C_{F(1,3)}$ (m/s)	T_i (us)	$T_{dCL(0,2)}$ (ms)	$T_{F(1,3)}$ (ms)	D_p (m)	D_p (actual) (m)	error (%)
120kHz T23 at 50% depth	3825	2945	96.1	0.672	0.759	1.1014	1.1	0.128
135kHz T22 at 50% depth	3862	3270	89.1	0.650	0.695	1.0831	1.1	-1.537
150kHz T22 at 60% depth	3881	3443	87.9	0.649	0.687	1.0888	1.1	-1.017

Table 5.4: Defect location, Dp and the defect location error at the three sample points of 120kHz (T3 at 50% depth), 135kHz (T22 at 50% depth) and 150kHz (T22 at 60% depth).

The location of the defect based on the L(0,2) mode and the mode converted, F(1,3) mode at three sample points, was calculated and tabulated in Table 5.4. The error was again found to be small at less than 2%. The error was mainly due to the difference in $\boldsymbol{C_{mode}}$ and $\boldsymbol{C_{L(0,2)}}$ as discussed earlier. The graphs of the sample points are given in Figure 5.9 (120kHz, T23 at 50% depth), Figure 5.10 (135kHz, T22 at 50% depth), and Figure 5.11 (150kHz T22 at 60% depth). Some variances were however noted between the velocities in T22 and T23 as reported in Table 5.3 and both the zero order and first order modes were affected. The variation in the copper tube material characteristics between T22 and T23 is the main reason for this and is typical of anisotropic material. This argument is supported by the large variation in attenuation obtained between the two tubes (see Section 5.3.2.2).

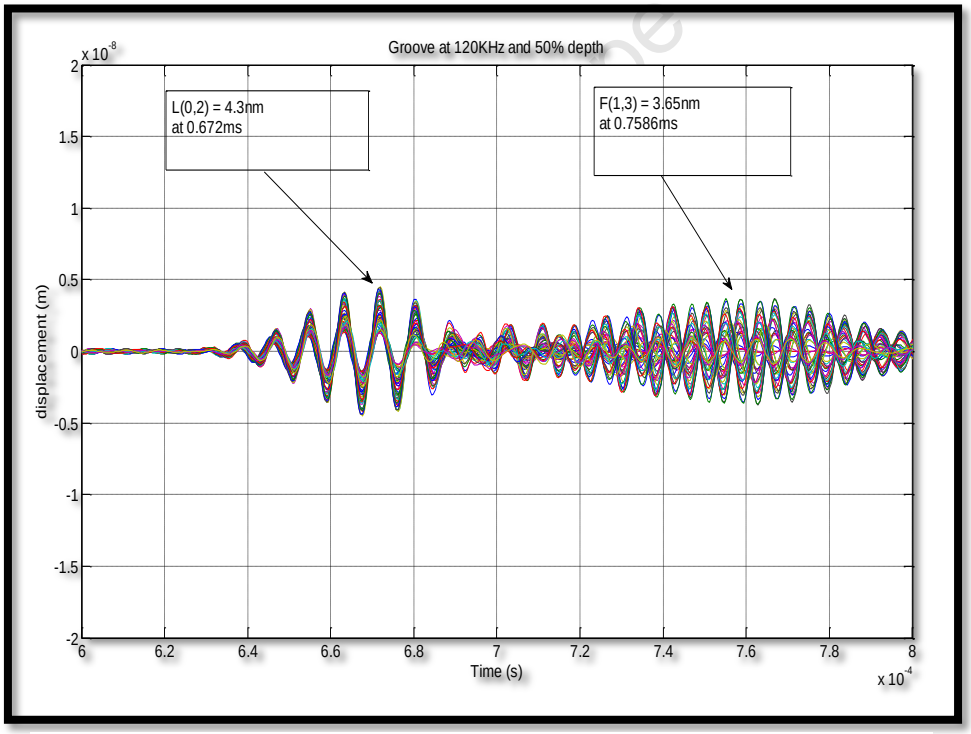

Figure 5.9: Graph of L(0,2) reflection and the mode converted F(1,3) reflection from the defect. The graph is for T23 at 120kHz and 50% depth.

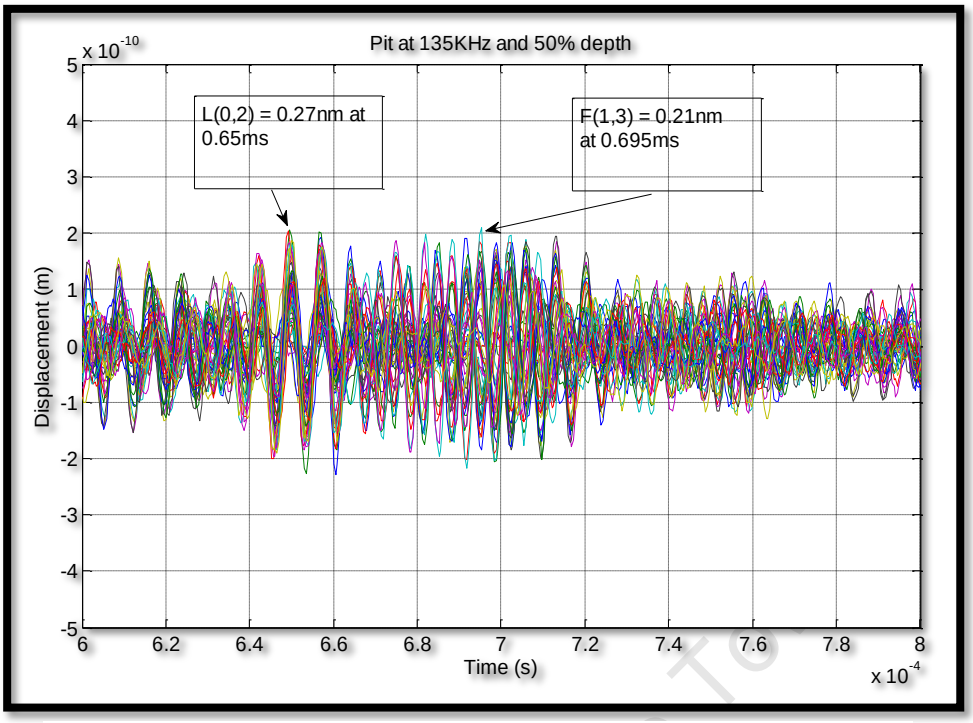

Figure 5.10: Graph of L(0,2) reflection and the mode converted F(1,3) reflection from the defect. The graph is for T22 at 135kHz and 50% depth.

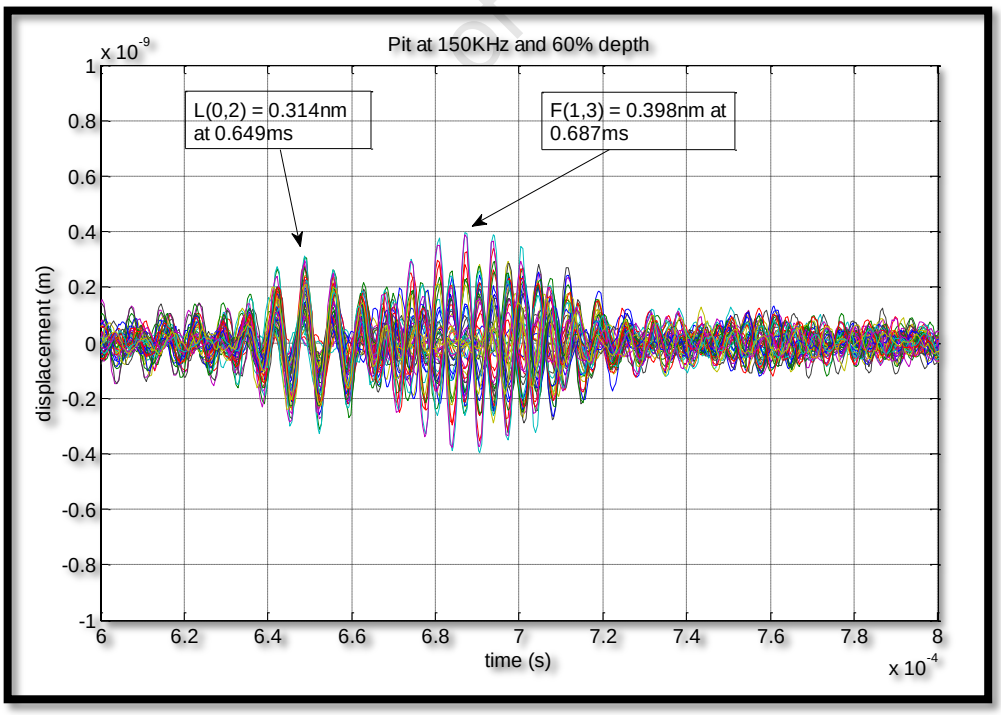

Figure 5.11: Graph of L(0,2) reflection and the mode converted F(1,3) reflection from the defect. The graph is for T22 at 150kHz and 60% depth.

As expected, both the L(0,2) and F(1,3) reflections from the groove were significantly larger (higher displacement amplitude) than that for the pit. The dispersive nature of the F(1,3) mode at 120kHz is evidenced by the long duration of the F(1,3) signal as shown in Figure 5.9. The 135kHz signal in Figure 5.10 was typical of the noise experienced with reflections from the pit defect.

5.3.2 Defect detection

The graphs of the displacement at all 48 nodes for the pit (T22) at 150kHz and 0 to 40% defect depth are given in Figure 5.12. The scales are the same for comparative purposes and variances in the input amplitudes are insignificant. The L(0,2) mode reflected from the 0.4mm depth pit is clearly visible (detectable), particularly when compared to the graph for 0% depth. At 40% depth, an amplitude of 214E-12m, i.e 214 picometers (pm) was obtained for the L(0,2) reflection while F(1,3) reflection is 237pm. The graphs consist of an in-phase, L(0,2) reflected signal as well as an out-of-phase, F(1,3) mode converted signal. The presence of the out-of-phase, F(1,3) mode in itself suggest the presence of a non-axisymmetric defect [82].

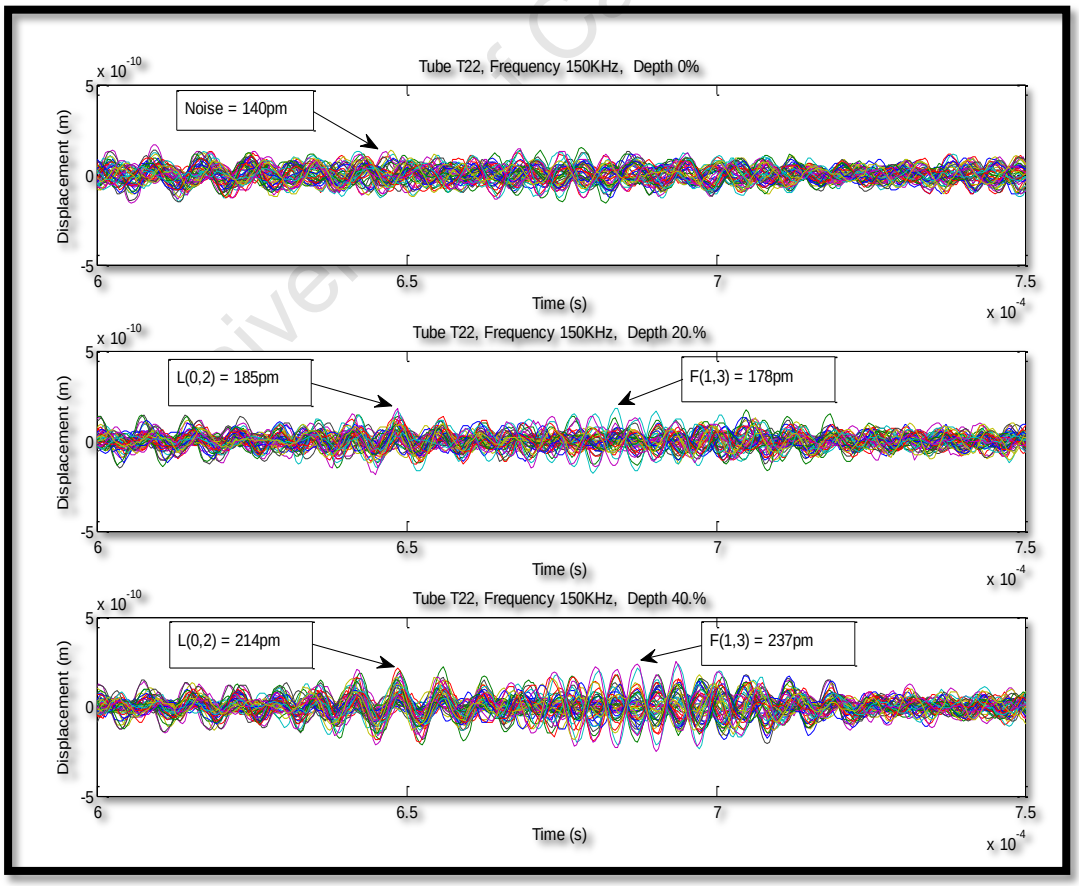

Figure 5.12: Graph of the L(0,2) and F(1,3) modes reflected from pit defects of 0%, 20% and 40% depth and 150kHz. The L(0,2) mode displays an in-phase signal while the F(1,3) mode displays an out-of-phase signal.

The L(0,2) reflected signal at 150kHz for the 20% defect depth was detectable without any signal processing although it was only marginally detectable. A 1mm diameter flat bottomed hole with a depth of 0.2mm represents 0.3% of the tube cross-sectional area.

The signal-to-noise ratio (SNR_{dB}) in decibels (dB) is given by [14]:

$$SNR_{dB} = 20log_{10}\left(\frac{A_{signal}}{A_{noise}}\right) \quad (5.4)$$

Where:

A_{signal} is the amplitude of L(0,2) reflection from the defect.

A_{noise} is the amplitude of the noise in the vicinity of L(0,2) reflection.

The L(0,2) SNR_{dB} for the 20% to 80% pit depth are given in Table 5.5. The noise level was reasonably constant at less than 151pm for varying depths. The SNR_{dB} increased from a low of 1.8dB for 20% pit depth to 8.5dB for 80% pit depth. At pit depths greater than 40%, the F(1,3) signal had a higher amplitude than the L(0,2) mode and therefore had a higher SNR. This suggests that the F(1,3), mode converted signal may be easier to recognise than the L(0,2) mode in certain cases. This appears to be contradictory to the findings of Demma et al [55] namely that the ratio of F(1,3)/L(0,2) < 1. There is no contradiction since Figure 5.12 and Figure 5.13 are the results obtained before any signal processing had been done. The ratio of the first order to zero order is indeed < 1, shown graphically in Figure 5.19.

L(0,2) reflected signal to noise ratio - no signal processing				
Data point T22 at 150kHz	Wall loss (%)	Amplitude of L(0,2) reflection from defect. (pm) (A_{signal})	Amplitude of noise (pm) (A_{noise})	SNR_{dB} (dB)
20%	0.3	185	151	1.8
40%	0.6	214	151	3.0
50%	0.8	218	151	3.2
60%	0.9	293	151	5.8
80%	1.2	400	151	8.5

Table 5.5: The L(0,2) SNRdB values for 20% to 80% pit defect depth.

The graphs of the displacement at all 48 nodes for tube 22 (pit) at 150kHz and 50% to 100% pit depth are given in Figure 5.13. The scales are the same for comparative purposes and variances in the input amplitudes are insignificant. The L(0,2) and F(1,3) reflections were both clearly detectable for all the defect depths and their amplitude increased monotonically. The F(1,3)

SNR_{dB} for 20% to 80% pit depths are given in table 5.6. The SNR_{dB} increased from a low of 1.4dB for 20% pit depth to 9.8dB for 80% pit depth.

F(1,3) reflected signal to noise ratio - no signal processing			
Data point T22 at 150KHz	Amplitude of F(1,3) reflection from defect. (pm) (A_{signal})	Amplitude of noise (pm) (A_{noise})	SNR_{dB} (dB)
20%	178	151	1.4
40%	237	151	3.9
50%	283	151	5.5
60%	388	151	8.2
80%	465	151	9.8

Table 5.6: The F(1,3) SNR_{dB} values for 20% to 80% pit defect depth.

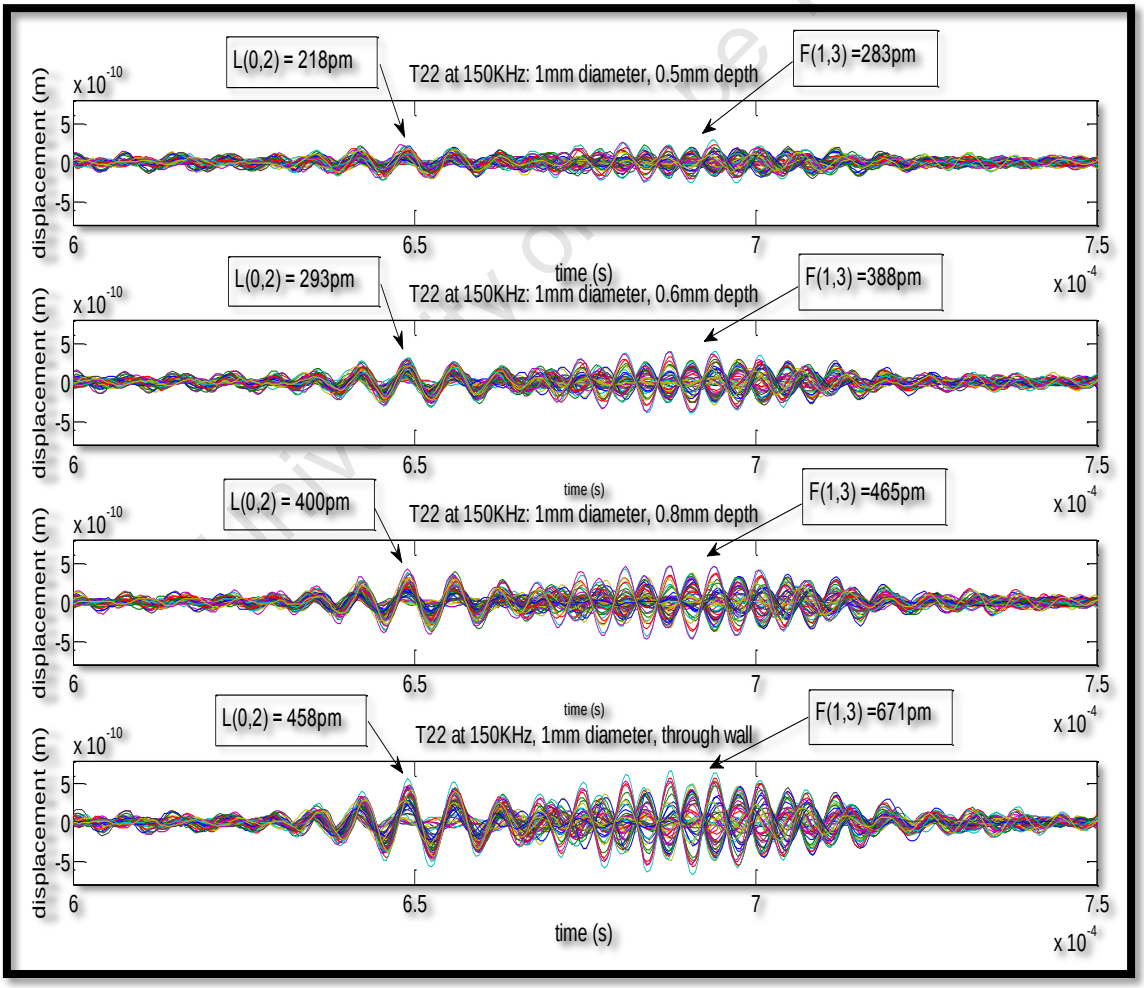

Figure 5.13: Reflection of the L(0,2) mode and F(1,3) modes for T22 (pit). The pit defects are clearly detectable.

Similarly, graphical representation of the L(0, 2) and mode converted, F(1,3) reflection from the groove (T23) is given in Figure 5.14 . Once again, the scales are the same for comparative purposes and variances in the input amplitudes are insignificant. In this case, the frequency is for 135kHz and defect depth up to 50%. The groove defects were all clearly detectable and both the L(0,2) and F(1,3) reflections increased monotonically for all the defect depths measured. A 30% depth groove represents a cross sectional area of 4.5% of the tube's cross sectional area. Two bad data points, which were each caused by a bad reflection point on the back of the transducer, are noted on the graph of the 30% groove depth.

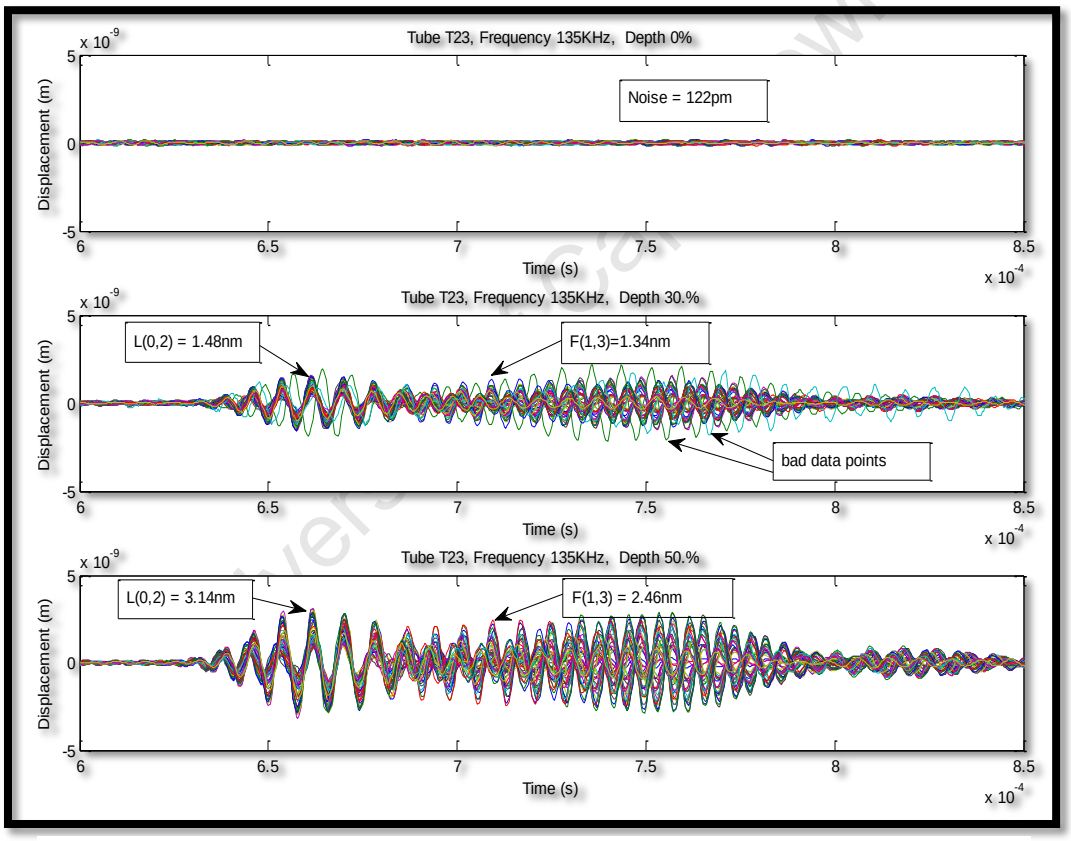

Figure 5.14: Graph of the L(0,2) and F(1,3) displacement for groove depths of 0%, 30% and 50% at 135kHz. The L(0,2) and F(1,3) reflections are clearly visible.

The L(0,2) SNR_{dB} increased from 20dB for 30% groove depth to 28dB for 50% groove depth, significantly larger than the SNR_{dB} for the pit. The F(1,3) SNR_{dB} does not increase in the same manner as that for the pit. While the F(1,3) SNR_{dB} for the pit increased beyond that of the L(0,2), no such increase was noted for the groove. Basic signal processing can significantly improve the SNR. Figure 5.15 is the mean displacement (sum of all 48 nodes divided by 48) for T22 at 150kHz and 20% depth. The signal to noise ratio improves from 1.8dB to 3.3dB. Taking the mean value eliminates the out-of-

phase components of noise as well as the higher order modes leaving the zero order mode. This is the subject of the next section.

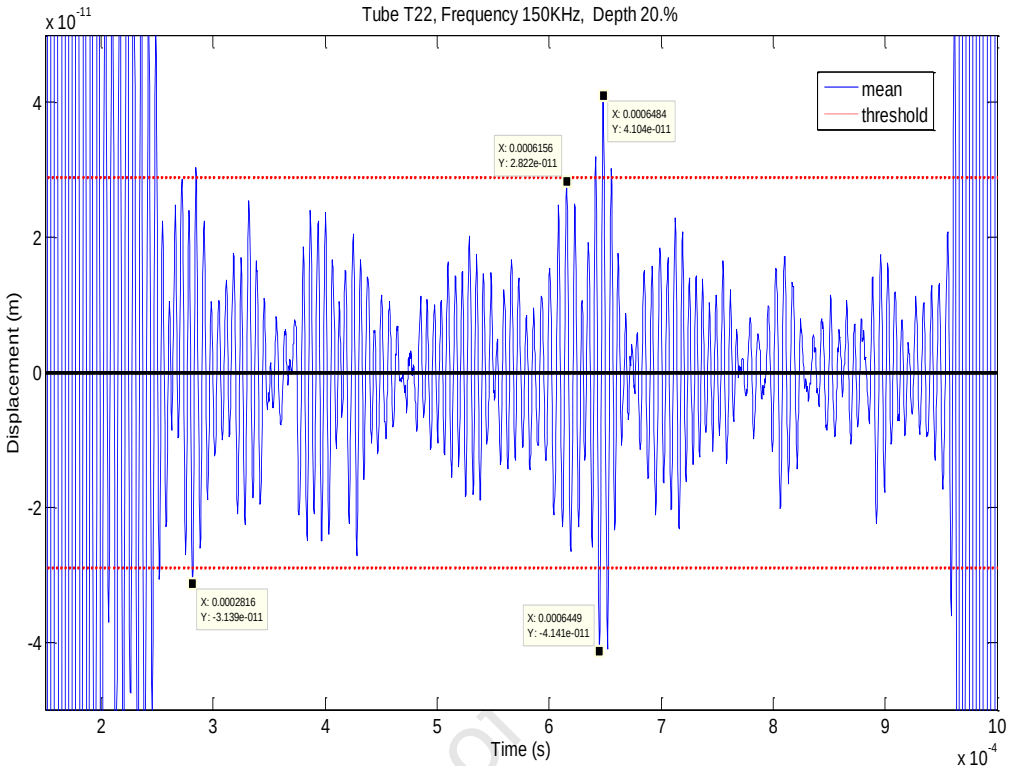

Figure 5.15: The mean displacement based on all 48 nodes for T22 at 150kHz and 20% depth. The SNR is significantly improved as the out-of-phase and higher order modes are eliminated.

5.3.2.1 Signal processing and mode separation

Zero order, axisymmetric modes can be extracted by summing up the displacements at N equally spaced locations around the circumference while non-axisymmetric modes can be extracted by a weighted sum of the displacement at each of these positions. More generally, the particle displacement at an arbitrary circumferential position, θ can be determined by the function [21], [75]:

$$u(\theta) = \sum_{n=-\infty}^{+\infty} A_n e^{in\theta}$$

Where:

A_n is the amplitude of the nth circumferential order

The above equation was based on studies where the radial displacement was measured on the outer circumference. In this study, the *axial displacement* is measured however mode separation is applied in the same manner as follows:

$$U_0 = \frac{1}{16}\sum_{N=1}^{16} u_z(N) \tag{5.5}$$

$$U_n = \frac{1}{16}\sum_{N=1}^{16} u_z(N)\cos\left(n\left(\frac{N\theta}{2\pi}\right)\right) \tag{5.6}$$

The Equation 5.6 assumes that the mode's maximum displacement (position of the pit or centre of the groove) occurs at the reference (θ=0). A more generalised equation is given by:

$$U_n = \frac{1}{16}\sum_{N=1}^{16} u_z(N)\cos\left(n\left(\frac{N\theta}{2\pi} + \emptyset\right)\right) \tag{5.7}$$

Where:

U_0 is the displacement amplitude of the zero order mode, L(0,2).

U_n is the displacement amplitude of the higher order modes, 1, 2, 3…

u_z(N) is the axial displacement measured at node N.

N is the number of nodal points around the circumference, 3 sets of 16 points.

θ is the angular position of the node from the reference. See Figure 5.20.

ϕ is the angle between the reference and the defect.

For the modes of interest, L(0,2), F(1,3) and F(2,3), the axial displacement dominates the radial displacement in the frequency region 120kHz to 150kHz. This is in contrast to the L(0,1) mode and its flexural counterparts, F(1,1) and F(2,1) where the radial displacement dominates. The zero order (L(0,2)) and the first order (F(1,3)) signals are analysed for the sample points selected previously namely, T23 at 120kHz and 50% depth, T22 at 135kHz and 50% depth and T22 at 150kHz and 60% depth. These are given in Figures 5.16, Figure 5.17 and Figure 5.18 respectively. Neither the zero order nor the first order modes are normalised, i.e., they have not been divided by 16, the number of points summed. The T(0,1) and L(0,1) modes do not appear on the graphs. This is due to the method of measurement i.e. only axial displacement is measured. The L(0,1) mode has a very small axial component while the T(0,1) mode only has a θ component.

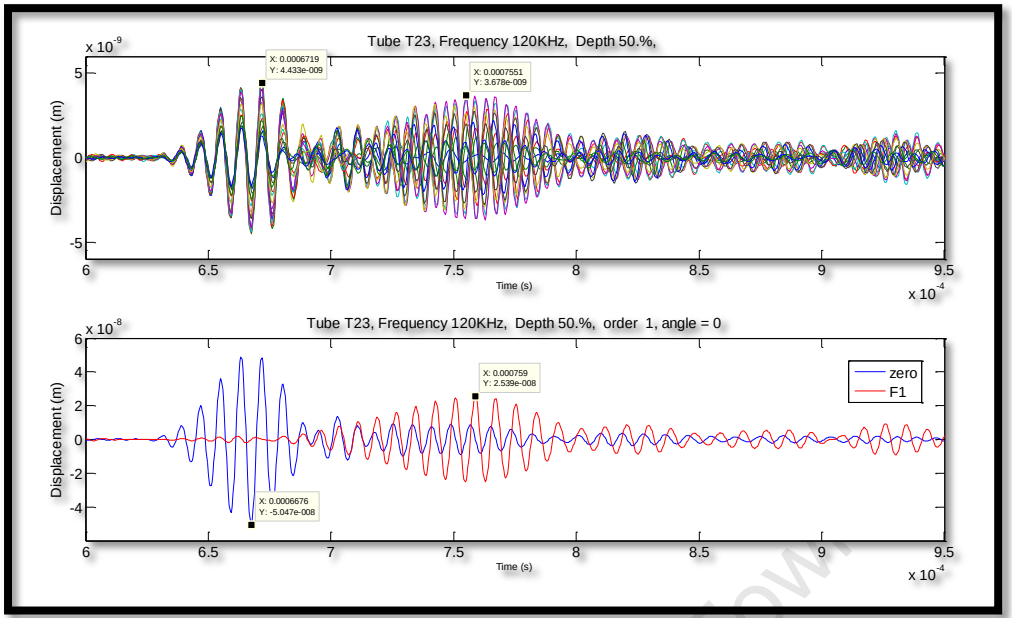

Figure 5.16: The 16 displacements of the outer circle nodes for T23 at 120kHz and 50% depth as well as the zero order (L(0,2) in blue) and first order (F(1,3) in red) modes reflected from the defect.

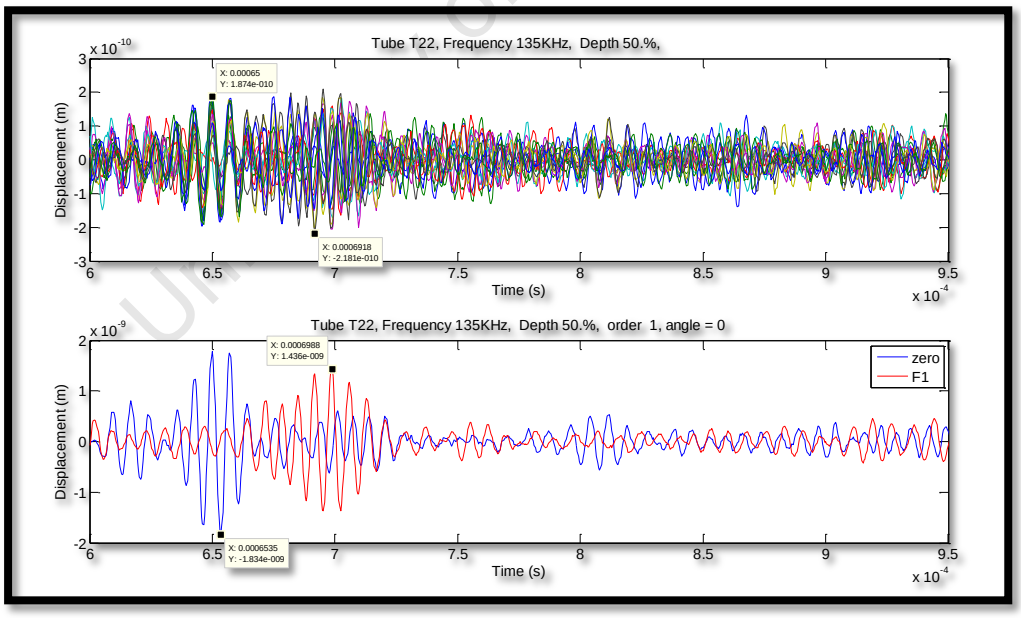

Figure 5.17: The 16 displacements of the outer circle nodes for T22 at 135kHz and 50% depth as well as the zero order (L(0,2) in blue) and first order (F(1,3) in red) modes reflected from the defect.

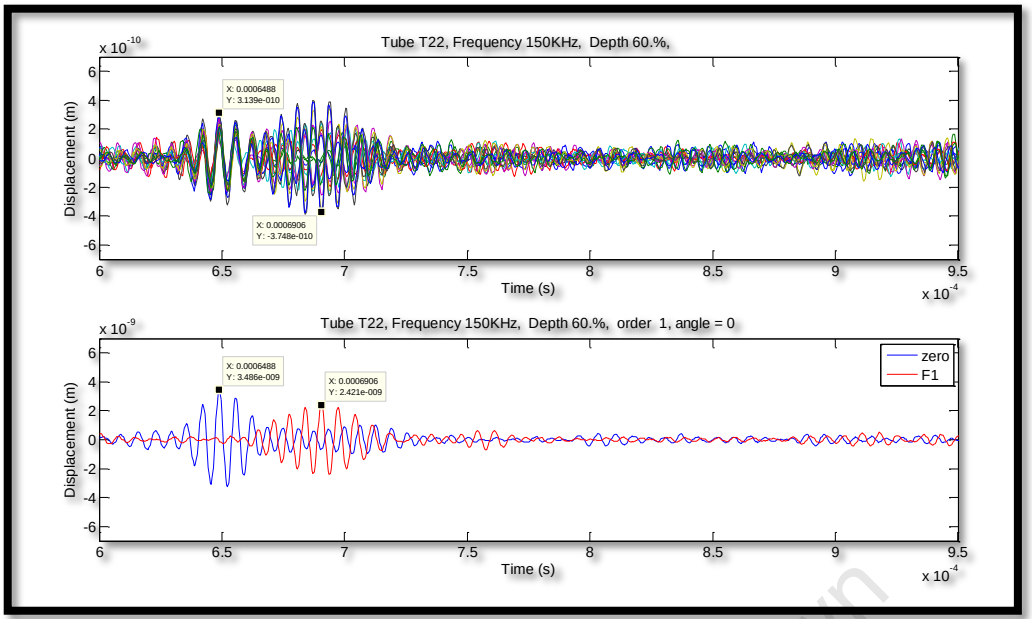

Figure 5.18: The 16 displacements of the outer circle nodes for T22 at 150kHz and 60% depth as well as the zero order (L(0,2) in blue) and first order (F(1,3) in red) modes reflected from the defect.

In each of the three examples, the following is noted:

- The zero order, corresponding to the L(0,2) mode compares well with the expected defect location.
- The first order, corresponding to F(1,3), the mode converted reflection from the defect, also compares well with the expected defect location.
- At 120kHz, F(1,3) is quite dispersive and this shows in the shape (length) of the F(1,3) reflection which is much longer than that for the 135kHz and 150kHz signals.
- The ratio of the first order to zero order reflection is larger for T22 (Pit) than for T23 (groove). The results for T22 and T23 at 150kHz is graphed in Figure 5.19. A more detailed analysis of this phenomena is provided in Chapter 6.

It was found that the ratio of the F(1,3) mode converted signal reflected from the defect to the L(0,2) reflection from the defect was reasonably independent of defect depth for both the pit and the groove. The ratio of the first order mode converted signal to the zero order signal is inversely proportional to the circumferential length [55].

The L(0,2) mode, mode converts to the F(1,3), F(2,3), F(3,3) family and so on. However, 150kHz is below the cut-off frequency of F(3,3) while F(2,3) is highly dispersive below 150kHz. Furthermore, due to the low velocity of F(2,3), the time period of interest is in the region that shares several other possible reflected modes. Little benefit was therefore obtained from analysis of higher order modes besides the benefit in determining the circumferential location of

the defect as discussed in Section 5.3.3. In addition to the L(0,2) mode, unwanted modes are also generated which further complicates the analysis beyond the back wall reflection of the L(0,2). Finally, it was found that the higher order modes did not resolve completely, i.e. some 'leakage' remained after applying Equation 5.6 and Equation 5.7. This was mainly due to the excitation and measuring points being off the same transducer (they are not from discrete transducers) and therefore the individual measurements were influenced by each other.

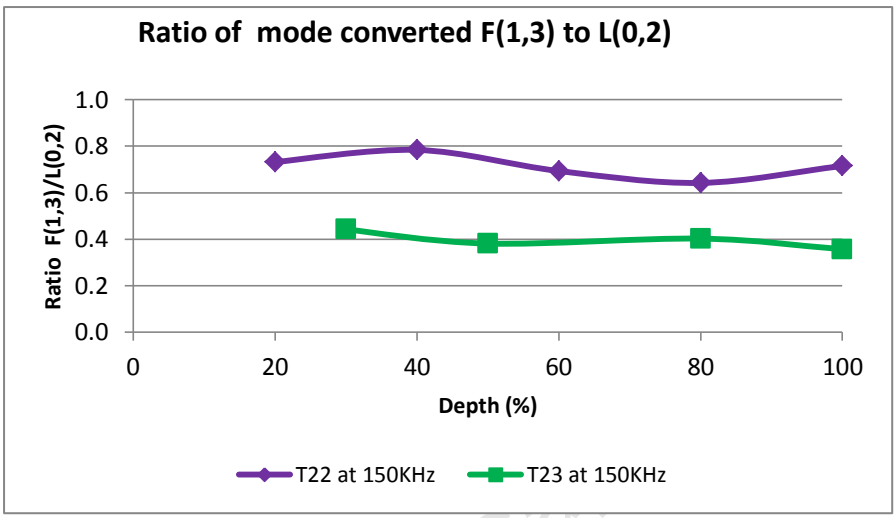

Figure 5.19: Graph of the ratio of F(1,3) reflection to L(0,2) reflection versus defect depth for T22 and T23 at 150kHz.

5.3.2.2 Attenuation of the L(0,2) mode

The attenuation of the ultrasonic guided wave is an important consideration to determine the capability of the guided wave to inspect the full length of the condenser tube. Table 5.7 and Table 5.8 lists the attenuation for T22 and T23 respectively. The attenuation is calculated as follows [14]:

$$A = 20\log_{10}\left(\frac{BW\ amplitude}{input\ amplitude}\right) \quad (5.8)$$

attenuation (T22 at 0 depth)	150kHz			
	input(A0)	1st BW	2nd BW	3rd BW
displacement (m)	4.77E-06	1.68E-06	1.09E-06	7.22E-07
change in intensity	-9.1		-3.8	-3.6
Attenuation to first BW (dB/m)	-2.5		-1.1	-1
Attenuation overall (dB/m)	-1.5			

Table 5.7: The attenuation for T22 over three back wall echos.

attenuation (T23 at 0 depth)	150kHz			
	input(A0)	1st BW	2nd BW	3rd BW
displacement (m)	7.41E-06	6.08E-07	3.35E-07	1.85E-07
change in intensity	-21.7		-5.2	-5.2
Attenuation to first BW (dB/m)	-6.0		-1.4	-1.4
Attenuation overall (dB/m)	-3.0			

Table 5.8: The attenuation for T23 over three back wall echoes.

The attenuation was found to be 1.5dB/m for T22 and 3dB/m for T23 at 150kHz. An attenuation of 1.6dB and 2.5dB was obtained at 120kHz for T22 and T23 respectively. A test of several of the copper tubes yielded a range of attenuation values between -1.3dB/m and 3.2dB/m at 150kHz using this procedure. At such high attenuation, inspection of tubes greater than approximately 2 meters long will be a challenge.

5.3.3 Circumferential location of the defect

Having obtained the axial location of the defect, the circumferential location can be estimated by determining the location of the maximum amplitude reflection from the first order, F(1,3) mode [21].

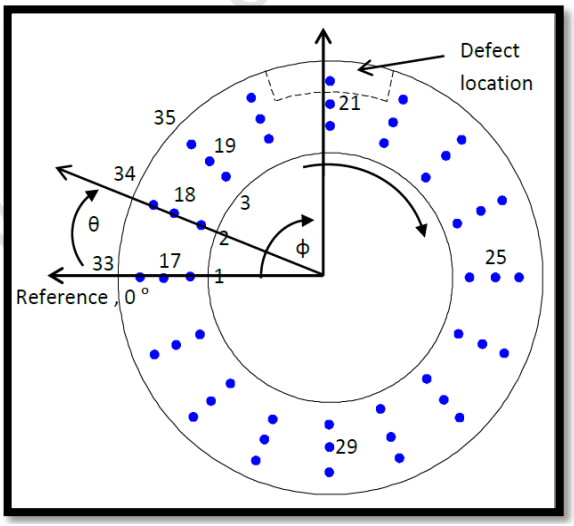

Figure 5.20: Setup of the reference angle, node angle and defect angle. The defect for T22 and T23 is located at 90^0 from the reference.

The first order mode will give two maximum values, 180^0 apart. The F(1,3) reflection from each node as a function of the angle from the reference node is given in Figure 5.21 for T22 at 150kHz, 60% depth. Node 33 was used as the reference which is the default reference of the laser, see Figure 5.20. The maximum displacement was obtained at 90^0 and 270^0 from the reference as shown. All measurements for T22 and T23 provided a similar result, i.e. two peaks,

180^0 apart and 180^0 out of phase. This is again illustrated in Figure 5.22 for the case, T22 at 135kHz and 80% depth. Here it can be seen that the peaks actually occur at 112.5^0 (maximum) and 292.5^0 (minimum). This is as a result of the 22.5^0 (360/16) accuracy provided by the sixteen measurement points and the fact that the pit was not always perfectly at the top (90^0) position.

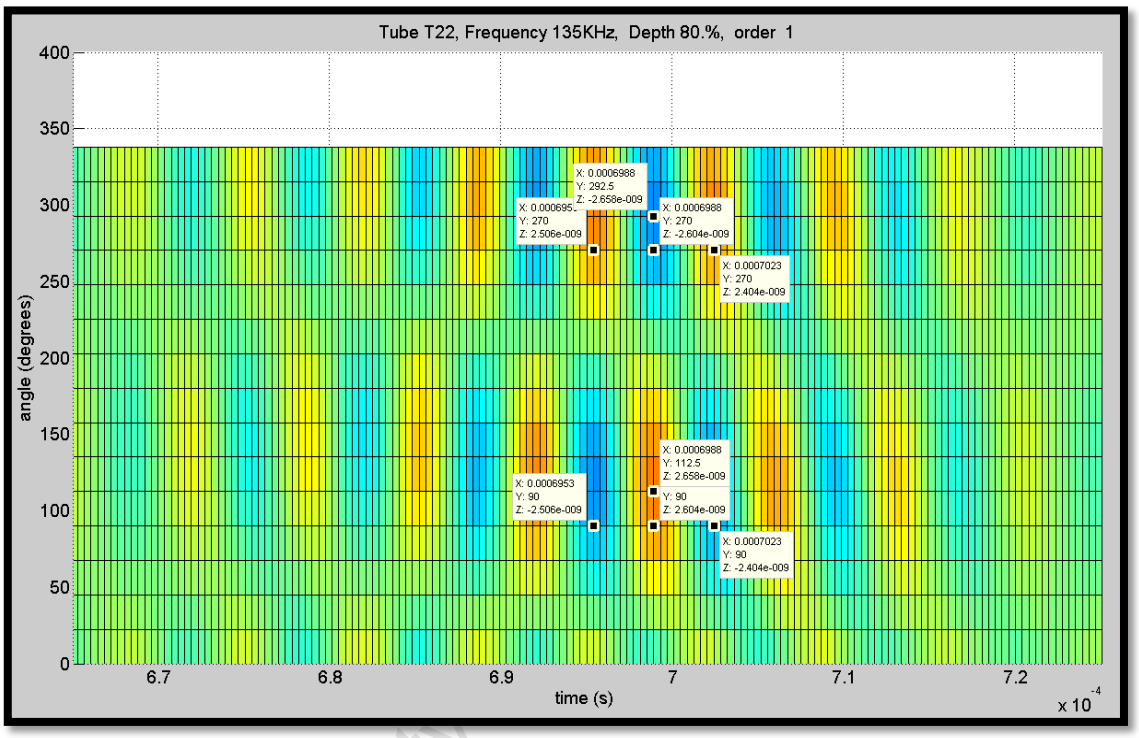

Figure 5.21: Maximum reflected signal for F(1,3) as a function of the defect angle for T22 at 135kHz and 80% depth. Two peaks occur, at 112.5^0 and 292.5^0, 180^0 out of phase.

The nature of ammonia grooving is such that it will occur on the outer surface, at the top of the tube. With the above information, a reasonable conclusion can be drawn that the centre of the defect is at 112.5^0 as opposed to 292.5^0 from the reference, provided of course that the defect is indeed an ammonia groove. Pitting on the other hand is more unpredictable. Pitting generally occur where the chlorides are deposited. This is most likely to occur at the top, outer surface or the bottom, inner surface of the condenser tube. It can however occur anywhere on the circumference of the tube. The same conclusions therefore cannot be drawn for pitting as for grooving. By analysing the higher order modes and increasing the number of measurement points, the circumferential location can be determined more accurately but this analysis is outside the scope of this thesis.

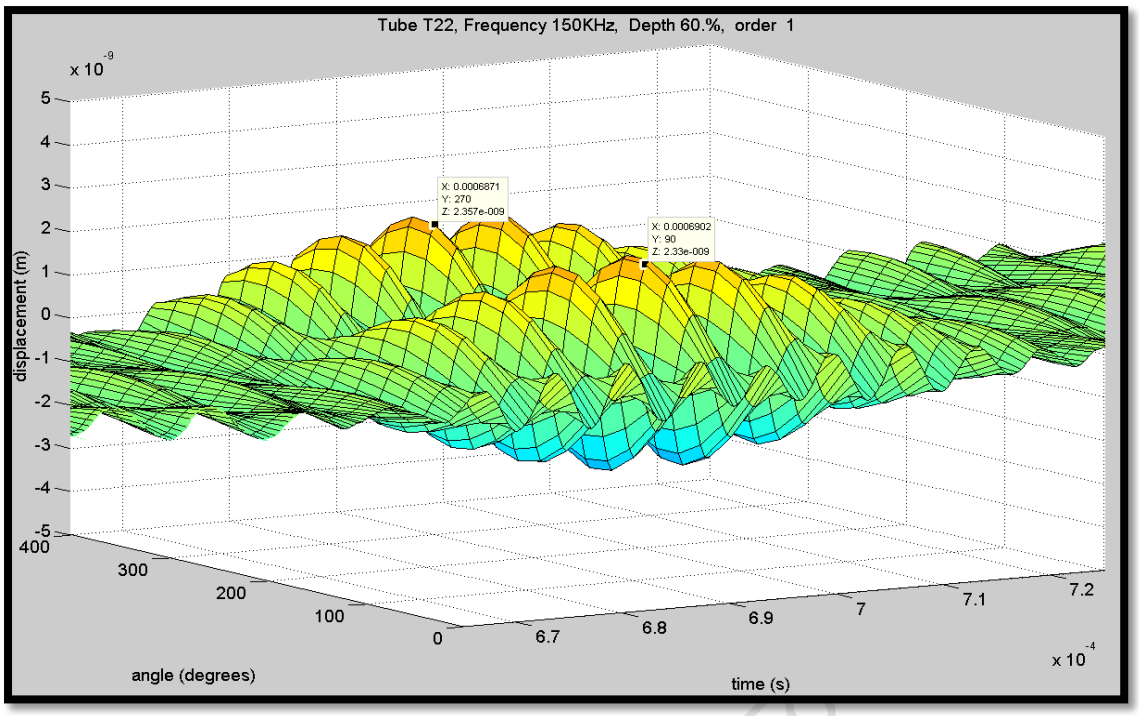

Figure 5.22: Maximum reflected signal for F(1,3) as a function of the defect angle for T22 at 150kHz and 60% depth. Two peaks which are 180^0 out of phase occur at 90^0 and 270^0.

5.3.4 Reflection coefficient of the L(0,2) mode

The reflection coefficient (RC) was calculated for the L(0,2) reflection from the defect, for both the groove and the pit, each defect depth and each frequency. The RC for the L(0,2) mode was calculated as follows:

$$RC_{L(0,2)} = \frac{\sum_{N=1}^{48} u_{L(0,2)}(N)}{\sum_{N=1}^{48} u_{L(0,2)BW}(N)}$$

Where,

$u_{L(0,2)}$(N) is the L(0,2) reflection from the defect measured at node N.

$u_{L(0,2)BW}(N)$ is the L(0,2) reflection from the backwall for no defect, measured at node N.

N is the number of nodal points around the circumference, 48 points.

The graph of the RC for L(0,2) reflection from the pit is given in Figure 5.23 while that for the groove is given in Figure 5.24. Each graph provides the RC at 120kHz, 135kHz and 150kHz. It was found that the RC for both the pit and the groove increased monotonically as depth increased. Furthermore, the RC for the pit which varies from 0.12% to 0.83% is significantly

smaller than that for the groove which varies from 4.6% to 24.4%. This suggest that the correlation between RC and defect depth is not as representative as RC and cross sectional area since a through wall depth pit can have a smaller RC than a 30% defect depth groove.

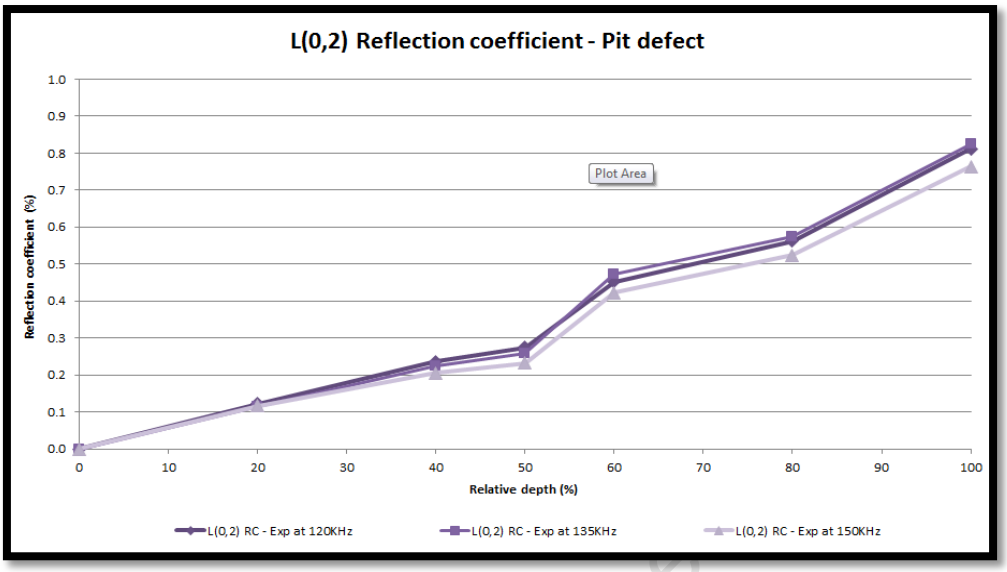

Figure 5.23: The reflection coefficient for L(0,2) reflection from the pit defect at varying depths for 120kHz, 135kHz and 150kHz.

The RC for both the pit and the groove showed a larger increase from 50% to 100% depth than from 0% to 50% depth. The largest increase from 0 to 50% depth for the pit was 34% of the total RC and occurred at 120kHz. The largest increase from 0 to 50% depth for the groove was 41% of the total RC and occurred at 150kHz. The RC as a function of defect depth is relatively

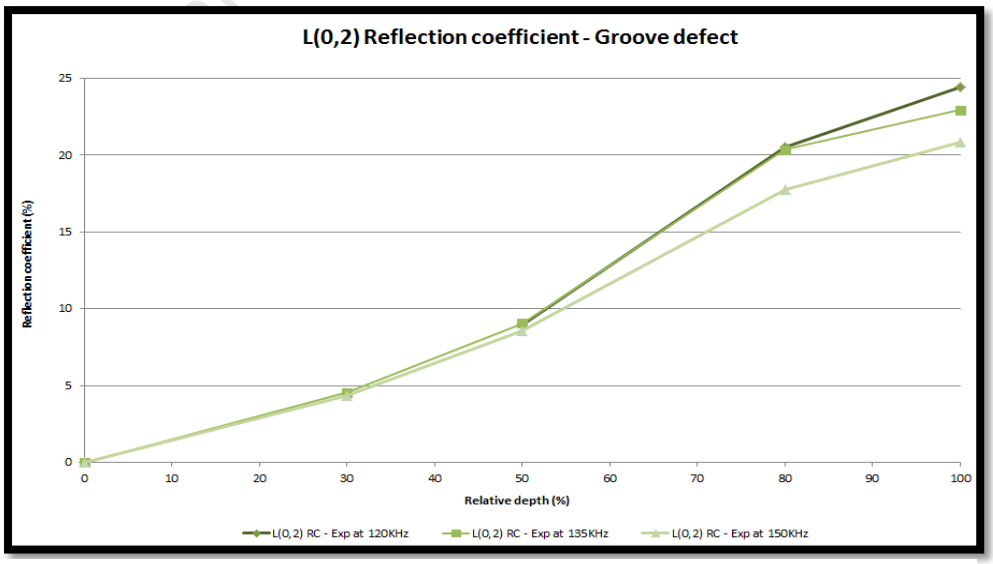

Figure 5.24: The reflection coefficient for L(0,2) reflection from the groove defect at varying depths for 120kHz, 135kHz and 150kHz.

insensitive to the three frequency variations.

5.3.5 Reflection coefficient of F(1,3) mode

The graph of the RC for F(1,3) reflection from the pit is given in Figure 5.25. The graph of the RC for F(1,3) reflection from the groove is given in Figure 5.26. Each graph provides the RC at 120kHz, 135kHz and 150kHz. It was found that the RC for both the pit and the groove increased monotonically as depth increased. Furthermore, the RC for the pit which varies from 0.09% to 0.55% is significantly smaller than that for the groove which varies from 2.1% to 13.1%. Based on Figure 5.19, where the ratio of first order to zero order reflection was found to be independent of defect depth, the difference in RC for the pit and the groove is more representative of their difference in circumferential extent. The pit had a circumferential extent of 1mm compared with a circumferential extent of 10mm for the groove.

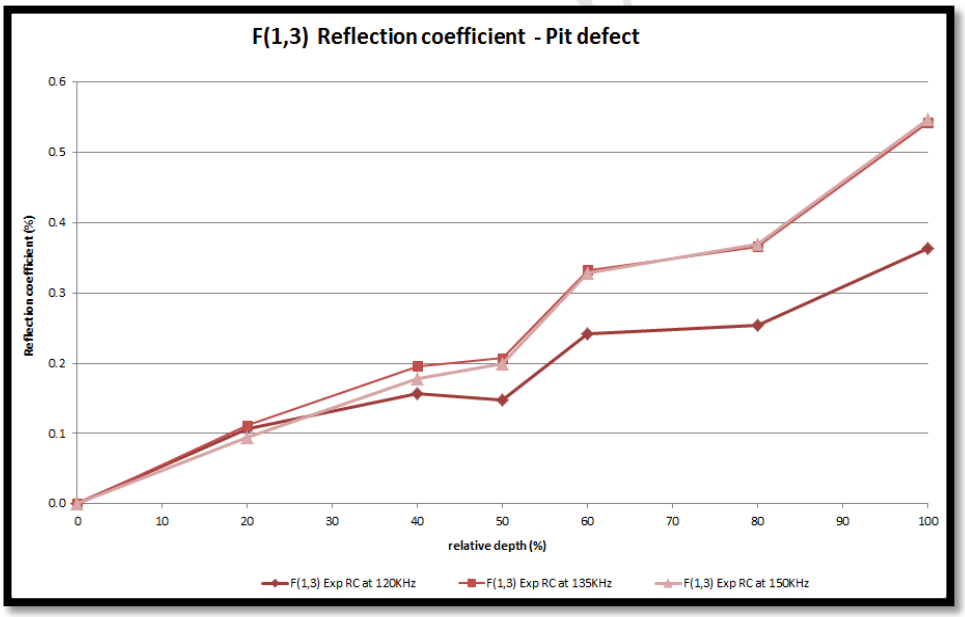

Figure 5.25: The RC for F(1,3) reflection from the pit defect at varying defect depth for 120kHz, 135kHz and 150kHz.

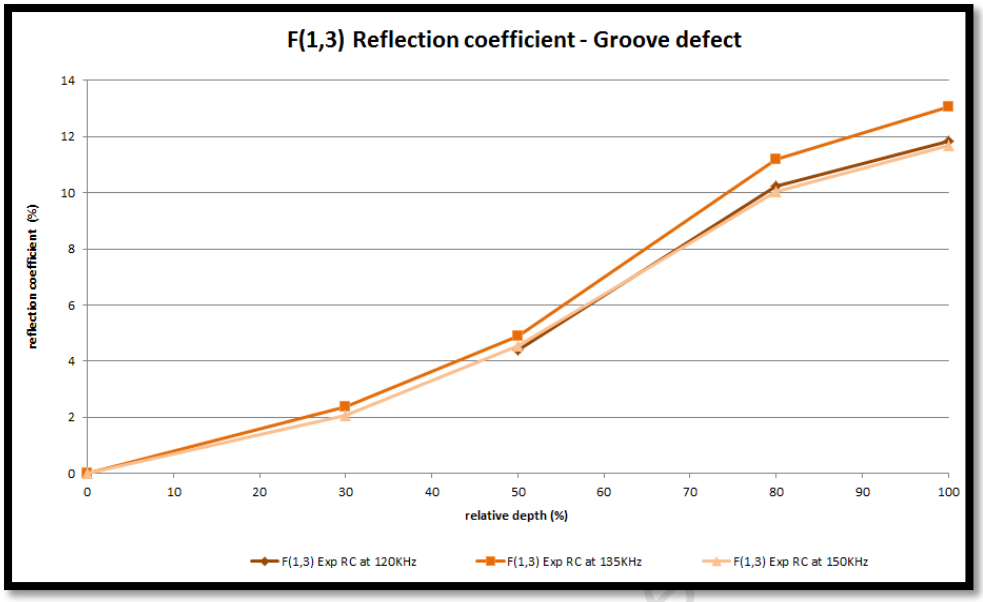

Figure 5.26: The RC for F(1,3) reflection from the groove defect at varying defect depth for 120kHz, 135kHz and 150kHz.

5.4 Summary

Pit defects that represent a wall loss of less than 1% could be detected in copper condenser tubes as described in this experiment. There was a monotonic increase in zero order RC and first order RC for both the pit and the groove. The SNR_{dB} can be improved through signal manipulation but attenuation limits the length of the copper tube that can be reliably inspected. One can distinguish between isolated pitting and grooving by analysing:

- The magnitude of the RC.
- The circumferential location of the defect.
- The F(1,3)/L(0,2) ratio.

The remaining wall thickness cannot be determined, however the value of guided waves as a screening tool for condenser tubes is enhanced by its ability to detect defects that have a cross sectional area as small as 0.2mm^2 and provide intelligence on the defect type.

Chapter 6

Modelling the interaction of the L(0,2) mode with isolated pitting and grooving defects in copper tubes.

6.1 Introduction

Finite element (FE) modelling has been used successfully to investigate the interaction of guided waves with defects [16], [38], [93]. Various commercial software packages are available such as ***CIVA***, ***COMSOL*** and ***ABAQUS***. In this study, ***ABAQUS 6.7-1*** was used to model the interaction of the L(0,2) mode with pitting and grooving defects of varying depth in 1mm thick copper tubes typically used in heat exchangers. Guided waves have been proposed as a screening tool for heat exchangers due to its ability to inspect the full volume of the tube from a single location. Studies in thin walled tubing have focussed on defects with cross sectional wall loss of greater than 1%. In this study, pits that represent a wall area loss as low as 0.3% are investigated. Furthermore, the ability to distinguish between pitting and grooving is investigated as this can provide valuable information on further action to be taken, for example, in condenser health programs.

This chapter begins with a description of the model parameters used. The focus is on comparing selected modelling results with those obtained experimentally. The results of a sample point for a groove and a pit is selected and their L(0,2) and mode converted, F(1,3) reflections from the defect are displayed and discussed to confirm defect location and model length. The ratio of the mode converted, F(1,3) signal to the L(0,2) signal is also investigated. Finally, the zero order and first order reflection coefficients are discussed for both grooves and pits.

This particular work has been conducted in collaboration with A Galvagni at Imperial College London, whose support is gratefully acknowledged.

6.2 Description of finite element model

6.2.1 Finite element model of the copper tube

Figure 6.1 presents the model used in this study. It consists of a three-dimensional mesh representing a copper tube, 0.2m long and 22mm outside diameter and 1mm thick (Note: The drawing is not to scale). The material properties applied are Young's Modulus of 110GPa and a density of 8900kg/m^3.

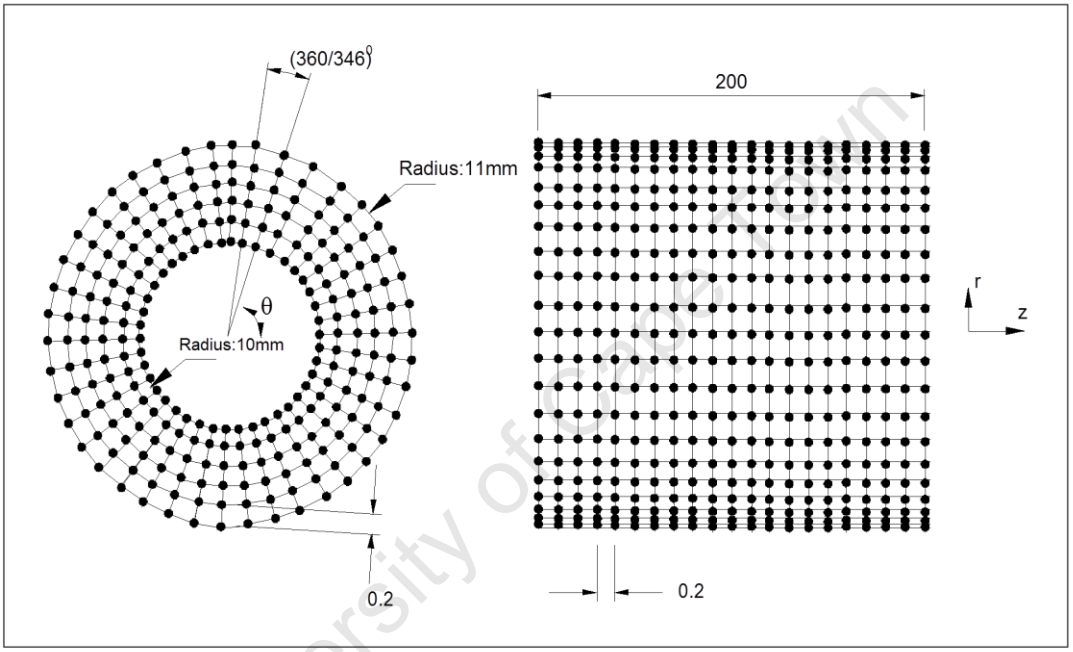

Figure 6.1: Finite Element model of the tube. Tetrahedral elements of 0.2mm were used.

The mesh consisted of regularly spaced hexahedral elements referred to as C3D8 or C3D8R elements in ***ABAQUS 6.7-1***. The mesh size applied is given in Table 6.1.

Mesh size	
Axis	Element dimension
z-axis (tube length)	0.2mm
r- axis (tube radius)	0.2mm
Θ-axis (tube circumference)	(360/346) degrees

Table 6.1: Summary of the mesh size applied to the finite element model.

A 50ns time step was applied.

6.2.2 The defects

Two defect types were investigated namely, ammonia grooves and isolated pitting. In each case, the defect was located at 0.1m (halfway) along the tube length. The defect dimensions for the pit and the groove is given in Table 6.2 and Table 6.3 respectively.

Pit defect dimensions					
depth (mm)	0.2	0.4	0.6	0.8	1
diameter (mm)	1	1	1	1	1
x-section area (mm^2)	0.2	0.4	0.6	0.8	1
Wall loss (%)	0.3	0.6	0.9	1.2	1.5

Table 6.2: The dimensions of the pit defect.

Groove defect dimensions					
depth (mm)	0.2	0.4	0.6	0.8	1
Circumferential length (mm)	10	10	10	10	10
Axial width (mm)	1.5	1.5	1.5	1.5	1.5
x-section area (mm^2)	2	3.9	5.8	7.7	9.5
Wall loss (%)	3	6	8.8	11.7	14.5

Table 6.3: The dimensions of the groove defect.

The defects were modelled by simply removing nodes to obtain the appropriate size defect. The defect location is shown in Figure 6.2.

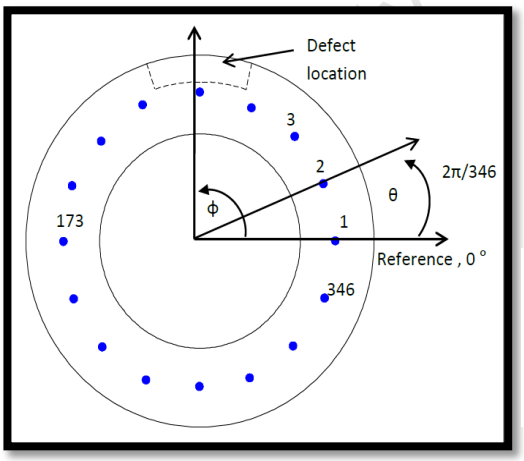

Figure 6.2: The defect and measuring node locations for the FE model. There are 346 nodes and the defect was located at 90^0 from the reference.

6.2.3 The applied force

A time varying force of 1μN was applied axially for 5,5 cycles enclosed by a Hanning window. The axial displacement was monitored at 346 equally spaced nodes around the circumference of the tube. Three centre frequencies of 120kHz, 135kHz and 150kHz were applied for each of the defect depths.

6.3 Results and discussion

6.3.1 Incident mode and defect location based on L(0,2) and F(1,3) reflections

Equations 5.1, 5.2 and 5.3 were applied to confirm the L(0,2) mode and the defect location. The results are summarised in Table 6.4 for the sample plots given in Figure 6.3 (groove defect at 120kHz and 40% depth) and Figure 6.4 (pit defect at 150kHz and 80% depth).

Frequency	$C_{L(0,2)}$ (m/s)	$C_{F(1,3)}$ (m/s)	T_i (us)	$T_{dCL(0,2)}$ (us)	$T_{F(1,3)}$ (us)	D_p (mm)	D_p (actual)	error (%)
Groove, 120kHz at 40% depth	3825	2945	24.2	76.3	84.8	99.6	100	-0.4
Pit, 150kHz at 80% depth	3881	3443	19.3	78.2*	76.0	102	100	11.5

Table 6.4: Summary of the results from Figure 6.3 and Figure 6.4 confirming location of the defect, Dp based on L(0,2) mode. Excellent agreement was obtained between expected and measured results for the groove defect.

Equations 5.5, 5.6 and 5.7 was applied to generate the zero order and first order graphs given in Figure 6.3 and Figure 6.4 with N = 346 nodes.

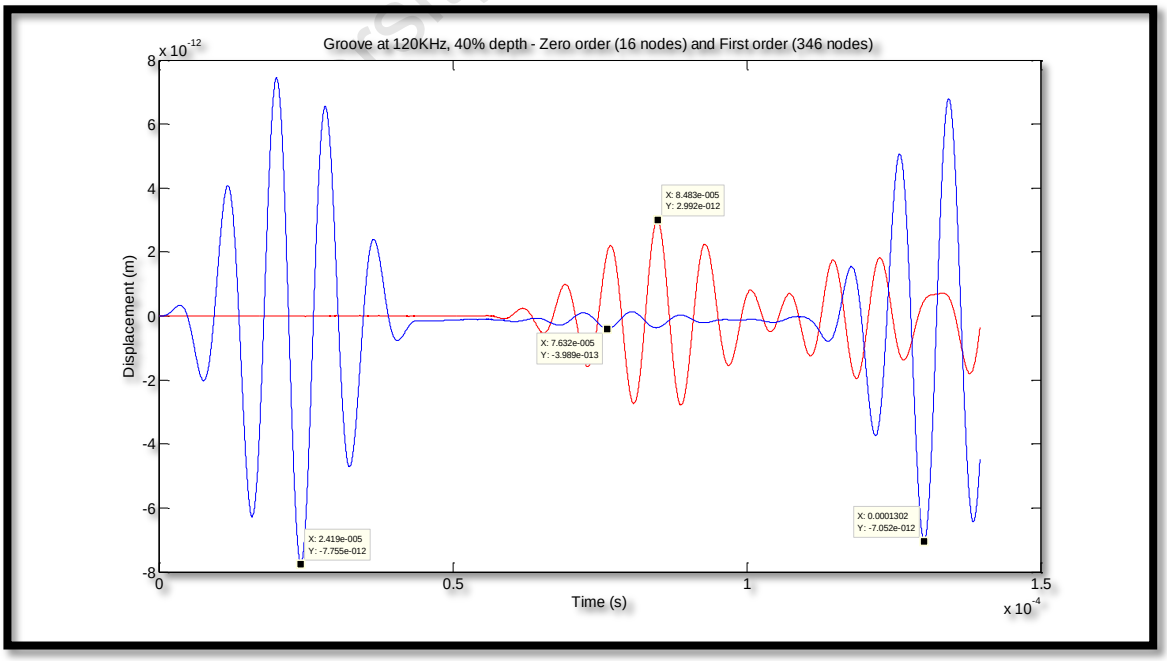

Figure 6.3: The L(0,2) and mode converted, F(1,3) modes for the groove defect at 40% depth and 120kHz. To facilitate scaling, the zero order mode is the sum of 16 equally spaced nodes while the first order is the weighted sum of all 346 nodes.

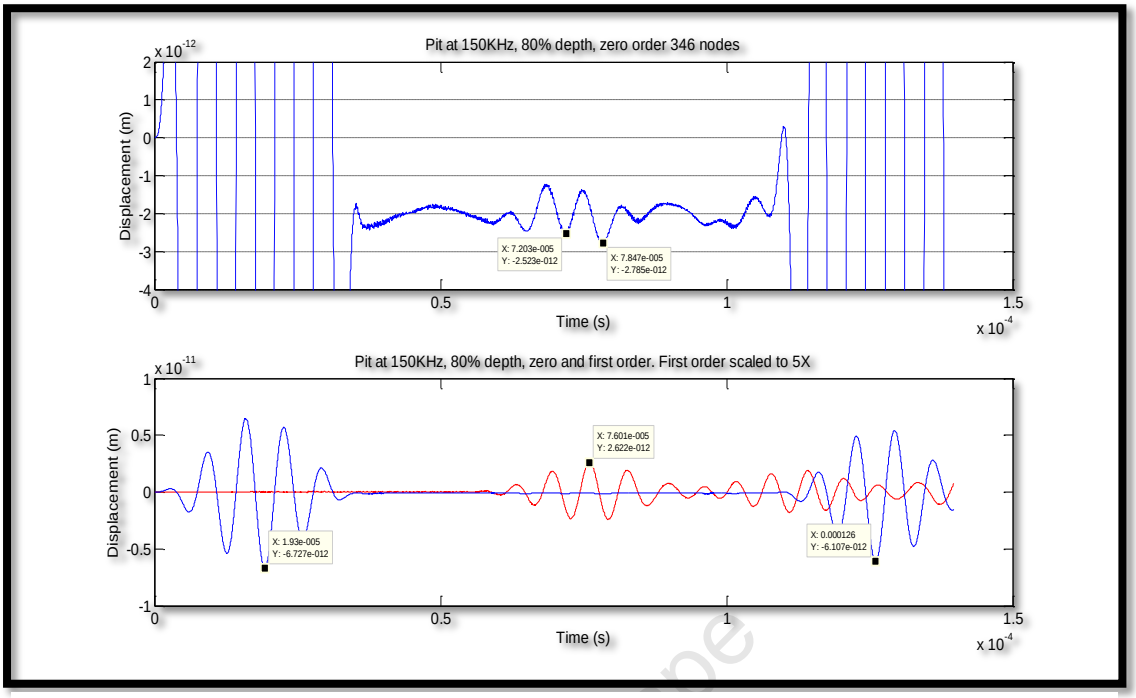

Figure 6.4: The L(0,2) and mode converted, F(1,3) modes for the pit defect at 80% depth and 150kHz. An offset for the zero order mode of roughly 2.1pm was noted.

Excellent agreement was obtained between the model's defect location, D_p and the calculated D_p based on the L(0,2) and F(1,3) velocities obtained from the dispersion curve (Figure 6.4) for the groove defect. The results were consistent for all frequencies. For the pit however, a zero offset which varied with frequency was noted. Figure 6.5 illustrate this phenomenon. The offset was estimated to be -2.7pm (120kHz), -2.4pm (135kHz) and -2.2pm (150kHz). The offset was large enough to affect the location of the absolute maximum signal and hence the defect location. For example, when correcting for the offset, the zero order maximum was at 68.5µs whereas it was at 78.2µs without correction. Now, it could not be at 78.2µs due to the known location of F(1,3) which was unaffected by the zero offset and occurred at 76µs. A correction was therefore required. ***The FE results for the pit need to be viewed with caution in the light of these findings***. The offset however only affected the zero order (see Figure 6.3 and Figure 6.4) and since the nature of the error appeared to be a zero offset rather than a random error, some benefit could be derived from further analysis of the FE results for the pit. The offset was due to the input force having an overall negative sum.

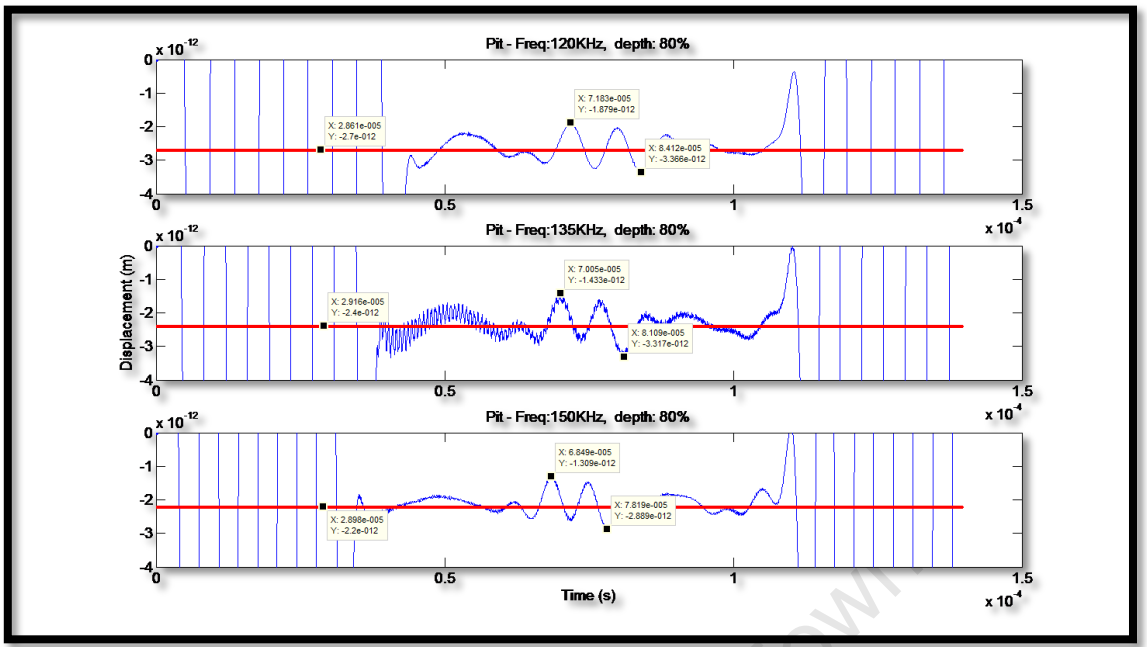

Figure 6.5: An illustration of the zero offset experienced with the zero order results for pit defects. An off set of -2.7pm, -2.4pm and -2.2pm was estimated at 120kHz, 135kHz and 150kHz respectively.

It was also found that the 0.2mm and 0.4mm depth pits were not detectable without signal manipulation. The 0.6mm pit however was clearly detectable even without signal manipulation.

6.3.2 Ratio of the mode converted F(1,3) reflection to L(0,2) reflection from the defect

The ratio of the mode converted, F(1,3) reflection to the L(0,2) reflection from the defect was found to be inversely proportional to the circumferential extent and was independent of defect depth [55]. In Demma's study, it was found that the ratio was insensitive to circumferential lengths less than approximately 15%. In this study, the circumferential length was 14.5% (10mm) for the groove and 1.5% (1mm) for the pit. The results are presented in Figure 6.6 and Figure 6.7 for the pit and groove respectively.

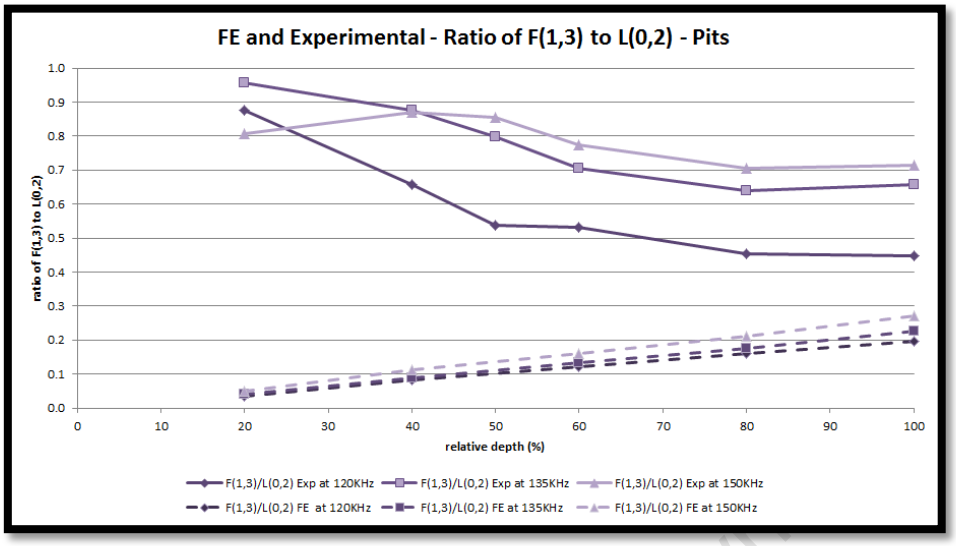

Figure 6.6: The ratio of the mode converted, F(1,3) reflection to the L(0,2) reflection from the defect for both the FE (dotted) and experimental results for the pit defect. Significant differences at low defect depths exist between the FE and experimental results.

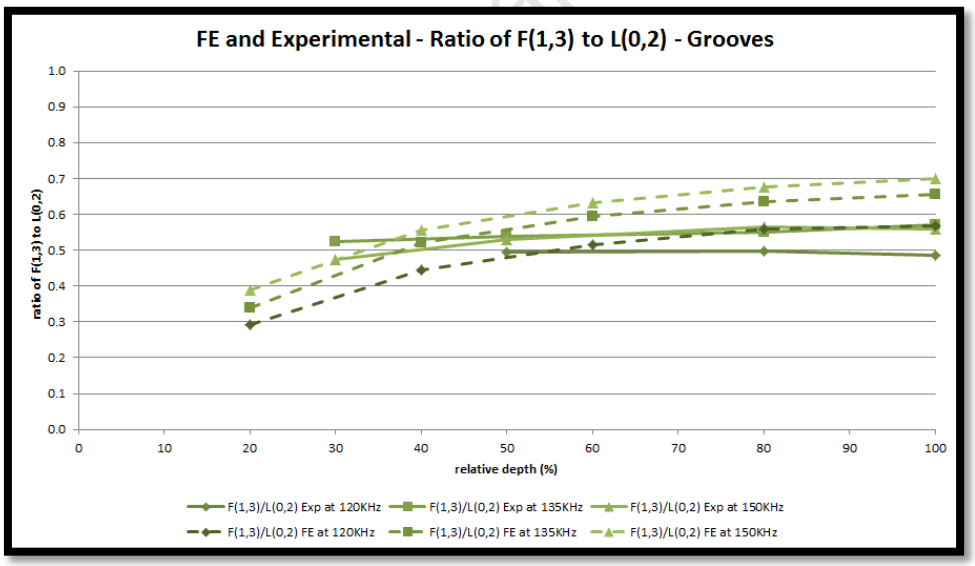

Figure 6.7: The ratio of the mode converted, F(1,3) reflection to the L(0,2) reflection from the defect for both the FE (dotted) and experimental results for the groove defect. There was good agreement between FE and experimental results.

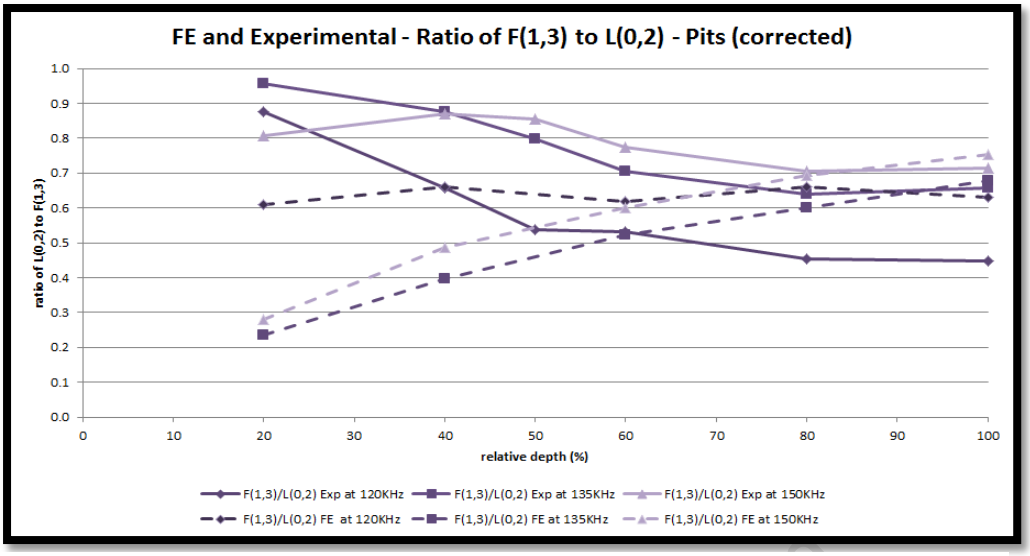

Figure 6.8: The corrected ratio of the mode converted, F(1,3) reflection to the L(0,2) reflection from the defect for both the FE (dotted) and experimental results for the pit defect. Differences between the FE and experimental results decreased considerably after applying corrections for the offset.

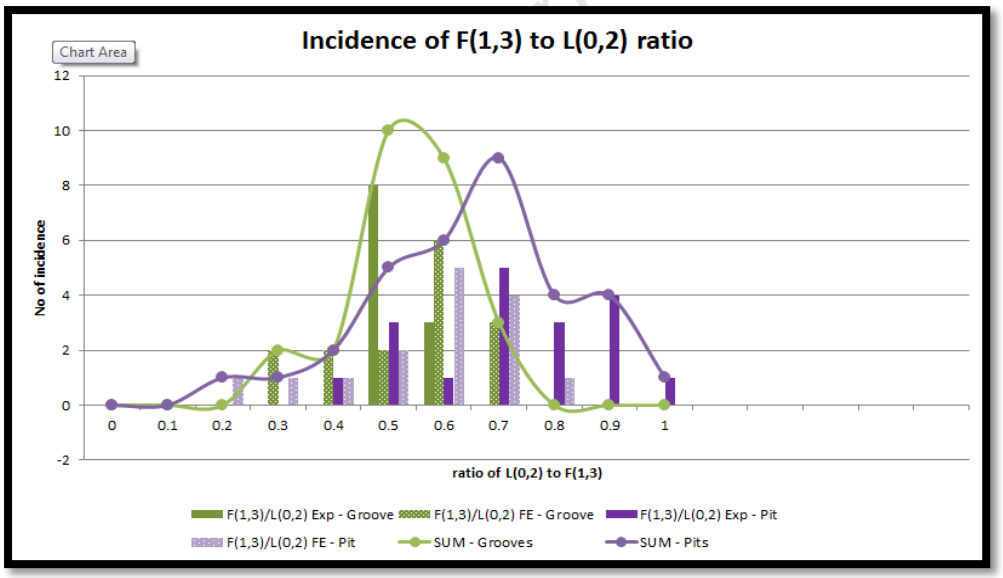

Figure 6.9: The bar chart of incidences of the ratio of the mode converted, F(1,3) reflection to the L(0,2) reflection from the defect for pits (purple) and grooves (green) incorporating FE and experimental results.

For both the groove and the pit, the ratio obtained from the FE model increases as defect depth increases. This is consistent for all three frequencies. For the pit however, the difference between the FE and the experimental results is significant particularly at low defect depths. One of the reasons for the large variation is the offset discussed in Section 6.3.1. Correcting for the offset, reduced the difference considerably as shown in Figure 6.7 but remained large for defect depths less than 50%.

The scatter for the groove was less than that for the pit. Figure 6.9 shows the number of incidence of a particular ratio of F(1,3) to L(0,2). For the pit, a median of 0.7 was obtained while a median of 0.5 for the groove was obtained. The large scatter gives an indication of the confidence in the results.

6.3.3 Circumferential location of the defect

The circumferential location could be located in the same manner as discussed in Section 5.3.3. Two peaks were obtained, 180^0 apart and 180^0 out-of-phase for the first order mode as shown in Figure 6.10. Here the defect was located 90^0 from the reference and two peaks were located at 90^0 and 270^0. To reduce the burden on computer memory, only every 21st data point (not all

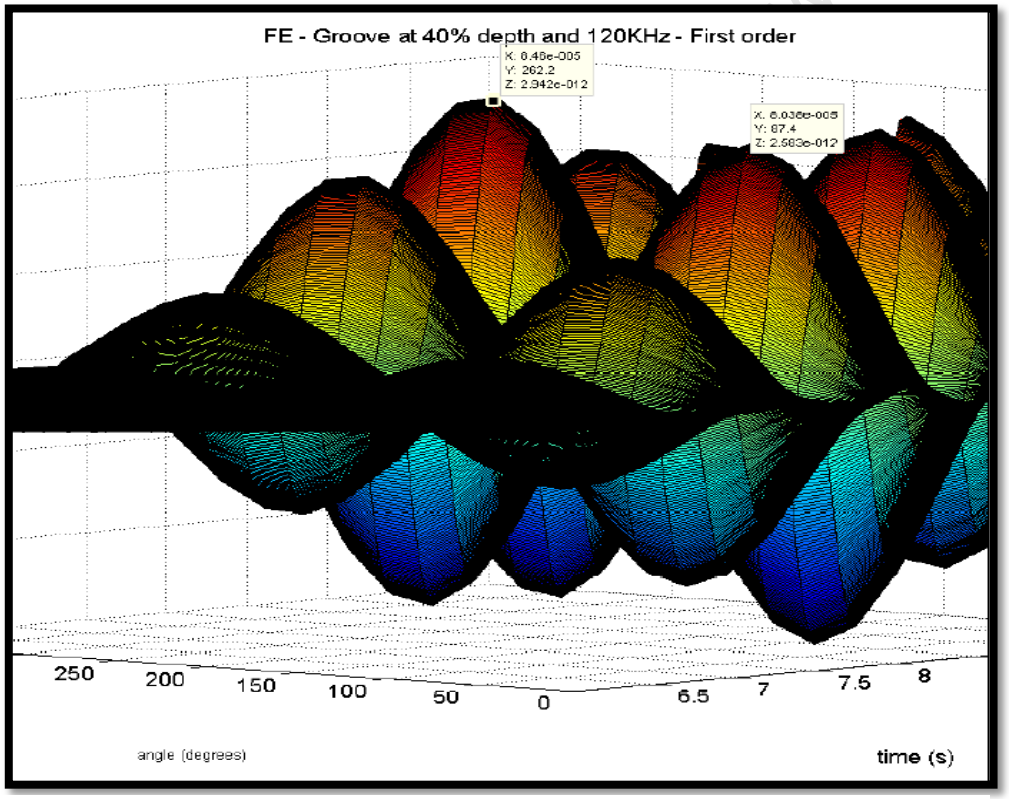

Figure 6.10: The circumferential location of the defect is at 90^0 or 270^0 where two maxima are obtained for the F(1,3) reflection from the defect.

346) were plotted resulting in reduced accuracy with peaks indicating at 87.40 and 262.2 degrees.

6.3.4 The reflection coefficients – L(0,2) mode

The graph of the FE and experimental L(0,2) reflection coefficient (RC) for the pit defect is given in Figure 6.11. The FE RC differs roughly by an offset of between 1% (120kHz) and 2% (135kHz) from the experimental results obtained. This is significant given that the experimental maximum RC was very low at 0.825%, obtained for the pit at 135kHz and 100% defect depth. The difference between the FE and experimental results reduced considerably after a correction for the offset was applied as discussed in Section 6.3.1. The corrected graph is shown in Figure 6.12. The RC increased monotonically in all cases (FE and experimental at all frequencies) for the pit. While this is not surprising, given a constant axial extent, it does suggest that an increase in cross sectional area of 0.3% is consistently detectable. At such low RC's, SNR is an important consideration. As discussed in Section 5.3.2.2, signal processing and the evaluation of both the L(0,2) and mode converted, F(1,3) reflected signals significantly increased the SNR and the probability of detection.

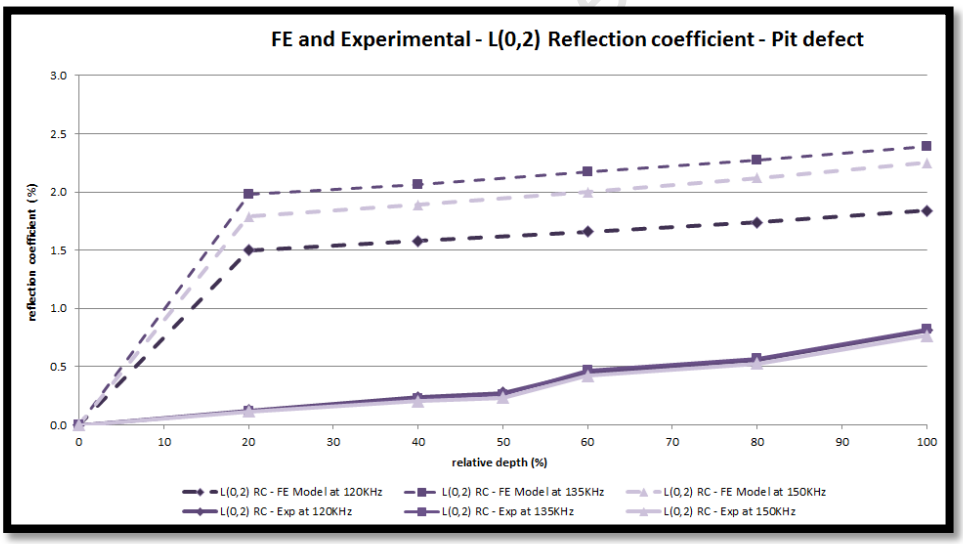

Figure 6.11: The FE (dotted) and experimental L(0,2) reflection coefficient for the pit defect. A large difference between the FE and experimental results exist.

The graph of the FE and experimental L(0,2) reflection coefficient (RC) for the groove is given in Figure 6.13. An L(0,2) RC of 24.4% at 100% defect depth and 120kHz is obtained for the experimental results while a RC of 19.2% is obtained for the corresponding FE result. Here the RC's are much larger than that obtained for the pit. This is expected given the much larger cross sectional area of the groove defect compared to the pit defect, roughly 10 times larger.

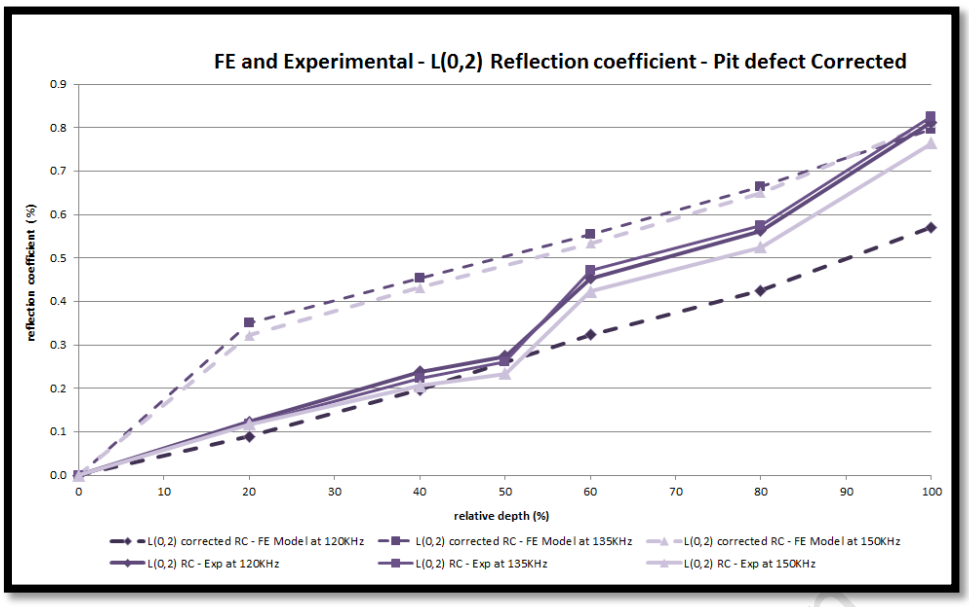

Figure 6.12: The corrected FE (dotted) and experimental L(0,2) reflection coefficient for the pit defect. The large difference between the FE and experimental results is reduced after correcting for the offset.

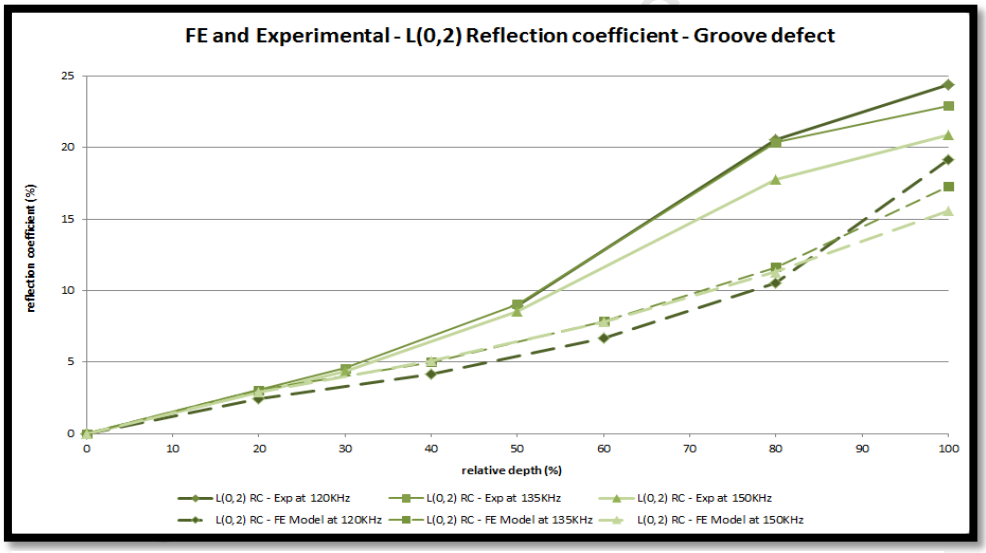

Figure 6.13: The FE (dotted) and experimental L(0,2) reflection coefficient for the grooves defect. The difference between the FE and experimental results is greatest at 80% defect depth.

Despite considerable improvement between the FE and experimental results for the pit following correction for the offset, large difference still remain between both the FE results at the three frequencies and between the FE results and the experimental results. Some of the differences experienced in the RC results are explained by the following:

- The defect model is based on a 'square' hole which will have less scatter than a round hole and therefore greater L(0,2) reflection than the experimental case.

- The length of the model is 200mm, 1600mm shorter than the tube used in the experiments. The model defect is 1000mm closer to the applied force (input signal) than the actual defect. Greater attenuation will therefore be experienced in the experimental setup than in the case of the model.
- The number of measuring nodes for the FE model is 346, 298 more than the experimental setup. A higher number of measuring nodes serve to provide a more accurate result provided that they remain equally spaced. In the case of the experimental setup, an increase in the number of bad data measuring nodes could negate the accuracy obtained by an increase in data measuring nodes.

6.3.5 The reflection coefficients – F(1,3) mode

Once again, the F(1,3) RC for the pit defect is very low, ranging from 0.05% (FE, 20% depth at 120kHz) and increasing to 0.6% (FE, 100% depth at 150kHz). There was good agreement between the FE and the experimental F(1,3) RC results for the pit and the groove, given in Figures 6.14 and 6.15. In all cases, the increase from 50% depth to 100% depth is higher than that from 0 to 50%.

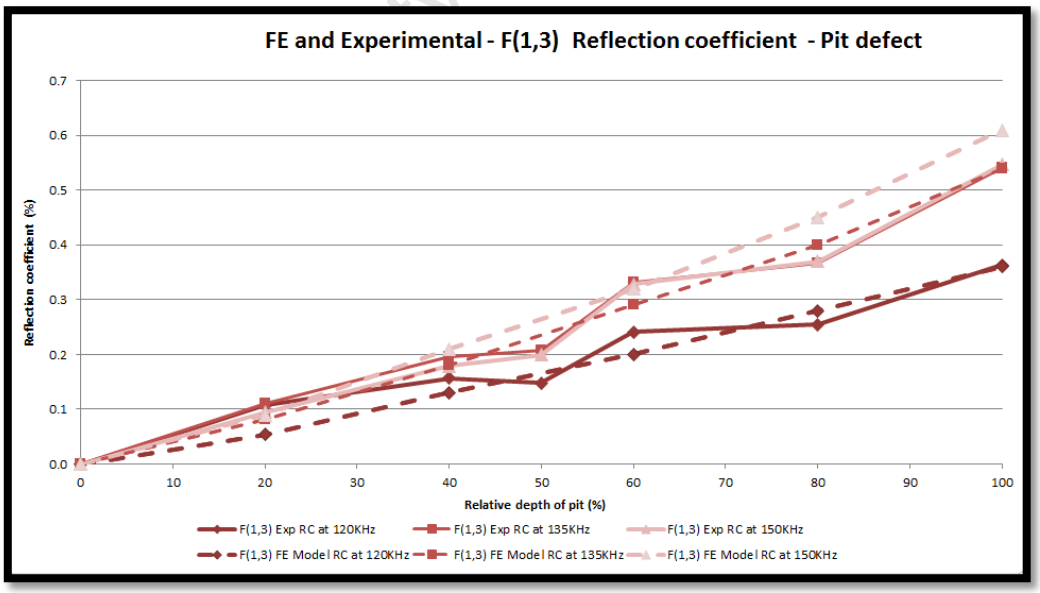

Figure 6.14: The FE (dotted) and experimental F(1,3) reflection coefficient for the pit defect. There is good agreement between the FE and experimental results.

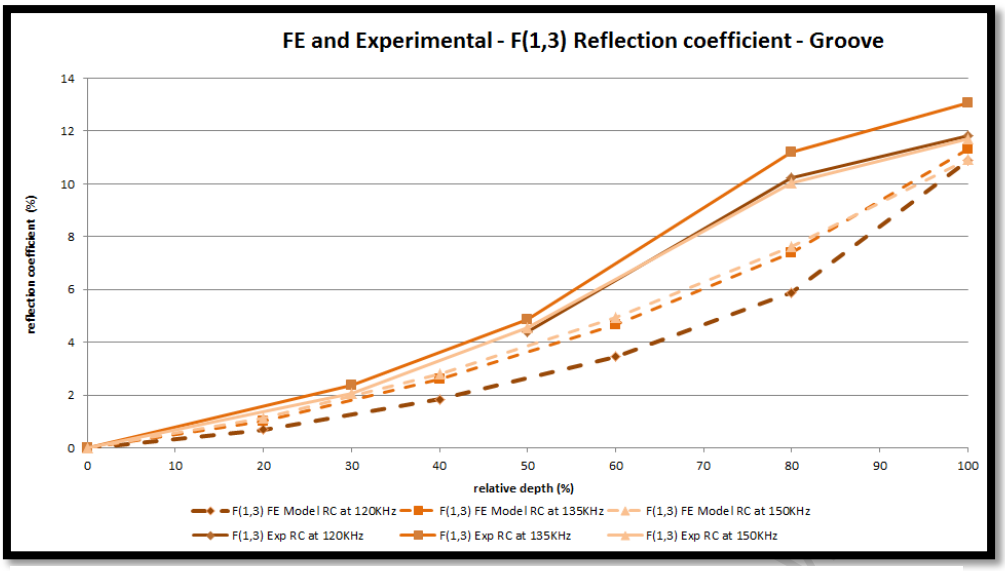

Figure 6.15: The FE (dotted) and experimental F(1,3) reflection coefficient for the groove defect. As for the L(0,2) RC for the groove, the largest difference between the FE and experimental results exist at a defect depth of 80%.

6.4 Summary

The pit FE results for the L(0,2) reflection was affected by a zero offset error and therefore these results must be viewed with caution. The groove results, whilst also affected by this phenomenon, the magnitude of the reflection amplitudes for grooves are much larger and therefore the effect on its results is negligible. The first order (and higher order) results are unaffected. The FE results do however confirm the conclusions drawn from the experimental results obtained namely:

- Defects with a cross sectional area of 0.2mm^2 could be detected.
- There is a monotonic increase in the zero order and first order RC for both the pit and the groove.
- One can distinguish between the pit and the groove defect on the basis of its circumferential location, magnitude of the RC and the magnitude of the ratio of the mode converted, F(1,3) and the L(0,2) mode.

Chapter 7

Discussion

7.1 Introduction

There are two main parts to this chapter. First, a discussion of the experimental results obtained from the use of conventional (bulk wave) ultrasonic equipment to generate guided waves in steel plates and copper tubes containing pits and grooves is provided. The main objective here was to determine the viability of using such readily available equipment to study guided waves for research purposes. Frequencies of 1MHz to 4MHz were applied using standard ultrasonic transducers. An important phenomenon identified is the successive group velocity minima that occur at 2300m/s in steel plate and this is discussed first in the early part of the chapter. Mode recognition and noise is then discussed, together with this method's defect detection capability. The limitations of the procedure is then discussed and finally the relevance of this work to the experimental work performed using the laser vibrometer is discussed.

In the second part of this chapter, the experimental results obtained from the interaction of the L(0,2) mode with pits and grooves in condenser tubes is discussed. In this case, frequencies of 120kHz, 135kHz and 150kHz is applied. The main objective was to determine the capability of the L(0,2) mode to detect pit defects with a cross sectional area as low as $0.2mm^2$ and to distinguish between pit defects and groove defects on the basis of the signal obtained from the interaction of the L(0,2) mode with these defects. Here, defect detection capability is discussed first followed by signal processing and mode separation. A discussion on defect sizing is also provided before the limitations of this work are discussed. A summary is provided at the end of the chapter.

7.2 Discussion on the results obtained using the conventional equipment

The use of existing, standard, bulk wave equipment to generate guided waves for basic research purposes was demonstrated. Basic concepts of mode conversion and back wall reflection coefficients synonymous with guided waves were explored in plates and tubes using this equipment. The implications of results obtained are discussed below.

7.2.1 Group velocity minima

It was found that the 45^0, 4MHz shear wave transducer produced coherent, well defined signals of the A1, S1, A2 and S2 modes depending on the plate thickness, see Figure 4.17. The 45^0 shear wave transducer produced a phase velocity of 4578m/s in steel plate. This phase velocity corresponds to a group velocity minimum of 2300m/s for all modes beyond the fundamental modes, A0 and S0. So depending on the frequency bandwidth and plate thickness several guided wave modes can be generated at the same group velocity. There is great benefit in being able to generate several modes at the same group velocity minimum. First, minor variations in frequency-thickness product will not affect the group velocity as the group velocity is constant over a short period where the minimum occurs. Second, multiple modes generated that have the same group velocity will not contribute to the coherent noise that typically occurs when many modes are generated unintentionally, each of which have a different velocity (see for example Figure 4.18). Third, since multiple modes are present, the sensitivity to defects of various position and orientation is enhanced [78].

Furthermore, it is interesting to note that the shear wave velocity in steel of 3240m/s would travel the same lateral distance (displacement) in roughly the same time as the A1, A2, S1 and S2 modes at their group velocity minimum of 2300m/s. That is, for the 45^0 shear wave transducer, an effective velocity of 2291m/s (3240/√2) is achieved. This is within 0.5% of the guided wave group velocity. The signal response for the 4MHz 45^0, shear wave transducer can therefore also be that of a shear bulk wave that skips along the plate length. This is quite unique in that an operating point is experienced where both the bulk wave and the Lamb wave modes 'co-exist'. This approach could possibly provide advantages over manual bulk wave pulse-echo inspection methods as the technique could inspect a larger volume from a single location and therefore improve the probability of defect detection. The characteristics of this technique, which excludes the fundamental modes, may be more suited to detecting defects that occur in the volume of the material rather than surface breaking defects.

Similar success (well defined, coherent guided wave signals) is obtained with the 70^0 degree shear wave transducer (see Figure 4.16) at a phase velocity of 3448m/s and a corresponding group velocity of roughly 3000m/s. This is not due to the presence of the group velocity minima but the "skipping" bulk wave discussed earlier. The corresponding effective velocity of the shear bulk wave skipping at an incident angle of 70^0 is 3240*sin(70) =3044m/s. This is within 2% of the guided wave group velocity.

The group velocity minima described here is also present in tubes and pipes and can provide similar benefits. This is illustrated in Figure 7.1. The repeated minima occur from L(0,3) mode. As for plates, this warrants further investigation as a possible application for improving detection capability over shorter lengths in, for example, boiler tubes.

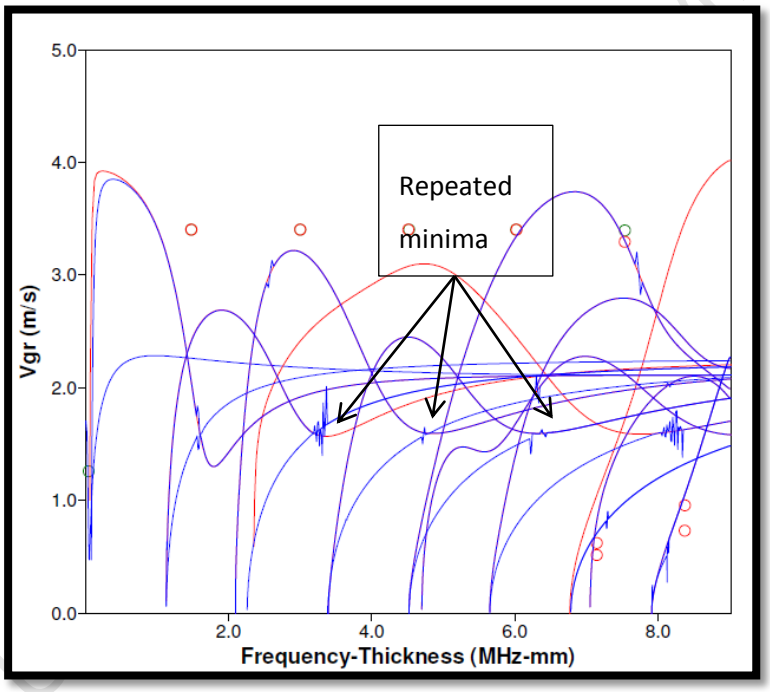

Figure 7.1: Repeated minima for copper tubes, 22mm diameter, 1mm thick is obtained from L(0,3) onwards. The group velocity dispersion curve is generated using *Disperse* [39].

7.2.2 Mode recognition and noise

There are several reasons for the inaccuracies and so called 'unexplained' signals that make some of the transducer's unsuitable to generate the selected guided waves. The incident velocity, the angle of incidence and the frequency of the ultrasonic wave are crucial to determining the phase velocity and hence the selected guided wave mode to be generated. The incident velocity, angle of incidence and the frequency is affected by the transducer's

bandwidth, beam spread, near zone effects and coupling efficiency amongst others. A detailed discussion of the extent to which these phenomena contribute to the noise and unexplained signals is outside the scope of this thesis, but it is clear that they do not affect the 4MHz transducer to such a large extent but could very well be the cause of the noise experienced with the other transducers. This is supported by the fact that the 2MHz, 45^0 shear wave transducer which also produce a group velocity of 4578m/s do not perform as well as the 4MHz, 45^0 shear wave transducer when operating at the same frequency-thickness product.

The results obtained for the 1.8MHz longitudinal wave transducer was particularly poor (see Figure 4.15). The longitudinal bulk wave mode converts easily to a bulk shear wave at the plate boundary which in turn can generate unintended guided wave modes. Shear waves are less susceptible to this and could readily skip along with minimal bulk wave mode conversion.

The use of standard bulk wave transducers limits the range of incident phase velocities that can be produced. Standard shear and longitudinal wave transducer angles are 0^0, 45^0, 60^0 and 70^0 in steel. The 2MHz, 60^0 shear wave transducer produce a phase velocity in steel of 3741m/s. This corresponds to a group velocity region of S0 that is highly dispersive in 1.3mm plate and therefore this is not an ideal region (see Figure 4.18). Perspex wedges can be used to vary the angle and hence change the mode generated as discussed in Section 2.3.7.2 (in plates) and 2.3.7.3 (in tubes).

The wedge method applied to the tubes generate flexural modes as well as the L(0,2) mode. The Perspex wedge used resulted in significant noise in the region from 0 to 100mm as shown in Figure 4.28 and Figure 4.29. This is due to the wedge design. Unwanted reflection is obtained from the Perspex boundaries which can be reduced through improved design.

7.2.3 The detection of defects

The presence of a defect can be recognised from the presence of a mode converted signal, the reflection of the incident mode or a reduction in the amplitude of the back wall echo. Together, the analyses of these three parameters enable defect depths of 0.25mm in 3mm thick steel plate, 0.2mm in 1.6mm thick steel plate and 0.25mm in 0.9mm thick copper tube to be detected using the basic conventional ultrasonic equipment. Figure 4.20 to Figure 4.23 obtained using the 45^0, 4MHz shear wave transducer to inspect for 1.5mm pits in 1.6mm plates provides an excellent illustration of the behaviour of these three parameters which are discussed below.

7.2.3.1 The mode converted signal

With a pit depth of 0.2mm, a well-defined mode converted signal is present and the reflection of the incident mode is present. The back wall echo dominates as expected. At a depth of 1.2mm, the mode converted signal is no longer clearly visible but the amplitude of the reflected signal has increased slightly, while that of the back wall has reduced to nearly 50% of its original amplitude. The mode converted signal which is produced as a result of the asymmetry present in the cross-section of the plate diminishes as the defect reaches through wall depth. Essentially, the degree of asymmetry decreases as the defect depth increases. Figure 4.25 and Figure 4.27 both also illustrate this fact. The reflection coefficient of the mode converted signal decreases to zero once through wall depth has been achieved for both the groove and the pit. This is contrary to the mode converted signal in tubes where a through-wall pit or groove does not result in the mode converted signal diminishing to zero. Mode conversion for tubes is discussed in more detail later. There are several modes that can be mode converted from the incident, S1 mode that is generated from the 4MHz shear transducer in 1.6mm plate. The A0, A1, A2, S0, S2 and S3 are all present in the frequency-thickness region of 6MHz-mm to 7MHz-mm. While this can be viewed as a drawback given the potential for noise and potentially false indications, it can also be seen as improving the probability of generating a mode converted signal if a defect is present.

7.2.3.2 The incident mode

The amplitude of the reflected signal is dependent on several factors as discussed in Section 3.3.3.1. The reflection coefficient of the incident signal (S2 and possibly A2 modes) for grooves of 5mm length and 15mm length converges as defect depth increases (see Figure 4.24). The reflection coefficient for the pits remains significantly less (20% once through-wall depth has been reached) compared to grooves (120% once through wall depth has been reached). This is true for both plates and tubes. The amplitude of the reflected incident mode is strongly related to the cross sectional area of the defect.

7.2.3.3 The back wall echo

In Figure 4.20, the back wall echo amplitude of the incident mode reduced by nearly 50% despite only a marginal increase in the amplitude of the incident mode reflected from the defect. The amplitude of the back wall reflection is therefore also an important parameter to monitor when inspecting for defects in plates or tubes. The back wall amplitude decrease sharply after 50% defect depth has been reached. This is illustrated by Figures 4.20 to Figure

4.23 and Figure 4.26. For this setup, the rate at which the back wall echo amplitude decreases may provide insight into the depth of the defect. This however is not a universal rule as different modes will react differently to different defect geometries. Furthermore, guided waves, which typically propagate over long distances, may encounter several discontinuities that are not defects along the way which may result in reduction in the amplitude of the back wall echo. Dispersion and attenuation are other factors that could affect the amplitude of the back wall echo. Nevertheless, further investigation into this phenomenon is warranted for specific applications.

7.2.4 Limitations of procedures used

Although several concepts were successfully studied using the basic ultrasonic equipment there are limitations that need to be considered. First, coupling of the transducers to the test sample introduces variations between measurements as the coupling is not always 100% efficient. This is one of the main reasons for obtaining a reflection coefficient greater than 100% (see Figure 4.24). Second, the manual manipulation of the transducers is not ideal as the reflection amplitude is sensitive to the angle of the guided wave to the defect. Scatter and a consequent reduction in the reflected signal are observed when even minor changes are experienced in the angle between the incident mode and the defect. This is more pronounced for pits as expected because of the limited cross sectional area as well as the ease with which the incident wave scatter from the circular face of the pit. Third, a maximum plate thickness of 6mm was inspected using this method. While theoretically it should be possible to use this method on any plate thickness or pipe thickness, the transducer energy input and transducer frequency applied will limit the maximum thickness. Finally, the higher frequencies applied here result in high levels of attenuation. A length of 300mm for steel plates could be inspected while a length of 800mm of copper tube could be inspected using these methods. The value of the method is therefore not the ability of guided waves to travel long distances but rather that material can be inspected for defects from a single location.

7.2.5 Relevance to the work done using the laser vibrometer

Although the objective of the tests were to determine the viability of using the basic ultrasonic equipment for research purposes, the tests conducted also provided an opportunity to study the interaction of guided waves with pits and grooves. The tests using the basic ultrasonic equipment therefore served as a preliminary study to identify opportunities to improve the test methods and procedures but also to identify areas requiring more detailed investigation. The defect location along the tube was only 50mm away from the tube end for the preliminary

studies. This was not ideal to study the reflection of the incident mode and the mode converted mode while not interfering with the back wall echo signal. The defect was therefore moved to a location of 1100mm away from the transducer for the tests using the laser vibrometer. Another improvement identified in the preliminary studies was to leave the transducer bonded to the tube rather than transfer it between tubes. This reduced the variability introduced between measurements due to changes in the coupling effectiveness. Noteworthy examples of findings from the preliminary studies that required more detailed investigation using the laser vibrometer was the effect that the circumferential location of the defect had on the reflected signal and the large variation between the L(0,2) reflection coefficient of the pit compared to that of the groove. Both these findings were analysed in detail in the subsequent tests and is discussed later.

7.3 Discussion on the results obtained with the laser vibrometer

The interaction of the L(0,2) mode with pitting and grooving defects in condenser tubes was studied to determine its capability to detect defects with a cross sectional area from as low as 0.2mm^2. The results of this study are discussed below.

7.3.1 Detection of defects that represent a wall loss of less than 1%

Defect detection is essentially about the recognition of the signals associated with the three parameters namely mode conversion, the incident mode and back wall echo as discussed in Section 3.3.3 and again in Section 7.2.3. Pit defects are challenging to detect at an early stage because of their small circumferential extent (typically less than 2.5mm once through-wall). The cross sectional area of the pit can be as low as 1mm^2 once through-wall has been achieved. Tubes are plugged if the through-wall loss is greater than 60% (0.6mm depth in the case of an isolated, 1mm diameter pit in a 1mm wall thickness tube) as there is a high probability that the tube would fail before the next opportunity to inspect the tube. Since tube failure could result in the shutdown of the power station to effect repairs, such defects must be detected with a very high degree of reliability. This was accomplished by analysing the mode conversion, incident mode and the back wall echo signals, which is discussed below.

7.3.1.1 The mode converted signal

The pattern obtained from the reflection of the mode converted signal is recognisable from the incident mode by its out-of-phase component. Figure 5.12 illustrates this for the pit defect. An out-of-phase component (F(1,3) mode) is clearly visible when the defect has reached 40% depth.

The presence of the mode converted signal indicates the presence of a non-axisymmetric defect [82] but in practice, a non-axisymmetric feature other than a defect can also result in an out-of-phase, mode converted signal. This complication can, to a large extent, be overcome by obtaining a baseline measurement to identify all the out-of-phase reflections caused by the design features of the condenser discussed in Chapter 1. Subsequent measurements can then be compared to the baseline to determine if any new mode converted signals are present. Still, new mode converted signals may not be due to defects but instead caused by characteristics that occur during the service life of the condenser, such as surface scale and sagging of the tube plates onto the sag plates (tube support plates). So, while the presence of the mode converted signal exists and can be clearly recognised for pit defects with a depth of 0.4mm, in practice the mode converted signal may increase the probability of a false positive result.

7.3.1.2 The incident signal

The degree to which the incident signal reflected from the defect can be recognised (and hence the degree to which the defect can be detected) can be measured in terms of the concept of SNR. The signal to noise ratio obtained for the pit at 150kHz is given in Table 5.5. The signal to noise ratio for the pit at 0.2mm depth is very low at 1.8dB. It improves marginally to 3.2 at 50% depth but shows a significant improvement at 60% depth with a SNR_{dB} of 5.8dB. The SNR_{dB} was improved by simple signal processing as illustrated in Figure 5.15. A SNR_{db} of 3.3dB for 0.3% wall loss (0.2mm depth) and 10.8dB for 0.9% wall loss (0.6mm depth) could be achieved with this setup.

7.3.1.3 The back wall echo

The concept of the back wall echo in this study is similar to that in the preliminary study. The larger the defect's cross sectional area, the larger the reduction in back wall echo amplitude. The main difference is the extent of the attenuation experienced given the longer tube lengths. Attenuation is discussed later. Furthermore, while the study was based on a pulse-echo arrangement, a pitch catch arrangement can improve the attenuation and provide an alternative signal to that of the back wall namely the transmitted signal. This arrangement warrants further investigation.

7.3.1.4 The effect of frequency variation

The reflection coefficients of the zero order and first order for both the pit and the groove do not show a large degree of dependence on the frequency variation between 120kHz, 135kHz

and 150kHz. The effect of frequency variation is discussed in Section 3.3.2. At these frequencies, the axial extent of the pit and groove defects (a < 2mm) is much less than the L(0,2) wave length (λ = 25mm) i.e. a << λ. So it is not expected for the frequency to have significant effect on the reflection coefficient. This is true in practice for the defects of interest. The effect of frequency on the reflection coefficient increases as defect depth increases and is larger beyond 60% defect depth. One could then argue that the degree of sensitivity of these defects to frequency variation can also provide insight into changes in the defect depth.

7.3.1.5 Attenuation

The high rate of attenuation (up to 3dB/m at 150kHz) experienced is synonymous with copper and brass tubes and will limit the length of tube that can reliably be inspected for pit defects. The problem can be alleviated to some extent by suitable amplification while inspection from both condenser water box ends in a pitch catch arrangement will also improve the situation. The use of even higher centre frequencies to further improve sensitivity and engage higher order flexural modes will further increase attenuation.

7.3.1.6 Visualisation and signal recognition

To the trained eye, the difference between a zero order and a higher order mode may be recognised in an animation of the reflected signal. The laser vibrometer provides such an animation capability and one has also been developed by the author using ***MATLAB***. This provides another tool for defect recognition. The displacement of the transducer, bonded to the edge of the tube, is animated thus providing a visual model of the reflected signals received by the transducer. The code which is used to animate the displacement of the transducer is provided in Appendix A.11.

The mode separation techniques applied by Alleyne et al [21] is also applied to the data obtained in this study. The ability to separate the zero order modes from higher order modes makes pattern recognition significantly easier. This is best illustrated by Figure 5.15 and Figure 5.17. In Figure 5.15, the F(1,3) mode is eliminated by simply adding the signals obtained at each of the 48 nodes. Out-of-phase, flexural modes are therefore eliminated leaving the zero order modes only. This leads to an improvement in the signal-to-noise ratio. In Figure 5.17, the reflection of the first order mode indicated in red is separated from the zero order mode indicated in blue by the techniques discussed in Section 5.3.2.1. The zero order modes and first order modes can therefore be studied separately.

7.3.2 Criteria to distinguish between pits and grooves

There are 3 geometrical differences between pits and grooves that can be used to potentially discriminate between these defects. These are:

- The circumferential extent – The pit defect is typically less than 2mm in diameter (circumferential extent) while the groove can extend to around 150^0 (approximately 30mm). It was found that the F(1,3)/L(0,2) ratio is inversely proportional to the circumferential extent even at small circumferential extents. The groove, with a circumferential extent of 10mm and a F(1,3)/L(0,2) ratio of 0.4 can be distinguished from a pit with circumferential extent of 1mm and a F(1,3)/L(0,2) ratio of 0.7 based on 150kHz.
- The cross sectional area – The groove defect has a large cross section even at small defect depths. It can be assumed that at 30% depth, a groove can have a circumferential extent of atleast 10mm. For such a groove defect, an RC greater than 4% (L(0,2)) and 2% (F(1,3)) was obtained. This is more than three (3) times higher than that for the pit where an RC less than 1% (L(0,2)) and 0.6% (F(1,3)) was obtained for a *through wall defect*. It is possible that in the initiation phase of a grove defect, an RC similar to that displayed by a pit defect could be obtained in which case, a pit can be suspected when in fact a groove is present. In this study, defects with an RC less than 2% (L(0,2)) and 1% (F(1,3)) are identified as pit defects. Similar criteria can be established in practice. This assertion must be viewed with caution as it is based on the comparison of isolated pitting with ammonia grooves. The presence of multiple pits or erosion can dramatically change the RC. Nevertheless, multiple pits and erosion have their own 'signatures' that can potentially be used to distinguish them from isolated pitting. This however is not the subject of this thesis.
- Circumferential location – Ammonia groove defects, by their nature, typically occurs at the top of the tube, on the outside. Pitting on the other hand occurs anywhere around the circumference and on the inside or outside of the tube. The first order mode can be used to reliably determine the plane along which the defect is located. This is then sufficient to determine the location of the groove as it will be on top. Higher order modes are required to determine the location of the pit defect. While possible, it has not been further explored in this thesis. In both cases (pit and groove), the accuracy to which the circumferential location can be measured is dependent on the number of transducers located around the circumference (It is also dependent on the 'engagement'

of the higher order flexural modes). In practical terms, this is a significant challenge given the tube internal diameter.

7.3.3 Defect sizing

One of the primary objectives of inspecting condenser tubes is to determine whether the tube needs to be plugged to prevent tube leaks. The tubes are plugged based on remaining wall thickness; however guided waves cannot determine remaining wall thickness directly. The amplitude of the reflected signal is dependent on the axial extent, circumferential extent and the depth of the defect. Figure 5.23 shows the reflection coefficient of the zero order mode for pit defects. Simplistically, if a reflection coefficient between 0.4% and 0.5% is obtained, then from the graph, 60% through-wall depth has been reached and the tube must be plugged. However this is based on the assumption that the axial extent and circumferential extent of the defect has not changed and the increase in amplitude is brought about by the increase in defect depth only. Now the axial extent of isolated pitting and ammonia grooving should not affect the amplitude of the reflected signal (see Section 7.3.1.4) so this aspect can be ignored. The circumferential extent can be determined from the ratio of the mode converted F(1,3) to L(0,2) reflection [55]. However, this ratio is insensitive to small circumferential extents. Pit defects fall into this category as their circumferential extents is typically less than 4% and is 1.5% in this study (1mm/(22*pi)). Nevertheless, Figure 5.19 suggest that if a region of negligible dispersion is used (L(0,2) at 150kHz) then a reasonable approximation to the circumferential extent can be obtained even at such low circumferential extents. The ratio of F(1,3) to L(0,2) at circumferential extents below 5% warrants further investigation but would require some optimisation of the modelling procedures applied in Chapter 6. Should this be possible, then the approach applied by Demma et al [55] could be applied here with some degree of uncertainty in measurement as in the case of the work done by Demma et al and suggested by Figure 6.9. A specific study is required to determine the degree of uncertainty. It will not be possible to determine defect depth per se but may provide enough insight to categorise the signal response into one of two categories namely, defect > 60% through wall depth or defect < 60% through wall depth.

7.3.4 Limitations

This study is only applicable to isolated pitting and grooving defect types. While it is clear that the amplitude of the reflected signal is sensitive to the cross sectional area of the defect (as opposed to the defect depth, see Figures 5.23 and 5.24), several other parameters also affect the amplitude of the signal. The defect axial extent, the presence of other defects and tube supports amongst others, will affect the amplitude of the reflected signal. Again, many of these

limitations can be overcome by baseline measurements as discussed in 7.3.1.1 but it is important to note that one cannot simply take the reflection coefficient obtained from condenser tubes containing other defect types (e.g erosion or multiple pitting) and compare it to the reflection coefficient graphs obtained in this study. Furthermore, the effect of the condenser design parameters that could affect the guided wave signal (see Section 2.2.1) has not been considered here in this study.

Another important limitation is the high rate of attenuation. The L(0,2) mode has been applied at frequencies above 120kHz as it is increasingly dispersive below 120kHz. The higher frequency however results in a higher attenuation as copper is very attenuative. The length of tube that can be inspected is therefore limited to approximately 2m. Condenser tubes are typically in excess of 6m long although there are many heat exchangers in the power generation industry that have the same copper or brass tubes that have a length of less than 2m. The value of the guided wave however is diminished as its ability to travel over long distances is diminished. Improvements in, for example, signal generation, amplification and the transducers can significantly enhance the propagation distance and also bring about an improvement in signal-to-noise ratio. In practice, the T(0,1) mode can be applied instead of the L(0,2) mode. In this case, the frequency can be reduced until the sensitivity is enough to detect 20% depth pits and F(1,2) and F(2,2) modes are present. This corresponds to a lower limit of approximately 80kHz.

Chapter 8

Conclusions and recommendations

8.1 Introduction

This thesis concerned the detection of defects in plates and tubes using ultrasonic guided waves. Particular emphasis was placed on their application to condenser tubes. It started out by studying the geometry of defects that commonly occur in condenser tubes, and was followed by a study of the theoretical fundamentals of guided waves. A broad literature review was conducted which highlighted some of the important research conducted in this field, but also identified the areas that required further research. Preliminary studies were conducted using basic bulk wave equipment to detect pits and grooves using guided waves. This was followed by the detection of pits and grooves in copper tubes using a laser vibrometer. Finite element modelling using ***ABAQUS*** was then undertaken to confirm the results obtained with the laser vibrometer. Finally, the findings of the preliminary studies using bulk wave equipment and the experimental work conducted using the laser vibrometer were discussed in detail.

This chapter provides the conclusions from the work undertaken in this thesis as well as recommendations for further research.

8.2 Conclusions

The conclusions drawn from the preliminary studies, using basic bulk wave equipment is as follows:

- The repeated group velocity minima of the S_m and A_m modes (m = 1, 2, 3...) in plates can be exploited using basic bulk wave equipment. This method provides good directionality, coherence and sensitivity over distances of approximately 300mm

and a frequency of 4MHz. Defects with a cross sectional area that is less than 0.4mm^2 was detected using this procedure.

- The repeated group velocity minima also exist for the L(0,m) modes for m = 3, 4, 5… in tubes. This can be generated by applying Equation 2.25 to the wedge method described in study 3 (Chapter 4).

- Standard, bulk wave ultrasonic equipment can be used to conduct basic research and study guided waves in plates and tubes. Three studies are conducted which demonstrate the viability of using such equipment.

The conclusions drawn from the experimental results obtained from the interaction of the L(0,2) mode with pits and grooves, measured using the laser vibrometer, are listed below:

- Isolated pit defects with a cross sectional area of 0.2mm^2 representing a wall loss of 0.3% of the tube's cross sectional area can be detected using the L(0,2) mode in copper tubes that are less than 2m long.

- Isolated pits can be distinguished from grooves based on their defect location, magnitude of their reflection coefficients and the ratio of the mode converted, F(1,3) reflection from a defect to that of the L(0,2) mode.

8.3 Recommendations

- The wedge method should be applied to tubes (e.g carbon steel boiler tubes) at frequencies that would exploit the repeated group velocity minima that occur for the L(0,m) modes for m = 3, 4, 5… This method may have the potential to be more reliable in detecting defects such as creep and pitting, common in boiler tubes.

- Further evaluation of the capability of basic bulk wave equipment should be undertaken to detect defects in thin plates. In particular, the use of the 45^0 shear wave transducer to generate S_m and A_m modes (m > 0) to detect various defect types (e.g fatigue) in thin plates can be of great benefit. Thin plate structures are used extensively in, for example, the aircraft industry.

- The capability of guided waves should be investigated to detect real, in-service defects to gain confidence in the reliability of detection. In particular, guided waves status as a screening tool can be further enhanced by gaining confidence in their ability to limit the number of 'false-positives' (a defect is indicated when in fact no defect exist) and 'false-negatives' (a defect exist but is not detected).

- The use of the T(0,1) mode should be investigated as an alternative to the L(0,2) mode at a frequency of 80kHz. The T(0,1) mode is non-dispersive and a lower attenuation (given the lower frequency) should improve propagation distance.

- The finite element model should be refined to make provision for a hole (pit), extended tube length and corrected offset. While this will result in increasing the run-time significantly, benefits can be derived from modelling other common condenser tube defect profiles, for example multiple pitting.

References

[1] **ESKOM research and innovation department**, *"Condenser and cooling system HC forum- condenser failure statistics",* Rosherville*,* 26 August 2010.

[2] **T. Vogt, D. Alleyne and B. Pavlakovic**, "Application of guided wave technology to tube inspection", *Guided Ultrasonics Limited*, Nottingham, United Kingdom, 2006.

[3] **H. Kwun, J. F. Crane, S. Y. Kim, A. J. Parvin and G. M. Light**, "A torsional-mode guided-wave probe for long-range, in-bore heat exchanger tubing inspection", paper presented at *Middle East Non-destructive Testing Conference & Exhibition*, Bahrain, Manama, November 2005.

[4] **Electric Power Research Institute (EPRI)**, Non-destructive evaluation : guided wave ultrasonic technology applications for balance-of-plant heat exchanger tubes and tube support plate degradation, Palo Alto, California: EPRI, 1019138, December 2009.

[5] **S. A. Vinogradov, B. Jacobs and J. Godwin**, "Experimental and theoretical investigation for the use of guided eaves to detect and size corrosion/erosion defects in heat exchanger tubes", *7th EPRI Balance of Plant Heat Exchanger NDE Symposium*, Santa Ana Pueblo, New Mexico, 2002.

[6] **Electric Power Research Institute (EPRI)**, Nondestructive evaluation: Further developments of guided wave examination application - 2009 Status Report, Palo Alto, CA: EPRI, 1019116, 2009.

[7] **J.L. Rose**, "A baseline and vision of ultrasonic guided wave inspection potential", *Journal of pressure vessel technology*, vol. 124, pp. 273 - 282, 2002.

[8] **M. J. S. Lowe and P. Cawley**, "Long range guided wave inspection usage – current commercial capabilities and research directions", *Department of Mechanical Engineering, Imperial College London*, March 2006.

[9] **J. Davies and P. Cawley**, "The application of synthetic focusing for imaging crack-like defects in pipelines using guided waves", *IEEE Transactions on ultrasonics, ferroelectrics, and frequency control*, Vol. 56, No. 4, pp. 759-771, April 2009.

[10] **M. G. Silk and K.F. Bainton**, "The propagation in metal tubing of ultrasonic wave modes equivalent to Lamb waves", *Ultrasonics*, vol. 17, pp. 11-19, 1979.

[11] **Electric Power Research Institute (EPRI)**, "Condenser Application and Maintenance Guide", Palo Alto, 2001.

[12] **B. Buecker***,* "Key condenser failure mechanisms", *Power engineering*, October 2000.

[13] **Metallurgical Consultants,** "Failures of heat exchangers", (Heat exchangers), [online] 2011, http://www.materialsengineer.com/DA-Heat-Exchanger.htm (accessed: 13 April 2011).

[14] **J. Krautkrämer and H. Krautkrämer**, *Ultrasonic testing of materials*, Springer Verlag, 1983.

[15] **J.L. Rose, K. Rajana, and F. T. Carr,** "Ultrasonic Guided Wave Inspection Concepts for Steam Generator Tubing", *Materials Evaluation*, Vol. 52, No. 2, pp 307-311, February 1994.

[16] **D. N. Alleyne, M. J. S Lowe and P. Cawley**, "The reflection of guided waves by a part-circumferential notch in a pipe", *ASME J. Appl. Mech.*, Vol. 65, pp. 649-656, 1998.

[17] **Automated Electronic Solutions (AES)**, "*Tube inspections indications",* AES/TUBE-50-00-06, Rosherville, July 2007.

[18] **ESKOM research and innovation department**, "Lethabo Unit 4: Evaluation of condenser tubes and verification of Eddy Current testing", Rosherville, March 2007.
[19] **ESKOM sustainability and innovation department**, "Tutuka unit 4 BFPT condenser tubes evaluation", Rosherville, March 2010.
[20] **ESKOM research and innovation department**, "Failure investigation of a Matla Unit 1 and 2 condenser tubes", Rosherville, October 2007.
[21] **D. N. Alleyne, M. J. S Lowe and P. Cawley**, "The reflection of guided waves from circumferential notches in pipes", *ASME J. Appl. Mech.*, Vol. 65, pp. 635-641, 1998.
[22] **J.L. Rose**, *Ultrasonic waves in solid media*, Cambridge University Press, 1999.
[23] **J. Cheeke and N. David**, *Fundamentals and applications of ultrasonic waves*, Florida, USA, CRC Press. 2002.
[24] **I.A. Viktorov**, *Rayleigh and lamb waves*, New York: Plenum Press, 1970.
[25] **J. D. Achenbach**, *Wave propagation in elastic solids*, New York, USA, North-Holland, 1984.
[26] **B. A. Auld**, *Acoustic fields and waves in solids*, 2nd ed., Malabar, Florida, John Wiley and sons, 1973. Vol II.
[27] **D. C. Gazis**, "Three-dimensional investigation of the propagation of waves in hollow circular cylinders. I. analytical foundation", *The Journal of the Acoustical Society of America*, Detroit 2, Michigan, Vol 31, No. 5, May 1959.
[28] **Innerspec Technologies**, "Standard equipment for EMAT applications", Lynchburg, USA, 2009.
[29] **M. Ratassepp, M. J. S. Lowe, P. Cawley and A. Klauson**, "Scattering of the fundamental shear horizontal mode in a plate when incident at a through crack aligned in the propagation direction of the mode", *Acoustical Society of America*, Vol. 124, No. 5, pp. 2873-2882, November 2008.
[30] **H. Kwun and S.Y. Kim**, "Magnetostrictive sensor for generating and detecting plate guided waves", *Journal of pressure vessel technology*, vol. 127, pp. 1-6, 2005.
[31] **P. Rajagopal and M. J. S. Lowe**, "Scattering of the fundamental shear horizontal guided wave by a part-thickness crack in an isotropic plate", *Acoustical Society of America*, Vol. 124, No. 5, pp. 2895-2904, November 2008.
[32] **Rayleigh, Lord**, "On waves propagating along the plane surfaces of an elastic solid", Proc. London Math. Soc., 17 pp4-11, 1885.
[33] **Meeker, T.R. and A.H. Meitzler**,. *Guided waves propagation in elongated cylinders and plates*, New York, Academic Press, 1964.
[34] **E. Kreyszig**, *Advanced engineering mathematics, 6th ed*, New York: John Wiley & Sons, 1988.
[35] **The Welding Institute (TWI),** *Wave modes in a pipe* [online image], available:www.twi.co.uk/content/sprgejune07.html [accessed Feb 2010].
[36] **F. Honarvar, E. Enjilela, A. Sinclair**, "An alternative method for plotting dispersion curves", Ultrasonics vol 49 pp 15–18. 2009.
[37] **Y. Kim, S. Song, S. Kwon, Y. Cheong and H. Jung**, "Determination of ultrasonic wave velocities and phase velocity dispersion curves of Inconel 600 plate using resonant ultrasound spectroscopy and leaky lamb waves", *Ultrasonics*, pp. 551-555, 2004.
[38] **T. Hayashi and J.L. Rose**, "Guided wave simulation and visualisation by a semianalytical finite element method", *Materials evaluation*, vol. 423, pp. 75-79, 2002.
[39] **M. J. S. Lowe, B. Pavlakovic, P. Cawley**, "A model for predicting the properties of guided ultrasonic waves and illustrations of its applications to

NDT", New applications in modelling and inversion techniques for non-destructive testing. January 1999. Vol 6. pp 1 -5.

[40] **Instituto de Automática Industrial (CSIC)**, "PCDISP: A tool for the simulation of wave propagation in cylindrical waveguides", paper presented at *9th International Congress on sound and vibration*, Orlando, Florida, July 2002.

[41] **J. L Rose, D Hongerholt and D. J James**, "Laser based, guided wave experiments for tubing.", Materials evaluation, pp 165-168 vol 37, June 1997.

[42] **T. H. Lee, I. H Choi and K. Y. Jhang**, "Single-mode guided wave technique using ring-arrayed laser beam for thin-tube inspection", *NDT&E International*, Vol. 41, pp. 632-637, 2008.

[43] **American Piezo Company (APC) International,** "Piezo theory", (knowledge centre), [online] 2011, http://www.americanpiezo.com/knowledge-centre.html (accessed: 12 February 2011).

[44] **J. J. Ditri, J. L. Rose and G. Chen**, "Mode Selection Criteria for Defect Optimization using Lamb Waves", ", Review of progress in Quantitative NDE volume 11,Edited by D.O. Thompson and D.E. Chimenti, Plenum Press, 1992, pp. 2109-2115

[45] **D. C. Worlton**, "*Method of applying lamb waves in ultrasonic testing*", U.S. Patent 3165922, January 1965.

[46] **F. A. Firestone**, "*Methods and means for generating and utilising vibrational waves in plates*", U.S. Patent 2536128, May 1951.

[47] **J. Li and J. L. Rose**, "Excitation and propagation of non-axisymmetric guided waves in a hollow cylinder", *Acoustical Society of America*, Vol. 109, No. 2, August 2000.

[48] **H. J. Shin and J.L. Rose**, "Guided wave tuning principles for defect detection in tubing", *Journal of nondestructive evaluation*, vol. 17 (1), pp. 27-36, 1998.

[49] **X. Zhao and L. Rose**, "Guided circumferential shear horizontal waves in an isotropic hollow cylinder", *Acoustical Society of America*, vol. 115(5), pp. 1912-1916, 2004.

[50] **K. Jezzine and A. Lhemery**, "Simulation of guided wave inspection based on the recprocity principle and the semi- analytical finite element method", *American Institute of Physics*, vol. 26, pp. 39-46, 2007.

[51] **J.K. Van Velsor, J.L. Rose, J.B. Nestleroth and S.E. Owens**, "Coating disbond detection in pipe using circumferentially-oriented ultrasonic guided waves", paper presented at *4th Middle East NDT Conference and Exhibition*, Kingdom of Bahrain, December 2007.

[52] **V. N. Shah, K. L. Murty F. M. Haggag, P. E. MacDonald, P.Q. Miraglia, M. D. Mathew, D. W. Akers, and C. Sellers**, "Aging management of major LWR components with non-destructive evaluation", *6th International Conference on Nuclear Engineering*, Idaho Falls, May 1998.

[53] **Mohammad Ismail Al-Ammandi,** "Long range ultrasonic inspection (Guided wave UT), An end user's view", *Middle East Nondestructive Testing Conference & Exhibition*, Bahrain, Manama, 30 Nov 2005.

[54] **K. Edalati, A. Kermani, B. Naderi and B. Panahi**, "Defects evaluation in lamb wave testing of thin plates", paper presented at *Middle East Non-destructive Testing Conference & Exhibition*, Bahrain, Manama, www.ndt.net, November 2005.

[55] **A. Demma, P. Cawley, M. Lowe, A.G. Roosenbrand and B. Pavlakovic**, "The reflection of guided waves from notches in pipes: a guide for interpreting corrosion measurements", *NDT&E International*, Vol. 37, pp. 167-180, 2004.

[56] **W. Mohr and P. Höller**, "On inspection of thin-walled tubes for transverse and longitudinal flaws by guided ultrasonic waves", *IEEE Transactions on sonics and ultrasonics*, Vol. SU-23, No. 5, pp. 369-374, September 1976.

[57] **H. Lamb**, "On waves in an elstic plate", *Proceedings of the Royal Society*, A93, pp. 114-128, 1917.

[58] **L. Pochhammer**, "Uber die fortpflanzungsgeschwindigkeiten kleiner schwingugen in einem unbegrenzten isotropen kreiscylinder", *J. Math*. Vol 81, pp. 324–336, 1876.

[59] **J. W. S Rayleigh**, "On waves propagated along the plane surface of an elastic solid", *Proceedings of the London Math. Society*, London, 1885.

[60] **F. A. Firestone**, "*Surface and shear wave method and apparatus*", U.S. Patent 2439130, April 1948.

[61] **Potto Project,** *Lord Rayleigh* [online image], available: http://www.potto.org/gasDynamics/node56.html [accessed June 2010].

[62] **Encyclopaedia Britannica online,** *Sir Horace Lamb* [online image], available: http://www.britannica.com/EBchecked/media/29924/Sir-Horace-Lamb [accessed June 2010].

[63] **D.C. Worlton et al**, "*Ultrasonic method of measuring thickness using lamb waves*", U.S. Patent 3120120, February 1964.

[64] **K. F. Graff**, "Wave motion in elastic solids", New York, Dover Publications, 1975.

[65] **Imperial College London,** *Professor Peter Cawley* [online image], available: http://www3.imperial.ac.uk/engineering/research/impact/casestudies/peter cawley [accessed March 2011].

[66] **Pennsylvania State University (PSUltrasonics),** *Professor Joseph Rose* [online image], available: http://www.esm.psu.edu/ultrasonics/rosecontact.html [accessed March 2011].

[67] **D. Alleyne and P. Cawley**, "A two-dimensional fourier transform method for the measurement of propagating multimode signals", *Department of mechanical engineering*, Imperial College, London, SW72BX, England, September 1990.

[68] **M. J. S. Lowe,** " Matrix techniques for modelling ultrasonic guided waves in multilayered media, " IEEE transactions on Ultrasonics, ferroelectrics, and frequency control, vol. 42, No. 4, July 1995.

[69] **R. Sanderson, P. Catton and D. Liaptsis**, "Innovative techniques for sizing locally thinned areas in straight pipes and for inspection beyond pipe bends using guided waves", TWI Ltd, Granta Park, Great Abington Cambridge, United Kingdom, 2008.

[70] **H. Kwun and A. E. Holt**, "Feasibility of under-lagging corrosion detection in steel pipe using the magnetostrictive sensor technique", *NDT&E International*, Vol. 28, No. 4, pp. 211-214, 1995.

[71] **T. Hayashi, W Song, J. L. Rose**, "Guided wave dispersion curves for a bar with an arbitrary cross-section, a rod and rail example", *Ultrasonics,* vol. 41, pp. 175–183, 2003.

[72] **P. W. Loveday**, "Simulation of Piezoelectric excitation of guided waves using waveguide finite elements", *IEEE trans. on ultr., ferroelect., and freq. control*, vol. 55, pp. 2038-2045, September 2008.

[73] **J. L. Rose, Y. Cho and M. J. Avioli**, "Next generation guided wave health monitoring for long range inspection of pipes", *Journal of loss prevention in the process industries*, vol. 22, pp. 1010-1015, 2009.

[74] **R. Gangadharan, C. R. L. Murthy, S. Gopalakrishnan and M. R. Bhat**, "Time reversal technique for health monitoring of metallic structure using lamb waves", *Ultrasonics*, Vol. 49, pp. 696-705, 2009.

[75] **T.Hayashi and M Murase**, "Mode extraction technique for guided waves in a pipe", *Nondestructive testing and evaluation,* vol. 1, pp. 63-75, March 2005.

[76] **R. Sicard, J. Martel and H. Serhan**, "Defect detection and imaging from phased array focussing of ultrasonic guided waves", *National Conference of NDT*, Canada, www.ndt.net, [accessed 22 December 2009], August 2009.

[77] **D.N. Alleyne**, "The nondestructive testing of plates using ultrasonic lamb waves", *PhD thesis*, University of London, 1991.

[78] **T. Ghosh, T. Kundu and P. Karpur**, "Efficient use of lamb modes for detecting defects in large plates", *Ultrasonics*, Vol. 36, pp. 791-801, 1998.

[79] **H.D. Jeong, H.J. Shin and J.L. Rose**, "Detection of defects in a thin plate using ultrasonic guided wave", paper presented at *15th World conference on NDT*, Rome, October 2000.

[80] **O. Diligent, T. Grahn, A. Boström, P. Cawley and M. J. S. Lowe**, "The low-frequency reflection and scattering of the S_0 Lamb mode from a circular through-thickness hole in a plate: Finite Element, analytical and experimental studies", *Acoustical Society of America*, Vol. 112, No. 6. pp. 2589-2601, December 2002.

[81] **P. Cawley, M. J. S. Lowe, F. Simonetti, C. Chevalier and A. G. Roosenbrand**, "The variation of the reflection coefficient of extensional guided waves in pipes from defects as a function of defect depth, axial extent, circumferential extent and frequency", Vol. 216, Part C, pp. 1131-1143, 2002.

[82] **J. J. Ditri**, "Utilization of guided elastic waves for the characterization of circumferential cracks in hollow cylinders", *Acoustical Society of America*, Philadelphia, Pennsylvania, Vol. 96, No. 6, pp. 3769-3775, December 1994.

[83] **F.C.R. Marques and A. Demma**, "Ultrasonic guided waves evaluation of trials for pipeline inspection", paper presented at *17th world conference on NDT*, Shanghai, October 2008.

[84] **S. Izadpanah, G.R. Rashed and S. Sodagar**, "Using ultrasonic guided wave in evaluation of pipes", paper presented at *2nd International Conference on technical inspection and NDT*, Tehran, Iran, October 2008.

[85] **R. Grimberg**, "Electromagnetic nondestructive evaluation: present and future", *The 10th International conference of the Slovenian Society for Non-destructive testing*, Ljubljana, Slovenia, September 2009.

[86] **D. H. Hur, M. S. Choi, D. H. Lee, S. J. Kim and J.H. Han**, "A case study on detection and sizing of defects in steam generator tubes using eddy current testing", *Nuclear engineering and design*, vol. 240, pp. 204-208, 2010.

[87] **Guided NDE LLC,** "Baseline inspection of heat exchanger tubing using guided waves and magnetostrictive sensor technology", www.guided-nde.com**,** [accessed 12 October 2010].

[88] **Guided Wave Analysis LLC,** *MsSR 3030 system* [online image], available: http://www.gwanalysis.com/specifications.html [accessed October 2010].

[89] **The Welding Institute (TWI),** *Teletest Focus flaw detector* [online image], available: http://www.twi.co.uk/content/c1443.html [accessed October 2010].

[90] **Guided Ultrasonics Limited,** *Wavemaker G3 inspection system* [online image], available: http://www.guided-ultrasonics.com [accessed October 2010].

[91] **P. W. Loveday**, "Development of piezoelectric transducers for a railway integrity monitoring system", S*mart Systems for Bridges, Structures and Highways, Proceedings of SPIE,* Vol. 3988, pp. 330-338, 2000.

[92] **NDT Resource Centre,** "Signal-to-Noise Ratio", (Ultrasound) [online], http://www.ndt-ed.org/EducationResources/CommunityCollege/ Ultrasonics/Physics/signaltonoise.htm (accessed: 13 April 2010).

[93] **W. Zhu**, "An FEM simulation for guided elastic wave generation and reflection in hollow cylinders", *ASME J of Pressure vessel technology*, vol. 124, pp. 108-117, 2002.

[94] **Krautkramer,** *USN 52R/USN 52L technical reference and operating manual***,** ident No. 28642**,** March 1999**.**

[95] **GE sensing and Inspection technologies**, *Ultrasonic transducers for flaw detection and sizing*, GEIT-20117EN, April 2008.

[96] **The American Society for Nondestructive Testing (ASNT)**, *Nondestructive testing handbook*, Columbus, Ohio, ASNT Inc, 1959.

Appendices

A.1 Material properties and relevant equations [96]

$$\nu = \frac{E}{2G} - 1$$

$$C_L = \sqrt{\frac{E(1-\nu)}{\rho(1+\nu)(1-2\nu)}}$$

$$C_T = \sqrt{\frac{G}{\rho}}$$

$$C_0 = \sqrt{\frac{E}{\rho}}$$

A.2 Drawing of mild steel plate test samples (grooves)

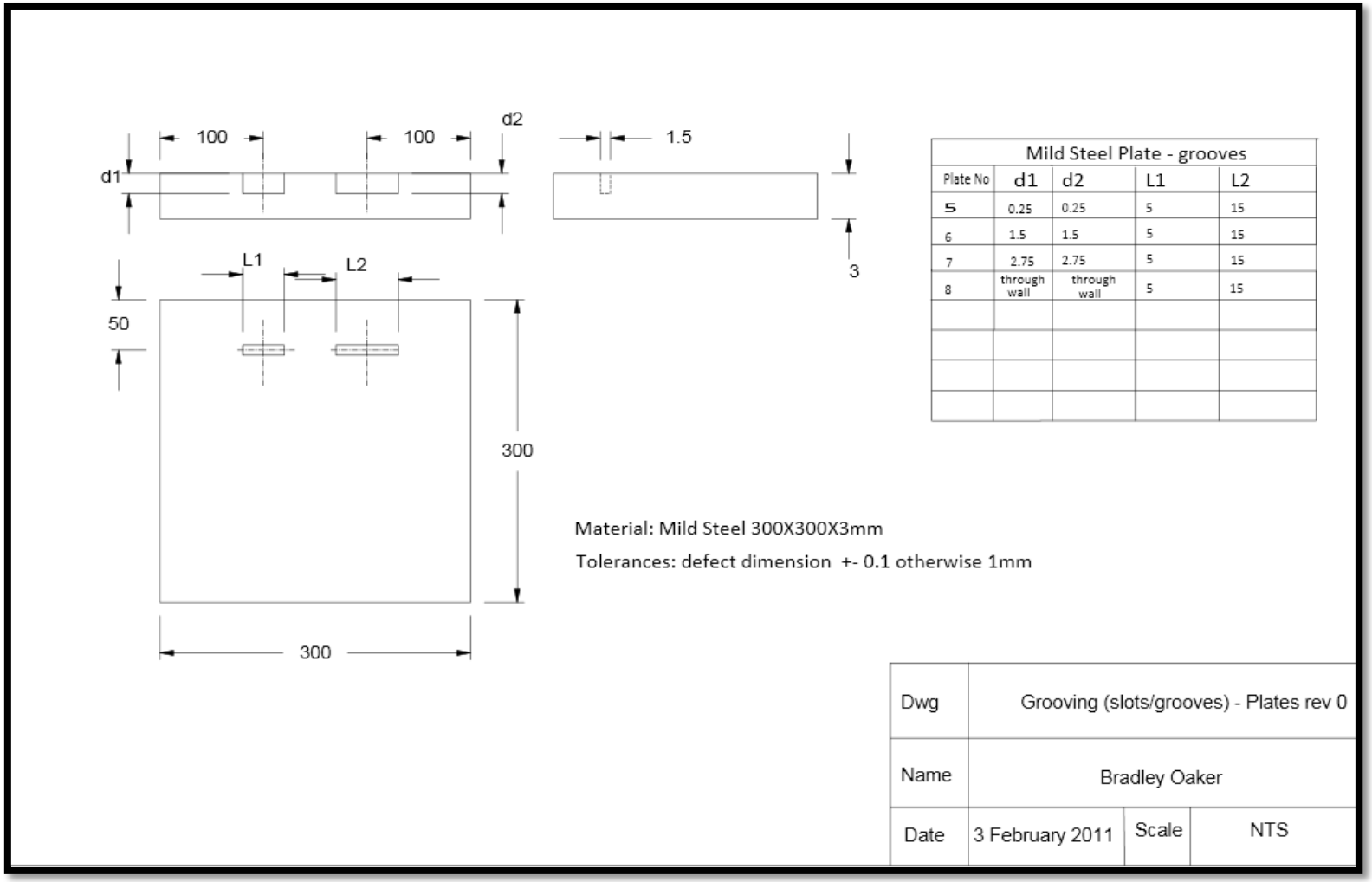

Mild Steel Plate - grooves				
Plate No	d1	d2	L1	L2
5	0.25	0.25	5	15
6	1.5	1.5	5	15
7	2.75	2.75	5	15
8	through wall	through wall	5	15

A.3 Drawing of mild steel plate test samples (pits)

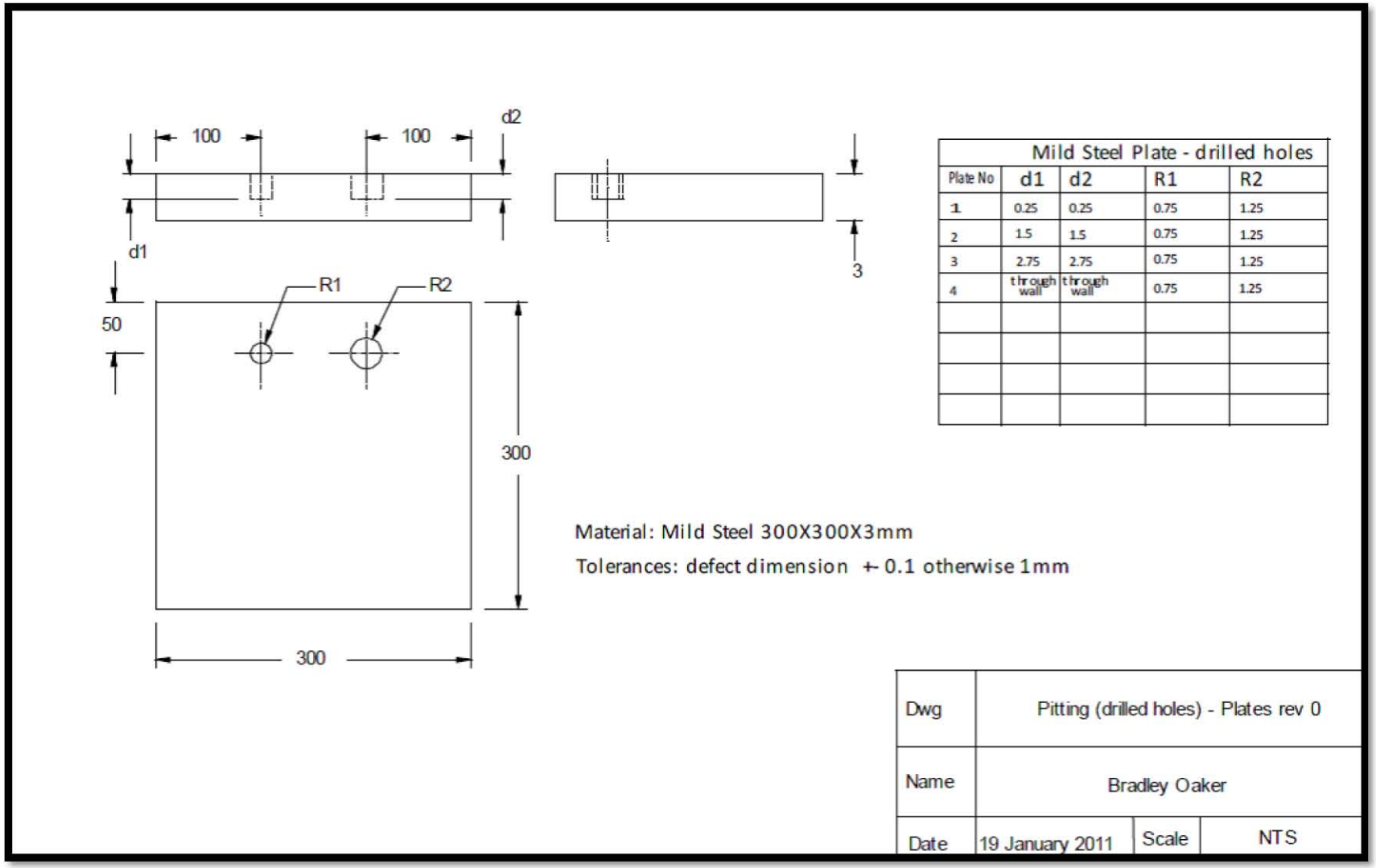

Mild Steel Plate - drilled holes				
Plate No	d1	d2	R1	R2
1	0.25	0.25	0.75	1.25
2	1.5	1.5	0.75	1.25
3	2.75	2.75	0.75	1.25
4	through wall	through wall	0.75	1.25

A.4 Drawing of copper tube test samples (grooves)

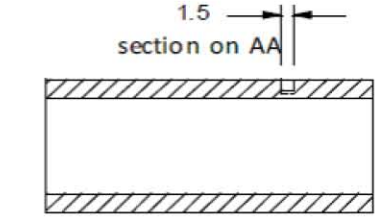

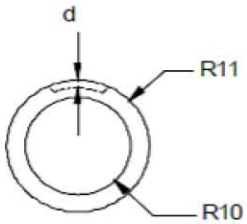

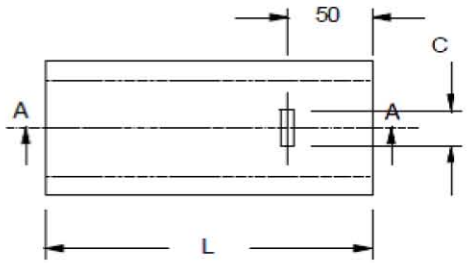

Copper tube - grooves				
Tube No	d	C	L	Quantity
9	0.25	10	800	1
10	0.5	10	800	1
11	0.75	10	800	1
12	through wall	10	800	1
13	0.25	20	800	1
14	0.5	20	800	1
15	0.75	20	800	1
16	through wall	20	800	1
17	0.5	70 (full circle)	800	1

Material: copper tube 22mm outer diameter, 0.9mm thick.
Tolerances: defect dimension +- 0.1 otherwise 1mm

Dwg	Grooving (slotted grooves) - tubes rev 0		
Name	Bradley Oaker		
Date	19 January 2011	Scale	NTS

A.5 Drawing of copper tube test samples (pits)

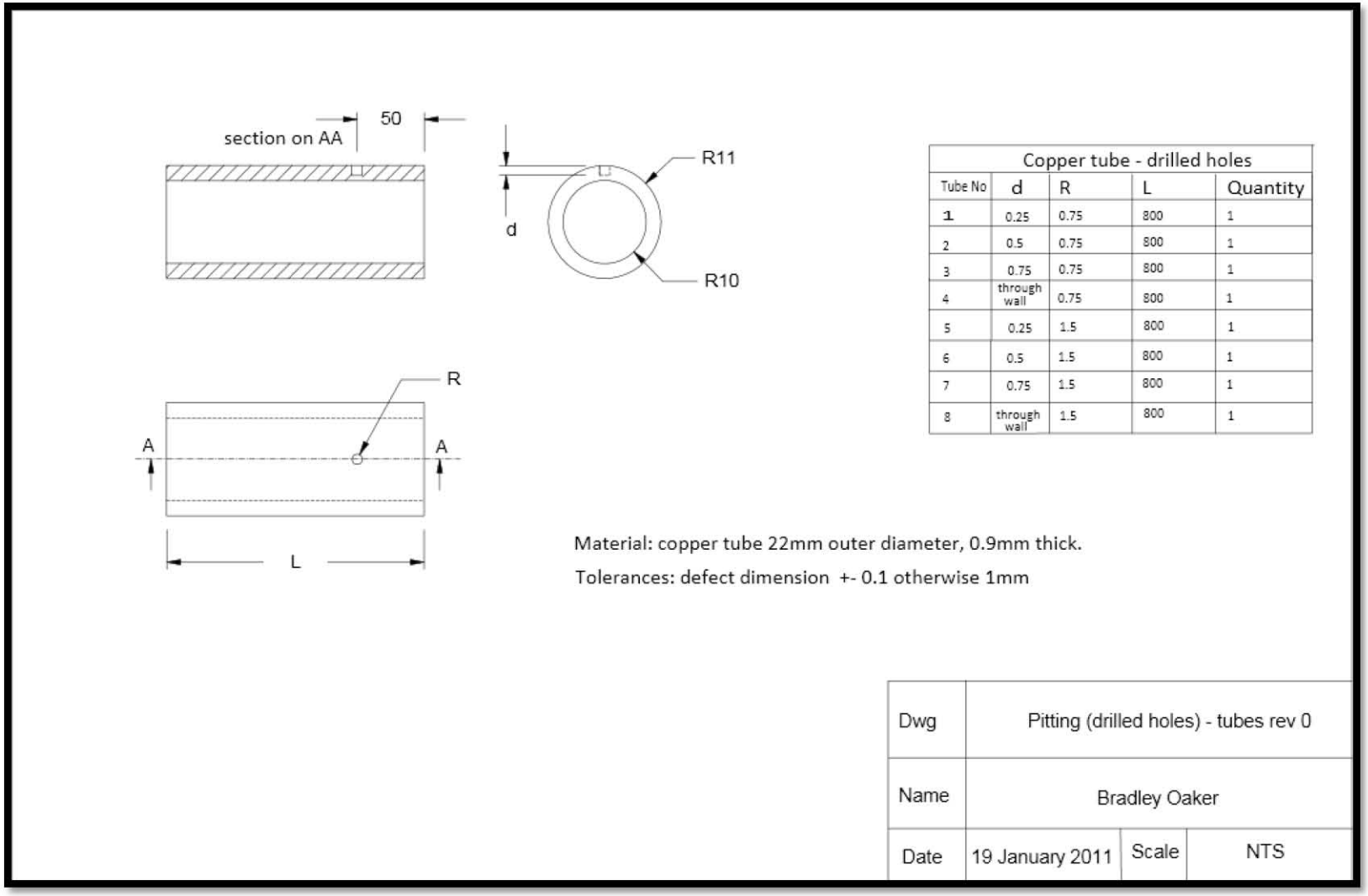

Copper tube - drilled holes				
Tube No	d	R	L	Quantity
1	0.25	0.75	800	1
2	0.5	0.75	800	1
3	0.75	0.75	800	1
4	through wall	0.75	800	1
5	0.25	1.5	800	1
6	0.5	1.5	800	1
7	0.75	1.5	800	1
8	through wall	1.5	800	1

Material: copper tube 22mm outer diameter, 0.9mm thick.

Tolerances: defect dimension +- 0.1 otherwise 1mm

Dwg	Pitting (drilled holes) - tubes rev 0		
Name	Bradley Oaker		
Date	19 January 2011	Scale	NTS

A.6 Drawing of 1.8m long copper tube test samples (grooves)

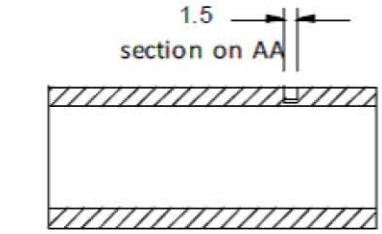

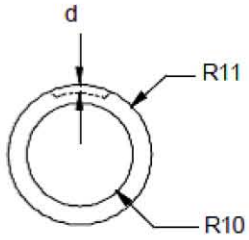

Copper tube - grooves				
defect No	d	C	L	Quantity
7	0.3	10	1800	
8	0.5	10	1800	
9	0.8	10	1800	
10	Through wall	10	1800	

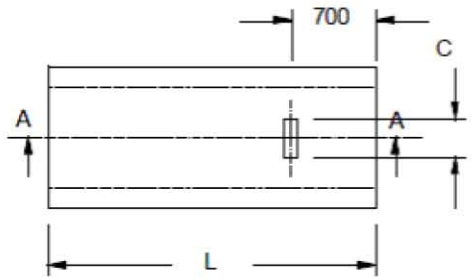

Material: copper tube 22mm outer diameter, 1mm thick.

Tolerances: defect dimension +- 0.01 otherwise 1mm

Dwg	Grooving (slotted grooves) - tubes rev 0		
Name	Bradley Oaker		
Date	19 January 2011	Scale	NTS

A.7 Drawing of 1.8m long copper tube test samples (pits)

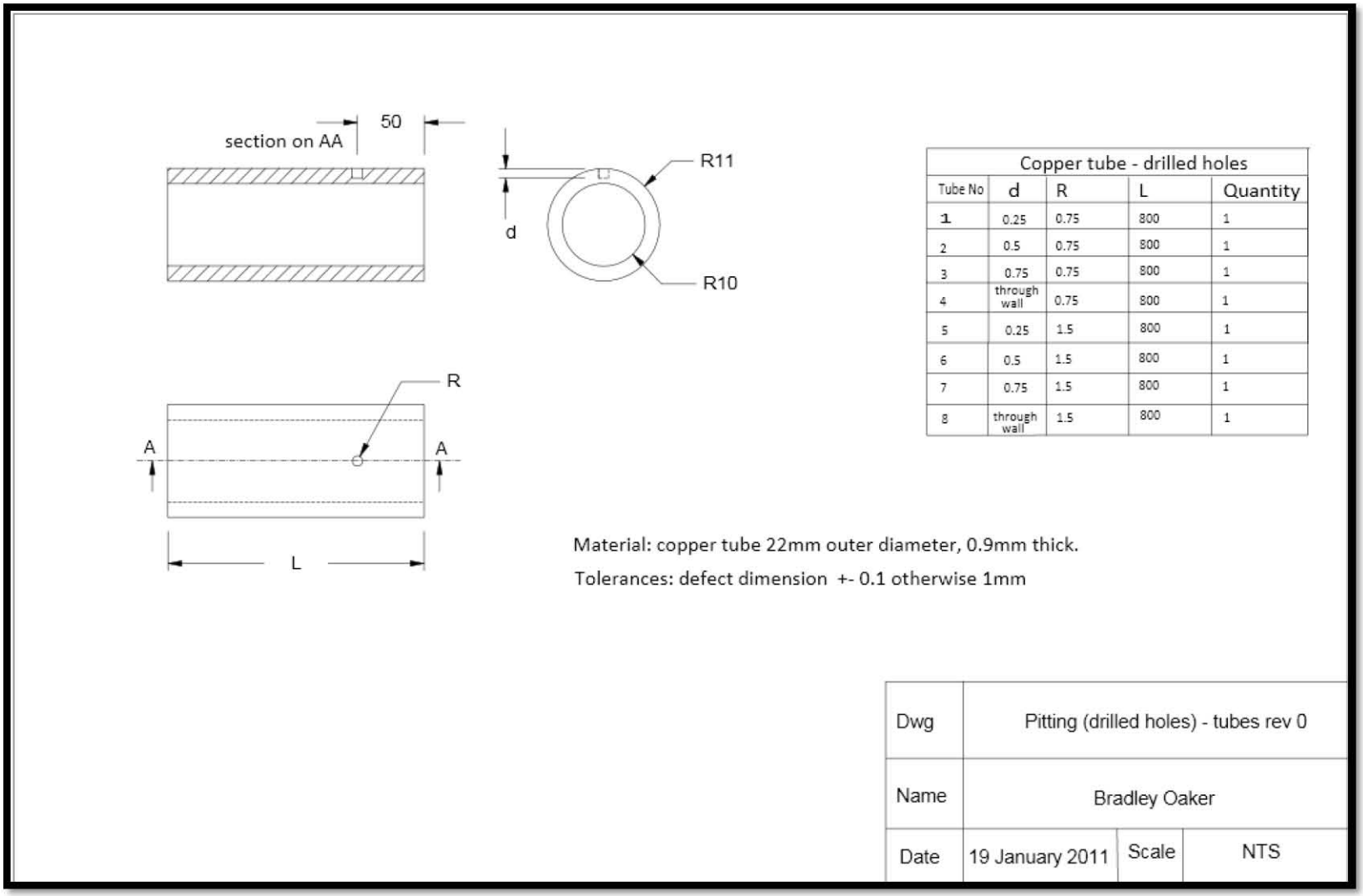

Copper tube - drilled holes				
Tube No	d	R	L	Quantity
1	0.25	0.75	800	1
2	0.5	0.75	800	1
3	0.75	0.75	800	1
4	through wall	0.75	800	1
5	0.25	1.5	800	1
6	0.5	1.5	800	1
7	0.75	1.5	800	1
8	through wall	1.5	800	1

Material: copper tube 22mm outer diameter, 0.9mm thick.

Tolerances: defect dimension +- 0.1 otherwise 1mm

Dwg	Pitting (drilled holes) - tubes rev 0		
Name	Bradley Oaker		
Date	19 January 2011	Scale	NTS

A.8 Calculated values for the L(0,2) mode for tube 22 (pits)

Frequency				**T22, 120KHz**			
depth (mm)	0%	20%	40%	50%	60%	80%	100%
Max Input (m)	4.08E-06	5.25E-06	3.89E-06	3.90E-06	3.89E-06	3.68E-06	3.71E-06
Initial Input time (s) T_i	8.67E-05	9.10E-05	8.67E-05	8.67E-05	8.67E-05	8.67E-05	8.67E-05
Max Backwall (m)	1.53E-06	1.14E-06	1.43E-06	1.43E-06	1.43E-06	1.28E-06	1.31E-06
BW Actual RC at 120KHz		74.4%	93.7%	93.7%	93.7%	83.8%	85.7%
Backwall time T_{BW}	1.02E-03	1.01E-03	1.02E-03	1.02E-03	1.02E-03	1.02E-03	1.02E-03
Velcocity (m/s) C_{mode}	3866	3930	3866	3866	3866	3866	3866
Average velocity C_{mode}				3875			
$C_{L(0,2)}$ (m/s)				3825			
Difference (m/s)				50			
Frequency				**T22, 135KHz**			
depth (mm)	0%	20%	40%	50%	60%	80%	100%
Max Input (m)	5.10E-06	4.68E-06	4.88E-06	4.87E-06	4.91E-06	4.57E-06	4.59E-06
Initial Input time (s) T_i	8.91E-05	8.91E-05	8.91E-05	8.91E-05	8.91E-05	8.91E-05	8.91E-05
Max Backwall (m)	1.73E-06	1.41E-06	1.54E-06	1.53E-06	1.55E-06	1.42E-06	1.45E-06
BW Actual RC at 135KHz		81.3%	88.8%	88.4%	89.4%	82.1%	84.1%
Backwall time T_{BW}	1.01E-03	1.01E-03	1.01E-03	1.01E-03	1.01E-03	1.01E-03	1.01E-03
Velcocity (m/s) C_{mode}	3913	3918	3918	3918	3918	3918	3918
Average velocity C_{mode}				3917			
$C_{L(0,2)}$ (m/s)				3862			
Difference (m/s)				55			
Frequency				**T22, 150KHz**			
depth (mm)	0%	20%	40%	50%	60%	80%	100%
Max Input (m)	4.77E-06	5.21E-06	5.37E-06	5.37E-06	5.42E-06	5.02E-06	5.04E-06
Initial Input time (s) T_i	8.95E-05	9.10E-05	9.10E-05	9.10E-05	8.79E-05	9.10E-05	9.10E-05
Max Backwall (m)	1.68E-06	1.13E-06	1.29E-06	1.29E-06	1.33E-06	1.22E-06	1.26E-06
BW Actual RC at 150KHz		67.0%	76.8%	76.8%	78.8%	72.5%	74.9%
Backwall time T_{BW}	1.01E-03	1.01E-03	1.01E-03	1.01E-03	1.01E-03	1.01E-03	1.01E-03
Velcocity (m/s) C_{mode}	3898	3930	3930	3930	3917	3930	3930
Average velocity C_{mode}				3924			
$C_{L(0,2)}$ (m/s)				3881			
Difference (m/s)				43			

A.9 Calculated values for the L(0,2) mode for tube 23 (grooves)

Frequency	**T23, 120KHz**				
depth (mm)	0%	30%	50%	80%	100%
Max Input (m)	1.08E-05		1.12E-05	1.10E-05	1.11E-05
Initial Input time (s) T_i	9.18E-05		9.61E-05	9.18E-05	9.61E-05
Max Backwall (m)	1.49E-06		1.44E-06	9.88E-07	9.82E-07
BW Actual RC at 120KHz	100.0%		96.3%	66.3%	65.9%
Backwall time T_{BW} (s)	1.03E-03		1.03E-03	1.03E-03	1.03E-03
Velcocity (m/s) C_{mode}	3837		3855	3854	3855
Average velocity C_{mode}	3850				
$C_{L(0,2)}$ (m/s)	3825				
Difference (m/s)	25				
Frequency	**T23, 135KHz**				
depth (mm)	0%	30%	50%	80%	100%
Max Input (m)	9.77E-06	9.50E-06	9.85E-06	9.42E-06	9.79E-06
Initial Input time (s) T_i	9.02E-05	9.02E-05	9.02E-05	9.02E-05	9.41E-05
Max Backwall (m)	1.02E-06	1.00E-06	9.69E-07	6.85E-07	6.74E-07
BW Actual RC at 135KHz	100.0%	98.2%	95.1%	67.2%	66.1%
Backwall time T_{BW} (s)	1.02E-03	1.02E-03	1.03E-03	1.02E-03	1.02E-03
Velcocity (m/s) C_{mode}	3855	3872	3851	3872	3888
Average velocity C_{mode}	3868				
$C_{L(0,2)}$ (m/s)	3862				
Difference (m/s)	6				
Frequency	**T23, 150KHz**				
depth (mm)	0%	30%	50%	80%	100%
Max Input (m)	7.41E-06	6.99E-06	7.45E-06	6.86E-06	7.32E-06
Initial Input time (s) T_i	8.91E-05	8.91E-05	8.91E-05	8.91E-05	8.91E-05
Max Backwall (m)	6.08E-07	5.59E-07	5.48E-07	3.76E-07	3.80E-07
BW Actual RC at 150KHz	100.0%	92.0%	90.2%	61.8%	62.6%
Backwall time T_{BW}	1.02E-03	1.01E-03	1.02E-03	1.01E-03	1.02E-03
Velcocity (m/s) C_{mode}	3871	3905	3871	3905	3871
Average velocity C_{mode}	3885				
$C_{L(0,2)}$ (m/s)	3881				
Difference (m/s)	4				

A.10 Plots of experimental results

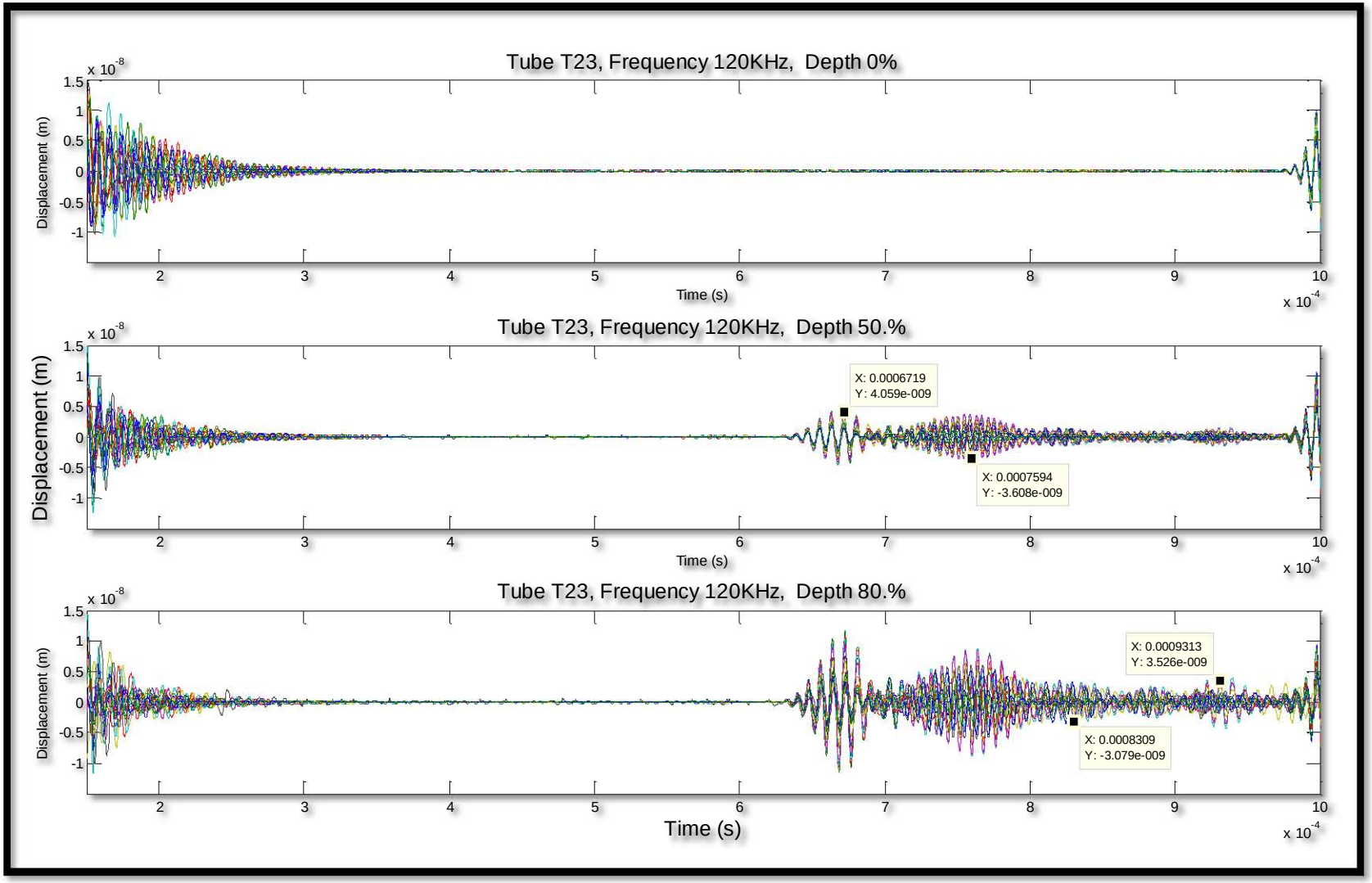

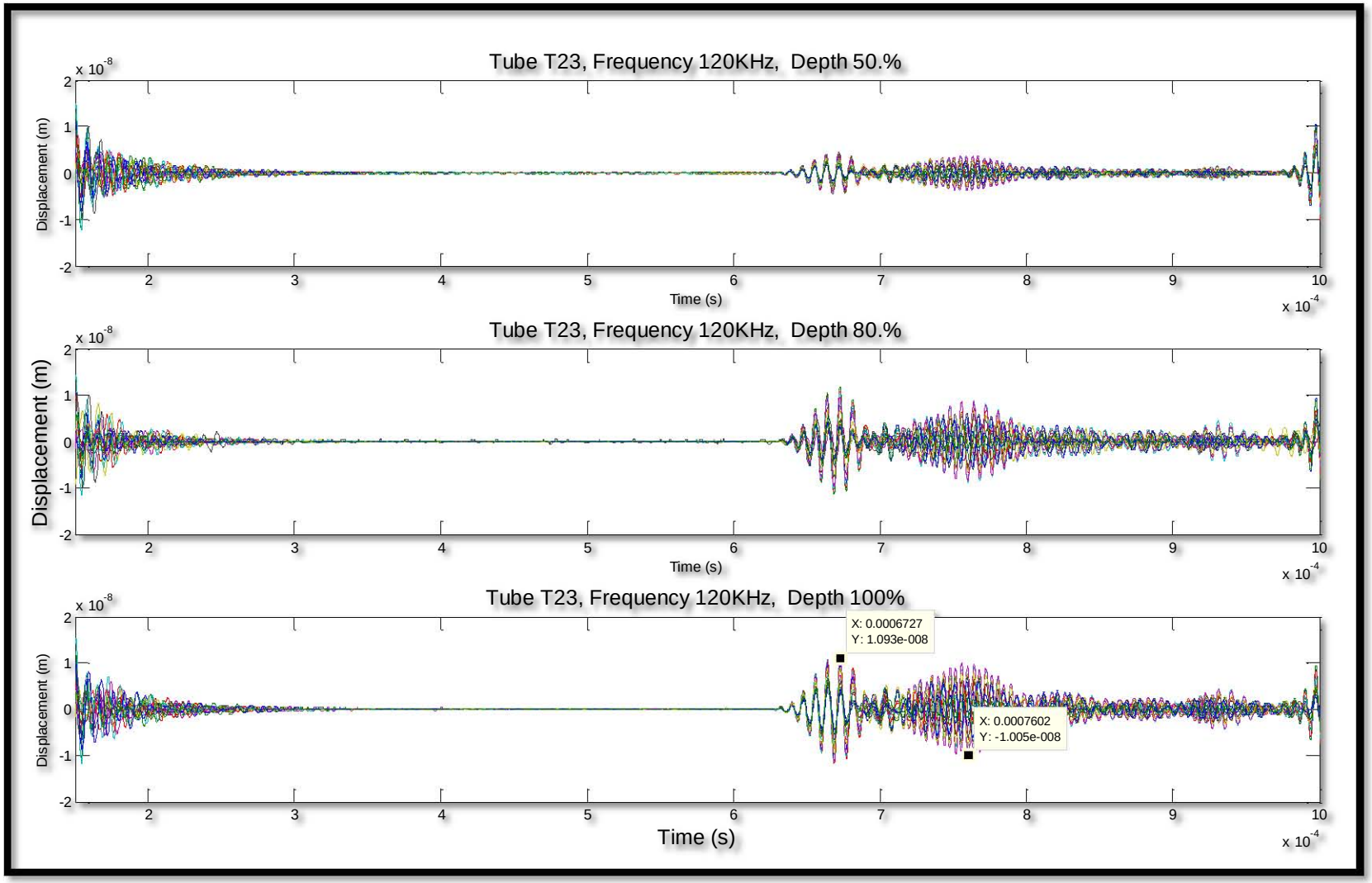
Tube T23, Frequency 120KHz, Depth 50.%
x 10^-8
Displacement (m)
Time (s)
x 10^-4
Tube T23, Frequency 120KHz, Depth 80.%
x 10^-8
Displacement (m)
Time (s)
x 10^-4
Tube T23, Frequency 120KHz, Depth 100%
x 10^-8
X: 0.0006727
Y: 1.093e-008
X: 0.0007602
Y: -1.005e-008
Displacement (m)
Time (s)
x 10^-4

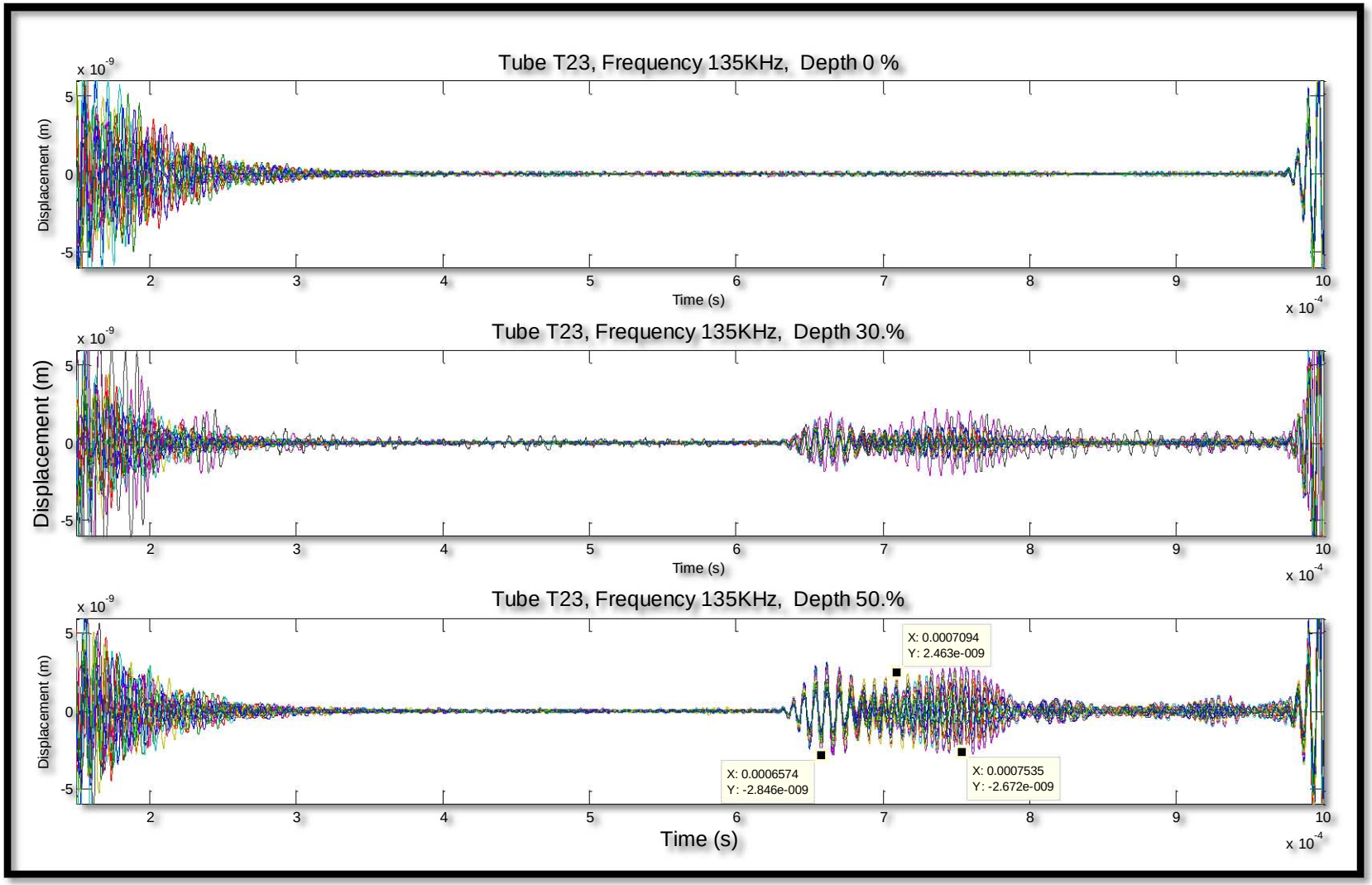
Tube T23, Frequency 135KHz, Depth 0 %
x 10^-9
Displacement (m)
Time (s)
x 10^-4
Tube T23, Frequency 135KHz, Depth 30.%
Tube T23, Frequency 135KHz, Depth 50.%
X: 0.0007094
Y: 2.463e-009
X: 0.0006574
Y: -2.846e-009
X: 0.0007535
Y: -2.672e-009

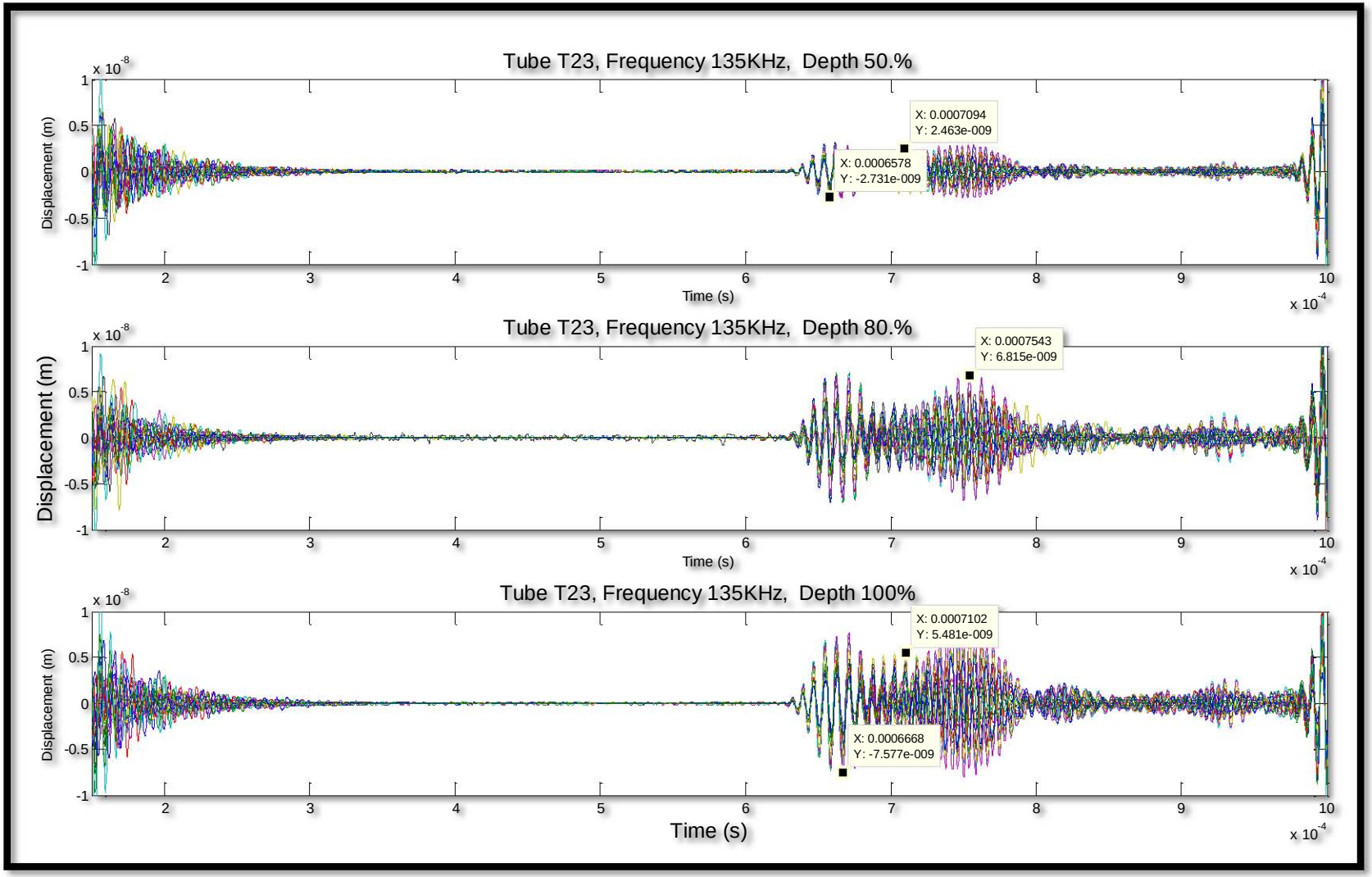
Tube T23, Frequency 135KHz, Depth 50.%
x 10^-8
Displacement (m)
X: 0.0007094
Y: 2.463e-009
X: 0.0006578
Y: -2.731e-009
Time (s)
x 10^-4
Tube T23, Frequency 135KHz, Depth 80.%
X: 0.0007543
Y: 6.815e-009
Tube T23, Frequency 135KHz, Depth 100%
X: 0.0007102
Y: 5.481e-009
X: 0.0006668
Y: -7.577e-009

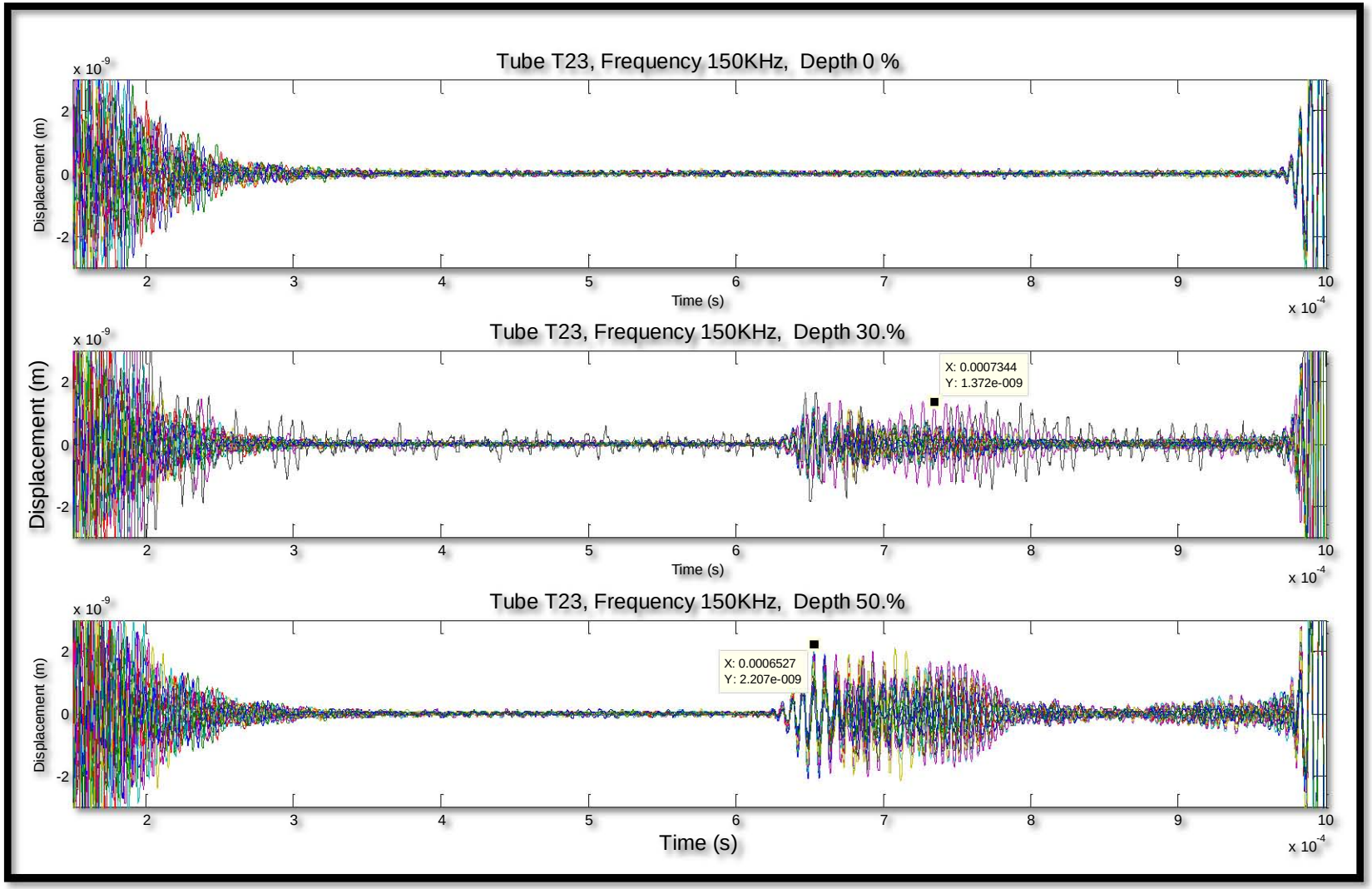
Tube T23, Frequency 150KHz, Depth 0 %
x 10^-9
Displacement (m)
Time (s)
x 10^-4
Tube T23, Frequency 150KHz, Depth 30.%
X: 0.0007344
Y: 1.372e-009
Tube T23, Frequency 150KHz, Depth 50.%
X: 0.0006527
Y: 2.207e-009

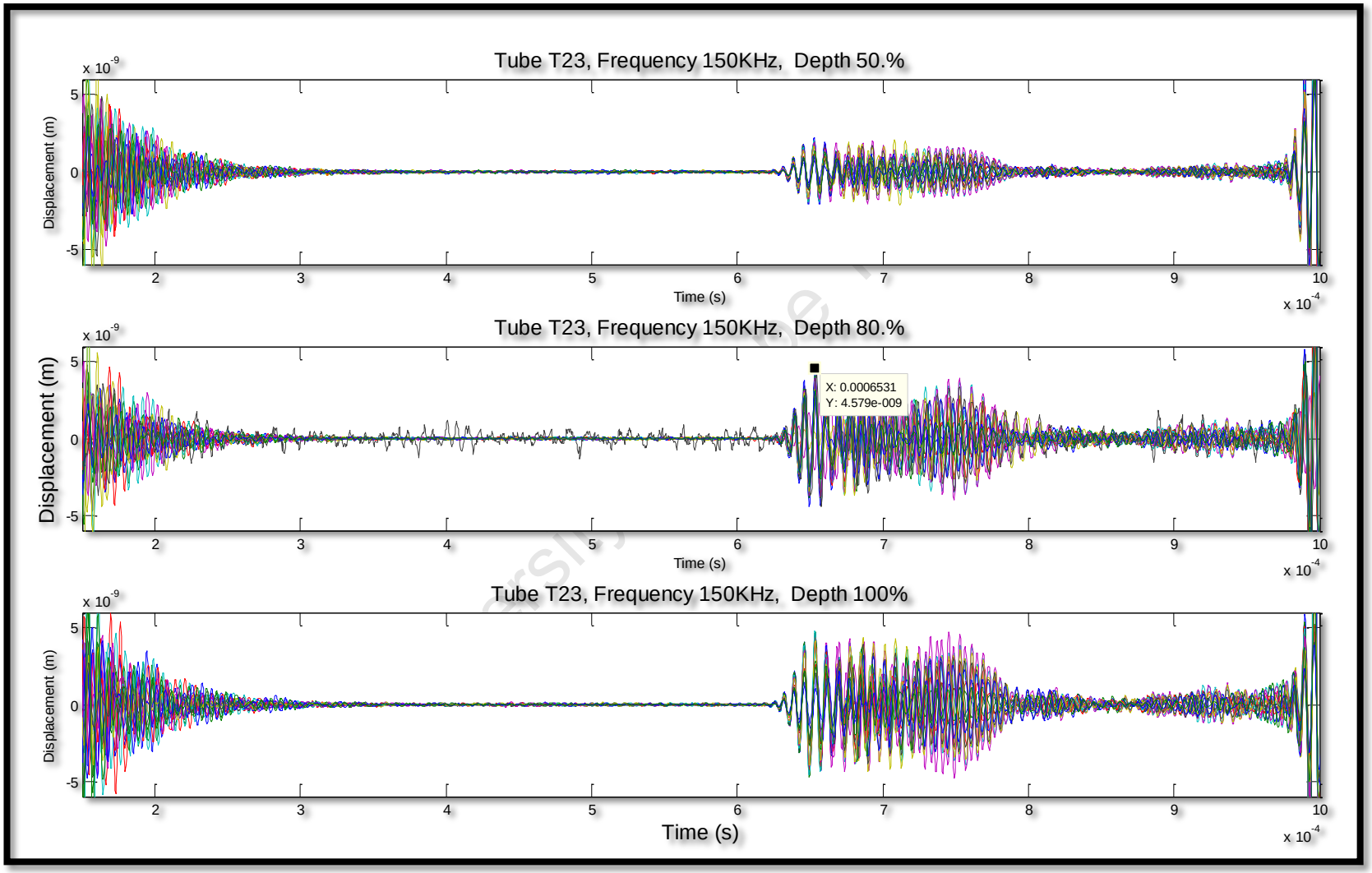
Tube T23, Frequency 150KHz, Depth 50.%
x 10^-9
Displacement (m)
Time (s)
x 10^-4
Tube T23, Frequency 150KHz, Depth 80.%
X: 0.0006531
Y: 4.579e-009
Tube T23, Frequency 150KHz, Depth 100%

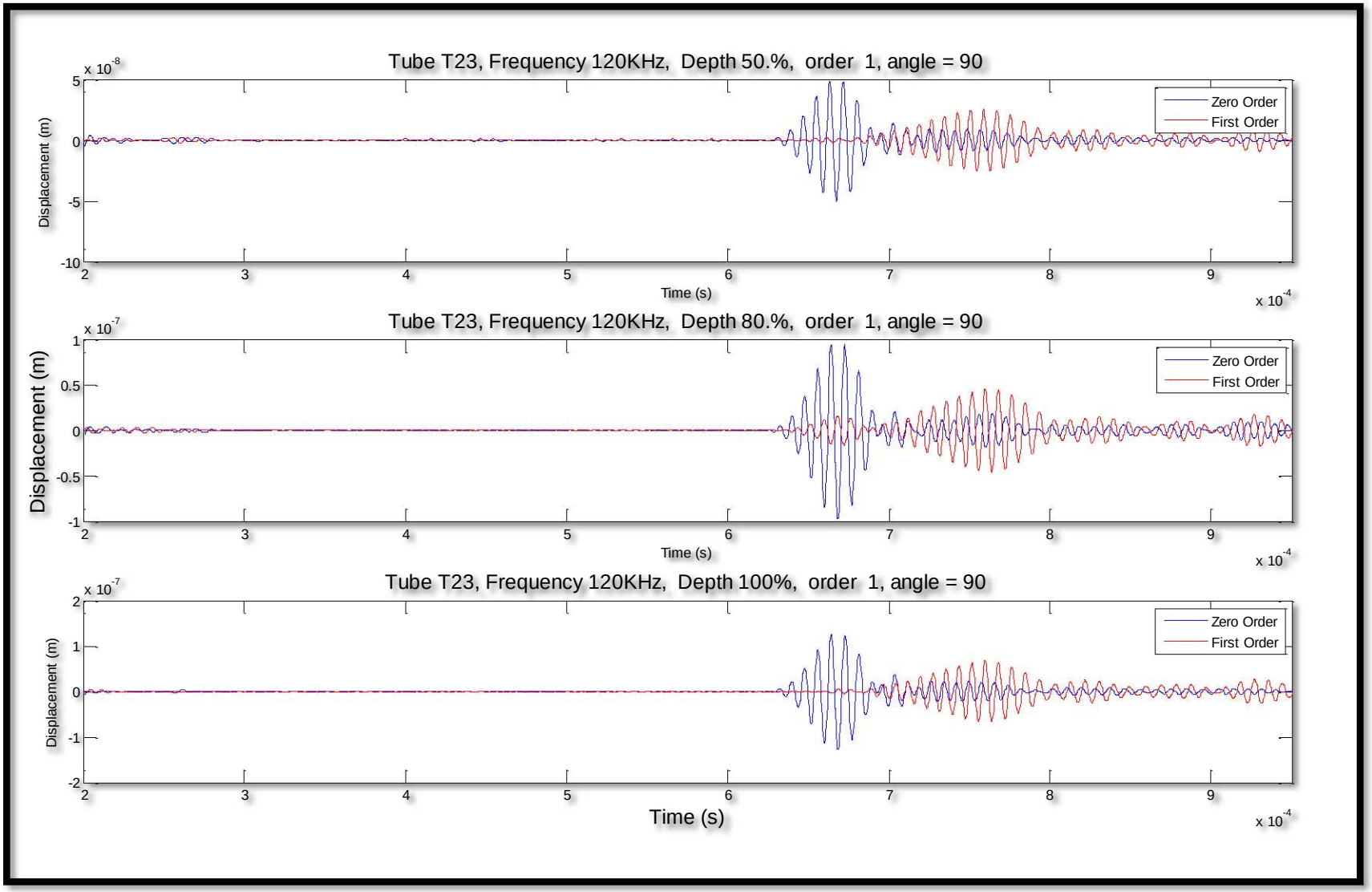
Tube T23, Frequency 120KHz, Depth 50.%, order 1, angle = 90
x 10^-8
Displacement (m)
Time (s)
x 10^-4
Zero Order
First Order
Tube T23, Frequency 120KHz, Depth 80.%, order 1, angle = 90
x 10^-7
Displacement (m)
Time (s)
x 10^-4
Zero Order
First Order
Tube T23, Frequency 120KHz, Depth 100%, order 1, angle = 90
x 10^-7
Displacement (m)
Time (s)
x 10^-4
Zero Order
First Order

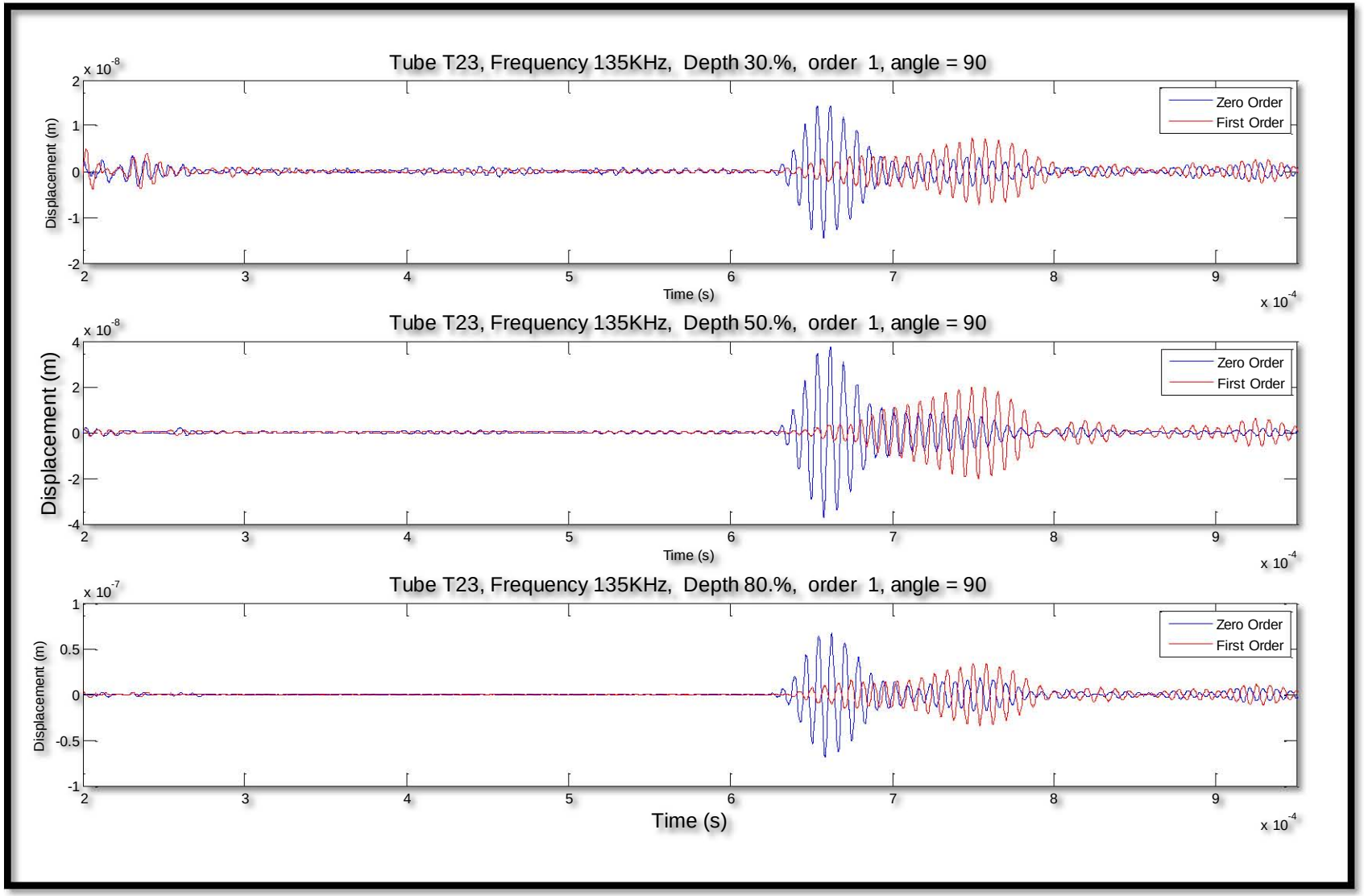
Tube T23, Frequency 135KHz, Depth 30.%, order 1, angle = 90
x 10^-8
Displacement (m)
Time (s)
x 10^-4
Zero Order
First Order
Tube T23, Frequency 135KHz, Depth 50.%, order 1, angle = 90
x 10^-8
Displacement (m)
Time (s)
x 10^-4
Zero Order
First Order
Tube T23, Frequency 135KHz, Depth 80.%, order 1, angle = 90
x 10^-7
Displacement (m)
Time (s)
x 10^-4
Zero Order
First Order

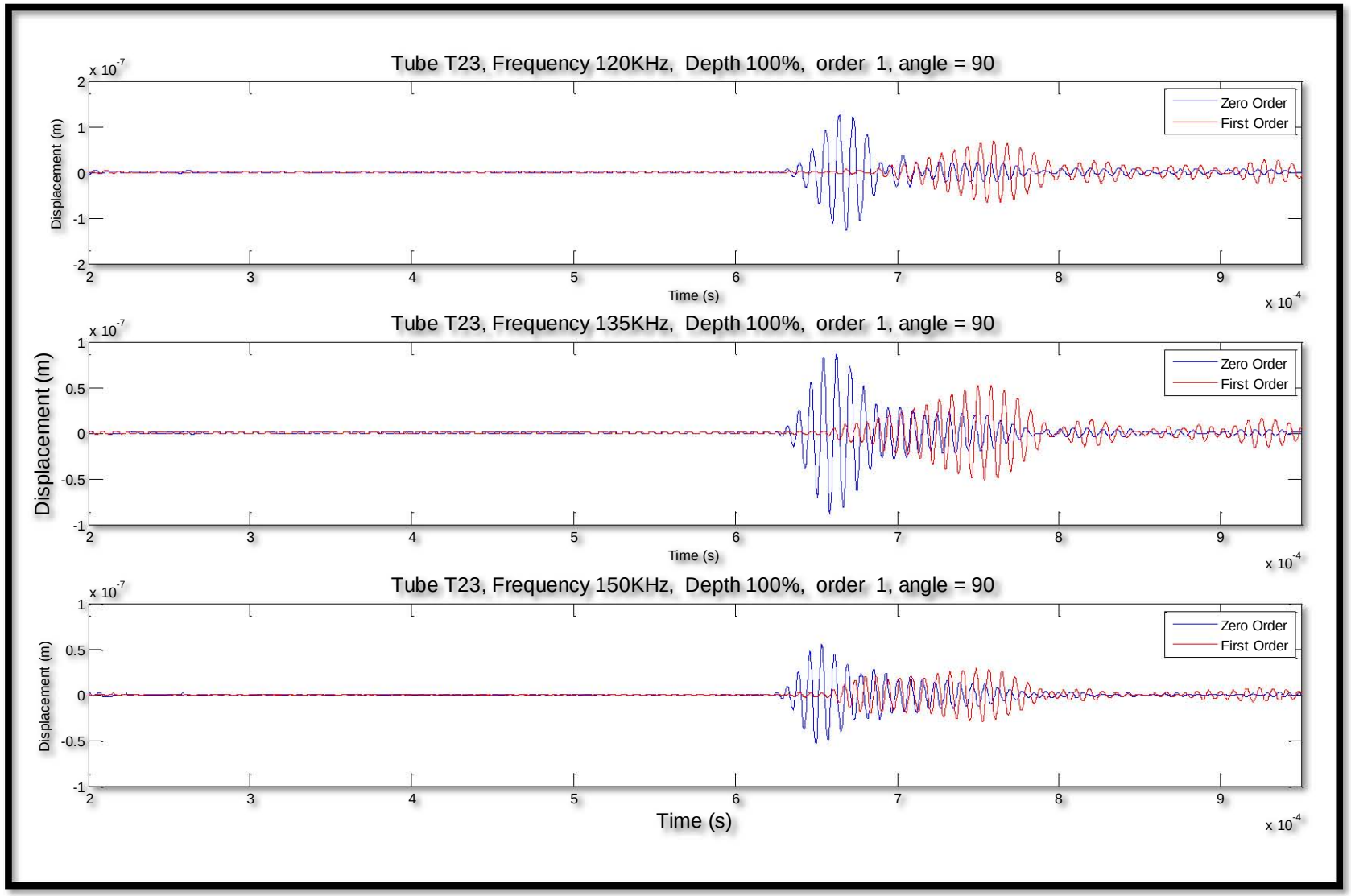
Tube T23, Frequency 120KHz, Depth 100%, order 1, angle = 90
x 10^-7
Displacement (m)
Time (s)
x 10^-4
Zero Order
First Order
Tube T23, Frequency 135KHz, Depth 100%, order 1, angle = 90
x 10^-7
Displacement (m)
Time (s)
x 10^-4
Zero Order
First Order
Tube T23, Frequency 150KHz, Depth 100%, order 1, angle = 90
x 10^-7
Displacement (m)
Time (s)
x 10^-4
Zero Order
First Order

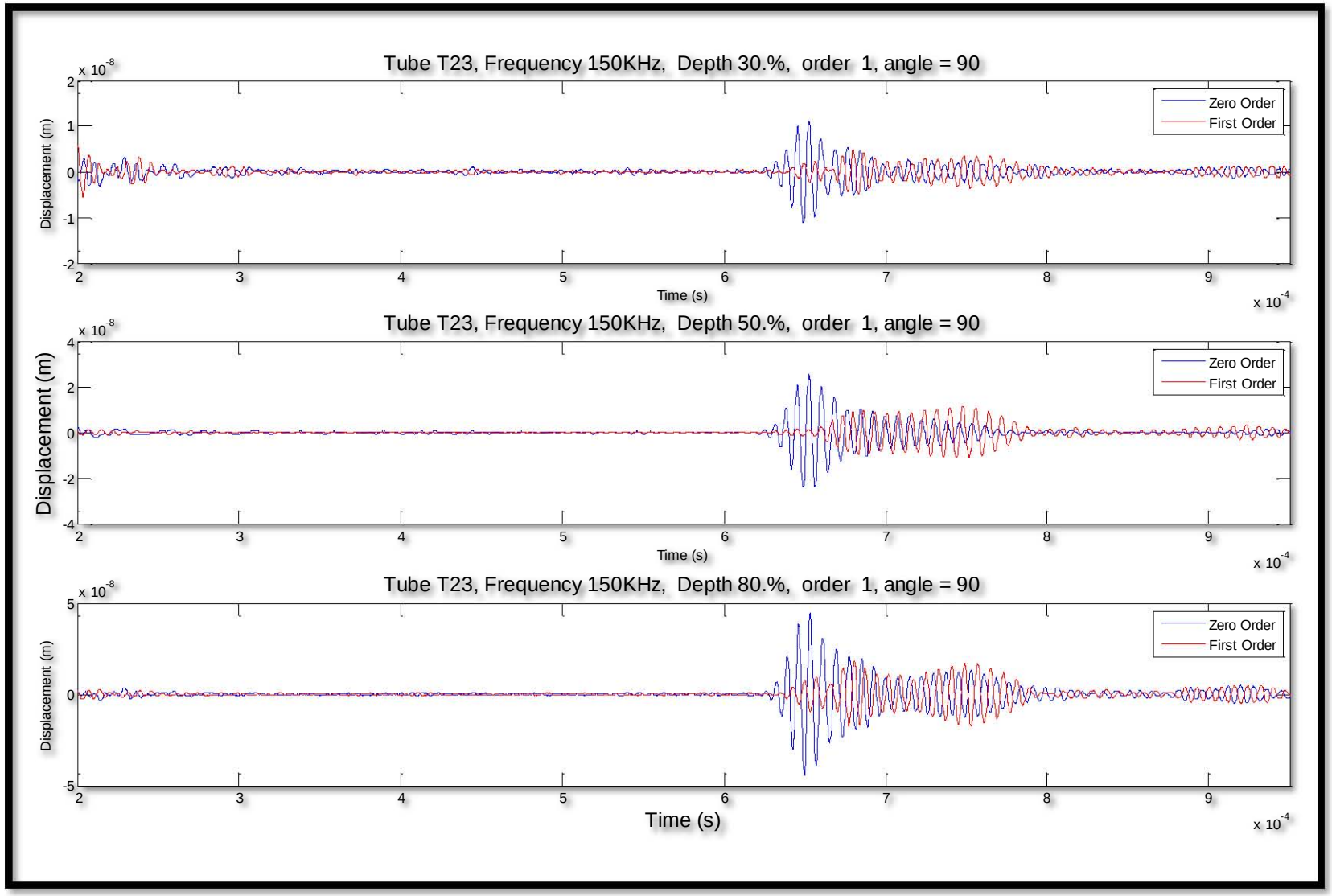
Tube T23, Frequency 150KHz, Depth 30.%, order 1, angle = 90
x 10^-8
Displacement (m)
Time (s)
x 10^-4
Zero Order
First Order
Tube T23, Frequency 150KHz, Depth 50.%, order 1, angle = 90
x 10^-8
Displacement (m)
Time (s)
x 10^-4
Zero Order
First Order
Tube T23, Frequency 150KHz, Depth 80.%, order 1, angle = 90
x 10^-8
Displacement (m)
Time (s)
x 10^-4
Zero Order
First Order

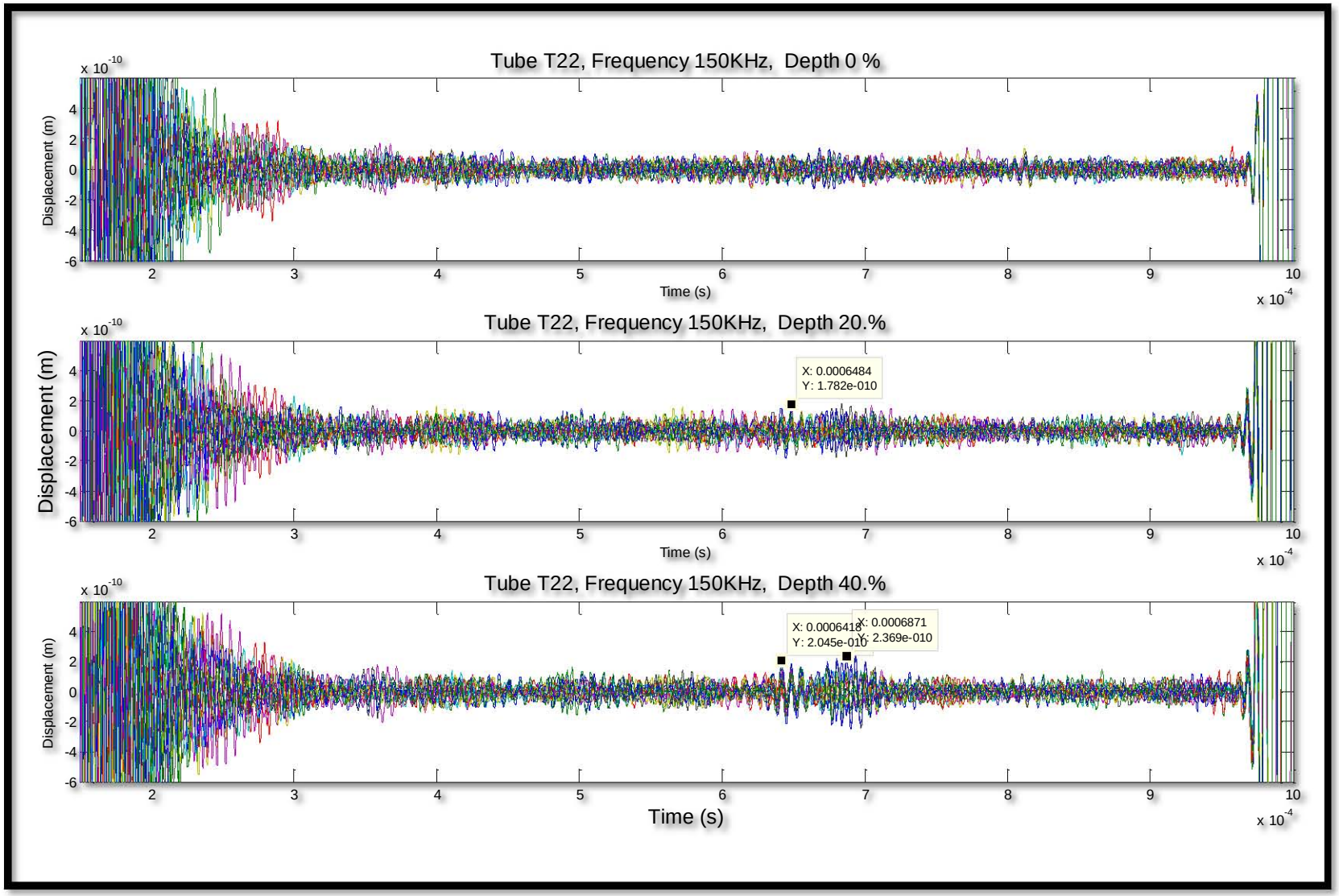
Tube T22, Frequency 150KHz, Depth 0 %
x 10^-10
Displacement (m)
Time (s)
x 10^-4
Tube T22, Frequency 150KHz, Depth 20.%
X: 0.0006484
Y: 1.782e-010
Tube T22, Frequency 150KHz, Depth 40.%
X: 0.0006418
Y: 2.045e-010
X: 0.0006871
Y: 2.369e-010

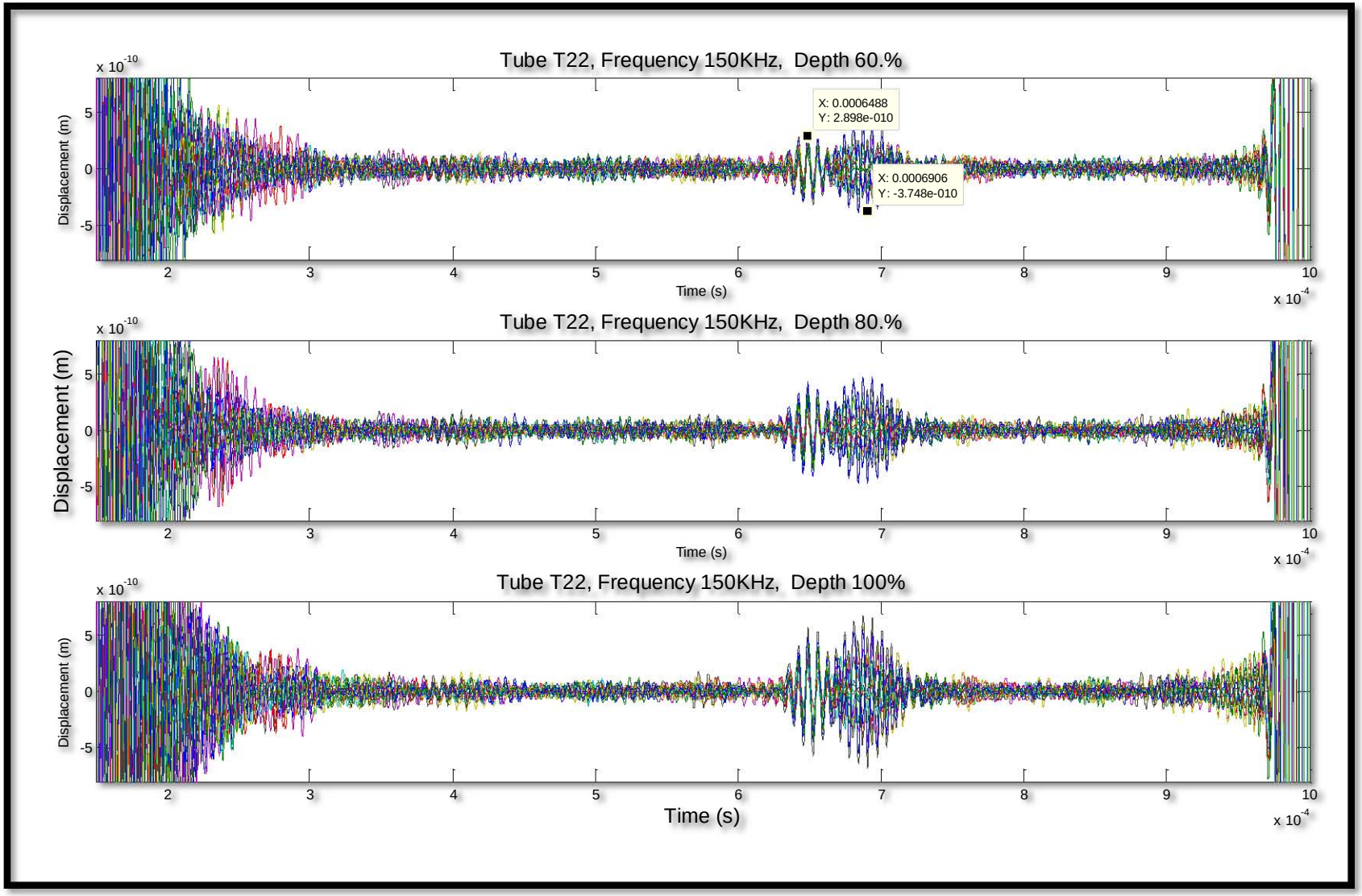
Tube T22, Frequency 150KHz, Depth 60.%
x 10^-10
Displacement (m)
X: 0.0006488
Y: 2.898e-010
X: 0.0006906
Y: -3.748e-010
Time (s)
x 10^-4
Tube T22, Frequency 150KHz, Depth 80.%
Displacement (m)
Time (s)
Tube T22, Frequency 150KHz, Depth 100%
Displacement (m)
Time (s)

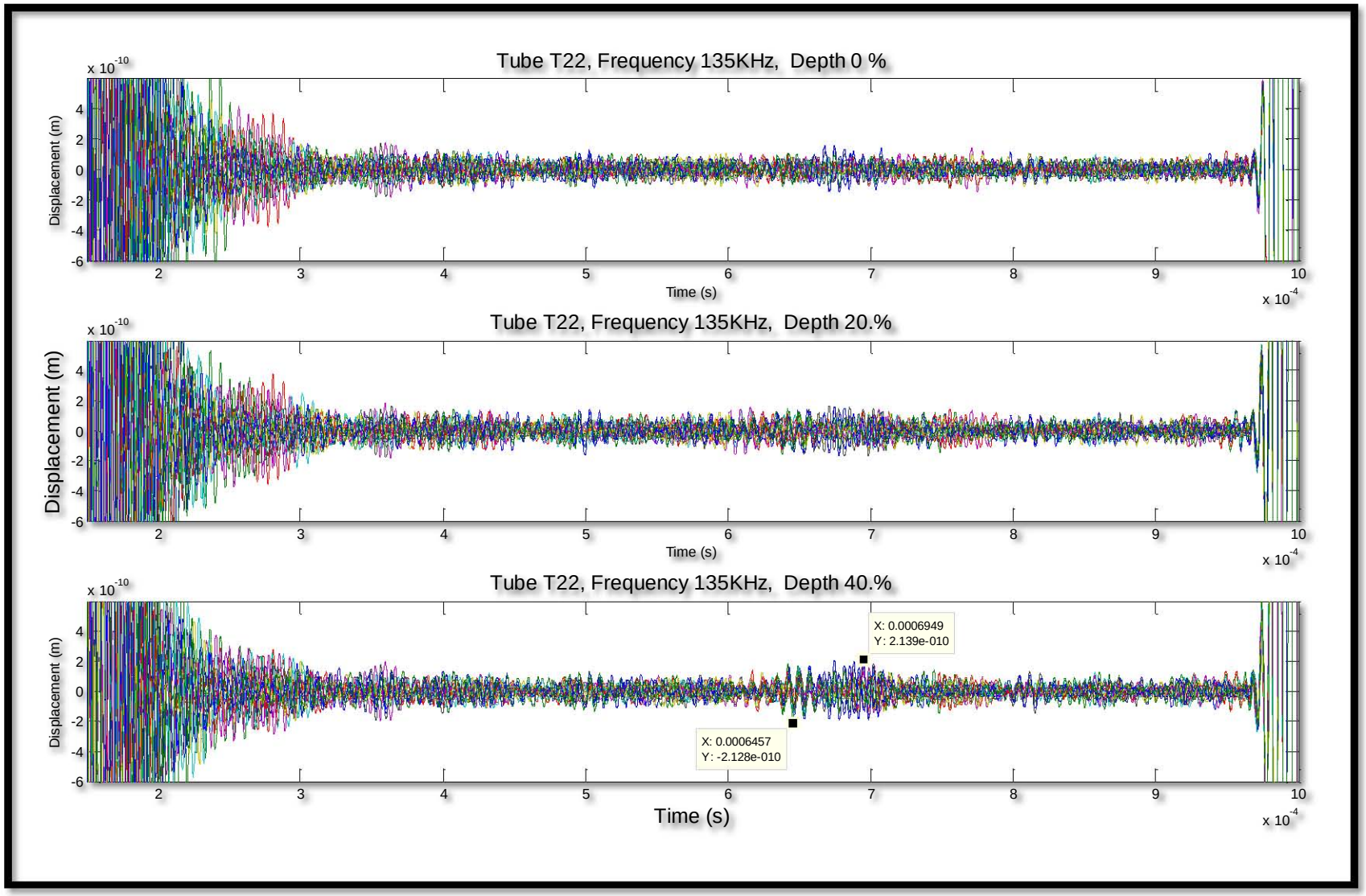
Tube T22, Frequency 135KHz, Depth 0 %
x 10^-10
Displacement (m)
Time (s)
x 10^-4
Tube T22, Frequency 135KHz, Depth 20.%
x 10^-10
Displacement (m)
Time (s)
x 10^-4
Tube T22, Frequency 135KHz, Depth 40.%
x 10^-10
X: 0.0006949
Y: 2.139e-010
X: 0.0006457
Y: -2.128e-010
Displacement (m)
Time (s)
x 10^-4

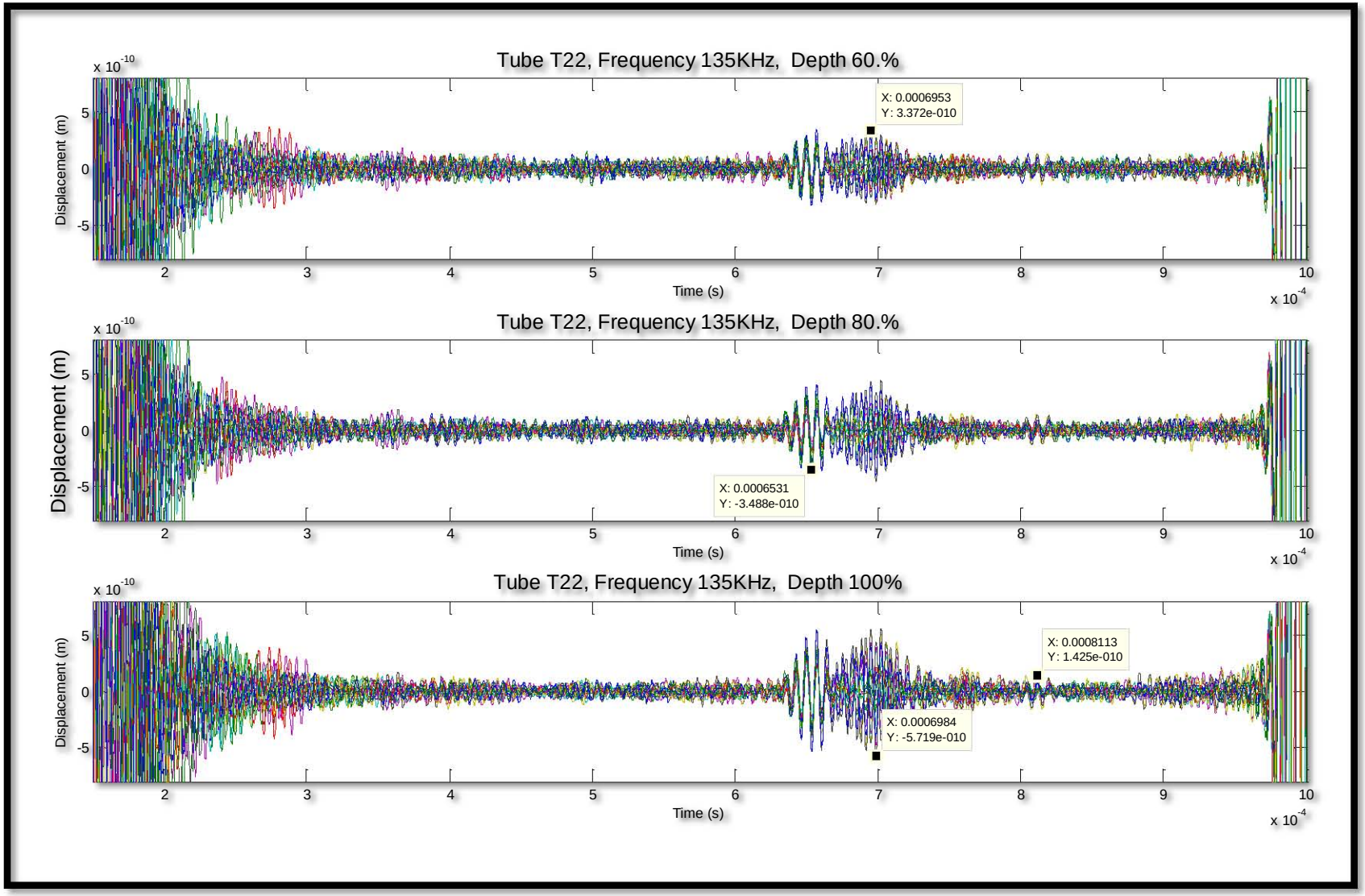
Tube T22, Frequency 135KHz, Depth 60.%
x 10^-10
Displacement (m)
X: 0.0006953
Y: 3.372e-010
Time (s)
x 10^-4
Tube T22, Frequency 135KHz, Depth 80.%
x 10^-10
Displacement (m)
X: 0.0006531
Y: -3.488e-010
Time (s)
x 10^-4
Tube T22, Frequency 135KHz, Depth 100%
x 10^-10
Displacement (m)
X: 0.0008113
Y: 1.425e-010
X: 0.0006984
Y: -5.719e-010
Time (s)
x 10^-4

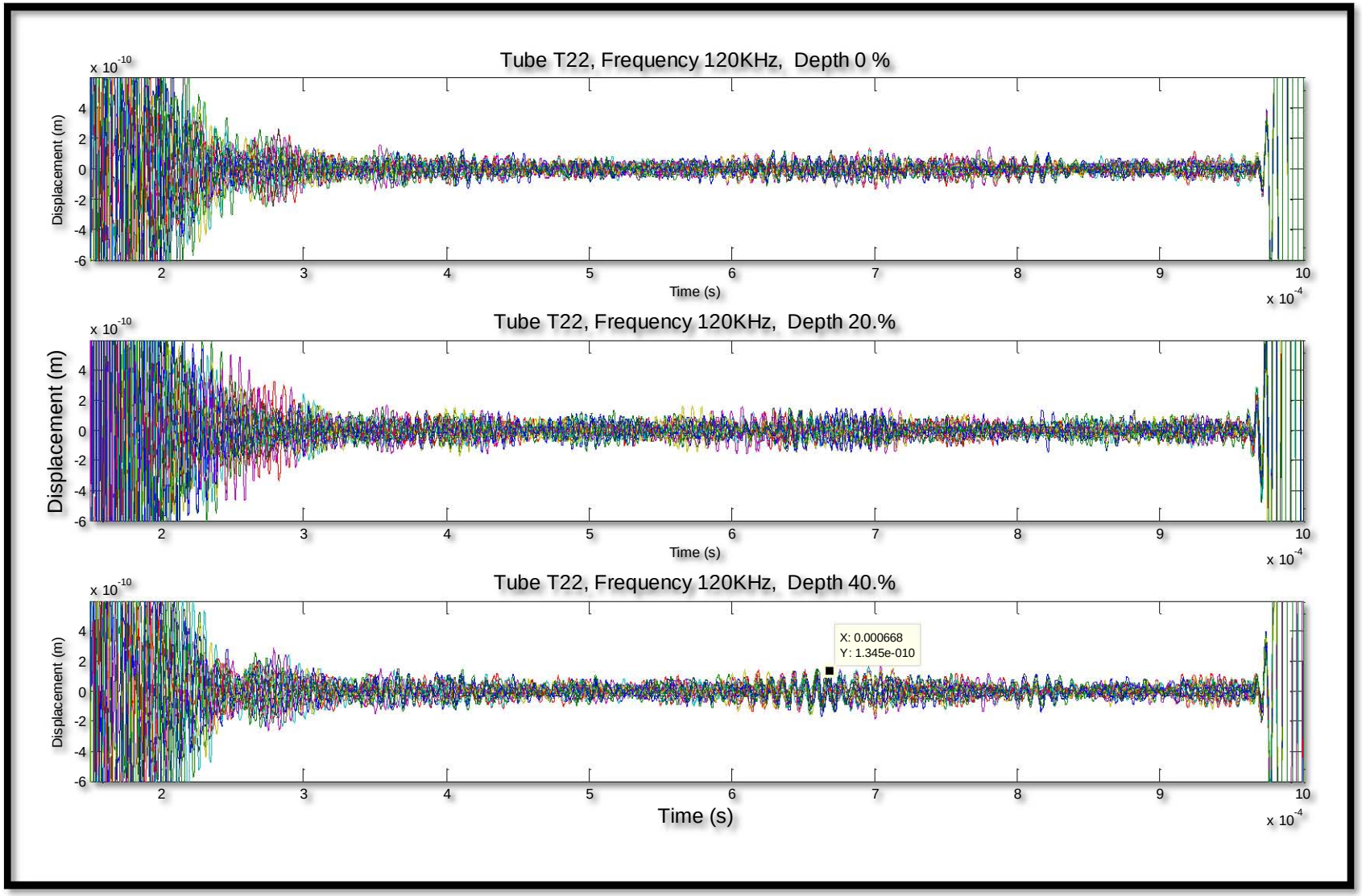
Tube T22, Frequency 120KHz, Depth 0 %
Tube T22, Frequency 120KHz, Depth 20.%
Tube T22, Frequency 120KHz, Depth 40.%
Displacement (m)
Time (s)
x 10^-10
x 10^-4
X: 0.000668
Y: 1.345e-010

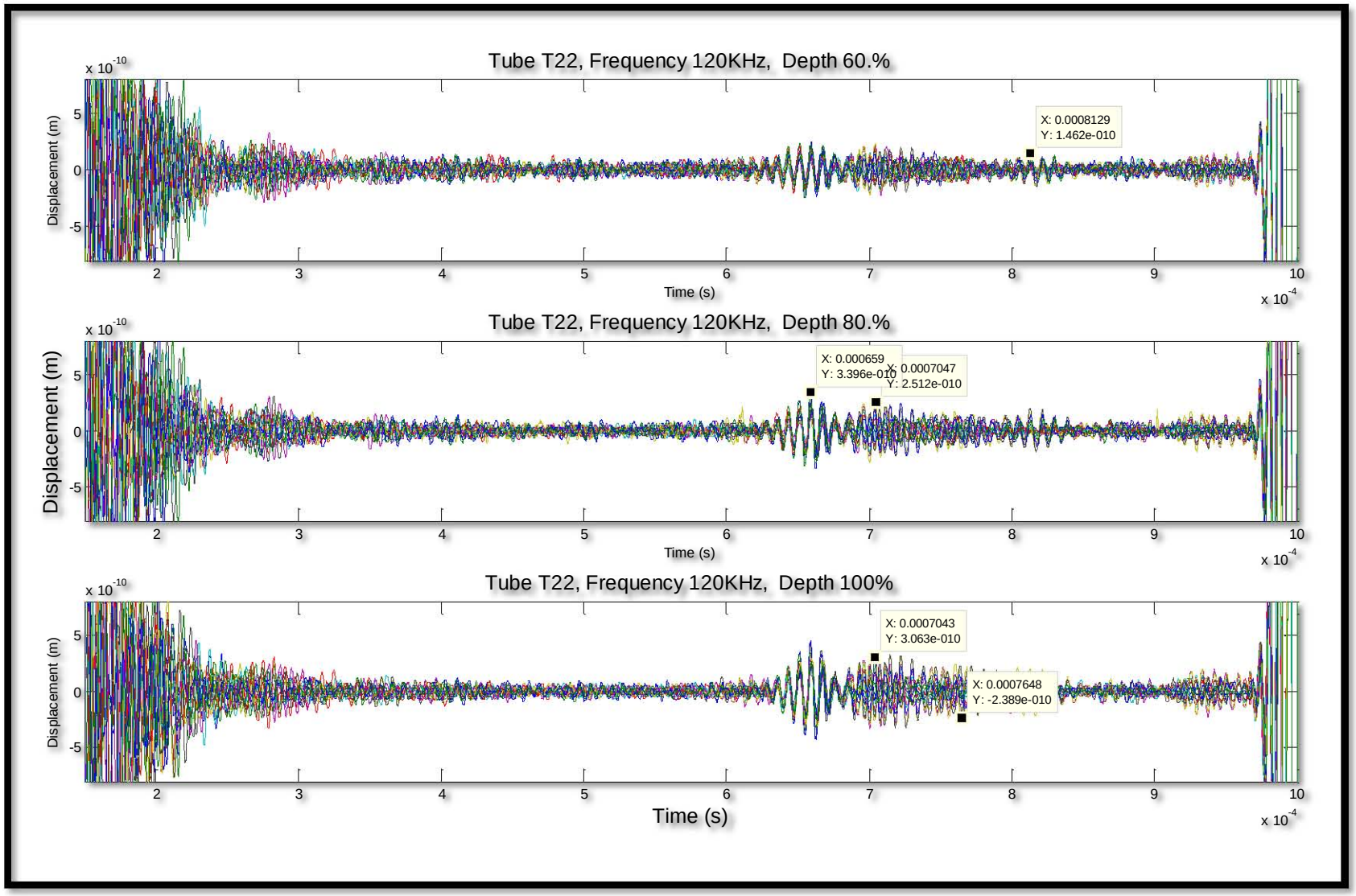
Tube T22, Frequency 120KHz, Depth 60.%
x 10^-10
Displacement (m)
X: 0.0008129
Y: 1.462e-010
Time (s)
x 10^-4
Tube T22, Frequency 120KHz, Depth 80.%
X: 0.000659
Y: 3.396e-010
X: 0.0007047
Y: 2.512e-010
Tube T22, Frequency 120KHz, Depth 100%
X: 0.0007043
Y: 3.063e-010
X: 0.0007648
Y: -2.389e-010

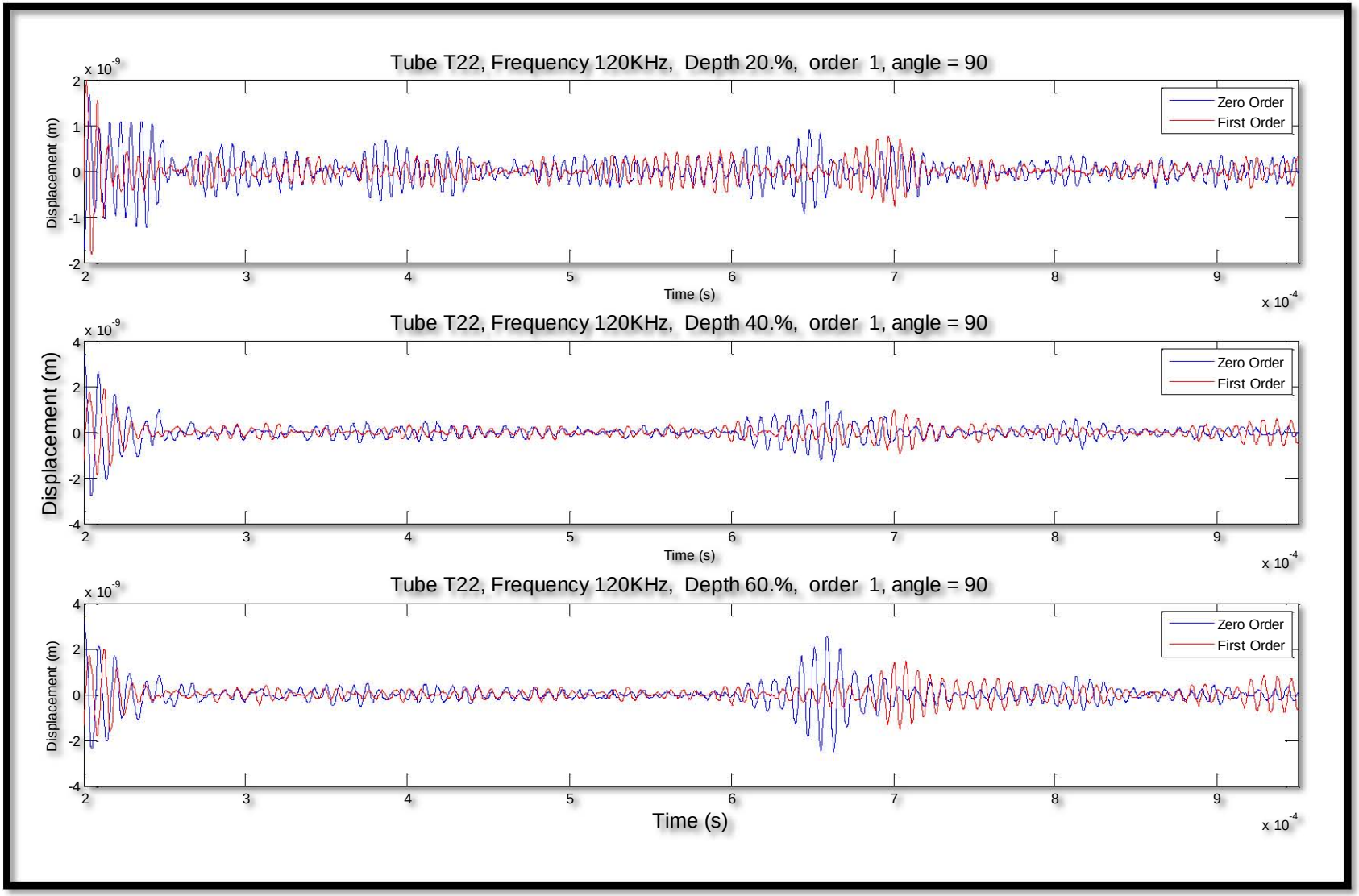
Tube T22, Frequency 120KHz, Depth 20.%, order 1, angle = 90
x 10^-9
Displacement (m)
Time (s)
x 10^-4
Zero Order
First Order
Tube T22, Frequency 120KHz, Depth 40.%, order 1, angle = 90
x 10^-9
Displacement (m)
Time (s)
x 10^-4
Zero Order
First Order
Tube T22, Frequency 120KHz, Depth 60.%, order 1, angle = 90
x 10^-9
Displacement (m)
Time (s)
x 10^-4
Zero Order
First Order

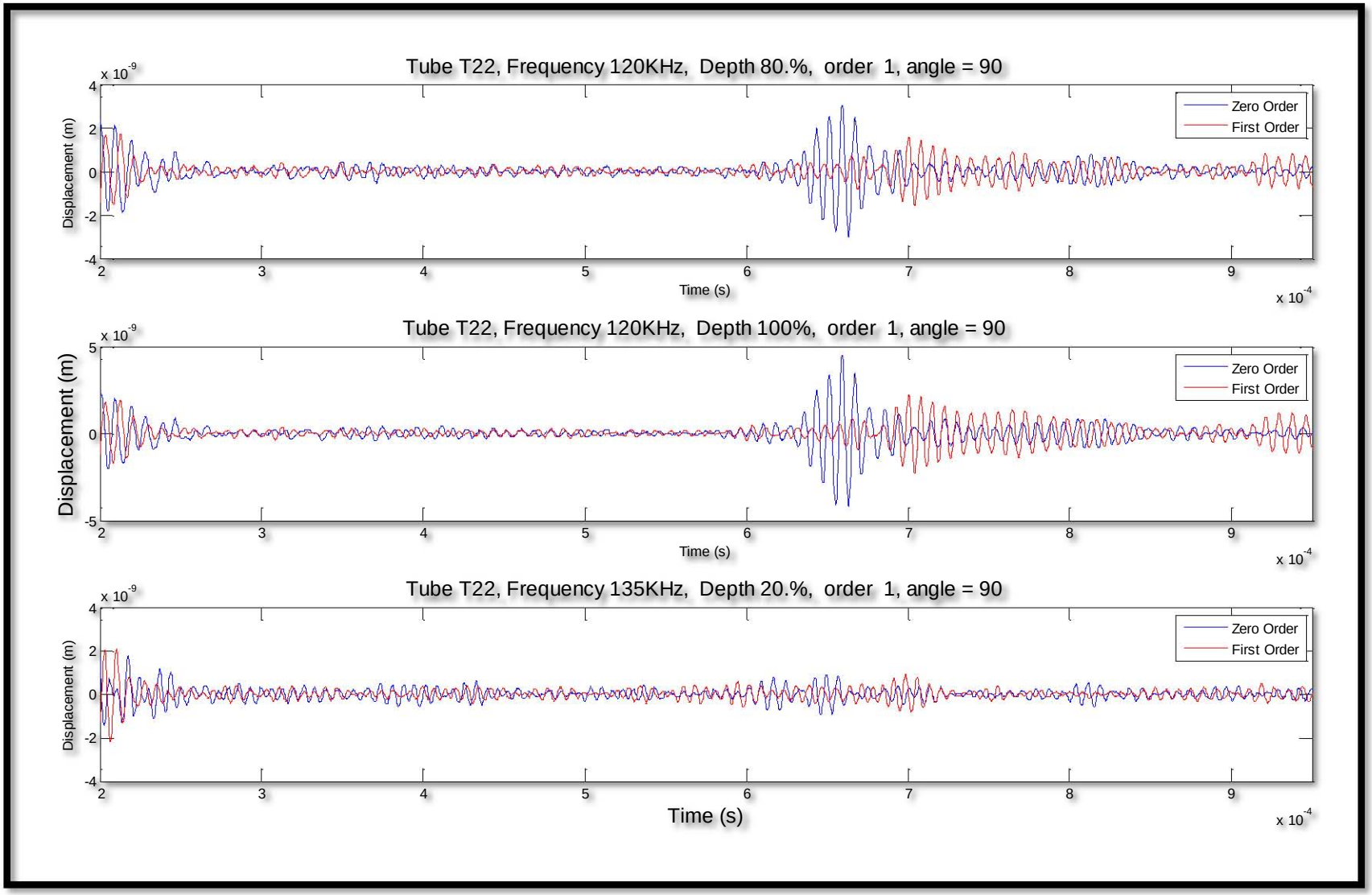
Tube T22, Frequency 120KHz, Depth 80.%, order 1, angle = 90
x 10^-9
Displacement (m)
Time (s)
x 10^-4
Zero Order
First Order
Tube T22, Frequency 120KHz, Depth 100%, order 1, angle = 90
x 10^-9
Displacement (m)
Time (s)
x 10^-4
Zero Order
First Order
Tube T22, Frequency 135KHz, Depth 20.%, order 1, angle = 90
x 10^-9
Displacement (m)
Time (s)
x 10^-4
Zero Order
First Order

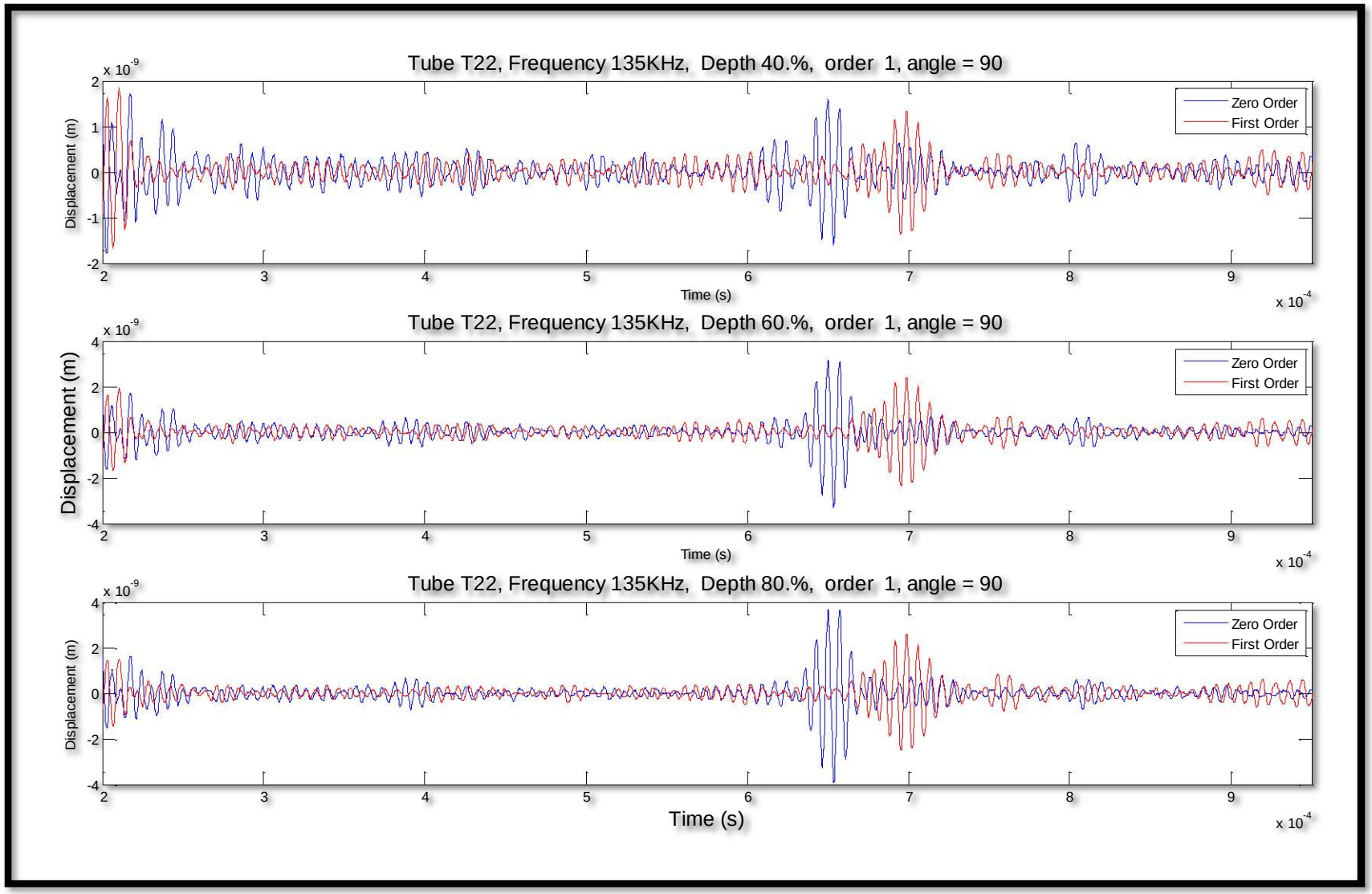
Tube T22, Frequency 135KHz, Depth 40.%, order 1, angle = 90
x 10^-9
Displacement (m)
Time (s)
x 10^-4
Zero Order
First Order
Tube T22, Frequency 135KHz, Depth 60.%, order 1, angle = 90
x 10^-9
Displacement (m)
Time (s)
x 10^-4
Zero Order
First Order
Tube T22, Frequency 135KHz, Depth 80.%, order 1, angle = 90
x 10^-9
Displacement (m)
Time (s)
x 10^-4
Zero Order
First Order

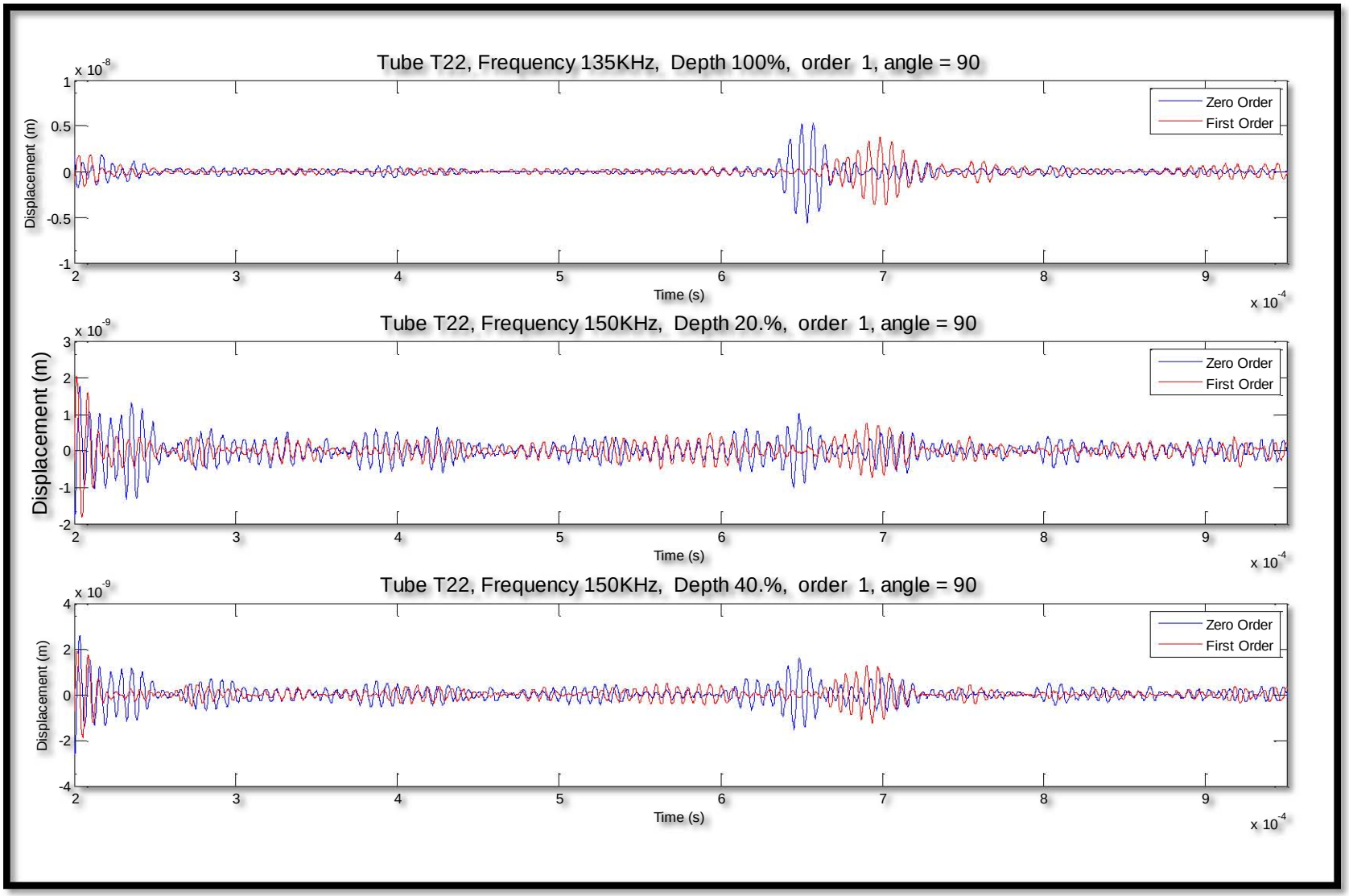
Tube T22, Frequency 135KHz, Depth 100%, order 1, angle = 90
x 10^-8
Displacement (m)
Time (s)
x 10^-4
Zero Order
First Order
Tube T22, Frequency 150KHz, Depth 20.%, order 1, angle = 90
x 10^-9
Displacement (m)
Time (s)
x 10^-4
Zero Order
First Order
Tube T22, Frequency 150KHz, Depth 40.%, order 1, angle = 90
x 10^-9
Displacement (m)
Time (s)
x 10^-4
Zero Order
First Order

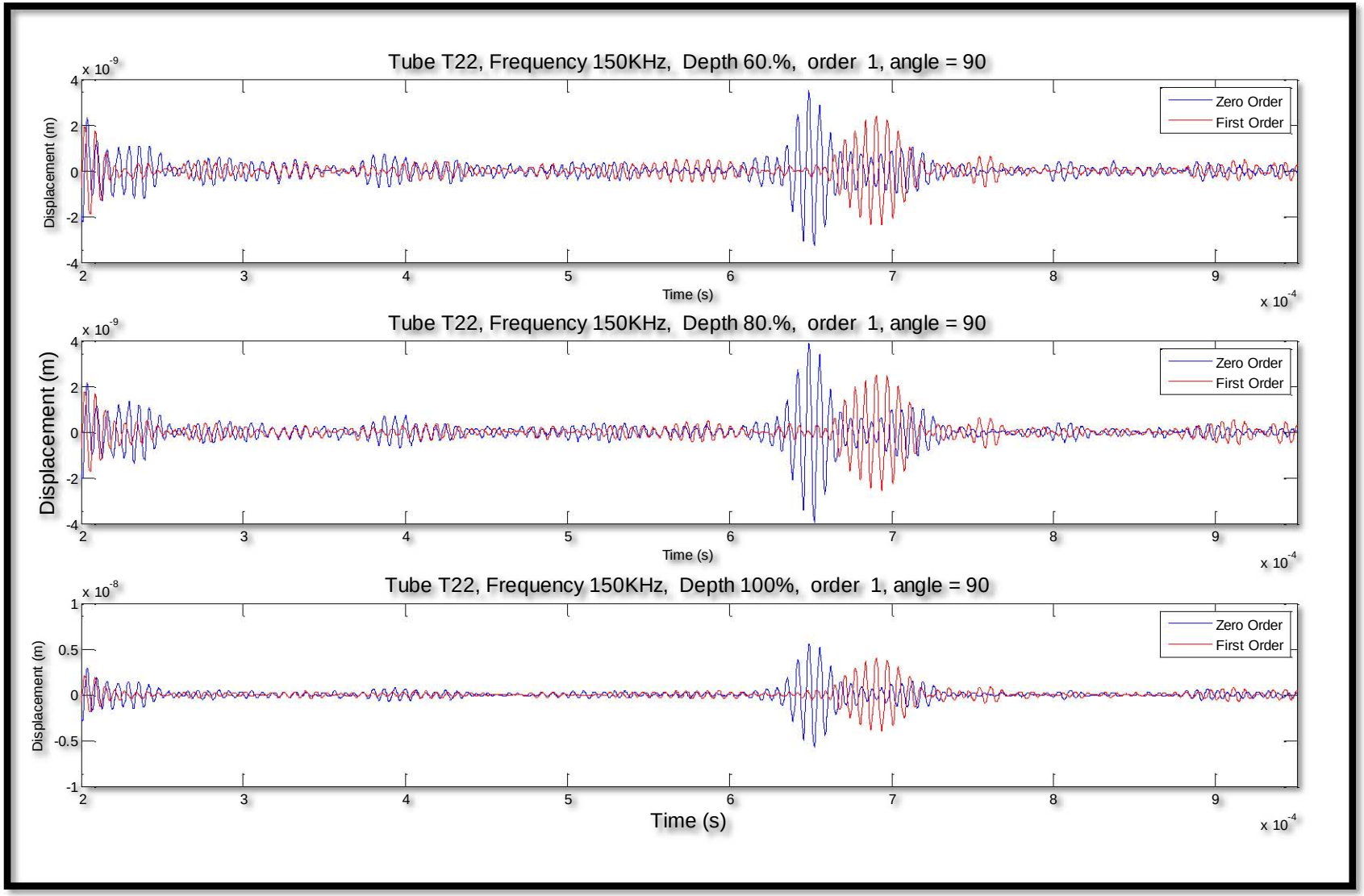
Tube T22, Frequency 150KHz, Depth 60.%, order 1, angle = 90
x 10^-9
Displacement (m)
Time (s)
x 10^-4
Zero Order
First Order
Tube T22, Frequency 150KHz, Depth 80.%, order 1, angle = 90
x 10^-9
Displacement (m)
Time (s)
x 10^-4
Zero Order
First Order
Tube T22, Frequency 150KHz, Depth 100%, order 1, angle = 90
x 10^-8
Displacement (m)
Time (s)
x 10^-4
Zero Order
First Order

A.11 *MATLAB* code for the animation of experimental data

```
% view_scan.m
% file to animate the scan data in time
load 'T23_120_55_100';

%%% filter the data to remove high frequency noise - optional
  time=filter(ones(1,20)/20,1,time(:,:));
  disp=filter(ones(1,20)/20,1,disp(:,:));


scan_pts = 1:1:length(XYZ);
exclude_pts = [];

scan_pts_sel = setdiff(scan_pts,exclude_pts);

%XYZ = XYZ(scan_pts_sel,:);
TRI = delaunay(XYZ(scan_pts_sel,1),XYZ(scan_pts_sel,2));

% figure(1)
% plot(time(1, :)*1e6,disp(1:48,:));



for ti = 1000:2450
  figure(2)
trisurf(TRI,XYZ(scan_pts_sel,1),XYZ(scan_pts_sel,2),disp(scan_pts_sel,ti),1)
%xlim([0    0.6e-3])
zlim([-7e-9 7e-9]);
tim=num2str(fix(time(ti)*1e6));
title(['Time (micro seconds) :  ', tim ]);
end

% disp(ti,scan_pts_sel)
```